# ATOMIC AND PLASMA–MATERIAL INTERACTION DATA FOR FUSION
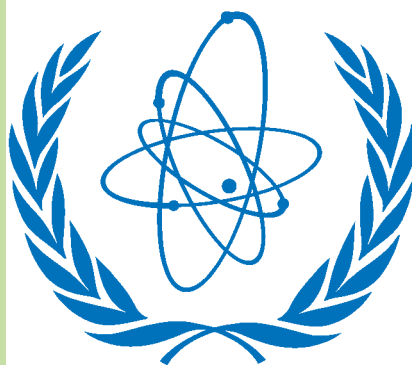
## VOLUME 14

**IAEA**

# ATOMIC AND PLASMA–MATERIAL INTERACTION DATA FOR FUSION

## VOLUME 14

INTERNATIONAL ATOMIC ENERGY AGENCY
VIENNA, 2008

The volumes of ATOMIC AND PLASMA–MATERIAL INERACTION DATA FOR FUSION are published by the International Atomic Energy normally once a year.

For these volumes, papers, letters and reviews are accepted which deal with the following topics:

— Elementary collision processes in fusion plasmas involving photons, electrons, ions, atoms and molecules;
— Collision processes of plasma particles with surfaces of fusion relevant materials;
— Plasma–material interaction phenomena, including the thermophysical response of materials.

Each submitted contribution should contain fusion relevant data and information in either of the above areas. Original contributions should provide new data, using well established methods. Review articles should give a critical analysis or evaluation of a wider range of data. They are normally prepared on the invitation by the Editor or on prior mutual consent. Each submitted contribution is assessed by two independent referees.

Every manuscript submitted must be accompanied by a *disclaimer* stating that the paper has not been published and is not being considered for publication elsewhere. If no copyright is claimed by the authors, the IAEA automatically owns the copyright of the paper.

Manuscripts and correspondence should be addressed to: The Editor, ATOMIC AND PLASMA–MATERIAL INERACTION DATA FOR FUSION, International Atomic Energy Agency, Wagramer Strasse 5, P.O. Box 100, 1400 Vienna, Austria.

# Foreword

Plasmas in fusion energy devices consist of hot core plasmas with cooler regions near the edge. The temperatures are much lower in the edge region than in the core and there is a relatively high population of neutral species. Neutral and charged molecular species may form in this region and influence the plasma diagnostics. A variety of molecules, including species of hydrocarbons, form in the edge region, and hydrocarbon species up to $C_3H_8$ may be produced. As the plasma interacts with the surface of the containment vessel, erosion from the surface will take place. There is then the potential for a number of chemical reactions to occur near the surface. A wide variety of interaction processes will take place involving these molecules in the edge region. It is not well known to what extent these processes affect the efficiency of the divertor itself. Thus there is a need to gather spectroscopic and collisional data to better understand the extent to which these processes are important in the edge regions, including data derived from infrared spectroscopy.

The importance of these molecular processes to fusion research led to a strong recommendation from the A+M Subcommittee of the International Fusion Research Council at its twelfth meeting in May 2000 to initiate a coordinated research project (CRP) to address data needs in this area. The IAEA initiated the CRP on Data for Molecular Processes in Edge Plasmas in 2001. The purpose of the CRP was to identify the specific molecular processes that are important to the plasma physics in the edge region and to provide data for some of these processes.

During the course of the CRP that concluded in 2005, new data have been generated for a variety of processes impacting a number of issues in the edge region of fusion plasmas. Essentially all the goals of the original work plan were fulfilled during the course of the CRP, with the generation of new theoretical and measured cross-sections for a variety of processes in molecules relevant to fusion plasmas. A great deal of the data have now been made available in electronic form for several modelling codes, and have already had a positive impact in a number of fusion applications. Data have also been added to the database, maintained by the IAEA, for direct and cost-free use by all fusion researchers.

The present volume of Atomic and Plasma–Material Interaction Data for Fusion represents the results of the co-ordinated effort of leading experimental and theoretical groups within the CRP. The contributions of the participants of this CRP, contained in the present volume, significantly enlarge the available databases for processes involving molecules found in fusion plasma edge regions. This information is an important ingredient in many modelling and diagnostic studies of fusion plasmas.

The IAEA takes this opportunity to acknowledge the efforts of the CRP participants in the preparation of this volume. The IAEA officer responsible for this publication was R.E.H. Clark of the Division of Physical and Chemical Sciences.

# Contents

# Electron impact ionization/dissociation of hydrocarbon molecules relevant to the edge plasma

*S. Denifl, S. Feil, M. Winkler, M. Probst, O. Echt, S. Matt-Leubner, V. Grill, P. Scheier, T.D. Märk*

Institut für Ionenphysik der Leopold Franzens Universität Innsbruck, Technikerstrasse 25, A-6020 Innsbruck, Austria

## Abstract

Total and partial cross-sections for electron impact ionization of various C1, C2 and C3 hydrocarbon molecules have been determined experimentally from a threshold up to 1000 eV. Here we will discuss as an illustrative example ionization and dissociation reactions of methane and acetylene. Using a deflection and retarding field method, the ion kinetic energy distributions of all product ions are measured. Extensive three-dimensional ion trajectory simulations of the ion source are performed to determine the ion loss resulting from high initial kinetic energy of ions. Discrimination factors are determined as a function of the initial ion kinetic energy. Multiplication of these factors with the measured ionization efficiency curves leads to accurate relative partial ionization cross-sections. In combination with the kinetic energy distributions measured as a function of the electron energy it is also possible to determine cross-sections that are differential with respect to the initial kinetic energy of the ion. Thereby different reaction pathways, such as Coulomb explosion and dissociative single ionization, that lead to a specific product ion, can be identified. Moreover, as a particular instructive example unimolecular dissociation processes of $C_3H_5^{2+}$ formed via electron impact ionization of the hydrocarbon molecule propane have been studied and will be presented here. Fragment ions are identified and the kinetic energy release distribution of the Coloumb explosion of $C_3H_5^{2+}$ is determined utilizing the mass analysed ion kinetic energy scan technique. In parallel, high level ab initio quantum chemical calculations of the structure and energetics of $C_3H_5^{2+}$ have been performed.

## 1. Introduction

Hydrocarbon molecules are abundant constituents of planetary atmospheres and major compounds in combustible gas mixtures and in fusion edge plasmas [1–5]. Carbon based materials are today widely used in current tokamaks because of their obvious advantages such as low radiative capacity and high heat resistivity. They (e.g. in the form of graphite or carbon–carbon composites) were also considered as one of the plasma facing materials in the divertor design of the International Thermonuclear Experimental Reactor (ITER) [6]. However, the interaction of the tokamak plasma with these carbon based walls leads to the formation of a variety of hydrocarbon molecules or ions. These compounds are then further modified in subsequent collisions with the plasma (electrons and protons), including ionization, dissociation and recombination reactions. It is interesting to note that two recent workshops dedicated to the atomic and molecular data situation for tokamak fusion science [7] revealed that more qualitative and quantitative data are urgently needed on these processes.

Dissociative ionization of molecules by electron impact (see reaction (1)) is an important process not only in edge plasmas in fusion reactors, but also in many other areas such as low temperature plasmas, radiation chemistry, mass spectrometry, and chemical analysis [1–5]:

$$AB + e \rightarrow A^+ + B + KER \tag{1}$$

The ionic fragment ($A^+$) and the neutral fragment (B) produced via dissociative ionization often carry substantial amounts of kinetic energy. The kinetic energy release distribution (KERD) of a particular fragment determines the energy deposition and the energy transfer pathways in the corresponding media (plasmas), i.e. for modelling such environments, not only the relative abundance of fragment ions (the partial ionization cross-sections) but also their kinetic energy distribution (energy differential cross-sections) are required. Moreover, the kinetic energy distribution for a given fragment ion can depend strongly on the electron energy due to different threshold energies of formation (different exothermicities) [8, 9].

For an accurate determination of absolute partial und total ionization cross-sections recently, especially dedicated instruments were constructed to ensure complete collection efficiency [10, 11]. For commercial mass spectrometers, which collect fragment ions with high kinetic energy less

1

efficiently [12–15], accurate values can be only obtained after determination of the discrimination factor for each electron energy. This has been shown by Poll et al. [12] using ion trajectory calculations of the extraction region for a standard double focusing two sector field mass spectrometer equipped with a modified Nier type ion source. The kinetic energy of the ions was investigated by a deflection method applied in the direction perpendicular to the plane of the mass spectrometer (z direction) [12].

Hydrocarbon molecules are known to form fragment ions with broad kinetic energy distributions ranging from thermal energies to many eV [12, 16–18]. It turned out that methane ions are formed with (i) a low-energy component comprised of thermal and/or quasi-thermal ('slow') ions with a maximum kinetic energy of ~0.3 eV and in addition with (ii) a high energy component consisting of energetic ('fast') ions with a broad energy distribution from 0.5 eV to ~10 eV [16, 19–23].

Methane and acetylene are the most studied hydrocarbon molecules. Thus absolute total und partial ionization cross-sections for photon [24–26] and electron [27–32] impact and nascent fragment ion energy distributions [8, 16, 26, 33, 34] have been studied extensively for these molecules. Electron impact total ionization cross-sections have also been determined theoretically, applying the BEB (Binary-Encounter-Bethe) model [35], the DM (Deutsch–Märk) method [36] and the JK (Jain-Khare) method [37]. Partial electron impact ionization cross-sections have been calculated for methane [38, 39] as well as total electron impact cross-sections for various $CH_x$, radicals [40]. The dissociation pathways of partially and fully deuterated acetylene were investigated to obtain information of one of the smallest dications known to exist, i.e. $C_2H_2^{2+}$ [41, 42].

Often ionization of molecules leads to the formation of so called metastable ions that are sufficiently stable to leave the ion source but decay on the way to the detector. Unimolecular (metastable) decay reactions can provide information about the structure, stability and energetics of the corresponding molecular ion. The kinetic energy that is released in a metastable decay process is often substantially different for singly and doubly charged molecular cations. This information can be used to distinguish between the following different reaction pathways, reaction (2) and (3), that lead to the same fragment ion $A^+$ in the ion source:

$$AB + e \rightarrow (AB^{++})^* \rightarrow A^+ + B^+ + KER \qquad (2)$$
$$\rightarrow A^+ + B + KER \qquad (3)$$
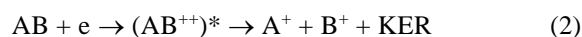
Small, doubly charged molecules are formed in high abundance in the gas phase (for recent reviews, see Refs [43, 44]). Most of them are metastable, and charge separation by tunneling, thermal activation, curve crossing or other mechanisms, leads to two ionic fragments that are accelerated to several eV in their mutual electrostatic field (Coulomb explosion). It has been suggested that these

systems may be used for energy storage [45]. An accurate procedure to measure kinetic energy release (KER) distributions for metastable decays is the MIKE (mass analysed ion kinetic energy) scan technique. It has been applied to several systems that are unstable with respect to Coulomb explosion, prepared by charge stripping, photon or electron impact ionization of singly charged precursors [43, 46]. Other reports pertain to metastable decay of doubly charged molecules [47–50] and clusters [51].

In the present review we summarize recent results from our laboratory on electron impact ionization of methane [52], acetylene [53] and propane [54]. For the latter molecule the KER for the Coulomb explosion of the metastable $C_3H_5^{2+}$ fragment ion is determined.

## 2. Experimental set-up

All the experiments discussed in the present work were performed utilizing the mass spectrometer schematically shown in Fig. 1. It consists of a commercially available high resolution double focusing mass spectrometer (Varian MAT CH5-DF) of reversed Nier-Johnson type geometry that has been modified several times. A detailed description can be found in earlier publications [12, 55, 56].
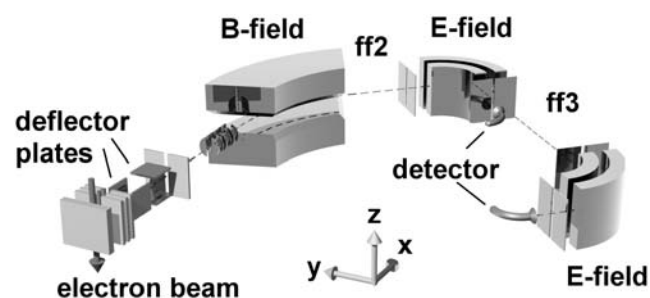


**Figure 1.** Schematic view of the experimental set-up.

Neutral gas phase molecules are introduced via a capillary leak gas inlet system into the collision chamber of the ion source. The ions are produced in a NIER type electron impact ion source (typical electron currents 10 µA) which is kept at a temperature of about 200°C to avoid contamination of the source. The kinetic energy of the electrons can be varied from about 0 to 1000 eV as set by a computer. The spread of the electron energy distribution (full width at half maximum) is about 0.5 eV. The ions formed via the interaction of the electrons with the neutrals are extracted from the ion source housing by a pusher lens and several extraction lenses towards the mass spectrometer. Before the ions enter the analysing section of the mass spectrometer through the entrance slit they are accelerated through a potential drop of 3 kV (standard acceleration voltage) and then pass two pairs of perpendicular deflection plates which allow steering of the ion beam. For cross-section measurements, the deflection plates are used to sweep the ion beam across the entrance slit [56] and the

cross-section is obtained from the integrated ion signal. In all other modes of operation, the deflection plates are kept at fixed voltages for maximum ion current. After the mass spectrometer entrance slit, the ions pass the first field free region ff1 with a length of 61 cm. Then they reach the 48.5° magnetic sector field B where momentum analysis takes place. The ions pass the second field free region (ff2; length: 33 cm) and enter the first 90° electrostatic sector. The ions can be detected by a Faraday cup or channeltron type secondary electron multiplier that can be moved in and out of the path of the ion beam. In the case that the Faraday cup and the channeltron are removed from the ion beam axis the ions enter a recently added third field free region (ff3, length 92 cm), pass through another electrostatic sector field (E2), and are detected by an electron multiplier.

Unimolecular decomposition of ions in ff2 and ff3 is studied utilizing the mass analysed ion kinetic energy (MIKE) scan technique. Thereby the mass to charge ratio of the fragment ion of a decay reaction

$$m_p^{z_p+} \rightarrow m_f^{z_f+} + \textit{neutral and/or charged particles} \quad (4)$$
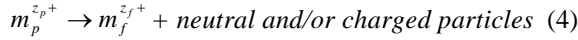
is determined from the position of the centre of the MIKE peak of the fragment ion and the mass to charge ratio of the parent ion via

$$\frac{m_f}{z_f} = \frac{E}{E_0} \cdot \frac{m_p}{z_p}. \quad (5)$$

$m_p$ and $m_f$ denote the mass and $z_p$ and $z_f$ the charge state of the parent and corresponding fragment ion, respectively, and the ratio $E/E_0$ is the centre of the MIKE peak of the fragment ion in relative units of the sector field voltage. At the sector field voltage $E_0$ the parent ion passes through the electrostatic analyser.

The parent ions have a finite kinetic energy distribution which leads to a finite width and characteristic peak shape of the MIKE scans. Moreover, any KER in the decay will modify the peak shape of the fragment ion [55, 57, 58]. When the KER distribution is a Maxwell–Boltzmann distribution (which is often the case for a reaction without a reverse activation barrier), and the exit slit of the electric sector field is long enough that it does not discriminate against ions that are emitted in the $z$ direction, i.e. perpendicular to the beam axis and parallel to the length of the slit (see Fig. 1), a Gaussian peak is observed. The decay of $C_3H_8^{+*}$ into $C_3H_7^+ + H$ which is shown in the left panel of Fig. 2 is such an example.

A flat rectangular peak is obtained when the KER distribution is narrow and starts at energy values larger than zero, but at the same time even at the highest KER values all ions can reach the detector, i.e. with no discrimination against ions emitted perpendicularly to the flight direction of the precursor ion (see $C_3H_6^+$ formed via $H_2$ loss from $C_3H_8^{+*}$ in Fig. 2). A dished peak is obtained when the KER is single valued and large such that the finite length of the exit slit

leads to strong discrimination against ions that are emitted with large $z$ components. For extreme discrimination a double peak (split peak) is observed that is located symmetrically with respect to the sector field voltage given by equation 5 (see Fig. 2, right hand side of the panel, the reaction $C_3H_5^{2+} \rightarrow C_2H_2^+ + CH_3^+$). The high energy component of the split peak arises from ions that dissociate with the fragment of interest being expelled in the forward direction; it will be somewhat more intense than the low energy component due to different degrees of discrimination.
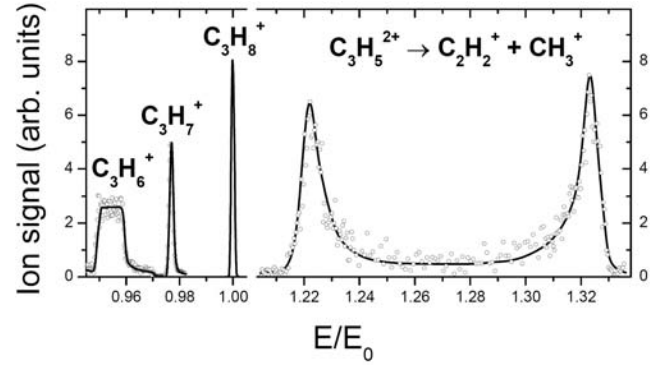


**Figure 2.** MIKE scans of the parent ion $C_3H_8^+$ and the fragment ions $C_3H_7^+$ and $C_3H_6^+$ that are formed via unimolecular dissociation of the $C_3H_8^{+*}$. The right hand side double peak structure is a MIKE scan of the product ion $C_2H_2^+$ that is formed via Coulomb explosion of $C_3H_5^{2+}$. All decay reactions occurred in the second field free region of the mass spectrometer shown in Fig. 1. The ion yield of the fragment ions is normalized to roughly the same intensity for a better comparison ($C_3H_6^+$ and $C_2H_2^+$ are multiplied with $10^4$ and $C_3H_7^+$ with $10^3$). Please note the different shape of the fragment ions, i.e. Gaussian for $C_3H_8^{+*} \rightarrow C_3H_7^+$, flat topped for $C_3H_8^{+*} \rightarrow C_3H_6^{+*}$ and a double peak for $C_3H_5^{2+} \rightarrow C_2H_2^+$ (see text).

## 3. Results and discussion

### 3.1. $CH_4$

The mass spectrum of methane measured at the electron energy of 100 eV is shown in Fig. 3. The electron current is $10\,\mu A$ and the pressure of methane in the ion source is $6 \times 10^{-5}$ Pa. Ions formed via the ionization of the residual gas in the background ($9 \times 10^{-7}$ Pa) are subtracted by means of a mass spectrum which is recorded without the presence of methane in the ion source. The mass spectrum is not corrected for discrimination effects due to different initial kinetic energies of fragment ions and thus the peak heights do not correlate with the partial cross-section values for this electron energy given below.

Figures 4 and 5 show the ion beam profiles in the z direction for the parent ion $CH_4^+$ and the fragment ion $C^+$ measured at different electron energies from the respective threshold up to 800 eV. The recorded z profiles can be converted to kinetic energy distributions, because the kinetic energy of the ion is directly proportional to the square of the applied z voltage. Ion kinetic energy distributions are derived by plotting the first derivative of the z profile as a
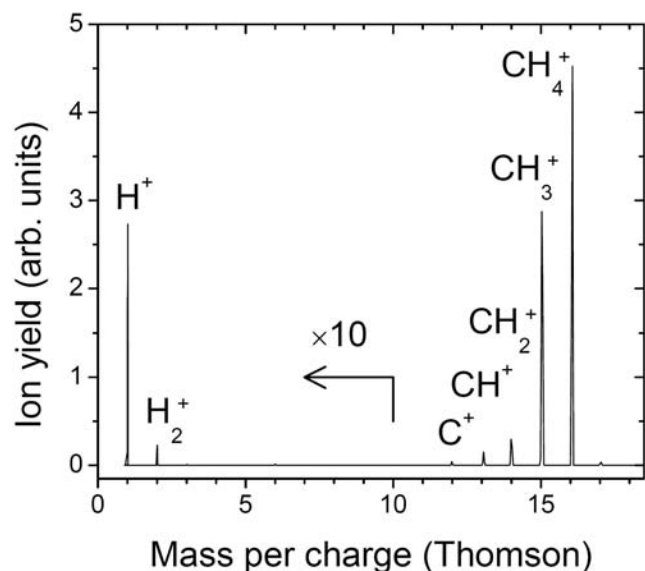
**Figure 3.** Positive ion mass spectrum of $CH_4$ ionized by 100 eV electrons and 10 μA electron current. The ion signal of masses below 10 Da is multiplied with a factor of 10 (this figure is taken from Ref. [52]).

function of the square of the z deflection voltage and multiplied with a factor that is determined by the geometry of the deflector plates and the acceleration voltage of the mass spectrometer (for details see Ref. [12]). For a few electron energies, the resulting ion kinetic energy distributions are included in Figs 4 and 5. For a comparison, the graph of the kinetic energy distributions for $CH_4^+$ also includes the corresponding data of $Ar^+$. The kinetic energy of the latter ion is only determined by the ion source temperature (approximately 500 K). There is a surprising difference in the mean energy distribution between the $Ar^+$ and the $CH_4^+$ parent ion, which increases from 0.5 meV for electron energies below 30 eV to 1.7 meV for electron energies larger than 30 eV. The average value of all electron energies is 1.3 meV. This result can be explained in two

ways: (i) Ar is introduced as a narrow collimated gas jet in the y direction and thus the kinetic energy of the neutral atoms corresponds to lower temperaturees than 500 K and (ii) the $^{12}CH_4^+$ ion yield is contaminated by the fragment ion $^{13}CH_3^+$ (same mass as parent ion) with a relative abundance of ~1%. The latter cation has a higher average kinetic energy than the parent ion. The ion kinetic energy distribution of $CH_4^+$ shows almost no dependence on the electron energy, which is not the case for all other fragment ions, which reveals a pronounced dependence on the electron energy (see the example $C^+$ in Fig. 5), i.e. exhibiting wider distributions for higher electron energies. Moreover, the z profile deviates clearly from a single Gaussian curve (Fig. 5) and thus the resulting kinetic energy distribution will not have a Maxwell–Boltzmann type shape. For the $C^+$ fragment ion the kinetic energy distribution consists of two different contributions, i.e. a low one with an average kinetic energy of about 200 meV and a high energy part with an average value of about 400 meV. The relative height of the two distributions (due to ion pair formation or fragmentation of a singly charged precursor ion) changes with the energy of the ionizing electron and this leads to the observed dependence of the average ion kinetic energy on the electron energy.

In previous investigations it was pointed out that the ion collection efficiency is strongly influenced by high kinetic energies of fragment ions and thus on the resulting cross-sections derived from ion efficiency curves [2, 12–15]. Poll et al. [12] determined via ion trajectory simulations of their ion source the discrimination factors for ions with different initial kinetic energies. These previous calculations for a similar experimental set-up as the present one neglected the presence of a magnetic field for guiding the electrons. The effect of this magnetic field (strength of about 40 mT) can be neglected for all heavy ions. However, very light ions like $H^+$ and $H_2^+$ are substantially deflected into the y direction. Using a newer version of SIMION [59], the
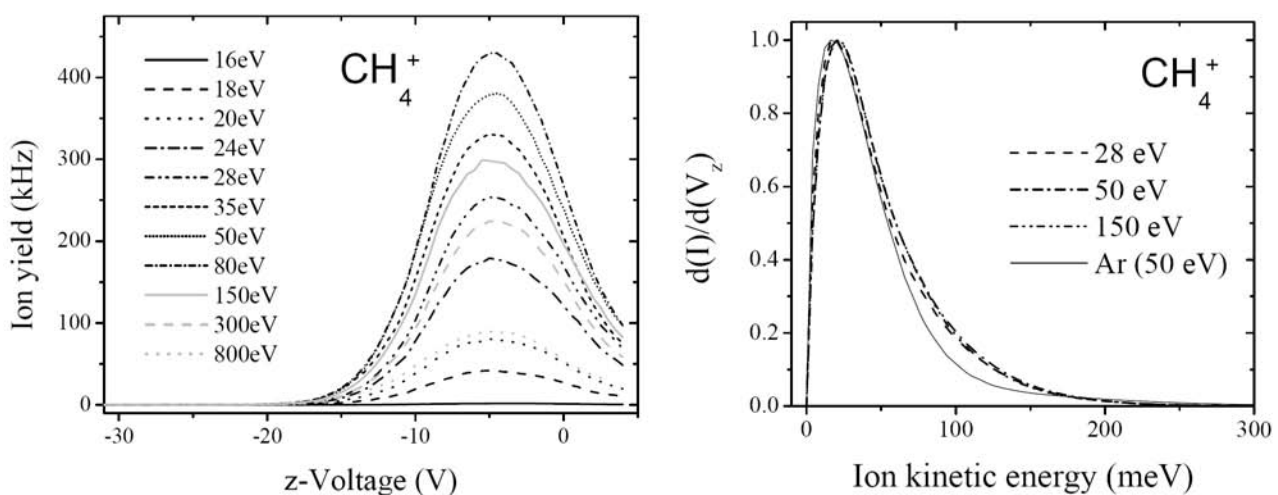


**Figure 4.** The left panel shows the ion beam profile of the $CH_4^+$ parent ion in the z direction as a function of the voltage on the z deflector pair. The beam profiles are shown for electron energies ranging from 16 eV to 800 eV, respectively. In the right panel the initial ion kinetic energy distributions were calculated from these z profiles for three electron energies and compared to $Ar^+$ (this figure is adapted from Ref. [52]).
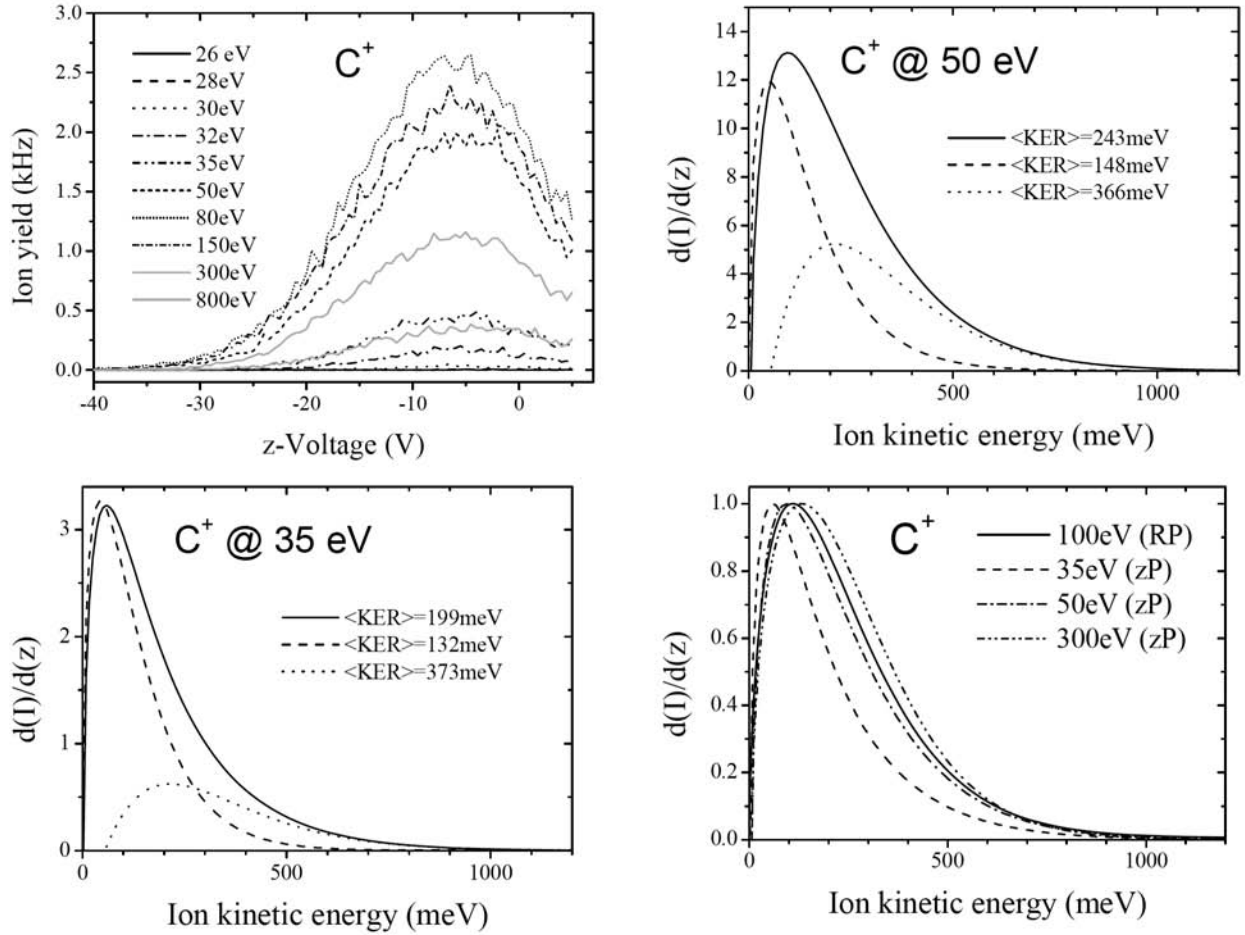
**Figure 5.** The upper left panel shows the ion beam profile of the C$^+$ fragment ion in the z direction measured as a function of the voltage on the z deflector pair for different electron energies ranging from 26 eV to 800 eV, respectively. In the top right and lower left panel the initial ion kinetic energy distributions are calculated from these z profiles for the electron energies of 50 and 35 eV, respectively. The total ion kinetic energy distribution can be separated into two Maxwell–Boltzmann distributions with average energies of ~150 meV and ~400 meV. With higher electron energy the abundance of the high energy part increases, leading to a higher overall average kinetic energy. The lower right panel shows comparison of the overall ion kinetic energy distributions determined by the z deflection method (zP) and determined applying a retarding field technique (RP) [18] (this figure is adapted from Ref. [52]).

extraction of the ions from the Nier type ion source was simulated here with increased resolution of the potential array, for different mass per charge ratios and including the magnetic field. Moreover, the lenses were treated fully three-dimensionally with no approximations of planar or spherical geometry. Thus more reliable discrimination factors can be derived than in Ref. [12], where constant discrimination factors were used for correction. In addition, the present discrimination factors (shown in Fig. 6 and using the electron energy dependent z profiles) are determined using the complete kinetic energy distributions and not only the first momentum of the curve, which is important as the correction factor is not a linear function of the kinetic energy.

Multiplying the mass selected ion signal at each electron energy with the corresponding discrimination factors leads to the relative partial cross-section. The sum of all ion signals represents the total electron impact ionization
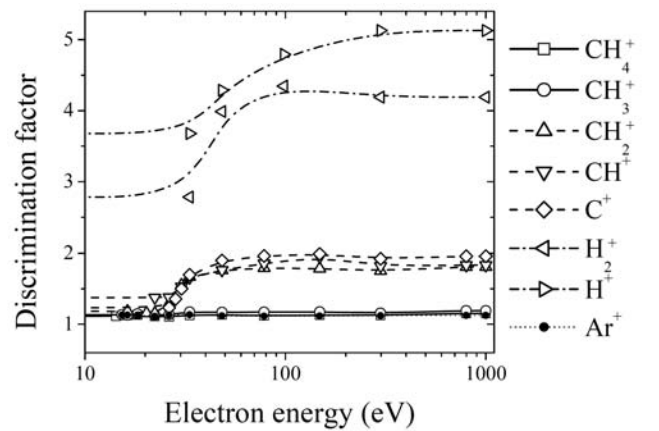


**Figure 6.** Discrimination factors for each product ion plotted as a function of the electron energy. The factor was derived by calculating the first momentum of the product of the ion kinetic energy distribution and the discrimination factor as a function of the initial kinetic energy obtained by ion trajectory simulations (this figure is taken from Ref. [52]).

5

cross-section. At the electron energy of 100 eV we normalized our relative total cross-section to the absolute total cross-section of Rapp and Englander Golden [60], which gives a certain calibration factor (summation method, see Ref. [2]). Using this normalization factor, absolute partial cross-sections for all product ions are derived, which are shown in Fig. 7. For comparison, the diagrams in Fig. 7 also include some of the previously published partial cross-sections for $CH_4$ product ions formed by electron impact. Good agreement is observed to the data determined with specially designed instruments for complete ion collection efficiency [10, 11]. In contrast, the values by Adamczyk et al. [15] and Chatham et al. [27] (not shown in Fig. 7) are, for all fragment ions except $CH_3^+$, significantly smaller than the present data. In the case of $H^+$ the data differ by a factor of 5. The present work clearly shows that (modified) commercial instruments can be applied for the determination of partial ionization cross-sections. Moreover, differential partial cross-sections with respect to the ion kinetic energy can be obtained. For details and data see Ref. [52].

### 3.2 $C_2H_2$

Another method for determination of the initial ion kinetic energy distribution and the extraction efficiency from the ion source for a given product ion is to fit the experimentally determined ion beam z profiles with a superposition of simulated ion beam profiles. At 57 different discrete initial kinetic energies of a product ion, $2 \times 10^6$ ion trajectories are calculated. The position where these ions are formed is randomly taken within the volume that is covered by the electron beam. Thereby, ion loss to the walls of the ion source housing is included in the resulting z profiles of the ion beam. Note that in the earlier method described by Poll et al. [12] the measured z profiles are assumed to be unaffected by discrimination. In contrast to the method described by Poll et al. [12], the fitting of a weighted superposition of 3-D simulated z profiles to the experimental data allows the analysis of ion beam profiles of highly energetic fragment ions that are affected by reduced ion extraction efficiency. As an example the ion beam profiles of product ions formed by electron impact ionization of acetylene ($C_2H_2$) at the electron energy of 100 eV are analysed with this method and shown in Fig. 8.

The experimentally determined z profiles for two product ions formed by electron impact ionization of $C_2H_2$ at the electron energy of 100 eV are shown in Fig. 8 with the corresponding best fit to the experimental data obtained by weighted superposition of a set of simulated z profiles for 57 different ion kinetic energies (in steps of 0.05 eV between 0 and 2 eV and in steps of 0.5 eV from 2.5 to 10 eV) utilizing $2 \times 10^6$ individual ion trajectories at each energy. The kinetic energy distribution can then be directly determined by plotting the weighting factors as a function of the ion kinetic energy of each simulated z profile.

Table 1 lists the average kinetic energies and the fraction of ions extracted from the ion source (discrimination factor) for all ions obtained by electron impact of $C_2H_2$. The average kinetic energies are determined as the first momentum of the kinetic energy distributions that are determined via two different methods: (i) differentiation of the z profile and normalization of the energy axis [12] and (ii) fit of a complete set of simulated z profiles to the experimental data [53]. The determination of the ion kinetic energy distribution using a set of simulated z profiles yields directly also the discrimination factor. Poll et al. [12] derived discrimination factors from 2-D ion trajectory simulations. For all thermal ions, i.e. for singly or doubly charged parent ions and dehydrogenated fragment ions, good agreement is observed. However, the kinetic energy distribution of energetic fragment ions depends strongly on the method used. Furthermore, for the two fragment ions $H^+$ and $CH^+$ the kinetic energy distribution at high kinetic energies reveals two contributions in the 3-D analysis that cannot be resolved using the earlier method [12].

**Table 1.** Average initial ion kinetic energies and extraction efficiencies obtained by the analysis of the z profiles of several product ions of acetylene formed by electron impact ionization at the electron energy of 100 eV. Average initial ion kinetic energies are calculated from the ion kinetic energy distributions shown in Fig. 8.

| Ion | Fit of z profiles with a set of 3-D simulated profiles | | Differentiation of z profiles and 2-D simulation after Ref. [12] | |
|---|---|---|---|---|
| | $\langle E_{kin} \rangle$ | Extraction efficiency | $\langle E_{kin} \rangle$ | Extraction efficiency |
| $H^+$ | 2479 | 0.38 | 1344 | 0.38 |
| $C^+$ | 1228 | 0.50 | 754 | 0.51 |
| $CH^+$ | 1086 | 0.53 | 760 | 0.60 |
| $CH_2^+$ | 1548 | 0.52 | 1037 | 0.59 |
| $C_2H_2^+$ | 59 | 0.92 | 57 | 0.95 |

As shown in Fig. 8, the initial ion kinetic energy distributions determined by fitting a set of simulated z profiles to the measured data differ substantially from the results obtained by the method of Poll et al. [12]. Furthermore, the average ion kinetic energies determined by the more advanced 3-D method are systematically larger than the values of Ref. [12]. However, the ion extraction efficiencies determined with the two methods are very similar, at least for the lighter ions. According to Poll et al. [12, 61] it is possible to correct the partial cross-sections for the reduced ion extraction efficiency by multiplying the ion yield with the discrimination factor of the average initial kinetic energy of the corresponding product ion. However, it is obvious that the real discrimination factor can only be calculated as the first momentum of the initial kinetic energy distribution,

where each point is multiplied with its corresponding discrimination factor. This method is used for the calculation of the extraction efficiencies shown in the third column of

Table 1. It is interesting to note that two simplifications that are made in the 2-D method of Poll et al. [12] seem to cancel their errors and that the resulting discrimination factors for
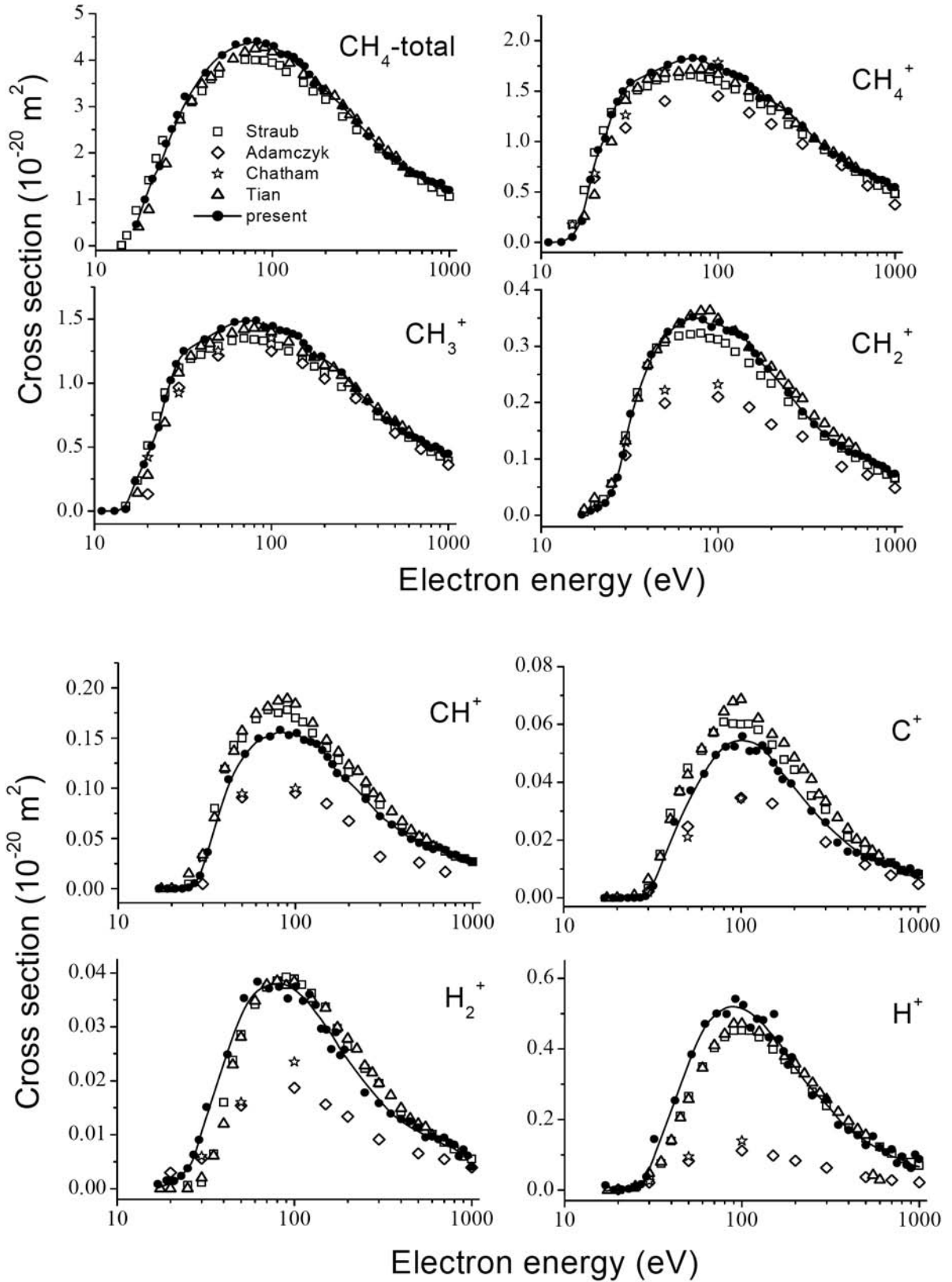


**Figure 7.** Absolute partial cross-sections for the formation of product ions by electron impact ionization of $CH_4$. The present values (filled symbols and line) are compared with data from the literature. Good agreement is observed with two experiments where complete ion detection was demonstrated (open square: Straub et al. [13] and open triangle: Tian and Vidal [14]) (this figure is taken from Ref. [52]).
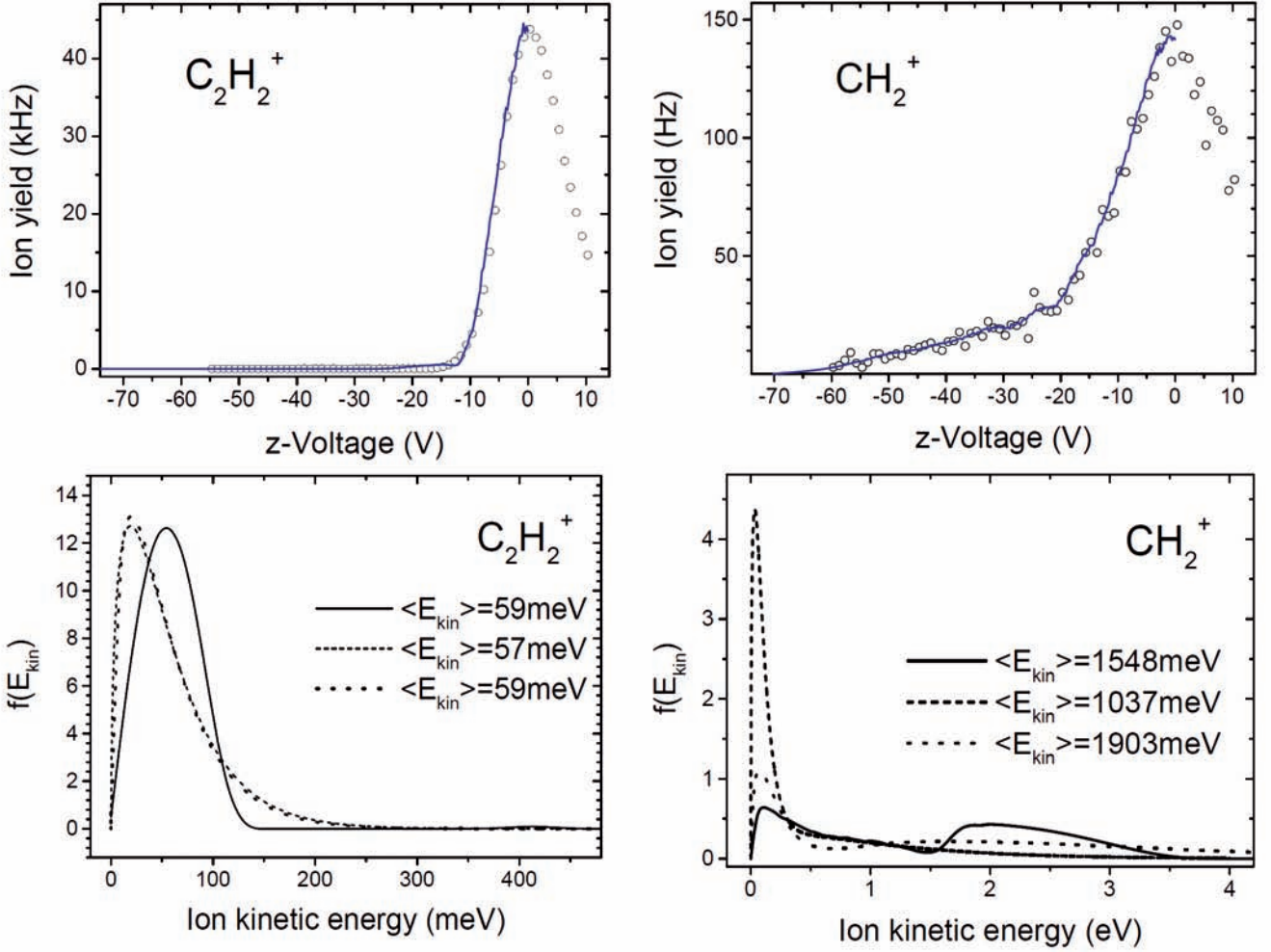
**Figure 8**. The upper panels show the left half of the z profiles of the product ions $C_2H_2^+$ and $CH_2^+$ formed via electron impact ionization of $C_2H_2$ at the electron energy of 100 eV. The experimental data are shown as open circles and the solid lines are the best fits to the experiments derived by a superposition of a set of simulated z profiles. The lower panels show the corresponding ion kinetic energy distributions. The solid line corresponds to weighting factors resulting from the fit of the z profiles (see text). The dashed line is derived according to the method developed by Poll et al. [12, 61] and the dotted line is derived by dividing the dashed line with the ion extraction efficiency curve determined from the 3-D ion trajectory simulations (this figure is adapted from Ref. [53]).

the two methods are more or less the same for all ions. However, the 3-D simulation (as a more rigorous method) leads to more reliable results than the 2-D method of Poll et al. [12]. Moreover, the necessary discrimination factor for each product ion, which is of importance for reliable partial ionization cross-sections, is directly observed with the more advanced method based on the 3-D simulated z profiles.

### 3.3.  $C_3H_5^{2+}$

Figure 9 (a) shows the MIKE spectra of the singly charged fragment ions obtained for the Coulomb explosion reaction (6) of $C_3H_5^{2+}$ in ff2:

$$C_3H_5^{2+} \rightarrow C_2H_2^+ + CH_3^+. \qquad (6)$$
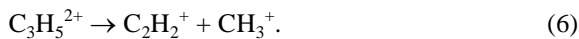
According to equation (5), the fragment ion $CH_3^+$ will produce a metastable peak at a normalized sector field voltage $E/E_0 = 0.735$. However, as mentioned above, for a large KER a pair of peaks appearing symmetrically with

respect to $E/E_0 = 0.735$ is observed. The experimental data show several peaks around this predicted centre which do not yield at first sight unambiguous information about this decay channel of $C_3H_5^{2+}$. Most of these peaks can be ascribed to artifacts which arise from the decay of metastable ions $(m_1,z_1)$ into $(m_2,z_2)$ with $m_2 < m_1$, $z_2 \leq z_1$ in ff1. These fragment ions $(m_2,z_2)$ are transmitted through the magnet and contribute to the MIKE spectrum, if their apparent mass $m^* = m_2^2 z_1 / z_2^2 m_1$ is approximately equal to the mass to charge ratio of $C_3H_5^{2+}$, i.e. 20.5 Thomson. These artifact peaks are a common contamination in 'normal' MIKE spectra, when the decay of polyatomic molecules or large atomic clusters is studied [57, 62].

As shown in reaction (6), besides $CH_3^+$ another charged fragment, $C_2H_2^+$, is also formed in the decay. The latter ion should appear in a MIKE scan at $E/E_0 = 1.273$ (see equation 5). The experiment shows a widely separated pair of peaks that are located symmetrically with respect to $E/E_0 = 1.273$ (Fig. 9 (a)). As mentioned in Section 2, this peak
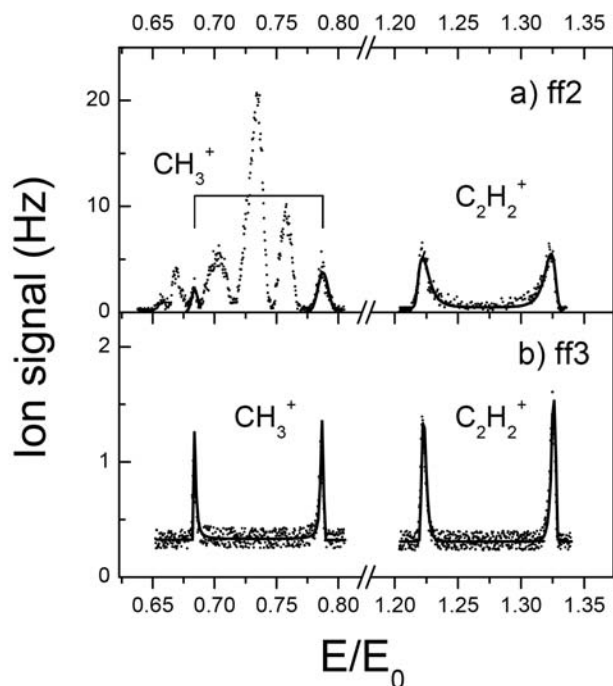
**Figure 9.** Scans of electric sector field voltages which show the formation of the fragment ions $CH_3^+$ and $C_2H_2^+$ from $C_3H_5^{2+}$: a) MIKE scan of E1, monitoring metastable reactions in ff2. (b) MIKE scan of E2, monitoring metastable reactions in ff3. Each split peak corresponds to one specific fragment ion that recoils either parallel or antiparallel to the ion beam axis. Solid lines indicate non-linear least squares fits of pairs of asymmetric Gaussians.

shape indicates that the KER is single valued and large and that only fragment ions which dissociate in either forward or backward direction contribute to the detected ion signal. Moreover, we do not observe contaminations by artifact peaks formed in this range of sector field voltage because fragment ions produced in ff1 cannot appear above $E = E_0$ unless they arise by charge separation.

Fig. 9 (b) shows the MIKE spectra for the same dissociation process (6) in ff3 (in this case the voltage of the second electrostatic sector is scanned). This spectrum is free of artifact peaks, because ions formed in ff1 have a reduced kinetic energy and will not pass the first electrostatic sector field [63]. These spectra clearly show the formation of $CH_3^+$ and $C_2H_2^+$. The assigned masses (15.02 Da and 26.02 Da) agree with those derived from the centroids of the split peaks with the help of Eq. (5) within $\pm 0.03$ Da. Thus (only) two product ions and no neutrals are produced in this reaction channel.

The peaks measured in ff3 are significantly narrower than in Fig. 9 (a), which is due to enhanced discrimination against fragment ions that do not recoil exactly in forward or backward direction. The third field free region is nearly three times longer than ff2, hence the average distance between the point of fragmentation and the beam-defining exit slit is larger, and thus the acceptance angle is smaller. The average KER may be estimated from the separation of the two 'horns' of a split peak by the equation:

$$\bar{\varepsilon} = \frac{z_f^2 m_p^2 U_{ac}}{16 z_p m_f \left(m_p - m_f\right)} \left(\frac{\Delta E}{E_0}\right)^2 \tag{7}$$

For details, see Refs [48, 58]. Using Eq. (7), a KER of $4.36 \pm 0.19$ eV is deduced from both fragment peaks, i.e. $CH_3^+$ and $C_2H_2^+$, thus confirming that no neutral fragments are formed in this Coulomb explosion of $C_3H_5^{2+}$. This value is obtained as a weighted average of 4 different values, namely all split peaks shown in Figs 9 (a) and 9 (b). The quoted uncertainty reflects the *rms* standard deviation of those four values. However, this procedure using (7) gives KER values that are too low [49]. More accurate values can be obtained from the KER distribution which is computed from the function that is fitted to each single split peak. Therefore we derived the KER distributions for all MIKE peaks displayed in Fig. 9, except the $CH_3^+$ MIKE peak measured in ff2 (Fig. 9 (a)). From each of those distributions we compute average KER values by numerical integration; their uncertainties are estimated from the uncertainties of the fit parameters (the $\Delta E$ values and the steepness of the wings). Combining all values we obtain a weighted average $<KER> = 4.58 \pm 0.15$ eV.

Ab-initio quantum chemical calculations have been performed in order to examine the fragmentation process involved in the decay. Generally, there are various possible mechanisms for the metastable decay of ions, like vibrational predissociation of the parent ion in its ground electronic state, rotational predissociation, production of the parent ion in a metastable, electronically excited state, etc. We examined the first possibility by calculating the ground state potential energy surface of $C_3H_5^{2+}$.

All calculations are performed using the Gaussian 98 program package [64] on an SGI Origin 3800 computer and a Linux workstation. Figure 10 shows the lowest energy MP2/aug-cc-pVTZ [65] structure of a) $C_3H_5^{2+}$ (doublet, $C_s$ symmetry), (b) $C_3H_5^{2+}$ in the transition state, c) $C_2H_2^+$ (doublet, $C_{2v}$ symmetry), and d) $CH_3^+$ (singlet, $D_{3h}$ symmetry). All coordinates are relaxed except for the C2–C3 separation in the transition state. The structures shown in Fig. 10 suggest that fragmentation of $C_3H_5^{2+}$ occurs by breaking of the C2–C3 bond.

The potential energy of $C_3H_5^{2+}$ is calculated as a function of the C2–C3 distance, with all other coordinates optimized, obtained at the MP2/6–31G** [66] level. For a more accurate determination of the energetics, final CCSD(T)/cc-pVTZ//MP2/aug-cc-pVTZ calculations (single point energy CCSD(T)/cc-pVTZ calculation performed on the structure optimized at the MP2/aug-cc-pVTZ level) for the transition state and the ground states of the products have been carried out. They result in a reverse barrier of 4.37 eV, which is close to the experimentally determined average kinetic energy, $<KER> = 4.58 \pm 0.15$ eV, i.e. essentially all the available energy is partitioned into kinetic energy. An explanation for this result is that in the transition state the $CH_3^+$ and $C_2H_2^+$ groups have already adopted geometries

9
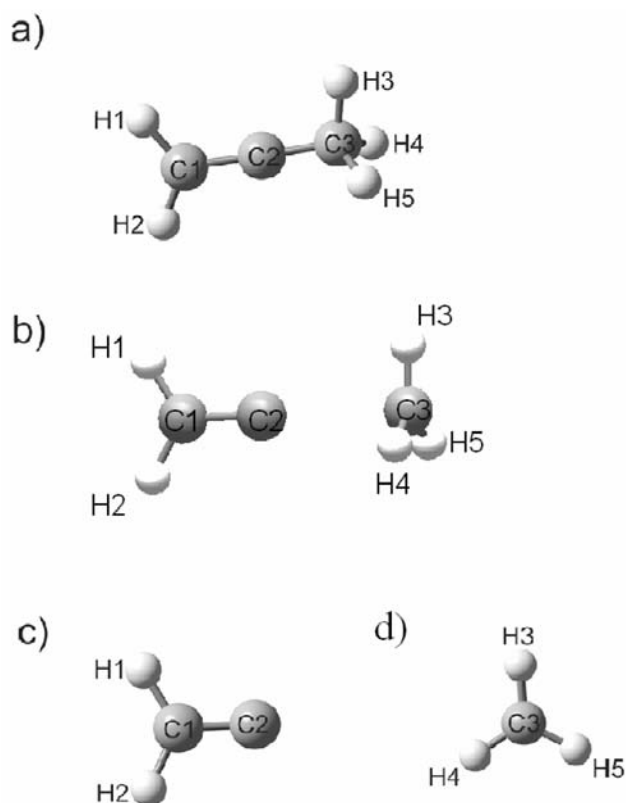
**Figure 10.** Structure of $C_3H_5^{2+}$ in (a) the ground state), (b) the transition state, (c) $C_2H_2^+$ (vinylidine), and d) $CH_3^+$. All structures obtained at the MP2/aug-cc-pVTZ level. Coordinates are fully optimized, except for the C2–C3 separation in the transition state (this figure is taken from Ref. [54]).

which closely resemble their geometries in the product state. Thus only a very small amount of energy will be partitioned into internal degrees of freedom when the groups separate past the transition state, and the distribution of kinetic energies will necessarily be very narrow.

Without ab-initio calculations one often estimates the fragment separation in the transition state by calculating the experimentally determined <KER> with the potential energy of two point charges separated by $r_{TS}$ in vacuum, and assuming that $r_{TS}$ corresponds to the length of the bond that will break [48, 49, 57]. In this model an average KER of $4.58 \pm 0.15$ eV would correspond to $r_{TS} = 3.14 \pm 0.10$ Å, which is much longer than the C2–C3 bond (2.55 Å), but much less than the C1–C3 separation (3.92 Å). However, the charge distribution in the transition state is neglected in this method. A Mulliken charge analysis shows that the net charge on C1 is only 0.002, but it is +0.418 on C2, and another +0.298 on each of the two terminal hydrogen atoms of the vinylidene group. Similarly, it is only +0.224 on C3 while the remaining charge resides on the hydrogen atoms of the methyl group. Thus, in the absence of detailed information about the charge distribution in the transition state, it is unreliable to estimate bond lengths in the transition state from the experimental KER value.

## References

[1] CHRISTOPHOROU, G. (Ed.), Electron Molecule Interactions and their Applications, Academic Press, Orlando, FL, 198.

[2] MÄRK, T.D., DUNN, G.H. (Eds), Electron Impact Ionization, Springer, Vienna, 1985.

[3] PITCHFORD, L.C., McKOY, B.V., CHUTJIAN, A., TRAJMAR, S. (Eds) Swarm Studies and Inelastic Electron-Molecule Collisions, Springer, New York, 1987.

[4] JANEV, R.K. (Ed.), Atomic and Molecular Processes in Fusion Edge Plasmas, Plenum, New York, 1995.

[5] MOHR, J.P., WIESE, W.L. (Eds), Atomic and Molecular Data and their Applications, AIP Conference Proceedings 434, AIP, Woodbury, NY, 1998.

[6] Technical basis for the ITER Final Design Report, ITER EDA Documentation Series No. 16, IAEA, Vienna, 1998.

[7] Annual ADAS workshop, Cadarache, 20–22 October 2002, and IAEA Technical Meeting on Atomic and Plasma–Material Interaction Data for Fusion Science and Technology, Jülich, 28–31 October 2002.

[8] LATIMER, C.J., MACKIE, R.A., SANDS, A.M., KOUCHI, N., DUNN, K.F., J. Phys. B: At. Mol. Opt. Phys. **32** (1999) 2667.

[9] STANTON, H.E., MONAHAN, J.E., J. Chem. Phys. **41** (1964) 3694.

[10] STRAUB, H.C., RENAULT, P., LINDSAY, B.G., SMITH, K.A., STEBBINGS, R.F., Phys. Rev. A **52** (1995) 1115.

[11] TIAN, C., VIDAL, C.R., J. Chem. Phys. **108** (1998) 927.

[12] POLL, H.U., et al., Int. J. Mass Spectrom. Ion Processes **177** (1998) 143.

[13] STRAUB, H.C., LIN, D., LINDSAY, B.G., SMITH, K.A., STEBBINGS, R.F., J. Chem. Phys. **106** (1997) 4430.

[14] TIAN, C., VIDAL, C.R., J. Phys. B: At. Mol. Opt. Phys. **31** (1998) 895.

[15] ADAMCZYK, B., BOERBOOM, A.J.H., SCHRAM, B.L., KISTEMAKER, J., J. Chem. Phys. **44** (1966) 4640.

[16] FUCHS, R., TAUBERT, R., Z. Naturforsch. **19a** (1964) 494.

[17] LOCHT, R., OLIVIER, J.L., MOMIGNY, J., Chem. Phys. **43** (1979) 425.

[18] FIEGELE, T., MAIR, C., SCHEIER, P., BECKER, K., MÄRK, T.D., Int. J. Mass Spectrom. **207** (2001) 145.

[19] LATIMER, C.J., MACKIE, R.A., SANDS, A.M., KOUCHI, N., DUNN, K.F., J. Phys. B: At. Mol. Opt. Phys. **32** (1999) 2667.

[20] BURROW, M.D., RYAN, S.R., LAMB, W.E., Jr., McINTYRE, L.C., Jr., J. Chem. Phys. **71** (1979) 4931.

[21] STOCKBAUER, R., Int. J. Mass Spectrom. Ion Phys. **25** (1977) 401.

[22] TAUBERT, R., Adv. Mass Spectrom. **1** (1959) 489.

[23] STANTON, H.E., MONAHAN, J.E., J. Chem. Phys. **41** (1964) 3694.

[24] KAMETA, K., KOUCHI, N., UKAI, M., HATANO, Y., J. Electron Spectrosc. Relat. Phenom. **123** (2002) 225.

[25] SAMSON, J.A.R., et al., J. Chem. Phys. **90** (1989) 6925.

[26] DUJARDIN, G., WINKOUN, D., LEACH, S., Phys. Rev. A **31** (1985) 3027.

[27] CHATHAM, H., HILLS, D., ROBERTSON, R., GALLAGHER, A., J. Chem. Phys. **81** (1984) 1770.

[28] ORIENT, O.J., SRIVASTAVA, S.K., J. Phys. B: At. Mol. Phys. **20** (1987) 3923.

[29] KRISHNAKUMAR, E., SRIVASTAVA, S.K., J. Phys. B: At. Mol. Opt. Phys. **23** (1990) 1893.

[30] VALLANCE, C., HARRIS, S.A., HUDSON, J.E., HARLAND, P.W., J. Phys. B: At. Mol. Opt. Phys. **30** (1997) 2465.

[31] STRAUB, H.C., LIN, D., LINDSAY, B.G., SMITH, K.A., STEBBINGS, R.F., J. Chem. Phys. **106** (1997) 4430.

[32] DURIC, N., CADEZ, I., KUREPA, M., Int. J. Mass Spectrom. Ion Proc. **108** (1991) R1.

[33] FUCHS, R., TAUBERT, R., Z. Naturforsch. **19a** (1964) 1181.

[34] BEN-ITZHAK, I., CARNES, K.D., JOHNSON, D.T., NORRIS, P.J., WEAVER, O.L., Phys. Rev. A **49** (1994) 881.

[35] IRIKURA, K.K., KIM, Y.K., ALI, M.A., J. Res. Nat. Inst. Stand. Tech. **107** (2002) 63.

[36] DEUTSCH, H., BECKER, K. MATT, S., MÄRK, T.D., Int. J. Mass Spectrom. **197** (2000) 37.

[37] KHARE, S.P., SHARMA, M.K., TOMAR, S., J. Phys. B: At. Mol. Opt. Phys. **32** (1999) 3147.

[38] DOSE, V., PECHER, P., PREUSS, R., J. Phys. Chem. Ref. Data **29** (2000) 1157.

[39] GALASSI, M.E., RIVAROLA, R.D., BEUVE, M., OLIVERA, G.H., FAINSTEIN, P.D., Phys. Rev. A **62** (2000) 022701.

[40] JOSHIPURA, K.N., VINODKUMAR, M., PATEL, U.M., J. Phys. B: At. Mol. Opt. Phys. **34** (2001) 509.

[41] THISSEN, R., et al., J. Chem. Phys. **99** (1993) 6590.

[42] DAVISTER, M., LOCHT, R., Chem. Phys. **191** (1995) 333.

[43] MATHUR, D., Phys. Rep. **225** (1993) 193.

[44] ECHT, O., MÄRK, T.D., in Clusters of Atoms and Molecules II (HABERLAND, H., Ed.), Springer, Berlin, 1994, Vol. **56**, p. 183; SCHRÖDER, D., SCHWARZ, H., J. Phys. Chem. **A103**, 7385 (1999); ECHT, O., SCHEIER, P., MÄRK, T.D., C. R. Phys. **3**, (2002) 353.

[45] TOSI, P., CORREALE, R., LU, W.L., FALCINELLI, S., BASSI, D., Phys. Rev. Lett. **82** (1999) 450.

[46] SCHEUERMANN, F., SALZBORN, E., HAGELBERG, F., SCHEIER, P., J. Chem. Phys. **114**, 9875 (2001); FIELD, T.A., ELAND, J.H.D., Int. J. Mass Spectrom. **192** (1999) 281.

[47] RABRENOVIC, M., BRENTON, A.G., BEYNON, J.H., Int. J. Mass Spectrom. Ion Proc. **52** (1983) 175.

[48] WEISKE, T., KOCH, W., SCHWARZ, H., J. Am. Chem. Soc. **115** (1993) 6312.

[49] VEKEY, K., SZILAGYI, Z., Int. J. Mass Spectrom. Ion Proc. **165** (1997) 1.

[50] VINCZE, A., YINON, J., PERES, T., LIFSHITZ, C., Int. J. Mass Spectrom. **192** (1999) 99.

[51] SCHEIER, P., et al., Phys. Rev. B **53**, 1091 (1996); SCHLATHÖLTER, T., HOEKSTRA, R., MORGENSTERN, R., J. Phys. B **31** (1998) 1321.

[52] GLUCH, K., et al., Int. J. Mass Spectrom. **228** (2003) 307–320.

[53] FEIL, S., et al., Int. J. Mass Spectrom. **233** (2004) 325–333.

[54] GLUCH, K., et al., J. Chem. Phys. **118** (2003) 3090–3095.

[55] MATT, S., et al., Int. J. Mass Spectrom. **187** (1999) 813.

[56] GRILL, V., WALDER, G., SCHEIER, P., KURDEL, M., MÄRK, T.D., Int. J. Mass Spectrom. Ion Proc. **129** (1993) 31.

[57] COOKS, R.G., BEYNON, J.H., CAPRIOLI, R.M., LESTER, G.R., Metastable Ions, Elsevier, Amsterdam, 1973.

[58] HOLMES, J.L., OSBORNE, A.D., Int. J. Mass Spectrom. Ion Phys. **23** (1977) 189.

[59] DAHL, D.A., SIMION 6.0, Idaho National Engineering and Environmental Laboratory.

[60] RAPP, D., ENGLANDER GOLDEN, P., J. Chem. Phys. **43** (1965) 1464.

[61] POLL, H.U., WINKLER, C., MARGREITER, D., GRILL, V., MÄRK, T.D., Int. J. Mass Spectrom. Ion Proc. **112** (1992) 1.

[62] PARAJULI, R., et al., Chem. Phys. Lett. **330** (2000) 53.

[63] GUILHAUS, M., BOYD, R.K., BRENTON, A.G., BEYNON, J.H., Int. J. Mass Spectrom. Ion Proc. **67** (1985) 209.

[64] FRISCH, M.J., et al., GAUSSIAN 98 (Gaussian Inc., Pittsburgh, PA, 1998).

[65] KENDALL, R.A., DUNNING, J.T.H., HARRISON, R.J., J. Chem. Phys. **96** (1992)6796.

[66] HARIHARAN, P.C., POPLE, J.A., Chem. Phys. Lett. **16** (1972) 217.

# Electron impact ionization to the constituents of the edge plasma: Appearance energies and temperature effects

*S. Matejčík[1], M. Stano[1], E. Vasekova[1], S. Denifl[2], J. D. Skalny[1], T.D. Märk[2]*

[1] Department of Experimental Physics, Comenius University Bratislava, Mlynska dolina F2, 84248 Bratislava, Slovakia
[2] Institut für Ionenphysik, Leopold Franzens Universität, Technikerstrasse 25, A-6020, Innsbruck, Austria

**Abstract**

The threshold behaviour of the cross-section for cations formed via electron impact ionization to methane ($CH_4$, $CH_3D$ and $CD_4$), ethane ($C_2H_6$) and propane ($C_3H_8$) has been studied in a crossed electron/neutral beams apparatus with mass spectroscopic analysis of the ions. The appearance energies of the ions formed via electron impact ionization to these molecules were determined at room and at elevated temperatures (about 700 K). At elevated gas temperatures a decrease of the appearance energies has been observed for all molecules (red shift). The red shift appears to depend on the size and on the isotopic composition of the molecules. These results indicate that at very high gas temperatures the cross-sections for electron impact ionization in the threshold region changes may substantially differ from the low temperature one. Additionally, differences in the appearance energies due to isotopic substitution have been observed for molecules $CH_4$, $CH_3D$ and $CD_4$.

## 1.    Introduction

The achieving, sustaining and controlling of the fusion plasma is strongly influenced by the conditions at the plasma edge. The radiative and collisional processes in this plasma edge region have to be considered with respect to the plasma properties. It is essential to possess detailed and quantitative information of these elementary processes by the determination of ionization energies, cross-sections, reaction rate coefficients, etc. Due to the relatively low temperature in the plasma edge the plasma contains (in addition to electrons and atomic ions) also a significant amount of molecules as impurities [1, 2] which are released due to chemical erosion caused by plasma–wall interaction. In the case of carbon covered surfaces, these molecules are small hydrocarbons $C_xH_y$ (x = 1…3, H = 4…8). Temperature effects of the electron impact ionization energies of hydrocarbon molecules may play an important role because the molecules in the edge of the fusion plasma are at elevated temperatures. Furthermore, small changes in the ionization energies may lead to large changes in the composition of the plasma [3].

This paper presents a summary of the studies of electron impact ionization reactions to small hydrocarbon molecules in which we have also considered the influence of the temperature of the neutral molecules on the appearance energy (AE) of the ions formed via this reaction. Using the high resolution crossed electron molecule beams

experiment, the temperature effects on the AEs of methane [4], ethane [5], propane and recently also the isotopomer of the methane $CH_3D$ and $CD_4$ [6] have been studied and a remarkable temperature effect on the AEs has been observed (e.g. Ref. [5]: $AE(C_2H_6)^+/C_2H_6$ (293K) = 11.46 ± 0.04 eV and $AE(C_2H_6)^+/C_2H_6$ (693K) = 11.2 ± 0.04 eV).

Fig. 1 (a) shows potential energy curves of a molecule M along the geometry coordinate Q. The figure illustrates the most important concepts for electron impact ionization, the vertical ionization energy (VIE), the adiabatic ionization energy (AIE) and the AE of an ion. The electron impact ionization is a fast process occurring in a much shorter time than the vibrational period of the molecule and thus we assume during the reaction that the atoms are fixed. The VIE is the energy necessary to ionize a molecule M in its ground electronic, vibrational and rotational state and at equilibrium geometry of the molecule. The AIE is defined as the difference between the ground electronic, vibrational and rotational states of the ion $M^+$ and molecule M. The ion yield is measured in an electron impact ionization experiment as a function of the kinetic energy of the electrons. The AE of the particular ion is estimated from the measured ion yield. In the case of electron impact ionization of an atomic target, the AE of the ion is identical to the ionization energy of the target. However, in the case of a molecular target, the situation is much more complex. In the present work, we use therefore the expression AE instead of ionization energy,
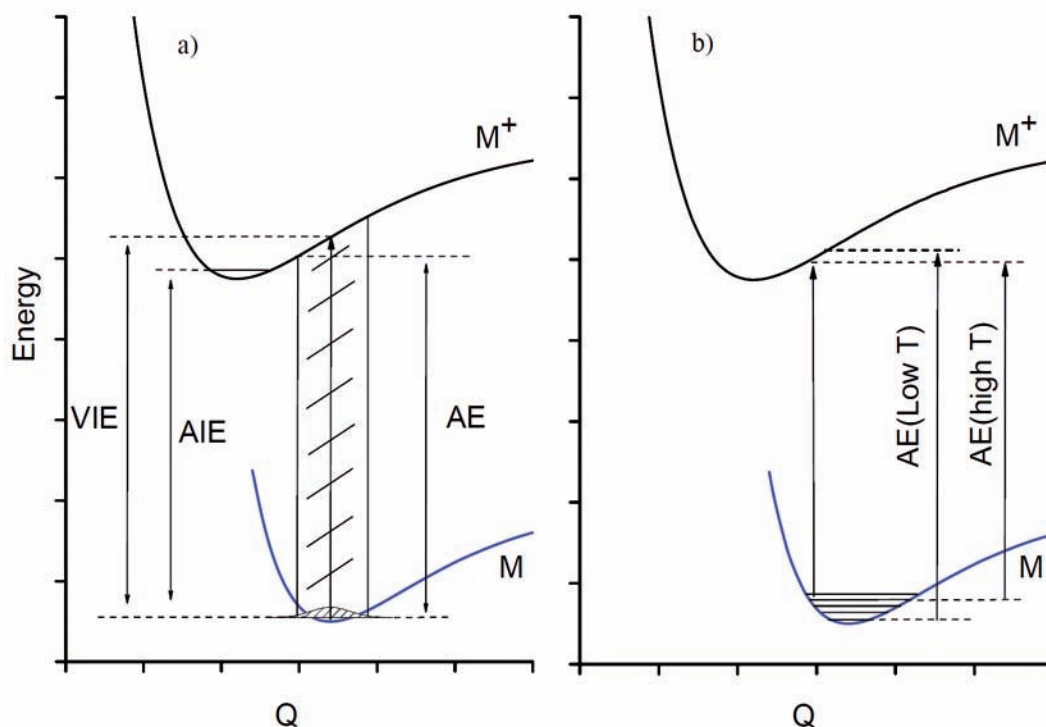
**Figure 1.** Potential energy curves of a system molecule — molecular ion along a coordinante Q. VIE — vertical ionization energy, AIE — adiabatic ionization energy, AE — appearance energy of an ion.

which is frequently used in previous literature. The measured AE does not directly represent the ionization energy of the molecule (either VIE or AIE). The AE of an ion from the molecule depends also on the internal state of the molecules. If the electrons interact with the molecules in an excited (vibrational and rotational) state (Fig. 1 (b)), the AE is lower in comparison with the AE measured for molecules in the ground vibrational and rotational state. The energy necessary to ionize a particular molecule also depends on the geometrical situation of the molecule at the moment of the electron interaction. The energy $E_1$ necessary to ionize the molecule at the coordinate $q_1$ is lower than the energy $E_2$ at coordinate $q_2$ and thus the AE corresponds to the ionization energy at coordinate $q_1$.

The measured AE values are compared with values obtained in previous experiments and in the case of the fragment ions also with values determined from thermo-chemical data available in Ref. [7]. In general, the AE value for a fragment cation X with the corresponding neutral radical R formed in electron impact ionization of a molecule M can be calculated according to Ref. [8]:

$$AE(X^+) = \Delta H_f(X) + \Delta H_f(R) - \Delta H_f(M) + IE(X) \quad (1)$$

$\Delta H_f$ represents the heat of formation and IE(X) is the ionization energy of the isolated neutral X. The value obtained in Eq. (1) represents the thermochemical threshold the transition from the rotational and vibrational ground state of the neutral to the cation in its ground state.

## 2. Experimental set-up

The experimental set-up used for the present measure-ments consists of a crossed electron/molecule beam apparatus combined with a quadrupole mass spectrometer (QMS). A schematic view of the set-up is shown in Fig. 2. A more detailed description can be found in Ref. [9]. The molecular beam (MB) is formed in a temperature controlled effusive molecular beam source (EMBS) which can be heated resistively up to 800 K. A deflector in the entrance of the beam source prevents the molecules from reaching the collision chamber of the monochromator without any collision with the walls of the EMBS. The latter are a very important condition for the internal energy of the neutral molecules, because only after a sufficient number of collisions are the molecules expected to be in thermal equilibrium with the walls of the EMBS, i.e. the molecules effusing from the EMBS through a hole with 0.5 mm have the same temperature as the EMBS. The neutral molecules interact in the collision region of the trochoidal electron monochromator (TEM) with the electron beam (EB). The maximum electron energy resolution of the TEM is about 30 meV. However, in the present measurements the energy resolution of 120 meV has been chosen, leading to a higher detection efficiency of the apparatus. The ions formed in the collision region are extracted into a QMS by a weak electric field and collected by a secondary electron multiplier. Using this method the ion efficiency curve for a selected mass was measured as a function of the electron energy. For the exact

derivation of the AE from the measured data a fitting method based on the Wannier threshold law [10] has been used, which fit function is convoluted with the energy distribution of the EB. A detailed description of the fitting method used can be found in Ref. [4]. In short, the ion efficiency curve is fitted with function f(E) over the energy range that includes the threshold region:

$$f(E) = b \qquad \text{if } E < AE_1 \qquad (2.1)$$
$$f(E) = b + c(E - AE_1)^{p_1} \qquad \text{if } AE_1 < E < AE_2 \quad (2.2)$$
$$f(E) = b + c(E - AE_1)^{p_1} + d(E - AE_2)^{p_2} \text{ if } E > AE_2 \quad (2.3)$$

The fit using Eqs (2.1) and (2.2) involves four parameters: the background signal $b$, the searched AE, a scaling constant $c$ which determines the slope of the cross-section above the AE, and finally an exponential factor $p$ (Wannier factor). For a second threshold in an ion efficiency curve (with $AE_2$), i.e. another ionic state of the ion becomes accessible or another ion is present at this mass, the fitting function is extended by Eq. (2.3), where the second ion efficiency curve is added above $AE_2$ to the first one.

The electron energy scale of the monochromator was calibrated by measuring the ionization efficiency curve of Ar under the same experimental conditions and using the well known spectroscopic ionization energy of $Ar^+/Ar$ (IE = $15.759 \pm 0.001$ eV [11]).
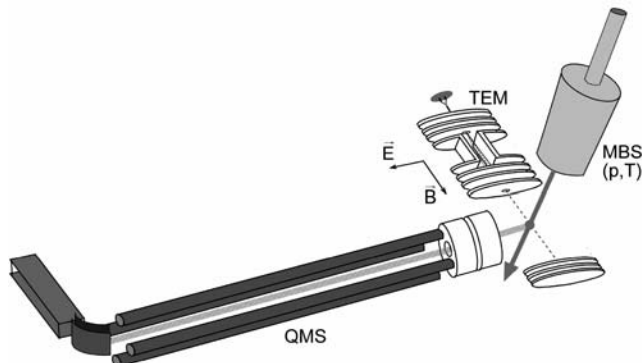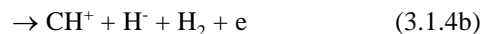


**Figure 2.** Schematic view of the experimental set-up showing the EMBS, where the MB is formed. The MB interacts with the EB in the collision region of the trochoidal electron monchromator (TEM). The formed ions are mass analysed using a QMS.

## 3. Results and discussion

### 3.1. CH$_4$

The CH$_4$ molecule is one of the simplest hydrocarbon molecules and its technological importance is well documented. In the past the AEs for electron impact ionization of CH$_4$ were measured in many studies [12–17]. Nevertheless, the scatter of the experimental values of the ionization energies is large. We consider as the most reliable data those obtained by Plessis et al. [12].

We have measured the electron impact ionization to CH$_4$ for the following reactions:

$$e + CH_4 \rightarrow CH_4^+ + 2e \qquad (3.1.1)$$
$$\rightarrow CH_3^+ + H + 2e \qquad (3.1.2a)$$
$$\rightarrow CH_3^+ + H^- \qquad (3.1.2b)$$
$$\rightarrow CH_2^+ + H_2 + 2e \qquad (3.1.3)$$
$$\rightarrow CH^+ + H + H_2 + 2e \qquad (3.1.4a)$$
$$\rightarrow CH^+ + H^- + H_2 + e \qquad (3.1.4b)$$
$$\rightarrow C^+ + 2H_2 + 2e \qquad (3.1.5)$$
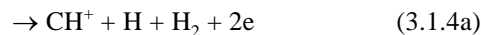
The results obtained for this molecule have been reported by Stano at al. [4]. The AEs for all reactions (3.1.1)–(3.1.5) were estimated for the temperature of 293 K. These AEs are presented in Table 1. The present value of the AE for reaction (3.1.1) is in good agreement with the value measured by Plessis et al. [12]. For the additional reactions, differences in AEs still exist.

**Table 1.** Appearance energies of the ions formed via electron impact ionization to CH$_4$ at 290 K.

| e + (CH$_4$) → | Present AE (eV) | EI [12] AE (eV) |
|---|---|---|
| (CH$_4$)$^+$ | $12.65 \pm 0.04$ $12.95 \pm 0.04$ | $12.63 \pm 0.02$ |
| (CH$_3$)$^+$ + H$^-$ | $13.58 \pm 0.1$ | $13.25 \pm 0.08$ |
| (CH$_3$)$^+$ + H | $14.34 \pm 0.1$ | |
| (CH$_2$)$^+$ + H$_2$ | $15.10 \pm 0.1$ | $15.06 \pm 0.02$ |
| (CH)$^+$ + H$_2$ + H | $19.6 \pm 0.1$ | $19.11 \pm 0.2$ $19.87 \pm 0.2$ |
| C$^+$ + 2H$_2$ | $20.5 \pm 0.2$ | $19.56 \pm 0.2$ |

In the case of CH$_4^+$, in addition to previous experiments beside the first threshold at 12.65 eV, a second threshold at 12.95 eV has been recognized. This second threshold we assign to a reaction forming CH$_4^+$ in an excited state. For the reaction channel (3.1.2) we could not confirm the value of the AE by Plessis et al. [12], moreover we were able to distinguish two thresholds in the ion yields. The first threshold in the CH$_3^+$ ion yield we have assigned to the reaction of the ion pair formation (3.2.2a) and the second one to the dissociative ionization channel (3.2.2b). This assignment is supported by the fact that the difference between these two thresholds corresponds very well with the electron affinity of the hydrogen atom.

The AEs for reactions (3.1.1) and (3.1.2) have also been measured at an elevated temperature of 693 K. Comparison of the AEs measured at 293 and 693 K is presented in Table 2. The values of the AEs at the elevated temperature show a systematic red shift of about 0.14 eV. This value of the shift corresponds very well to the increase

**Table 2.** The values of the AEs of $CH_4$ measured at two different temperatures.
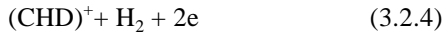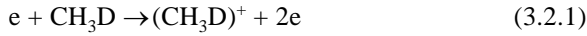
| e + ($CH_4$) → | AE(290K) (eV) | AE(690K) (eV) | Δ(AE(690K)-AE(290K)) (eV) |
|---|---|---|---|
| $(CH_4)^+$ | 12.65 ± 0.04 12.95 ± 0.04 | 12.51 ± 0.04 12.82 ± 0.04 | 0.14 ± 0.08 0.13 ± 0.08 |
| $(CH_3)^+ + H^-$ | 13.58 ± 0.1 | 13.45 ± 0.1 | 0.13 ± 0.2 |
| $(CH_3)^+ + H$ | 14.34 ± 0.1 | 13.20 ± 0.04 | 0.14 ± 0.14 |

of the rotational and vibrational energy in the $CH_4$ if we increase the temperature from 293 to 693 K [4]. Using the known vibrational energies of the $CH_4$ molecule and the rotational constants, we have calculated that the increase of the internal energy of the $CH_4$ molecule between 293 K and 693 K amount has a value of 0.12 eV. This value fits within error bars to the present experimental value of the shift. We would like to point out that the shift in the AE was observed also for the ion pair formation reaction (3.1.2b).

## 3.2. $CH_3D$

The electron impact ionization to $CH_3D$ has been examined for the following reaction channels:

$$e + CH_3D \rightarrow (CH_3D)^+ + 2e \qquad (3.2.1)$$
$$(CH_2D)^+ + H^- + e \qquad (3.2.2a)$$
$$(CH_2D)^+ + H + 2e \qquad (3.2.2b)$$
$$(CH_3)^+ + D + 2e \qquad (3.2.3)$$
$$(CHD)^+ + H_2 + 2e \qquad (3.2.4)$$

The AE for reaction (3.2.1) has been estimated in the past by Lossing et al. [18]. Using an electron impact ionization set-up they tried to measure differences in the AEs between $CH_3D$ and $CH_4$. His value of the AE ($CH_3D^+$/$CH_3D$) is about 0.37 eV higher than the present value. This is most probably due to low sensitivity and low resolution of the experimental set-up used. Present values of the AEs of the ions formed from $CH_3D$ are systematically higher than the AEs of $CH_4$ (Table 3). The differences in the AEs of $CH_4$ and $CH_3D$ are explainable by the isotopic effect.

**Table 3.** Appearance energies of the ions formed via electron impact ionization to $CH_3D$ at 293 K.

| e + $CH_3D$ → | Present AE (eV) | EII [18] AE (eV) |
|---|---|---|
| $(CH_3D)^+$ | 12.75 ± 0.03 12.99 ± 0.03 | 13.12 ± 0.02 |
| $(CH_2D)^+ + H^-$ $(CH_2D)^+ + H$ | 13.66 ± 0.07 14.42 ± 0.05 | – |
| $(CH_3)^+ + D$ | 14.54 ± 0.05 | – |
| $(CHD)^+ + H_2$ | 15.22 ± 0.1 | – |

The AEs for reactions (3.2.1)–(3.2.4) have also been studied at the elevated temperature of 693 K. The results are shown in Table 4. The shift of the AEs of the positive ions in the molecule $CH_3D$ is according to our expectations more pronounced than in the $CH_4$ molecule (ranging from 0.11 to 0.19 eV). This observation is consistent with our assumption that the shift depends on the vibrational and rotational excitation of the molecules.

**Table 4.** The values of the AEs of $CH_3D$ measured at two different temperatures.

| e + $CH_3D$ → | AE(293 K) (eV) | AE(693 K) (eV) | Δ(AE(693 K)-AE(293 K)) (eV) |
|---|---|---|---|
| $(CH_3D)^+$ | 12.75 ± 0.03 12.99 ± 0.03 | 12.58 ± 0.05 12.80 ± 0.07 | 0.17 ± 0.07 0.19 ± 0.08 |
| $(CH_2D)^+ + H$ | 13.66 ± 0.07 14.42 ± 0.05 | 13.49 ± 0.07 14.25 ± 0.05 | 0.17 ± 0.1 0.17 ± 0.06 |
| $(CH_3)^+ + D$ | 14.54 ± 0.05 | 14.42 ± 0.05 | 0.12 ± 0.05 |
| $(CHD)^+ + H_2$ | 15.22 ± 0.1 | 15.11 ± 0.1 | 0.11 ± 0.08 |

## 3.3. $CD_4$

The AEs for the electron impact ionization to $CD_4$ have been measured at 293 K and 693 K for the following reactions:

$$e + CD_4 \rightarrow (CD_4)^+ + 2e \qquad (3.3.1)$$
$$(CD_3)^+ + D + 2e \qquad (3.3.2)$$
$$(CD_2)^+ + D_2 + 2e \qquad (3.3.3)$$

The AEs of $CD_4$ have been measured in the past by Lossing et al. [18] and Honig [19] using the EII techniques. However, they estimated the value of AE only for the molecular ion $CD_4^+$. The AE of the molecular ion has been also published by Berkowitz et al. [20] using the photoionization (PI) technique. Using the same technique, Dibeler et al. [21] estimated AEs for several ions. Present values of the AEs compared with that one by Lossing et al. [18] and Dibeler et al. [21] are given in Table 5.

The value of the $CD_4^+$ AE by Lossing et al. [18] overestimates the present value substantially. This is

**Table 5.** Appearance energies of the ions formed via electron impact ionization to $CD_4$ at 293 K.

| e + $CD_4$ → | Present AE (eV) | EII [18] AE (eV) | PI [21] AE (eV) |
|---|---|---|---|
| $(CD_4)^+$ | 12.84 ± 0.02 13.07 ± 0.03 | 13.26 ± 0.02 | 12.87 ± 0.02 |
| $(CD_3)^+ + D$ | – 14.54 ± 0.03 | – | 14.38 ± 0.03 |
| $(CD_2)^+ + D_2$ | 15.41 ± 0.05 | – | 15.25 ± 0.04 |

consistent with the CH$_3$D case and supports our assumption about the low sensitivity and resolution in that experiment. Present AE for the CD$_4^+$ ion match the PI value by Dibbeler et al. [21], however for CD$_3^+$ and CD$_2^+$ small differences of about 0.2 eV still remain.

Using the temperature controlled neutral beam source, the ion efficiency curves were measured at two different gas temperatures, 293 and 693 K. We have observed remarkable temperature effects on the AEs for CD$_4$. The red shifts of the AEs of the ions formed via EII to CD$_4$ range from 0.2 to 0.24 eV. These values are consistent with the CH$_4$ and CH$_3$D values. We observe that with increasing number of deuterium atoms in the molecule the shift in the AE is increasing. The shift for CD$_4$ is larger than for CH$_3$D and moreover, for both molecules the temperature effect is more pronounced than for CH$_4$. Such a result can be explained by the higher population of vibrational and rotational levels for the deuterated species.

**Table 6.** The values of the AEs of CD$_4$ measured at two different temperatures.

| e + CD$_4$ → | AE(293K) (eV) | AE(693K) (eV) | Δ(AE(693K)– AE(293K)) (eV) |
|---|---|---|---|
| (CD$_4$)$^+$ | 12.84 ± 0.02 13.07 ± 0.03 | 12.60 ± 0.04 12.84 ± 0.04 | 0.24 ± 0.06 0.23 ± 0.06 |
| (CD$_3$)$^+$ + D | 14.54 ± 0.03 | 14.31 ± 0.05 | 0.23 ± 0.04 |
| (CD$_2$)$^+$ + D$_2$ | 15.41 ± 0.05 | 15.21 ± 0.05 | 0.2 ± 0.08 |

**Table 7.** The shifts of the AEs of the ions formed from CH$_3$D and CD$_4$ to the corresponding cations of methane (CH$_4$).

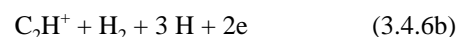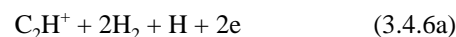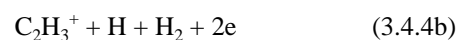| e + CH$_3$D → | Isotope shift (eV) | e + CD$_4$ → | Isotope shift (eV) |
|---|---|---|---|
| (CH$_3$D)$^+$ | 0.10 | (CD$_4$)$^+$ | 0.19 |
| (CH$_2$D)$^+$ + H | 0.08 | (CD$_3$)$^+$ + D | 0.20 |
| (CH$_3$)$^+$ + D | 0.20 | (CD$_2$)$^+$ + D$_2$ | 0.31 |
| (CHD)$^+$ + H$_2$ | 0.11 | | |

The AEs of cations formed via electron impact of CH$_3$D and CD$_4$ were compared with the AEs for CH$_4$ determined previously with the same apparatus and the same fitting procedure. For all measured cations, an isotope effect on the AE is observed (Table 7). The isotope effect is larger for CD$_4$ than for CH$_3$D. From the present results, several trends concerning the isotope effect on the AE can be deduced: (i) the smallest isotope effect is observed for the

parent cations, whereas (ii) for fragment cations, stronger isotope shifts are observed which become larger for smaller fragment cations. For fragment cations Dibeler et al. (PI) observed the reverse tendency, i.e. the AE isotope effect became weaker for smaller fragment cations [21]. The previous electron impact studies [18, 19] reported a similar shift for CD$_4^+$/CD$_4$. However, the previous AE values determined in electron impact experiments are much higher than the present AEs, which can be explained by the different experimental conditions (energy resolution, etc.).

### 3.4 C$_2$H$_6$

The AEs of a large number of ionization reactions have been measured in the case of electron impact ionization to ethane:

$$e + C_2H_6 \rightarrow C_2H_6^+ + 2e \qquad (3.4.1)$$
$$C_2H_5^+ + H^- + e \qquad (3.4.2a)$$
$$C_2H_5^+ + H + 2e \qquad (3.4.2b)$$
$$C_2H_4^+ + H_2 + 2e \qquad (3.4.3)$$
$$C_2H_3^+ + H^- + H_2 + e \qquad (3.4.4a)$$
$$C_2H_3^+ + H + H_2 + 2e \qquad (3.4.4b)$$
$$C_2H_2^+ + 2H_2 + 2e \qquad (3.4.5)$$
$$C_2H^+ + 2H_2 + H + 2e \qquad (3.4.6a)$$
$$C_2H^+ + H_2 + 3 H + 2e \qquad (3.4.6b)$$
$$C_2^+ + 3H_2 + 2e \qquad (3.4.7)$$
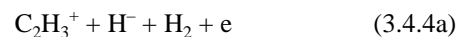
Appearance energies of C$_2$H$_6$ were already measured in previous electron impact ionization [22–26] and PI studies [27–30]. Nevertheless there still exists a large scatter in the experimental values for the measured AEs, specifically concerning processes (3.4.4)–(3.4.8). In our study we have estimated the AEs of the ions formed via reaction (3.4). We have published the results of these investigations in Ref. [5]. The AEs of the ions measured at 293 K are summarized in Table 8. Our values of the AEs are compared with earlier electron impact ionization [23] values and a recent synchrotron PI study [31]. There exists appreciable agreement between the AEs measured at room temperature using these three different techniques.

As with previous molecules we have focused in particular on the effect of the gas temperature on the AEs concerning reactions (3.4.1)–(3.4.3). The influence of the temperature on the AEs of the ions is summarized in Table 9. The red shift of the AEs of the ions formed via EII to C$_2$H$_6$ between 297 and 697 K ranges between 0.19 and 0.30 eV. The increased value of the shift in C$_2$H$_6$ in comparison to CH$_4$ is in agreement with the fact that the C$_2$H$_6$ molecule has more vibrational normal modes than the CH$_4$ and thus the increase of the internal energy between 297 K and 697 K in the ethane is larger than in methane.

**Table 8.** Appearance energies of the ions formed via electron impact ionization to $C_2H_6$ at 293 K.
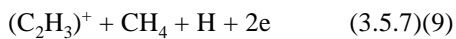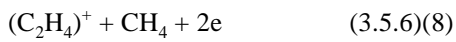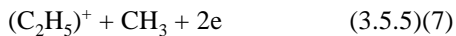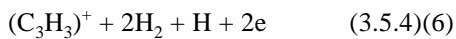
| e + $C_2H_6$ → | Present AE (eV) | EII [23] IE (eV) | PI [27] IE (eV) | Thermochemical thresholds [7] |
|---|---|---|---|---|
| $C_2H_6^+$ | 11.46 ± 0.04 | 11.57 ± 0.02 | 11.5 ± 0.1 | |
| $C_2H_5^+ + H^-$ | 12.06 ± 0.06 | 12.08 | | 11.72 |
| $C_2H_5^+ + H$ | 12.7 ± 0.1 | 12.45 | 12.4 ± 0.1 | 12.47 ± 0.03 |
| $C_2H_4^+ + H_2$ | 11.90 ± 0.04 | 11.81 ± 0.05 | 12.0 ± 0.1 | 11.92 ± 0.0006 |
| $C_2H_3^+ + H + H_2$ | 15.02 ± 0.1 | 14.50 ± 0.04 | 14.8 ± 0.1 | 14.47 ± 0.46 |
| $C_2H_2^+ + 2H_2$ | 15.02 ± 0.1 | 14.41 ± 0.01 | 14.9 ± 0.1 | 14.61 ± 0.01 |
| $C_2H^+ + 2H_2 + H$ | | 22.4 ± 0.3 | | 20.5 ± 0.15 |
| $C_2H^+ + H_2 + 3H$ | 25.7 ± 0.3 | | | 25.1 ± 0.15 |
| $C_2^+ + 3H_2$ | 22.6 ± 0.3 | 22.9 ± 0.3 | | 20.95 ± >0.3 |

**Table 9.** The values of the AEs measured at two different temparatures.

| e + $C_2H_6$ → | AE(297K) | AE(697K) | Δ(AE(697)-AE(297)) |
|---|---|---|---|
| $C_2H_6^+$ | 11.46 ± 0.04 | 11.2 ± 0.04 | 0.26 ± 0.08 |
| $C_2H_5^+ + H^-$ | 12.06 ± 0.06 | 11.87 ± 0.06 | 0.19 ± 0.12 |
| $C_2H_5^+ + H$ | 12.7 ± 0.1 | 12.4 ± 0.1 | 0.30 ± 0.2 |
| $C_2H_4^+ + H_2$ | 11.90 ± 0.04 | 11.60 ± 0.04 | 0.30 ± 0.1 |

*3.5. $C_3H_8$*

The formation of cations via electron impact ionization to neutral propane has been studied for the following reactions:

$$e + C_3H_8 \rightarrow (C_3H_8)^+ + 2e \qquad (3.5.1)(3)$$
$$(C_3H_7)^+ + H^- + e \qquad (3.5.2a)(4a)$$
$$(C_3H_7)^+ + H + 2e \qquad (3.5.2b)(4b)$$
$$(C_3H_5)^+ + H_2 + H + 2e \qquad (3.5.3)(5)$$
$$(C_3H_3)^+ + 2H_2 + H + 2e \qquad (3.5.4)(6)$$
$$(C_2H_5)^+ + CH_3 + 2e \qquad (3.5.5)(7)$$
$$(C_2H_4)^+ + CH_4 + 2e \qquad (3.5.6)(8)$$
$$(C_2H_3)^+ + CH_4 + H + 2e \qquad (3.5.7)(9)$$
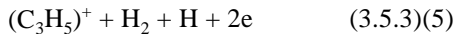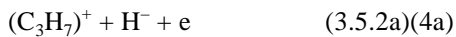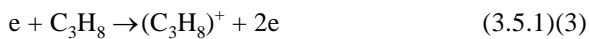
The ion efficiency curves of all studied cations have been measured at the gas temperature of 290 K in the electron energy range from about 1 eV below the reaction threshold up to about 2 eV above the onset. Using the fitting method introduced above, the corresponding AE values have been derived. The AEs obtained from the experimental data measured at 290 K are presented in Table 10. They are compared with values obtained from the most recent electron impact work of Fiegele et al. [31] (in the case of the AE for $(C_2H_3)^+$ which has been not measured in Ref. [31] the

present value is compared with the value of Ehrhardt et al. [32]), and results of previous PI spectroscopy works [33, 34]. Moreover, Table 1 includes the threshold energies for reactions (3.5.2)–(3.5.7) based on thermochemical data [11] applying equation (1), which can be expected as the low limit for the ionization process.

The present AE values at ambient temperature are in general lower than those from previous studies. This difference can be explained similarly as with previous molecules, with the high detection efficiency of the apparatus and long accumulation times of the ion signal which allows the detection of very weak ion efficiency yields. The present values are also lower than the calculated thresholds from thermochemical data, but it should be noted that these thresholds are based on experimental data which on their part are afflicted with experimental uncertainty.

The measured temperature effects on the AEs of propane are in good agreement with the previous studies concerning ethane and methane. When the temperature of the MB source was increased from 290 K to 690 K, a decrease of the AE for cations of propane in the range of about 0.21 ± 0.09 eV up to 0.42 ± 0.1 eV was observed. We expected this result, and the larger shift in comparison to methane and ethane can be explained by the fact that the propane molecule has more normal modes of vibration than the formerly studied molecules. Table 11 presents the AEs derived from the ion efficiency curves measured at two different gas temperatures.

## 4. Conclusions

The AEs have been determined for large number ions formed via electron impact ionization of the molecules $CH_4$, $CH_3D$, $CD_4$, $C_2H_6$ and $C_3H_8$ at room temperature. Additionally, for the first time the AEs were measured also at high temperature (700 K), and remarkable temperature effects on the AEs of the molecules have been observed.

**Table 10.** Appearance energies of the ions formed via electron impact ionization to $C_3H_8$.

| e + ($C_3H_8$) → | Present EI AE (eV) 290 K | EII [31] AE (eV) | PI [33][a] [34][b] AE (eV) | Thermochemical thresholds (eV) |
|---|---|---|---|---|
| $(C_3H_8)^+$ | $10.51 \pm 0.05$ $10.96 \pm 0.05$ | $11.22 \pm 0.05$ | $10.95 \pm 0.05^b$ | |
| $(C_3H_7)^+ + H^-$ | $10.33 \pm 0.1$ | | $\sim11.0^b$ | $10.95 \pm 0.02$ |
| $(C_3H_7)^+ + H$ | $11.20 \pm 0.04$ | $11.51 \pm 0.05$ | $11.59 \pm 0.01^b$ | $11.65 \pm 0.02$ |
| $(C_3H_5)^+ + H_2 + H$ $(C_3H_5)^+ + 3H$ | $13.48 \pm 0.05$ | $13.48 \pm 0.05$ | $13.5 \pm 1.0^a$ | $13.23 \pm 0.07$ $17.75 \pm 0.07$ |
| $(C_3H_3)^+ + 2H_2 + H$ | | | | $15.53 \pm 0.04$ |
| $(C_3H_3)^+ + H_2 + 3H$ | $15.39 \pm 0.04$ | $16.50 \pm 0.3$ | $16.5 \pm 1.0^a$ | $20.05 \pm 0.04$ |
| $(C_3H_3)^+ + 5H$ | | | | $27.71 \pm 0.04$ |
| $(C_2H_5)^+ + CH_3$ | $11.86 \pm 0.1$ | $11.91 \pm 0.06$ | $11.90 \pm 0.08^b$ | $11.96 \pm 0.02$ |
| $(C_2H_4)^+ + CH_4$ | $11.47 \pm 0.06$ | $11.94 \pm 0.1$ | $11.72 \pm 0.02^b$ | $11.37 \pm 0.001$ |
| $(C_2H_3)^+ + CH_4 + H$ | $14.13 \pm 0.05$ | $14.5 \pm 0.15$ | $14.0 \pm 1.0^a$ | $13.91 \pm 0.05$ |

**Table 11.** The values of the AEs measured at two different temperatures.

| e + ($C_3H_8$) → | AE(290K) (eV) | AE(690K) (eV) | Δ(AE(690K)- AE(290K)) (eV) |
|---|---|---|---|
| $(C_3H_8)^+$ | $10.51 \pm 0.05$ $10.96 \pm 0.05$ | $10.28 \pm 0.1$ $10.75 \pm 0.05$ | $0.23 \pm 0.07$ $0.21 \pm 0.09$ |
| $(C_3H_7)^+ + H^-$ | $10.33 \pm 0.1$ | $9.99 \pm 0.1$ | $0.34 \pm 0.08$ |
| $(C_3H_7)^+ + H$ | $11.20 \pm 0.04$ | $10.87 \pm 0.04$ | $0.33 \pm 0.05$ |
| $(C_2H_5)^+ + CH_3$ | $11.86 \pm 0.1$ | $11.48 \pm 0.07$ | $0.38 \pm 0.1$ |
| $(C_2H_4)^+ + CH_4$ | $11.47 \pm 0.06$ | $11.05 \pm 0.1$ | $0.42 \pm 0.1$ |

Generally, the AEs of the ions were decreasing with the increasing temperature of the molecules. The magnitude of the AE shift has been found to depend on the size of the molecule: the larger the molecules the larger the shift of the AE (0.14 eV for $CH_4$, 0.3 eV for $C_2H_6$ and 0.42 eV for $C_3H_8$). This phenomenon has been elucidated by the fact that with increasing temperature of the gas the internal energy of the molecules increases, and thus less energy is necessary to the molecule. Additionally, differences in the AEs of the ions formed from various isotopomers of methane have been observed, most of them for the first time in the electron impact ionization experiment.

The observed temperature effects on the AEs of the ions formed via electron impact ionization to small hydrocarbon molecules may have strong relevance to the high temperature plasma, specifically in the case of the fusion plasma. The relatively small changes in the AE of the ions may result in noticeable changes in the rate coefficient for electron impact ionization. In the future, therefore, careful measurements of the cross-sections at the reaction threshold associated with the temperature dependence measurements should be carried out and the gas temperature rate coefficients for electron impact ionization calculated.

## References

[1] JANEV, R.K. (Ed.), Atomic and Molecular Processes in Fusion Plasmas, Plenum, New York, 1995.

[2] HOFER, W.O., ROTH, E., Physical Processes of Interaction of Fusion Plasmas with Solids, Academic, New York, 1996.

[3] TAWARA, H., Electron Collision Processes Involving Hydrocarbons, in Atomic and Molecular Processes in Fusion Edge Plasmas, (JANEV R.K. Ed.), Plenum Press, New York and London, 1995.

[4] STANO, M., MATEJČIK, S., SKALNY, J.D., MÄRK, T.D., J. Phys. B: At. Mol. Opt. Phys. **36** (2003) 261.

[5] VAŠEKOVÁ, E., et al., Int. J. Mass Spectrom. **235** (2004) 155.

[6] DENIFL, S., MATEJČIK, S., MÄRK, T.D., $CH_3D,CD_4$, to be published.

[7] AFEEFY, H.Y., LIEBMAN, J.F., STEIN, S.E., Neutral Thermochemical Data, in NIST Chemistry WebBook, NIST Standard Reference Database Number 69, Eds. P.J. Linstrom and W.G. Mallard, National Institute of Standards and Technology, Gaithersburg, MD, 2003.

[8] FIELD, F.H., FRANKLIN, J.L., Electron impact phenomena, Academic Press, New York, 1957.

[9] MATEJČIK, S., FOLTIN, V., STANO, M., SKALNY, J.D., Int. J. Mass Spect. **223–224** (2003) 9.

[10] WANNIER, G.H., Phys. Rev. **90** (1953) 817.

[11] LIAS, S.G., et al., Ionization Energetics (IE, AE) Database, in NIST Standard Reference Database, 69, National Institute of Standards and Technology, Gaithersburg, MD.

[12] PLESSIS, P., MARMET, P., DUTIL, R., J. Phys. B **16** (1983) 1283.

[13] CHATHAM, H., HILS, D., ROBERTSON, R., GALLAGHER, A., J. Chem. Phys. **81** (1984) 1770.

[14] MORRISON, J.D., TRAEGER, J.C., Int. J. Mass Spectrom. Ion Phys. **11** (1973) 289.

[15] FINNEY, C.D.; HARRISON, A.G., Int. J. Mass Spectrom. Ion Phys. **9** (1972) 221.

[16] LOSSING, F.P., SEMELUK, G.P., Intern. J. Mass Spectrom. Ion Phys. **2** (1969) 408.

[17] SELIM, E.T.M., EL-KHOLY, S.B., Indian J. Pure Appl. Phys. **13** (1975) 233.

[18] LOSSING, F.P., TICKNER, A.W., BRYCE, W.A., J. Chem. Phys. **19** (1951) 1254.

[19] HONIG, R.E., J. Chem. Phys. **16** (1948) 105.

[20] BERKOWITZ, J., GREENE, J.P., CHO, H., RUSCIC, B., J. Chem. Phys. **86** (1987) 674.

[21] DIBELER, V.H., KRAUSS, M., REESE, R.M., HARLEE, F.N., J. Chem. Phys. **42** (1965) 3791.

[22] SUZUKI, I.H., MAEDA, K., Int. J. Mass Spectrom. Ion Phys. **24** (1977) 147.

[23] PLESSIS, P., MARMET, P., Can. J. Chem. **65** (1987) 1424.

[24] CHATHAM, H., HILS, D., ROBERTSON, R., GALLAGHER, A., J. Chem. Phys. **18** (1984) 1770.

[25] WILLIAM, J.M., HAMILL, W.H., J. Chem. Phys. **49** (1968) 4467.

[26] SELIM, E.T.M., Ind. J. Pure Appl. Phys. **14** (1976) 547.

[27] MACKIE, A., et al., J. Phys. B: At. Mol. Opt. Phys. **35** (2002) 1061–1069.

[28] CHUPKA, W., BERKOWITZ, J., J. Chem. **47** (1967) 2921.

[29] KAMETA, K., KOUCHI, N., UKAI, M., HATANO, Y., J. El. Spect. Rel. Phen. **123** (2002) 225.

[30] NICHOLSON, A.J.C., J. Chem. Phys. **43** (1965) 1171.

[31] FIEGELE, T., HANEL, G., TORRES, I., LEZIUS, M., MÄRK, T.D., J. Phys. B: At. Mol. Opt. Phys. **33** (2000) 4263.

[32] EHRHARD, H., TEKAAT, T., Z. Naturforschung **19a** (1964) 1382.

[33] AU, J.W., COOPER, G., BRION, C.E., Chem. Phys. **173** (1993) 241.

[34] CHUPKA, W.A., BERKOWITZ, J., J. Chem. Phys. **47** (1967) 2921.

# Product branching ratios in recombination of hydrocarbon ions ($C_nH_m^+$ n > 0, m > 0)

*M. Larsson*

Department of Physics, AlbaNova, Stockholm University, SE-106 91 Stockholm, Sweden

**Abstract**

The dissociative recombination of hydrocarbon ions ($C_nH_m^+$ n > 0, m > 0) leads to the formation of neutral reaction products that may influence the edge plasma in a fusion reactor. Whereas the rate constant for dissociative recombination of $C_nH_m^+$ ions has been measured with afterglow techniques, the product branching ratios can presently only be determined in ion storage rings. In this report we summarize the database developed at the storage ring CRYRING in Stockholm.

## 1.    Introduction

A single electron carrying a negligible amount of kinetic energy can cause considerable damage to a molecular ion by the process of dissociative recombination. The low energy electron is attracted to the molecular ion by the Coulomb force, accelerated towards the ion and finally captured into an autoionizing state by exciting a bound electron. The autoionizing state is often strongly repulsive so that the nuclei rapidly separate, thereby lowering the electronic energy to the point where autoionization becomes energetically prohibited. The electron capture is stabilized by molecular dissociation, hence the name dissociative recombination.

In a plasma cold enough to contain molecules, dissociative recombination is the most important neutralizing process. In a fusion reactor, molecular ions are present in the fusion edge plasma and in particular divertors. Hydrocarbon ion impurities are present because of the interaction of the plasma with the carbon containing first wall or the divertor plate segments. Hydrocarbon molecules released into the plasma are ionized and subsequently dissociated. In order to model the edge plasma, information on the dissociative recombination of hydrocarbon ions is needed [1, 2]. The complexity of the process makes it impossible to rely on theoretical calculation, which means that laboratory measurements are needed. Presently there is only one technique which allows measurements of product branching ratios of the dissociative recombination of hydrocarbon ions, namely the ion storage ring technique. We report here on the measurements of branching ratios that have been carried out at the storage ring CRYRING at Stockholm University.

## 2.    Measurements of branching ratios in CRYRING

Figure 1 shows the cooler storage ring CRYRING at the Manne Siegbahn Laboratory of Stockholm University. It was commissioned in 1992 and has by now hosted many prolific research programmes in atomic and molecular physics.
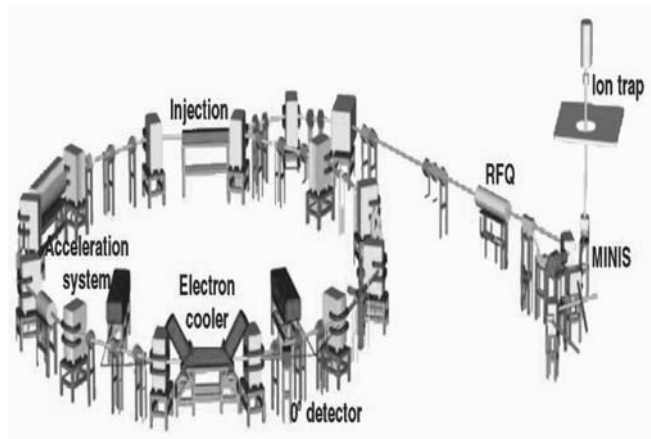


**Figure 1.** The ion cooler storage ring CRYRING at the Manne Siegbahn Laboratory, Stockholm University. The ring has a circumference of 51.6 m. Ions are produced in different ion sources; in this figure the hot filament discharge source MINIS is connected to the ring. For most molecular ions, the radiofrequency quadrupole (RFQ) device acts only as a focusing element. The ions are accelerated by the acceleration system, a drift tube connected to a radiofrequency power amplifier, and can reach a maximum energy of 96 ($Z^2$/A) MeV, where Z is the charge and A the mass. The electron cooler is used both to phase space cool the stored ion beam and as a target in the study of electron–ion collisions. Neutral reaction products are detected by the 0° detector. The ion trap is a separate experiment and has nothing to do with the ring.

The research programme in molecular physics at CRYRING and other small storage rings has been reviewed [3, 4]. In order to store molecular ions for tens of seconds, the ring is kept at ultrahigh vacuum, $10^{-11}$ torr, or else the ions would be destroyed by collisions with residual gas molecules in a short time. It is worth pointing out the advantages of applying ion cooler storage rings to the study of dissociative recombination:

(a) Vibrationally hot molecular ions that are injected into the ring can cool internally after a few seconds by emission of infrared radiation. The ro-vibrational temperature of the ions converges to equilibrium with the 300 K blackbody radiation from the vacuum pipes.

(b) Lighter molecular ions, broadly defined as ions containing no more than one second row atom, can be cooled translationally by means of the electron cooler. During each passage through the electron cooler, heat is transferred from the ion beam to the continuously renewed electron beam. A phase space cooled ion beam has low momentum spread in the longitudinal direction, and low emittance, i.e. low divergence and small cross-sectional area.

(c) The electron beam has a much larger diameter than the ion beam, even when it is uncooled, and since the electron beam is approximately homogeneous, absolute cross-sections can be measured without elaborate measurements of the form factor, which takes account of the area of overlap and the spatial density of both target (electron) and projectile (ion) beams. The form factor is simply reduced to the area of the electron beam, which is well known ($12.5$ cm$^2$), and independent of the shape of the ion beam.

(d) The high beam energy as compared with single pass experiments reduces electron capture in collisions between the stored ion beam and rest gas molecules. Since this process gives products with the same total mass as dissociative recombination, it contributes to a background. The combination of ultrahigh vacuum and high beam energy is a very effective remedy.

(e) While electron capture from residual gas molecules has a very low cross-section at high ion beam energies, charge stripping does not. By using energy resolving surface barrier detectors, charge stripping products are easily separated from the recombination signal. The detector efficiency is 100% at the beam energies used in storage rings.

(f) The merging of the electron and ion beams gives access to collisions at very low energies, where the cross-section is large. The electron beam can be made very cold, with an energy spread in the transverse direction corresponding to about 2 MeV, which gives high resolution.
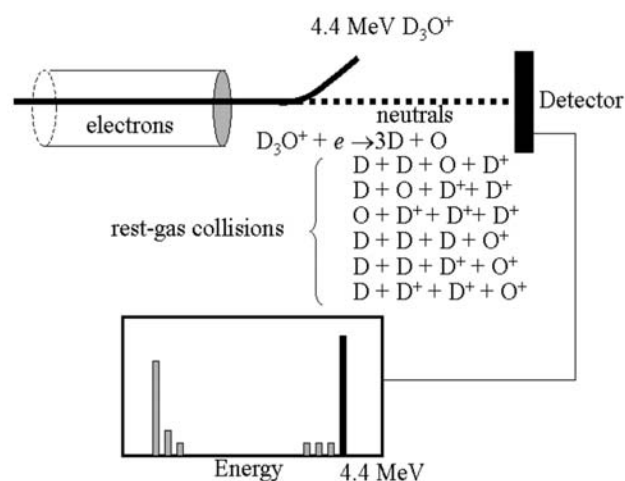


**Figure 2.** The basic principles for an ion storage ring experiment with a 4.4 MeV $D_3O^+$ beam. Neutral reaction products from dissociative recombination of $D_3O^+$ in the electron–ion interaction region (85 cm in CRYRING) leave the ring and hit a surface barrier detector which gives a pulse proportional to the amount of kinetic energy of the particle. The combined energy of 3D+O (in whatever combination of products) gives a pulse at 4.4 MeV, whereas rest gas collisions give pulses at fractions of this energy because charged products are deflected from the 0° direction by the dipole magnet (not shown here). The signal at 4.4 MeV is not sufficient to determine the branching ratios. If a grid with a known transmission is positioned in front of the detector, some products from dissociative recombination are blocked from reaching the detector. See the text for a description of how this is used to extract branching ratios.

Dissociative recombination cross-sections can be measured in storage rings, which gives direct information about the thermal rate constant over a broad electron temperature range, although not a broad range of ro-vibrational temperatures since the storage ring experiments usually, but certainly not always, are conducted for ions with an internal temperature of 300 K. Rate constants can also be measured directly using afterglow techniques. Complete product branching ratios can only be measured in ion storage rings.

Figure 2 shows how a measurement of an absolute cross-section for dissociative recombination of $D_3O^+$ is performed. The peak at 4.4 MeV is a direct measure of the cross-section, provided the electron and ion beam currents are measured, and the length of the interaction is known. The electron beam is straightforward to measure, whereas the ion beam must be measured non-destructively. This is done by measuring the magnetic field generated by the stored ion beam.

The peak at full beam energy of 4.4 MeV in Fig. 2 is produced independently of the combination of products. When $D_3O^+$ in its lowest vibrational level recombines with electrons, 4 decay channels are available; $D_2O + D$, $OD + D_2$, $OD + D + D$ and $O + D_2 + D$. The products from a single event hit the detector within a very narrow time window, which makes it very difficult to extract product information

**Table 1.** Hydrocarbon ions studied in CRYRING

| Molecule | | Branching ratio | Reference |
|---|---|---|---|
| $CH_2^+$ | $C + H + H$ | $0.63 \pm 0.06$ | [6] |
| | $CH + H$ | $0.25 \pm 0.04$ | |
| | $C + H_2$ | $0.12 \pm 0.02$ | |
| $CH_5^+$ | $CH_3 + H + H$ | $0.70 \pm 0.01$ | [7] |
| | $CH_2 + H_2 + H$ | $0.17 \pm 0.02$ | |
| | $CH + H_2 + H_2$ | $0.03 \pm 0.01$ | |
| | $CH_4 + H$ | $0.05 \pm 0.01$ | |
| | $CH_3 + H_2$ | $0.05 \pm 0.01$ | |
| $C_2H^+$ | $C_2 + H$ | $0.43 \pm 0.03$ | [8] |
| | $CH + C$ | $0.39 \pm 0.04$ | |
| | $C + C + H$ | $0.18 \pm 0.04$ | |
| $C_2H_2^+$ | $C_2H + H$ | $0.50 \pm 0.06$ | [9] |
| | $CH + CH$ | $0.13 \pm 0.01$ | |
| | $C_2 + H + H$ | $0.30 \pm 0.05$ | |
| | $CH_2 + C$ | $0.05 \pm 0.01$ | |
| | $C_2 + H_2$ | $0.02 \pm 0.03$ | |
| $C_2H_3^+$ | $C_2H_2 + H$ | $0.29 \pm 0.04$ | [10] |
| | $C_2H + H_2$ | $0.06 \pm 0.03$ | |
| | $C_2H + H + H$ | $0.59 \pm 0.06$ | |
| | $C_2 + H_2 + H$ | $0.03 \pm 0.01$ | |
| | $CH_3 + C$ | $0.006 \pm 0.002$ | |
| | $CH_2 + CH$ | $0.03 \pm 0.01$ | |
| $C_2H_4^+$ | $C_2H_3 + H$ | $0.11 \pm 0.07$ | [9] |
| | $C_2H_2 + H_2$ | $0.06 \pm 0.03$ | |
| | $C_2H_2 + H + H$ | $0.66 \pm 0.06$ | |
| | $C_2H + H_2 + H$ | $0.10 \pm 0.04$ | |
| | $CH_4 + C$ | $0.01 \pm 0.01$ | |
| | $CH_3 + CH$ | $0.02 \pm 0.02$ | |
| | $CH_2 + CH_2$ | $0.04 \pm 0.02$ | |
| $C_2D_5^+$ | $C_2D_4 + D$ | $0.12 \pm 0.03$ | [11] |
| | $C_2D_3 + D + D$ | $0.27 \pm 0.04$ | |
| | $C_2D_2 + D + D + D$ | $0.13 \pm 0.03$ | |
| | $C_2D_2 + D_2 + D$ | $0.29 \pm 0.03$ | |
| | $CD_3 + CD_2$ | $0.17 \pm 0.01$ | |
| $C_3H_4^+$ | $C_3H_3 + H$ | $0.87 \pm 0.04$ | [12] |
| | $C_3H_2 + H_2$ | $\leq 0.02$ | |
| | $C_2H_3 + CH$ | $0.01 \pm 0.01$ | |
| | $C_2H_2 + CH_2$ | $0.06 \pm 0.02$ | |
| | $C_2H + CH_3$ | $0.01 \pm 0.01$ | |
| | $C_3H_2 + H + H$ | $\leq 0.05$ | |
| $C_3H_7^+$ | C–C bond breaking | 0.34–0.39 | [13] |
| $C_3D_7^+$ | C–C bond breaking | 0.44 | [14] |
| $C_4D_9^+$ | C–C bond breaking | 0.39 | [14] |

from the detector signal. Instead, a grid with known transmission is placed in front of the detector. This results in some products being blocked from the detector, and a signal at a fraction of the full energy. For example, if OD passes the grid and $D_2$ is blocked, a pulse at 3.6 MeV occurs. The grid results in a redistribution of counts that all occurred at

4.4 MeV in the absence of the grid. This redistribution is related to the branching ratios via a probability matrix [5]. The beauty of the technique is its simplicity (a stainless steel grid normally used as a filter in beer production is a low-tech but very effective solution) and the fact that a complete set of branching ratios is obtained in a single experiment.

## 3. Results for hydrocarbon ions

The first hydrocarbon ion to be studied in CRYRING was $C_2H_2^+$, and this was before the co-ordinate research project started. Table 1 lists all results for hydrocarbon ion branching ratios measured in CRYRING. The complete results are given for $C_nH_m^+$ (n < 3), whereas only the results for the C–C bond breaking is given for $C_nH_m^+$ (n < 3). The level of detail concerning H atom loss channels differs for the isotopomers $C_3D_7^+$ and $C_3H_7^+$, with the more reliable results being those for $C_3D_7^+$ because of the larger mass separation provided by the D atoms. For $C_4D_9^+$ only the C–C bond breaking branching ratio could be determined.

Dissociative recombination of hydrocarbon ions has also been studied at the ASTRID storage ring in Aarhus. The complete branching ratios for the $CH_3^+$ ion was measured [15]. For $C_nH_m^+$ ions with n = 3 and 4, experiments at the storage ring ASTRID have covered to complete series of ions with m = 1–8 for n = 3 and m = 1–9 for n = 4 [16–18]. Only the C–C bond breaking was measured in these cases, and is in good agreement with the data from CRYRING when such are available.

The results from CRYRING, including attempts to rationalize the data in terms of enthalpy changes in the reactions, have been reviewed very recently [19]. The results from Aarhus have also been reviewed [20].

## References

[1] JANEV, R.K., REITER, D., Phys. Plasmas **9** (2002) 4071.
[2] JANEV, R.K., REITER, D., Phys. Plasmas **11** (2004) 780.
[3] LARSSON, M., Annu. Rev. Phys. Chem. **48** (1997) 151.
[4] LARSSON, M., Adv. Gas Phase Ion Chem. **4** (2001) 179.
[5] NEAU, A., AL-KHALILI, A., ROSÉN, S., LE PADELLEC, A., DERKATCH, A.M., SHI, W., VIKOR, L., LARSSON, M., SEMANIAK, J., THOMAS, R., NÅGÅRD, M.B., ANDERSSON, K., DANARED, H., AF UGGLAS, M., J. Chem. Phys. **113** (2000) 1762.
[6] LARSON, Å., LE PADELLEC, A., SEMANIAK, J., STRÖMHOLM, C., LARSSON, M., ROSÉN, S., PEVERALL, R., DANARED, H., DJURIC, N., DUNN, G.H., DATZ, S., Astrophys. J. **505** (1998) 459.

[7] SEMANIAK, J., LARSON, Å., LE PADELLEC, A., STRÖMHOLM, C., LARSSON, M., ROSÉN, S., PEVERALL, R., DANARED, H., DJURIC, N., DUNN, G.H., DATZ, S., Astrophys. J. **498** (1998) 886.

[8] EHLERDING, A., HELLBERG, F., THOMAS, R., KALHORI, S., VIGGIANO, A.A., ARNOLD, S.T. LARSSON, M., AF UGGLAS, M., Phys. Chem. Chem. Phys. **6** (2004) 949.

[9] DERKATCH, A.M., AL-KHALILI, A., VIKOR, L., NEAU, A., SHI, W., DANARED, H., AF UGGLAS, M., LARSSON, M., J. Phys. B **32** (1999) 3391.

[10] KALHORI, S., VIGGIANO, A.A., ARNOLD, S.T., ROSÉN, S., SEMANIAK, J., DERKATCH, A.M., AF UGGLAS, M., LARSSON, M., Astron. Astrophys. **391** (2002) 1159.

[11] GEPPERT, W., EHLERDING, A., HELLBERG, F., KALHORI, S., THOMAS, R.D., NOVOTNY, O., ARNOLD, S.T., MILLER, T.M., VIGGIANO, A.A., LARSSON, M., Phys. Rev. Lett. **93** (2004) 153201.

[12] GEPPERT, W.D., THOMAS, R., EHLERDING, A., HELLBERG, F., ÖSTERDAHL, F., AF UGGLAS, M., LARSSON, M., Int. J. Mass Spectrom. **237** (2004) 25.

[13] EHLERDING, A., ARNOLD, S.T., VIGGIANO, A.A., KALHORI, S., SEMANIAK, J., DERKATCH, A.M., ROSÉN, S., AF UGGLAS, M., LARSSON, M., J. Phys. Chem. **107** (2003) 2179.

[14] LARSSON, M., EHLERDING, A., GEPPERT, W.D., HELLBERG, F., KALHORI, S., THOMAS, R.D., DJURIC, N., ÖSTERDAHL, F., ANGELOVA, G., SEMANIAK, J., NOVOTNY, O., ARNOLD, S.T., VIGGIANO, A.A., J. Chem. Phys. (2005).

[15] VEJBY-CHRISTENSEN, L., ANDERSEN, L.H., HEBER, O., KELLA, D., PEDERSEN, H.B., SCHMIDT, H., ZAJFMAN, D., Astrophys. J. **483** (1997) 531.

[16] MITCHELL, J.B.A., REBRION-ROWE, C., LE GARREC, J.L., ANGELOVA, G., BLUHME, H., SEIERSEN, K., ANDERSEN, L.H., Int. J. Mass Spectrom. **227** (2003) 273.

[17] ANGELOVA, G., NOVOTNY, O., MITCHELL, J.B.A., REBRION-ROWE, C., LE GARREC, J.L., BLUHME, H., SVENDSEN, A., ANDERSEN, L.H., Int. J. Mass Spectrom. **232** (2004) 195.

[18] ANGELOVA, G., NOVOTNY, O., MITCHELL, J.B.A., REBRION-ROWE, C., LE GARREC, J.L., BLUHME, H., SVENDSEN, A., ANDERSEN, L.H., Int. J. Mass Spectrom. **235** (2004) 7.

[19] VIGGIANO, A.A., EHLERDING, A., ARNOLD, S.T., J. Phys: Conf. Ser. **4** (2005) 191.

[20] MITCHELL, J.B.A., ANGELOVA, G., REBRION-ROWE, C., NOVOTNY, O., LE GARREC, J.L., BLUHME, H., SEIERSEN, K., SVENDSEN, A., ANDERSEN, L.H., J. Phys: Conf. Ser. **4** (2005) 198.

# Electron impact ionization of molecules and free radicals

*K. Becker[1,2], V. Tarnovsky[1]*

[1] Department of Physics and Engineering Physics, Stevens Institute of Technology, Hoboken, NJ 07030, USA
[2] Center for Environmental Systems, Stevens Institute of Technology, Hoboken, NJ 07030, USA

## Abstract

We summarize the results of selected experimental electron impact ionization cross-section studies carried out as part of an IAEA Coordinated Research Project (CRP) on Molecular Processes in Edge Plasmas. Data for absolute total and partial ionization cross-sections are presented and discussed for the nitrogen–oxygen compounds NO, $NO_2$ and $N_2O$ as well as for the molecules $WF_6$ and $B_2H_6$. Experimental techniques employed include the fast neutral beam technique and a mass spectrometric technique utilizing a time of flight mass spectrometer (TOF-MS). To the extent possible, comparisons are made with other available experimental cross-section data and with calculated cross-sections.

## 1. Introduction

The ionization of an atom or molecule by electron impact is one of the most fundamental electron collision processes [1]. Electron ionization also plays a very important role in many applications as diverse as low temperature processing plasmas, fusion edge plasmas, gas discharges, planetary, stellar and cometary atmospheres, radiation chemistry, mass spectrometry, and chemical analysis. As part of the Coordinated Research Project (CRP) on Molecular Processes in Edge Plasmas, we have studied the experimental determination of absolute partial and total electron impact ionization cross-sections for selected molecules relevant to fusion edge plasmas. Our particular emphasis has been on the ionization of the $NO_x$ compounds NO, $NO_2$ and $N_2O$, which are ubiquitous in plasmas with even trace concentrations of $O_2$ and $N_2$, as well as the molecules $B_2H_6$ and $WF_6$. To the extent possible, comparisons are made with available data from other groups. Our experimental cross-section studies were also supported by semiclassical total ionization cross-section calculations using the Deutsch–Märk (DM) formalism [2, 3].

This manuscript is organized as follows: Section 2 provides some details regarding the experimental techniques used, Section 3 summarizes the results for the various targets, and Section 4 provides a brief summary of the major findings.

## 2. Experimental considerations

For the work reported here we used two different experimental apparatuses. Both experimental set-ups have been described in detail in previous papers [4–17]. The ionization cross-section measurements for the $NO_x$ compounds made use of our well characterized fast neutral beam apparatus, whose performance has just been improved by replacing the channeltron detector by a 2-dimensional position sensitive detector and by the introduction of a new electron gun, which can achieve a current density that is 10 times higher than that of the previously used electron gun. Figure 1 shows a schematic diagram of the fast beam apparatus before any changes were incorporated. Below we provide a brief summary of the fast beam technique. A DC discharge operated at a positive bias of typically 3 keV through a suitable target gas serves as the primary ion source. The primary ions after mass selection in a Wien filter are neutralized by near resonant charge transfer in a cell filled with an appropriately chosen charge transfer gas. Efficient charge transfer is not critically dependent on an exact match of the ionization energies of the charge transfer partners. The residual ions are removed from the beam by electrostatic deflection, and most target species in Rydberg states are quenched in a region of high electric field. The neutral beam is subsequently crossed at right angles by a
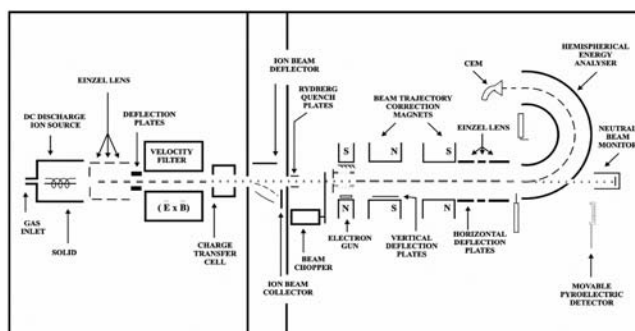


**Figure 1.** Schematic diagram of the fast neutral beam apparatus.

well characterized electron beam (5–200 eV beam energy, 0.5 eV FWHM energy spread, 0.03–0.4 mA beam current or up to 2 mA for the new electron gun). The product ions are focused in the entrance plane of an electrostatic hemispherical analyser which separates ions of different charge to mass ratios (i.e. singly from multiply charged ions and parent ions from fragment ions). The ions leaving the analyser are detected by a channel electron multiplier (CEM) (or by a new 2-dimensional position sensitive detector). The well established Kr or Ar absolute ionization cross-sections can serve as a convenient normalization standard to put the relative cross-section functions on an absolute scale. Even though the apparatus is capable of determining absolute ionization cross-sections without any normalization and without fitting the measured data to theory, it was found to be advantageous to use the Kr or Ar benchmark cross-sections to calibrate the pyroelectric crystal. The calibrated detector, in turn, is then used to determine the flux of the neutral target beam in absolute terms. This procedure avoids the frequent and prolonged exposure of the sensitive pyroelectric crystal to fairly intense ion beams and thus enhances significantly the stability and useful lifetime of the crystal.

We carried out a series of experimental studies supported by ion trajectory modelling calculations [4, 18] to establish for each target that all molecular fragment ions with an excess kinetic energy of less than 2–2.5 eV per fragment ion are collected and detected with 100% efficiency (with the exception of the light $H^+/D^+$ fragment ions where ion losses occur for excess kinetic energies as low as 0.5 eV per fragment ion). Furthermore, careful threshold studies were carried out in all cases in an effort to detect the presence of excited target species (vibrationally excited species, metastables and species in high lying Rydberg states) in the incident neutral beams. Additional considerations pertain to H/D containing targets. This is due to the fact that there is a mass difference of only 1 amu (2 amu for the deuterated target species) between the various primary ions extracted from the discharge source and between the various product ions produced from a given parent. The resolution of the Wien filter is sufficient in most cases to separate the various primary ions extracted from the ion source. On the other hand, the resolving power of the electrostatic hemispherical analyser is not always sufficient to fully separate the parent and the various fragment ions from a given neutral radical, and great care has to be exercised in those cases to obtain reliable partial ionization cross-sections.

Fragment ions from the dissociative ionization of the parent neutral are often produced with excess kinetic energy. This results in slightly divergent fragment ion beams emerging from the interaction region compared to the spatially well collimated parent ion beam which, in turn, causes the fragment ions to spread out spatially in the hemispherical analyser. This renders the separation of the various product ion signals more difficult. Previously, in an effort to assess the capability of the hemspherical analyser to separate the various product ions for a given target, a fixed beam energy and a fixed amount of excess kinetic energy, we employed a narrow moveable slit in front of the CEM entrance in order to separate the spatially well collimated parent ion signal from the spread out fragment ion signal. The fragment ion signals were obtained by sweeping the spatially spread out fragment ion signal across the CEM entrance cone and integrating the signal for a given fragment ion (after the narrow slit was removed and the well collimated parent ion peak was deflected away from the CEM entrance). Absolute ionization cross-sections can be determined with uncertainties of ±15% for the parent ionization cross-sections and ±18% for the dissociative ionization cross-sections. These error margins include statistical and all known systematic uncertainties and are typical for these types of experiments. We have now replaced the CEM detector with a position sensitive triple multichannel plate (MCP) detector, which is capable of recording the spatial distribution of product ions arriving at the detector. This allows an assessment of the spread of the product ion beam and, through a comparison with SIMION ion trajectory simulations, allows us to obtain an at least semi-quantitative measure of the excess kinetic energy distribution of the various product ions.

We have access — through a longstanding collaboration with the group of Dr. Baser and Dr. Schmidt at the Institut für Niedertemperaturplasmaphysik (INP) in Greifswald, Germany — to two other apparatuses that are capable of measuring absolute ionization cross-sections of stable molecules. These experimental set-ups include a dedicated high resolution electric/magnetic sector field mass spectrometer and time of flight mass spectrometer.

## 3.  Results and discussion

### 3.1.  *Electron impact ionization of NO, $NO_2$ and $N_2O$*

The oxides of nitrogen, nitric oxide (NO) and nitrogen dioxide ($NO_2$), along with nitrous oxide ($N_2O$), are among the most ubiquitous compounds in plasmas that contain even traces of air or $N_2/O_2$ mixtures. The plasma electrons dissociate oxygen ($O_2$) and nitrogen ($N_2$) molecules into their atomic constituents, which subsequently recombine to form NO. NO can be oxidized readily to $NO_2$, and further plasmachemical reaction pathways also lead to the formation of $N_2O$. While many studies have been carried out to elucidate the atomic and molecular properties of the molecules NO, $NO_2$ and $N_2O$, and their interactions with photons and electrons, there have only been a few measurements of the ionization properties of these molecules. Previous work on the ionization properties of these molecules include the early work of Rapp and Englander Golden [19], Märk and collaborators [20–22], Iga and co-workers [23], and the more recent studies of Lindsay et al.

[24], Lukic et al. [25] and Jiao et al. [26]. Calculated total single ionization cross-sections for all three targets have also been reported using the BEB formalism of Kim and collaborators [27, 28], and in the case of $NO_2$ another calculated cross-section based on the DM formalism has been reported [29]. A comparison of the various data sets published in the literature reveals significant discrepancies. This motivated us to carry out measurements of absolute partial cross-sections for the electron impact ionization and dissociative ionization of these three nitrogen–oxygen compounds NO, $NO_2$ and $N_2O$, using the fast neutral beam technique. To the best of our knowledge, this was the first time that ionization cross-sections for all three targets had been measured in the same apparatus using the same experimental technique. In the case of the $N^+$ and $O^+$ fragment ions, we only report absolute cross-sections for the formation of $N^+ + O^+$, as we were unable to fully resolve the respective $N^+$ and $O^+$ ion signals at the detector because of the appreciable excess kinetic energy distributions with which these two atomic fragment ions are formed in all three cases.

The diatomic molecule NO has one unpaired electron and may thus be classified chemically as a free radical. It is, however, a rather stable molecule. We found that the electron impact ionization of NO was clearly dominated by the formation of the parent $NO^+$ ion. As discussed above, we were not able to resolve the ion signals corresponding respectively to the $N^+$ and the $O^+$ fragment ions. Thus, we only give a partial cross-section for the combined formation of $N^+$ and $O^+$ ions. Our measured partial $NO^+$ cross-section can be compared with data reported by Kim et al. [20], Iga et al. [23] and Lindsay et al. [24]. The peak cross-section values from the different studies show a significant level of disagreement between the maximum value reported by Iga et al. [23], $3 \times 10^{-16}$ cm$^2$, and the minimum value reported by Lindsay et al. [24], $2 \times 10^{-16}$ cm$^2$. The present data and the data of Kim et al. [20] agree in terms of the maximum cross-section value ($2.5 \times 10^{-16}$ cm$^2$), but show a significant difference in the cross-section shape with the cross-section shape of Kim et al. [20], declining much more rapidly with increasing electron energy. A comparison of our total single NO ionization cross-section in comparison with the measured data from Refs [23, 24] and with the total NO ionization cross-section reported by Rapp and Englander Golden [19], and with the calculated NO cross-section from Ref. [27] using the BEB formalism, reveals the following facts (see also Fig. 2):

(a) The maximum values of the reported measured cross-sections range from $2.7 \times 10^{-16}$ cm$^2$ [24] to $3.6 \times 10^{-16}$ cm$^2$ [23], a spread of about 30%, which is slightly larger than the combined error margins of the cross-sections as reported in the original papers.

(b) Our cross-section data are very close, both in terms of the cross-section maximum ($3.4 \times 10^{-16}$ cm$^2$) and in
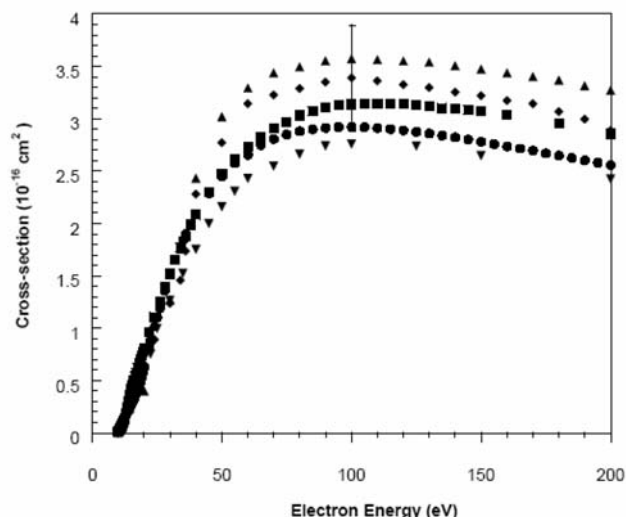


**Figure 2.** Present total (single) NO ionization cross-section from threshold to 200 eV (♦) in comparison with the data from Ref. [23] (▲) and Ref. [24] (▼), the total measured NO ionization cross-section of Rapp and Englander Golden [19] (■) and the calculated NO ionization cross-section of Ref. [27] (●). The single error bar refers to a typical margin of uncertainty in the present cross-section.

terms of the cross-section shape to the data reported by Iga et al. [23].

(c) The calculated cross-section of Kim and co-workers [27] shows a shape that is very similar to those of the two experimentally determined cross-sections, but its cross-section maximum is somewhat lower ($2.9 \times 10^{-16}$ cm$^2$).

(d) The recent data of Lindsay et al. [24] are below all other reported data and their cross-section shape is also different from all other reported cross-section shapes.

The measured total NO cross-section of Ref. [19] has a maximum value of about $3.2 \times 10^{-16}$ cm$^2$, but the cross-section declines much more gradually with increasing impact energy than the other cross-sections shown in Fig. 2.

Overall, the level of agreement in the reported NO ionization cross-sections is not as good as one would expect for the case of a simple diatomic molecule, where different measurements and calculations are often found to agree to better than 10% [3].

Nitrogen dioxide ($NO_2$) is a symmetrical, non-linear triatomic molecule with a bond angle of 134° that has one unpaired electron, which classifies it chemically as a free radical. In contrast to NO, the ionization of $NO_2$ is dominated by dissociative ionization. The various partial ionization cross-sections measured as part of this work are shown in Fig. 3. The formation of $NO^+$ fragment ions has the largest partial ionization cross-section. The cross-section for the formation of the ($N^+ + O^+$) fragment ions, which as for NO could not be resolved, is larger than the parent $NO_2^+$ ionization cross-section for impact energies above about
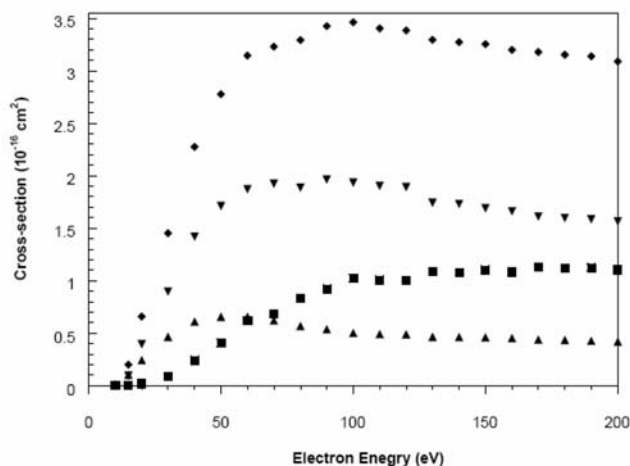
**Figure 3.** Present $NO_2^+$ (▲), $NO^+$ (▼), and combined ($N^+ + O^+$) (■) partial ionization cross-sections of $NO_2$ as a function of electron energy from threshold to 200 eV. Also shown is the sum of the partial cross-sections, which represents the total single $NO_2$ ionization cross-section (◆).

50 eV; at lower impact energies the $NO_2^+$ parent ionization cross-section exceeds the ($N^+ + O^+$) partial cross-section because of the much lower threshold for the formation of the parent ions. Our partial cross-sections for the formation of the $NO^+$ fragment ions are in good agreement with the measured data of Lindsay et al. [24] and Jiao et al. [26] in terms of the absolute cross-section values, but there are slight differences in the energy dependences of the three cross-section functions. For $NO_2^+$, we can also compare our data to those of Stephan et al. [21], which are substantially lower than all other data sets, which, in turn are in very good agreement with each other at higher impact energies above 100 eV. However, the cross-section functions show significant differences in their respective low energy behaviour. Our data exhibit the largest maximum cross-section value and peak at a lower energy compared to the other data sets, which also differ in their respective energy dependence. This discrepancy in the cross-section shape is difficult to understand. All experimental total $NO_2$ ionization cross-sections obtained by the different investigators and two calculated cross-sections using the DM formalism [29] and the BEB formalism [28] have peak cross-section values that are close to each other and range from $3.3 \times 10^{-16}$ cm$^2$ to $3.8 \times 10^{-16}$ cm$^2$. The total cross-sections measured by Lukic [25] and Lindsay et al. [24] and the BEB calculation [28], which have the largest peak cross-section value of $3.8 \times 10^{-16}$ cm$^2$, lie essentially on top of each other. Our cross-section curve lies about 10% below those cross-section curves, but exhibits a similar energy dependence. The cross-section curve of Jiao et al. [26] reaches a maximum value similar to the maximum reported by Lukic et al. [25], Lindsay et al. [24] and the BEB calculation [28], but shows a distinctly different energy dependence, peaking at lower impact energy and declining much more rapidly with increasing impact energy than the

other cross-section curves. The DM calculation [29] follows more closely our cross-section curve, but declines somewhat more rapidly towards higher impact energies.

$N_2O$ ('laughing gas'), which is a linear, triatomic molecule with an even number of electrons, is not considered an oxide of nitrogen. It has a molecular structure with the oxygen atom at one end and it resonates among three valence bond structures with double and triple bonds between N and N. This molecular structure of $N_2O$ is such that it cannot be satisfactorily represented by a single valence bond structure. The ionization cross-section database for this important molecule is rather limited, perhaps because of its peculiar molecular structure. In addition to the total $N_2O$ ionization cross-section measurement of Rapp and Englander Golden [19], there are the data of Märk et al. [22] for the formation of $N_2O^+$ parent ions and a set of partial ionization cross-sections reported by Iga et al. [23]. In addition, Kim and co-workers [28] calculated the $N_2O$ total single ionization cross-section using the BEB method.

As was the case for NO, the electron impact ionization of $N_2O$ is dominated by the formation of the parent ion, $N_2O^+$. However, as one might expect for a triatomic molecule, dissociative ionization channels are more important for $N_2O$ than they were for NO, with appreciable cross-sections for the formation of $NO^+$, $N_2^+$ and the unresolved atomic fragment ions ($N^+ + O^+$). A comparison of our measured partial $N_2O^+$ parent cross-section with data reported by Stephan et al. [22] and by Iga et al. [23] shows excellent agreement between the present data and those of Iga et al. [23] in terms of the absolute cross-section value, with a maximum value around $2 \times 10^{-16}$ cm$^2$. There is a slight difference in the measured cross-section shapes, with our cross-section curve peaking at a somewhat higher impact energy. The cross-section curve reported by Stephan et al. [21] lies roughly 25% below the other two cross-section curves and has a shape that is similar to the other two cross-section shapes.

There is only one data set with which we can compare the present dissociative ionization cross-sections of $N_2O$, i.e. $NO^+$, $N_2^+$ and ($N^+ + O^+$), the data reported by Iga et al. [23]. Overall, there is very good agreement between the two data sets for all three partial ionization cross-sections in terms of the maximum cross-section values and the cross-section shapes at higher impact energies. However, in all three cases there are significant discrepancies between our cross-section shapes and those of Ref. [23] in the low energy regime from threshold to about 50 eV for $NO^+$ and $N_2^+$ and up to 80 eV for ($N^+ + O^+$). In general, our measured appearance energies are lower (and closer to the minimum energies required for the formation of the various fragment ions [30–33]) than those reported by Iga et al. [23]. Furthermore, our cross-sections rise more rapidly in the near threshold region. This discrepancy in the cross-section shapes in the low energy regime is significant, as this energy region is particularly important in the modelling and simulation of the electron
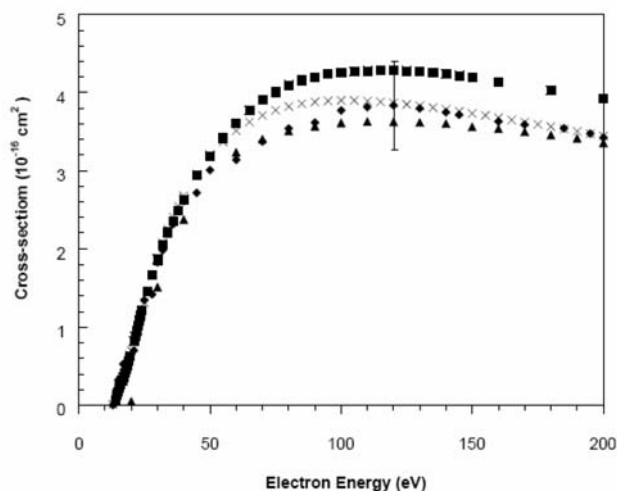
**Figure 4.** Present total (single) $N_2O$ ionization cross-section from threshold to 200 eV (◆) in comparison with the same measured cross-section from Ref. [23] (▲), the total measured $N_2O$ ionization cross-section of Rapp and Englander Golden [19] (■) and the calculated $N_2O$ ionization cross-section using the BEB method [28] (×). The single error bar refers to a typical margin of uncertainty in the present cross-section.
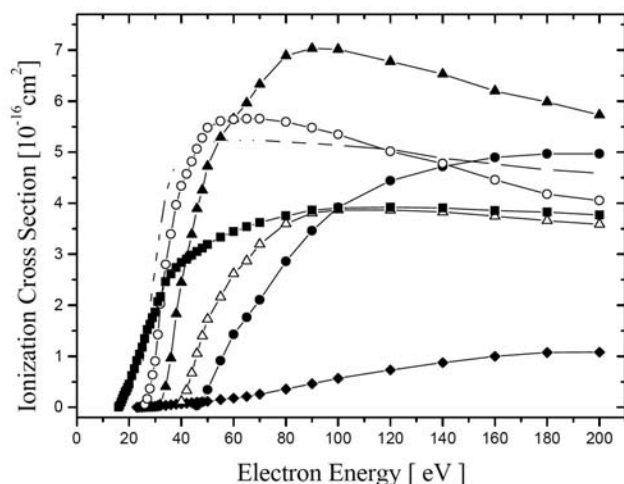


**Figure 5.** Absolute partial $WF_6$ ionization cross-sections for $WF_5^+$ (filled squares), $WF_4^+ \times 10$ (filled stars), $WF_3^+ \times 10$ (open circles), $WF_2^+ \times 10$ (filled triangles), $WF^+ \times 10$ (open triangles), $W^+ \times 10$ (filled circles) and $F^+$ (filled diamonds), as a function of electron energy up to 200 eV.

driven dissociative ionization processes in, e.g., discharges and plasmas containing $N_2O$.

Our total single $N_2O$ ionization cross-section can be compared with the measured data from Ref. [23] and with the total $N_2O$ ionization cross-section reported by Rapp and Englander Golden [19], as well as with a calculated $N_2O$ ionization cross-section [28] using the BEB formalism (see Fig. 4). The overall agreement between the various cross-section curves is somewhat better than in the case of NO. The total ionization cross-section reported by Rapp and Englander Golden [19] has a maximum value of $4.2 \times 10^{-16}$ cm$^2$, which is higher than all other data. The present data show a slightly smaller maximum cross-section of $3.9 \times 10^{-16}$ cm$^2$ and a cross-section shape that is similar to the one reported in Ref. [19]. The cross-section curve of Iga et al. [23] shows the lowest peak cross-section with a value of $3.6 \times 10^{-16}$ cm$^2$ and a cross-section shape that is somewhat different from the shapes of the other two experimental data sets, in particular at lower impact energies below 50 eV. The calculated $N_2O$ ionization cross-section [28] has a maximum value similar to our value ($3.9 \times 10^{-16}$ cm$^2$), but the cross-section curve reaches its peak at a somewhat lower impact energy, 80 eV, vs. 120 eV in our case and in Ref. [19].

### 3.2. *Electron impact ionization of WF$_6$*

Compounds of the element tungsten (W), including tungsten hexafluoride ($WF_6$), are trace contaminants in the edge plasma. We reported the first experimentally determined electron ionization cross-sections for $WF_6$ more than ten years ago [34]. The data were obtained using a sector field mass spectrometer with a very high mass resolution. Measurements carried out with this instrument

were highly susceptible to ion discrimination, i.e. fragment ions with excess kinetic energy were not detected with 100% efficiency. Moreover, it was not possible to carry out a complete quantitative correction of this ion loss. Therefore, the data were never published in a peer reviewed journal. Here we report new electron ionization cross-section data for $WF_6$ obtained in a time of flight mass spectrometer that allows us to determine reliable absolute partial ionization cross-sections without mass discrimination of the energetic fragment ions.

The cross-section curves of the singly and doubly charged ions resulting from the electron impact ionization of $WF_6$ from threshold to 200 eV are shown in Figs 5 and 6. The total $WF_6$ ionization cross-section is shown in Fig. 7 up to 900 eV, along with the total single $WF_6$ ionization cross-
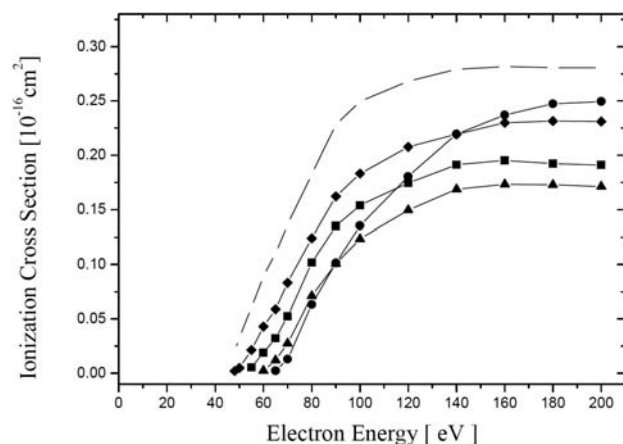


**Figure 6.** Absolute partial $WF_6$ ionization cross-sections for $WF_4^{++}$ (filled stars), $WF_3^{++}$ (filled diamonds), $WF_2^{++}$ (filled squares), $WF^{++}$ (filled triangles) and $W^{++}$ (filled circles), as a function of electron energy up to 200 eV.
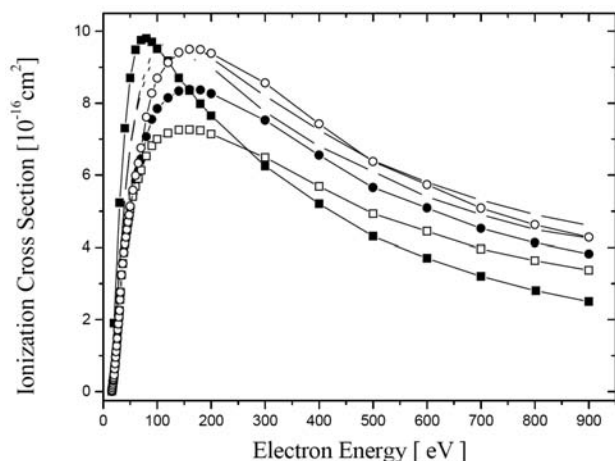
**Figure 7.** Our absolute total $WF_6$ ionization cross-section (open circles), single ionization cross-section (open squares) and counting ionization cross-section (filled circles) in comparison with a calculated total single ionization cross-section [35] (filled squares), and two calculated total counting ionization cross-sections [36] (filled and open stars) as a function of electron energy.

section and the total $WF_6$ counting ionization cross-section. The cross-section curves of all ions show a very similar shape as a function of impact energy. The cross-sections increase rapidly from threshold to a maximum and then decrease gradually towards higher impact energy. The maximum for the singly charged ions (Fig. 5) was found to be in the range between 50 and 100 eV. The only exceptions are the $W^+$ and $F^+$ ionization cross-sections, which reach their maximum value at 200 eV. It is obvious from the cross-section curves shown in Figs 5 and 6 that dissociative ionization is the dominant process in the entire range of impact energies. The largest maximum cross-section value was obtained for the $WF_5^+$ fragment ion, $3.92 \times 10^{-16}$ cm$^2$ at 120 eV. This ion accounts for about 43% of the total ionization cross-section of $WF_6$ at 120 eV. The ion spectrum in the lower energy region changes with increasing impact energy due to the different appearance energies for the various ions (Fig. 5), but is also dominated by $WF_5^+$.

Doubly charged ions appear at energies above 42 eV and show the largest cross-section values in the energy range between 150 and 200 eV. All maximum cross-section values are more than one order of magnitude lower compared with the maximum $WF_5^+$ cross-section. The charge weighted sum of all doubly charged fragment ions accounts for about 21% of the total ionization cross-section of $WF_6$ at 120 eV. The total ionization cross-section curve of tungsten hexafluoride derived as the charge weighted sum of all partial ionization cross-sections is shown in Fig. 7. The curve exhibits a maximum at 160 eV with a peak value of $9.5 \times 10^{-16}$ cm$^2$. Furthermore, Fig. 7 shows the comparison of various experimentally determined and calculated cross-sections available for $WF_6$. The total single ionization cross-section of $WF_6$ was calculated using the DM formalism [35]. The level of

agreement with the experimental total single cross-section is not very satisfactory below 150 eV. The calculated cross-section rises faster as a function of electron energy and shows a relative sharp peak at 80 eV. The other two calculated cross-section curves in Fig. 6 were obtained with two variants of the BEB method [36]. Both curves represent the total counting ionization cross-section of $WF_6$. A comparison of the BEB cross-sections with our experimental data shows a much better agreement in terms of the cross-section shape and in terms of the absolute cross-section values. The experimental cross-section values again are lower than both calculated cross-sections in the entire energy range. The deviation between the BEB results and the experimental data decreases with increasing energy. Overall, the level of agreement between the experimental data and the BEB calculations is of the order of the experimental uncertainty of 15% above 100 eV.

### 3.3. Electron impact ionization of $B_2H_6$

$B_2H_6$ with two hydrogen bridges connecting the two $BH_2$ groups and with no direct B–B chemical bond is known to be unstable even at room temperature [37]. The decomposition of the molecule follows a complex decay route via unstable intermediate species and leads to $B_4H_{10}$, $B_5H_{11}$ and $H_2$ as first stable decomposition products. We observed the thermal decomposition of $B_2H_6$ in our reservoir through traces of $B_4H_{10}$ and $B_5H_{11}$ that were identified by the mass spectrum [38], albeit with low intensities of less than 1% of the intensity of parent $B_2H_6^+$ ion peak. However, we did observe an intense $H_2^+$ ion signal, which increased with the residence time of the $B_2H_6$ in the storage reservoir. The main contribution of this signal was identified as arising from the direct ionization of the $H_2$ that was produced in the decomposition of $B_2H_6$ in the storage reservoir. Only a small fraction of the $H_2^+$ signal was attributable to $H_2^+$ fragment ions formed by dissociative ionization of $B_2H_6$. The $H_2$ resulting from the decomposition of $B_2H_6$ in the reservoir was routinely removed by repeatedly freezing the $B_2H_6$ and pumping out the reservoir. This procedure produced a target sample that was sufficiently free of $H_2$ contamination for about one hour, at which point the purification of the sample had to be repeated.

Earlier work on dissociative ionization of diborane includes mass spectrometric measurements of fragmentation, pyrolysis and the determination of appearance energies [39–43]. Appearance energies of the fragment ions were also studied by photoelectron spectroscopy [44–47]. The mass spectrum of diborane can also be found in standard mass spectral compilations [48]. To the best of our knowledge, no electron impact ionization cross-sections of this molecule existed prior to our work.

The mass spectrum of $B_2H_6$ at an electron energy of 70 eV derived from measurements carried out with the TOF-MS operated in the linear mode is shown in Fig. 8 and the result is compared to the mass spectrum of $B_2H_6$ found in the
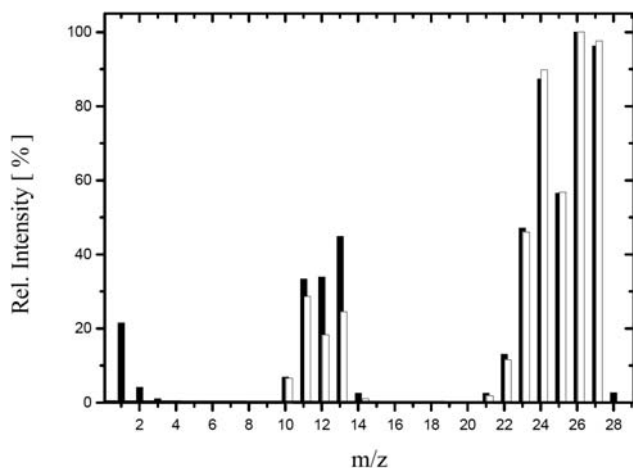
**Figure 8.** Mass spectrum of $B_2H_6$ at 70 eV measured with the time of flight mass spectrometer in the linear mode (filled bars) compared to the reference mass spectrum (open bars) from Ref. [38].



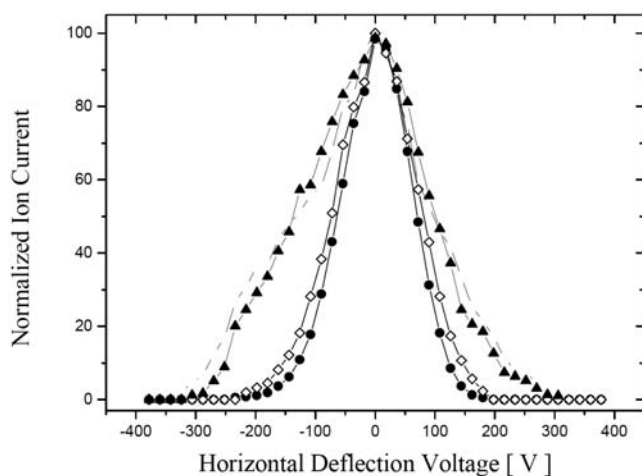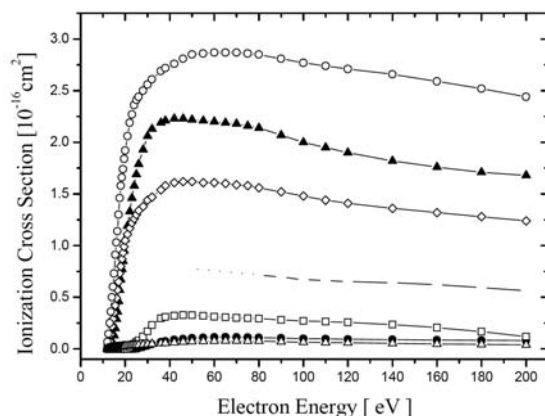**Figure 10.** Absolute partial $B_2H_6$ ionization cross-sections for $B_2H_6^+$/appearance energy: 11.4 ± 0.3 eV (open triangles), $B_2H_5^+$/ 11.5 ± 0.3 eV (open circles), $B_2H_4^+$/12.0 ± 0.3eV (open diamonds), $B_2H_3^+$/14.3 ± 0.5 eV (filled stars), $B_2H_2^+$/14.0 ± 0.4 eV (filled triangles), $B_2H^+$/21.0 ± 0.7 eV (open squares), and $B_2^+$/23.5 ± 1.2 eV (filled circles) up to 200 eV.

NIST database [38]. In both spectra the isotopic composition of the target, i.e. contributions from $^{10}B$ and $^{11}B$ at a ratio of 0.19:0.81 [49], was not resolved. Our results are in excellent agreement with the NIST data for the heavier ions, but noteworthy differences are apparent for ions of lower mass.

The intensities of the ions $BH_3^+$, $BH_2^+$ and $BH^+$ are distinctly higher in our spectrum than the corresponding intensities found in the NIST database [38]. The reason for this discrepancy may be a higher detection efficiency of our TOF-MS for ions which are formed with significant amounts of excess kinetic energy. We carried out qualitative determinations of the excess kinetic energy for all fragment ions by performing a full horizontal sweep of the extracted ion beam using a double focusing mass spectrometer [9, 14, 17]. The results of these measurements are presented in Fig. 9. The shape of the $Ar^+$ ion signal is characteristic of an

ion beam without excess kinetic energy. The shape of the ion signal at m/z = 24 (a mixture of 4% $^{10}B_2H_4^+$, 14% $^{10}B^{11}BH_3^+$ and 82% $^{11}B_2H_2^+$) is typical for the $H_2^+$ ion and all fragment ions of $B_2H_6$ containing two B atoms. The curve shows some broadening, which is indicative of a small amount of excess kinetic energy. All other ions show beam profiles that suggest a broad distribution of excess kinetic energies as shown for m/z = 12 (a mixture of 32% $^{10}BH_2^+$ and 68% $^{11}BH^+$) and m/z = 1, the $H^+$ fragment ion in Fig. 8. We also found measurable ion signals for the three ions $H^+$, $H_2^+$ and $H_3^+$. No appreciable ion signals were detected that corresponded to the formation of doubly charged ions.

Because the mass resolution of the TOF-MS is not sufficient to resolve the signals attributable to the two isotopes of B, we measured the ion efficiency curves corresponding to all ions that contribute to a given mass number. Using the known abundances of $^{10}B$ and $^{11}B$ (0.19 and 0.81 [49]) and the measured intensities of the uncontaminated ion peaks at m/z 10 ($^{10}B^+$) and at m/z 14 ($^{11}BH_3^+$), we then calculated successively the contribution of each ion to m/z = 11, 12 and 13 at every electron impact energy. A similar procedure was applied to all mass numbers from 20 to 28 by solving a system of linear equations resulting from the binominal intensity distribution of the isotope contributions of $^{10}B_2$:$^{10,11}B$:$^{11}B_2$ = 6.17:49.69:100 [50]. The calculation started with the measured intensity of $^{11}B_2H_6^+$ at m/z = 28 and resulted in the three separate isotopic contributions for each ion at all electron impact energies. The partial ionization cross-sections for the ions were then obtained by adding the three isotopic contributions. The partial ionization cross-sections and the total ionization cross-section (the sum of all partial cross-sections) as a function of the energy of the ionizing electrons from threshold to 200 eV are shown in Figs 10 and 11.

The measured appearance energies for the various ions with their respective uncertainties are given in the figure



**Figure 9.** Normalized ion currents of $Ar^+$ (filled circles), a mixture of 4% $^{10}B_2H_4^+$, 14% $^{10}B^{11}BH_3^+$ and 82% $^{11}B_2H_2^+$ (open diamonds), a mixture of 32% $^{10}BH_2^+$ and 68% $^{11}BH^+$ (filled triangles), and $H^+$ (open stars) as a function of the horizontal deflection voltage at 70 eV.
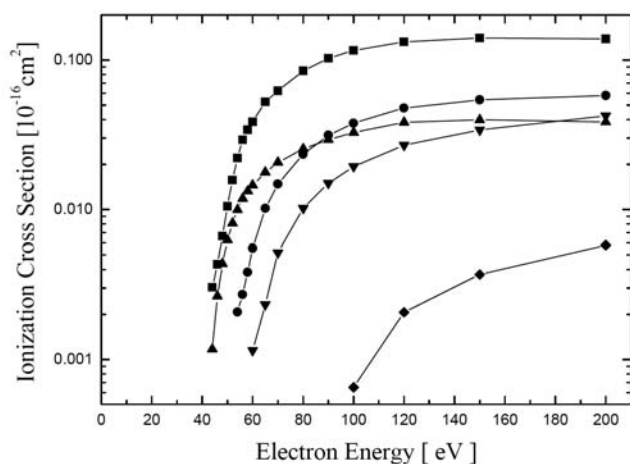
**Figure 11.** Our absolute $B_2H_6$ ionization cross-sections for $BH_3^+$/ $15.1 \pm 1.6$ eV (open squares), $BH_2^+$/$16.6 \pm 2.1$ eV (filled squares), $BH^+$/$19.0 \pm 2.3$ eV (filled triangles), $B^+$/$19.4 \pm 1.4$ eV (open circles), $H_3^+$/$36.0 \pm 3.5$ eV (filled circles), $H_2^+$/$16.0 \pm 1.4$ eV (filled stars), $H^+$/$30.0 \pm 2.5$ eV, and absolute total $B_2H_6$ ionization cross-section ($\times 0.1$, open triangles) up to 200 eV.

captions of the figures. The appearance energies were obtained from a linear extrapolation of the measured ion efficiency curve near threshold for all mass numbers without isotopic interferences. In the case of an ion mixture, the separation of the isotopic contributions was done as described before. Our appearance energy values are in agreement with previously reported electron impact data, as well as with photoionization data (see Ref. [38]) with the exception of the fragment ions $BH_x^+$ (x = 1–3), for which we obtained somewhat higher appearance energy values. It is noteworthy that we observed extended curvatures in the near threshold regions for the light fragment ions, which significantly exceeded the curvature in the threshold region that is attributable to the energy spread in the electron beam. In almost all cases, this extended curvature was responsible for the quoted uncertainty in the respective appearance energy determination. We attribute this curvature primarily to the generation of fragment ions with broad distributions of excess kinetic energy (see Fig. 9). Reference data for the appearance energy of $H^+$, $H_2^+$ and $H_3^+$ from $B_2H_6$ are not available. The formation process leading to $H_3^+$ fragment ions could not be uniquely identified. While it is well known that stable $H_3^+$ ions are formed in gas discharges by ion molecule reactions, e.g. between $H_2^+$ and $H_2$ with large rate constants [51], the formation of these ions has not been observed in the dissociative electron impact ionization of H containing molecules under single collision conditions. The unusual molecular structure of $B_2H_6$, in conjunction with the comparatively high appearance energy of the $H_3^+$ ion, might suggest that their formation proceeds via the initial breaking of one or both of the hydrogen bridges, followed by a rearrangement and subsequent decomposition of the $BH_3^+$ ions that are formed in this process.

The cross-section curves of all ions show a very similar shape as a function of impact energy. The cross-sections

increase rapidly from threshold to a maximum and then decrease slightly with higher impact energy. The maximum for the $B_2$ containing ions (Fig. 10) was found to be in the range between 40 and 70 eV and at higher energies around 80 eV for the B containing ions and $H^+$ (Fig. 11). The total ionization cross-section curve of diborane exhibits a maximum at 70 eV with a peak value of $10.74 \times 10^{-16}$ cm². It is obvious from the cross-section curves shown in Figs 10 and 11 that dissociative ionization is the dominant process for impact energies above 40 eV. Only the four fragment ions $H_2^+$, $H_3^+$, $BH_3^+$ and $B_2^+$ have maximum cross-section values of less than $0.1 \times 10^{-16}$ cm², which is comparable to the maximum value of the $B_2H_6^+$ parent ionization cross-section. The largest maximum cross-section values were obtained for the $B_2H_5^+$ fragment ion ($2.87 \times 10^{-16}$ cm² at 70 eV), followed by $B_2H_2^+$ ($2.18 \times 10^{-16}$ cm² at 70 eV), $B_2H_4^+$ ($1.59 \times 10^{-16}$ cm² at 70 eV) and $BH_2^+$ ($1.07 \times 10^{-16}$ cm² at 70 eV). These ions account for about 72% of the total ionization cross-section of $B_2H_6$ at 70 eV. The ion spectrum in the lower energy region, which is of special interest for low temperature plasma technology, changes with increasing impact energy due to different appearance potentials for the various ions, but is also dominated by $B_2H_5^+$, $B_2H_4^+$ and $B_2H_2^+$. For example, their contribution amounts to 88% of the total ionization cross-section value at 20 eV.

## 4. Summary

This paper summarizes the results of selected experimental electron impact ionization cross-section studies carried out as part of an IAEA CRP on Molecular Processes in Edge Plasmas. We present data for absolute total and partial ionization cross-sections for the nitrogen–oxygen compounds NO, $NO_2$ and $N_2O$, as well as for the molecules $WF_6$ and $B_2H_6$. Experimental techniques employed include the fast neutral beam technique and a mass spectrometric technique utilizing a time of flight mass spectrometer (TOF-MS). The present results are discussed in some detail and, to the extent possible, comparisons are made with other available experimental cross-section data and with calculated cross-sections using semi-rigorous approaches such as the BEB formalism and the DM method. Specifically, we highlight the following conclusions:

(a) Our measurements of the absolute partial cross-sections for the electron impact ionization and dissociative ionization of the three nitrogen–oxygen compounds NO, $NO_2$ and $N_2O$ is the first time that ionization cross-sections for all three targets have been measured with the same apparatus using the same experimental technique. Detailed comparisons with other available experimental data and with published calculated total single ionization cross-sections show a level of agreement between the various reported cross-section sets that is not as good as one might expect for

simple diatomic and triatomic molecules (see, e.g. Ref. [3]). This is particularly true for some of the partial cross-sections for dissociative ionization, in particular in the case of $NO_2$. There are also differences in the cross-section shapes reported by different authors using different experimental techniques, which tend to be more pronounced for the dissociative ionization cross-sections, but are generally less obvious in the total ionization cross-sections.

(b) We measured the absolute partial electron ionization cross-sections for the $WF_6$ molecule. The mass spectrum at 70 eV is in good agreement with known mass spectral cracking patterns of $WF_6$ for the higher ion masses. Differences with previously published data at lower ion masses can be explained in terms of a less than 100% ion collection efficiency for ions formed with excess kinetic energy, which may have affected the earlier measurements. A complete set of the absolute ionization cross-sections for the formation of all positive ions from $WF_6$ shows that dissociative ionization with the generation of $WF_5^+$ is the dominant process. The comparison of the experimental data with available theoretical predictions shows a much better agreement than was obtained before [34]. The absolute cross-section values measured here are indispensable for a microscopic understanding and the detailed modelling of the plasma chemical processes in $WF_6$ containing plasmas. The data presented here are also important for the critical evaluation of mass spectrometric plasma diagnostics data.

(c) We measured the absolute partial electron impact ionization cross-sections for the $B_2H_6$ molecule. The mass spectrum at 70 eV is in good agreement with known mass spectral cracking patterns of $B_2H_6$ for the higher ion masses. Differences with previously published data at lower ion masses can be explained in terms of the excess kinetic energy of these fragment ions, which may have affected the earlier measurements. Intensity and appearance energy values for the fragment ions $H_3^+$, $H_2^+$ and $H^+$ are given for the first time. A complete set of the absolute ionization cross-sections for the formation of all ions from $B_2H_6$ was determined with an overall uncertainty of ±15% in the energy range from threshold to 200 eV. These results represent the first complete set of electron impact ionization cross-section data of $B_2H_6$. The absolute cross-section values measured here are indispensable for a microscopic understanding and the detailed modelling of the plasma chemical processes in $B_2H_6$ containing plasmas. The data presented here are also important for the critical evaluation of mass spectrometric plasma diagnostics data.

The data presented in this report have been included in published peer reviewed journal articles [52–54].

## References

[1] MÄRK, T.D., DUNN, G.H. (Eds), Electron Impact Ionization, Springer Verlag (1985), Vienna.

[2] DEUTSCH, H., MÄRK, T.D., Int. J. Mass Spectrom. Ion Proc. **79** (1987) R1.

[3] DEUTSCH, H., BECKER, K., MATT, S., MÄRK, T.D., Int. J. Mass Spectrom. **197** (2000) 37.

[4] TARNOVSKY, V., KURUNCZI, P., ROGOZHNIKOV, D., BECKER, K., Int. J. Mass Spectrom. Ion Proc. **128** (1993) 181.

[5] TARNOVSKY, V., BECKER, K., J. Chem. Phys. **98** (1993) 7868.

[6] WETZEL, R.C., BIAOCCHI, F.A., HAYES, T.R., FREUND, R.S., Phys. Rev. A **35** (1987) 559.

[7] FREUND, R.S., WETZEL, R.C., SHUL, R.J., HAYES, T.R., Phys. Rev. A **41** (1990) 3575.

[8] TARNOVSKY, V., BERCKER, K., Z. Phys. D **22** (1992) 603.

[9] BASNER, R., SCHMIDT, M., BECKER, K., TARNOVSKY, V., DEUTSCH, H., Thin Solid Films **374** (2000) 291.

[10] BASNER, R., SCHMIDT, M., DENISOV, E., BECKER, K., DEUTSCH, H., J. Chem. Phys. **114** (2001) 1170.

[11] BASNER, R., SCHMIDT, M., DENISOV, E., LOPATA, P., BECKER, K., DEUTSCH, H., Int. J. Mass Spectrom. **214** (2002) 365.

[12] BASNER, R., SCHMIDT, M., TARNOVSKY, V., BECKER, K., DEUTSCH, H., Int. J. Mass Spectrom. Ion Proc. **171** (1997) 83.

[13] BASNER, R., FOEST, R., SCHMIDT, M., BECKER, K., DEUTSCH, H., Int. J. Mass Spectrom. **176** (1998) 245.

[14] TARNOVSKY, V., LEVIN, A., BECKER, K., BASNER, R., SCHMIDT, M., Int. J. Mass Spectrom. Ion Proc. **133** (1994) 175.

[15] BASNER, R., SCHMIDT, M., TARNOVSKY, V., LEVIN, A., BECKER, K., J. Chem. Phys. **103** (1995) 211.

[16] BASNER, R., et al., Int. J. Mass Spectrom. Ion Phys. **153** (1996) 65.

[17] BASNER, R., SCHMIDT, M., TARNOVSKY, V., BECKER, K., DEUTSCH, H., Int. J. Mass Spectrom. Ion Proc. **171** (1997) 83.

[18] GUTKIN, M., MAHONEY, J., TARNOVSKY, V., BASNER, R., BECKER, K., J. Chem. Phys. (2005).

[19] RAPP, D., ENGLANDER GOLDEN, P., J. Chem. Phys. **43** (1965) 1464.

[20] KIM, Y.D., STEPHAN, K., MÄRK, E., MARK, T.D., J. Chem. Phys. **74** (1981) 6771.

[21] STEPHAN, K., et al., J. Chem. Phys. **73** (1980) 303.

[22] MÄRK, E., MÄRK, T.D., KIM, Y.D., STEPHAN, K., J. Chem. Phys. **75** (1981) 446.

[23] IGA, I., RAO, M.V.V.S., SRIVASTAVA, S.K., J. Geophys. Res. **101** (1996) 9261.

[24] LINDSAY, B.G., MANGAN, M.A., STRAUB, H.C., STEBBINGS, R.F., J. Chem. Phys. **112** (2000) 9404.

[25] LUKIC, D., JOSIFOV, G., KUREPA, M.V., Int. J. Mass Spectrom. **205** (2001) 1.

[26] JIAO, C.Q., DEJOSEPH., C.A., Jr., GARSCADDEN, A., J. Chem. Phys. **117** (2002) 161.

[27] HWANG, W., KIM, Y.-K., RUDD, M.E., J. Chem. Phys. **104** (1996) 2956.

[28] KIM, Y.-K., HWANG, W., WEINBERGER, N.M., ALI, M.A., RUDD, M.E., J. Chem. Phys. **106**, (1997) 1026.

[29] PROBST, M., DEUTSCH, H., BECKER, K., MÄRK, T.D., Int. J. Mass Spectrom. **206** (2001) 13.

[30] LIAS, S.G., et al., J. Phys. Chem. Ref. Data **17** (1988) 1.

[31] WAGMAN, D.D., et al., J. Phys. Chem. Ref. Data **11** (1982) 1.

[32] CASE., M.W., Jr., et al., J. Phys. Chem. Ref. Data **14** (1985) 1.

[33] The Handbook of Chemistry and Physics, 65th edition, WEAST, R.C., ASTLE, M.J., W.H. BEYER, W.H. (Eds), CRC Press, Boca Raton (1985).

[34] BASNER, R., SCHMIDT, M., DEUTSCH, H., Proc. 45th Annual Gaseous Electronics Conference, Boston, (1992), GTE Laboratory Press, VICHARELLI, P. (Ed.), 181.

[35] PROBST, M., DEUTSCH, H., BECKER, K., MÄRK, T.D., Int. J. Mass Spectrom. **206** (2001) 13.

[36] HUO, W.M., KIM, Y.-K., Chem. Phys. Lett. **319** (2000) 576.

[37] GREENWOOD, N.N., EARNSHAW, A., Chemistry of Elements, Butterworth/Heinemann, Oxford, 2001.

[38] NIST Database (webbook.nist.gov/chemistry/form-ser.html).

[39] WILSON, J.H., McGEE., H.A., Jr., J. Chem. Phys. **46** (1967) 1444.

[40] KOSKI, W.S., KAUFMANN, J.J., PACHUKI, C.F., SHIPLO, F.J., J. Am. Chem. Soc. **80** (1958) 3202.

[41] MARGRAVE, J.L., J. Chem. Phys. **61** (1957) 38.

[42] FEHLER, T.P., KOSKI, W.S., J. Am. Chem. Soc. **86** (1964) 581.

[43] BAYLIS, A.B., PRESSLEY, G.A., Jr., STAFOORD, F.E., J. Am. Chem. Soc. **88** (1966) 2428.

[44] RUSIC, B., MAYHEW, C.A., BERKOVWITZ, J., J. Chem. Phys. **88** (1988) 5580.

[45] ASBRINK, L., SVENSSON, A., VON NIESSEN, W., BIERI, G., J. Electron Spectrosc. Relat. Phenom. **24** (1981) 293.

[46] LLOYD, D.R., LYNAUGH, N., Phil. Trans. Roy. Soc. (London) **A268** (1970) 97.

[47] BRUNDLE, C.R., ROBIN, M.B., BASCH, H., PINSKY, M., BOND, A., J. Am. Chem. Soc. **92** (1970) 3863.

[48] CRC Handbook of Chemistry and Physics, LIDE, D.R. (Ed.), CRC Press, Boca Raton (1999).

[49] McLAFFERTY, F.W., TURECK, F., in Interpretation von Massenspektren, Spektrum Verlag, Heidelberg (1995).

[50] SCHMIDT, M., Beitr. Plasma Phys. **9** (1968) 11.

[51] CANOSA, A., GOMET, J.C., ROWE, B.R., MITCHELL, J.B.A., QUEFFELEC, J.L., J. Chem. Phys. **97** (1992) 1028.

[52] LOPEZ, J., GUTKIN, M., TARNOVSKY, V., BEKKER, K., Int. J. Mass Spectrom. **225** (2003) 25.

[53] BASNER, R., BECKER, K., SCHMIDT, M., J. Chem. Phys. **118** (2003) 2153.

[54] BASNER, R., SCHMIDT, M., BECKER, K., Int. J. Mass Spectrom. **233** (2004) 25.

# Collisions of hydrocarbon ions of energies 10–50 eV with carbon surfaces: Ion survival, dissociation, chemical reactions, scattering

*Z. Herman[a,b], T.D. Märk[b]*

[a] V. Čermák Laboratory, J. Heyrovský Institute of Physical Chemistry, Academy of Sciences of the Czech Republic, Dolejškova 3, CZ-182 23 Prague 8, Czech Republic

[b] Institut für Ionenphysik, Leopold-Franzens Universität, Technikenstrasse 25, A-6020 Innsbruck, Austria

## Abstract

This paper summarizes data on collisions of slow (10–50 eV) ions of $C_1$–$C_3$ hydrocarbons and some non-hydrocarbons with room temperature (non-heated) and heated (to 600°C) carbon surfaces obtained mostly in recent measurements of ours. Mass spectra, translational energy distributions and angular distributions of product ions were measured. The carbon surface was represented by a highly oriented pyrolytic graphite (HOPG) surface, the incident angle was 60° with respect to the surface normal (30° with respect to the surface). Collisions with heated carbon surface showed only partial or substantial dissociation of the projectile ions. Interactions with the carbon surface at room temperature showed both surface induced dissociation of the projectiles and — in the case of radical cation projectiles — chemical reactions with a hydrocarbon layer on the surface. These reactions were (i) H atom transfer to the projectile, formation of protonated projectiles and their subsequent fragmentation, (ii) formation of a carbon chain buildup product in reactions of the projectile ion with the terminal $CH_3$ group of the surface hydrocarbons, and subsequent fragmentation (only for $C_1$ and $C_2$ hydrocarbon ions). The product ions were formed in inelastic collisions. Angular distributions of reaction products showed peaking at sub-specular angles. The absolute survival probability at the incident angle of 60° was less than 1% for $CH_3^+$, $CH_4^+$ and $C_2H_2^{+\bullet}$, close to 1% for ion like $C_2H_4^{+\bullet}$, $C_2H_5^+$, $C_3H_6^+$ and $C_3H_8^+$, and about 3–15% for $CH_5^+$, $C_2H_3^+$, $C_3H_7^+$, $C_3H_5^+$ and $C_3H_3^+$.

## 1. Introduction

Investigation of ion surface collisions offers an opportunity to obtain information on a broad range of physical and chemical processes. Considerable attention has been devoted, especially in the last decade, to collisions of slow ions of energies of about 1–100 eV [1–4]. This energy regime is usually referred to as the hyperthermal energy range [1, 4]. The collision energy in this range is comparable to or greater than typical bond energies, and the projectile ion incident energy is large enough to cause bond dissociation and yet not to obscure the chemical nature of the interactions [4]. Ion surface collisions can be a source of important data relevant to plasma–wall interactions in low temperature plasmas and fusion systems [5]. Hyperthermal plasma particles may collide with solid surfaces such as limiters and divertors in fusion devices, eroding the material by chemical and physical processes. Charged and neutral particles emitted from the surface may interact with the plasma and hit the surfaces again. In fusion devices, carbon is widely used as the material exposed to plasma, and the outcome of collisions between ions and carbon surfaces is of considerable interest. Quite recently, the importance of interaction of molecular ionic species in the gaseous phase and in collisions with surfaces in fusion devices has been recognized and demand for data on collisions of slow molecular ions, diatomic and simple polyatomic, has been repeatedly emphasized [5]. The list of the molecular ions of importance in this respect, as prepared in this Coordinated Research Project (CRP), contains in particular ions of the $C_1$-$C_3$ group hydrocarbons, $H_2O$, CO, $CO_2$, $BeH_n$, $SiH_n$.

In an effort to provide more data on this problem, we started a systematic investigation of interaction of small molecular ions, namely hydrocarbon ions $CH_n^+$ (n = 3–5), $C_2H_n^+$ (n = 2–5), $C_3H_n^+$ (n = 2–8) and their isotopic (D, $^{13}$C) variants, as well as some molecular non-hydrocarbon ions with carbon surfaces [6–8]. The ions were impinging on heated and non-heated (room temperature) carbon surfaces. As a suitable model of the carbon surface, highly oriented pyrolytic graphite (HOPG) surfaces were used. In our earlier paper [9], we showed that the properties of this surface (energy transfer, projectile fragmentation, chemical

reactions) were practically the same as for samples of carbon brick materials from fusion devices. The experimental data consisted of results of measurements of mass spectra, angular and translational energy distributions of the ion products. Analysis of the data made it possible to estimate the ion survival probability and to describe the projectile dissociation processes and chemical reactions with the surface material. Collisions with the HOPG surfaces heated to or above 600°C showed only fragmentation of the projectile ions. Collisions with room temperature HOPG surfaces showed both surface induced dissociation of the projectiles and chemical reactions of the projectile ions with the surface material.

In this review, we provide an overview of data so far published on the subject by others and then we summarize our data obtained in these experiments [6–8]. Earlier work on ion surface interaction of hydrocarbon ions includes studies of dissociation of small hydrocarbon $CH_n^+$ and fluorocarbon $CF_n^+$ (n = 1, 2,) ions on aluminium surfaces to gain insight into surface processes in plasma processing [10]. Significant charge neutralization (survival of about 0.3% for $CH_n^+$), dissociation of projectiles, and kinetic energies of fragments lower than 10 eV were observed for incident projectile energies up to 150 eV. In other studies, dissociative collisions of hydrogen ions ($H_2^+$, $H_3^+$ and their isotopic variants) on hydrocarbon-covered stainless steel surfaces were investigated [11]. The effect of initial internal energy of hydrocarbon projectiles $CH_n^+$ [12] and $C_2H_n^+$ [13] on the extent of surface induced fragmentation of the projectiles was studied and it was found that the initial internal energy was fully available in the fragmentation process. This work will be reported in more detail later on in this article.

For completeness, let us mention here that several papers were devoted to dissociative scattering of diatomic or small polyatomic (3–4 atoms) ions from single crystal or liquid surfaces, including energy and angular analysis of the product ions. Negative ion formation in collisions of hyperthermal, state selected $NO^+$ with O/Al(111) [14] and $OCS^+$ with Ag(111) [15] was investigated and conclusions about the mechanism were made. Dissociative scattering of 50–250 eV fluorocarbon ions $CF_n^+$ (n = 1–3) from surfaces covered by perfluoropolyether liquid film [16–18] was interpreted on the basis of elastic scattering from the surface layer terminal group.

Though this is not the main purpose of this paper, results on collisions of fullerene ions with carbon surfaces are worth mentioning. Changes in slow ion scattering and energy transfer for clean versus adsorbate covered graphite surfaces were described for surface interactions of fullerene ions [19]. The extent of fragmentation, kinetic energy of the scattered ions, and chemical reactions ($C_2$ pick-up on hydrocarbon-contaminated HOPG surface) changed dramatically after cleaning the surface by heating to 1000°C. Examples of pick-up chemical reactions of incident ions with surface material have been described; the results have
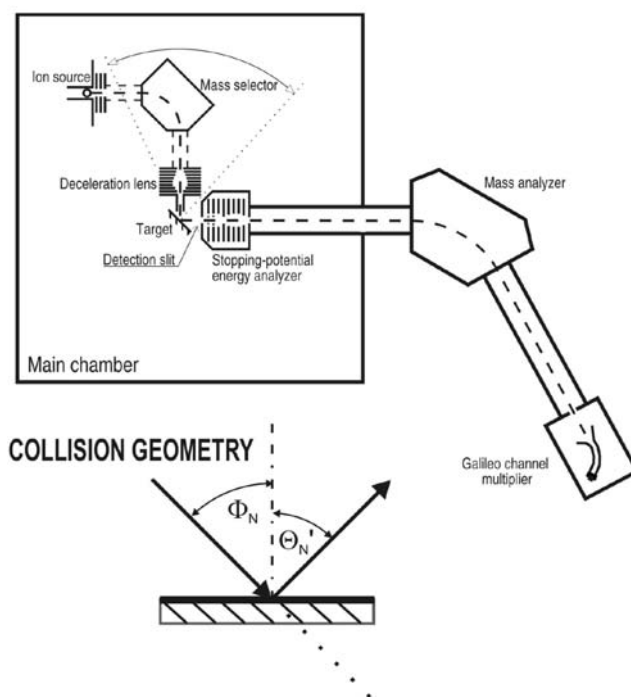


**Figure 1.** Schematics of the ion surface scattering apparatus.

been summarized in reviews [2, 4]. Significant changes in product ion kinetic energy distributions and the extent of incident to internal energy transfer were observed in scattering studies of $Si(CH_3)_3^+$ collisions with clean Au(111) surface and Au surface covered by hydrocarbon $C_6$ self-assembled monolayer [20].

## 2. Experimental

The experiments were carried out with the Prague beam scattering apparatus EVA II modified for ion surface collision studies (Fig. 1). The application of the apparatus to the described studies was depicted earlier [6–9, 21–24]. In the present experiments, projectile ions were formed by bombardment by 120 eV electrons of methane, acetylene, ethylene, ethane, propene, cyclopropane and propane (or their deuterated or $^{13}C$ labelled variants) at an ion source pressure of about $3.10^{-5}$ torr. The ions were extracted, accelerated to about 150–200 eV, mass analysed by a 90° permanent magnet and decelerated to a required energy in a multielement deceleration lens. The resulting beam had an energy spread of 0.2 eV, full width at half maximum (FWHM), angular spread of about 2°, FWHM, and geometrical dimensions of $0.4 \times 1.0$ mm². The beam was directed towards the carbon target surface under a pre-adjusted incident angle $\Phi_N$. Ions scattered from the surface passed through a detection slit ($0.4 \times 1$ mm²), located 25 mm away from the target, into a stopping potential energy analyser. After energy analysis the ions were focused and accelerated to 1000 eV into a detection mass spectrometer (a magnetic sector instrument), and detected with a Galileo channel multiplier. The primary beam exit slit, the target,

and the detection slit were kept at the same potential during the experiments, and this equipotential region was carefully shielded by μ metal sheets. The primary beam–target section could be rotated about the scattering centre with respect to the detection slit to obtain angular distributions. Either analog signal measurements on the output of the multiplier or pulse counting was used at various stages of the experiments.

The energy of the projectile ions was measured by applying to the target a potential exceeding the nominal ion energy by about 10 eV. The target area then served as a crude ion deflector directing the projectile ions into the detection slit. Their energy could be determined with accuracy better than about 0.2 eV. The incident angle of the projectile ions was adjusted before an experimental series by a laser beam reflection with a precision better than 1°. Incident ($\Phi_N$) and scattering ($\Theta'_N$) angles were measured with respect to the surface normal (see inset in Fig. 1).

The carbon surface target was a 5 × 5 mm sample of highly oriented pyrolytic graphite (HOPG) from which the surface layer was peeled off immediately before placing it into a vacuum. The sample was mounted into a stainless steel holder located 10 mm in front of the exit slit of projectile ion deceleration system. The thickness of the sample holder made angular measurements at scattering angles smaller than about 3° of the surface parallel difficult (scattering angles 87–90°). The carbon target surfaces in the experiments were kept either at room temperature or at an elevated temperature of about 600°C. For this purpose, the carbon surface could be resistively heated up to about 900°C and its temperature measured by a thermocouple and by a pyrometer. Practical absence of chemical reactions with surface hydrocarbons indicated that heating the surface to 600°C or higher decreased the concentration of hydrocarbons on the surface more than 100 times [7]. This temperature was then regarded as sufficiently high to essentially remove the hydrocarbon layer that covered the HOPG surface at room temperature (see Sections 3.3 and 3.4).

The scattering chamber of the apparatus was pumped by a 2000 L/s diffusion pump (convalex polyphenyl ether pump fluid), and the detector by a 65 L/s turbomolecular pump; both pumps were backed by rotary vacuum pumps. The background pressure in the apparatus was about $5 \times 10^{-7}$ torr. During the experiments the pressure was about $5 \times 10^{-6}$ torr due to the leakage of the source gas into the scattering chamber.

## 3. Results and discussion

### 3.1. Ion survival probability

The main process in the interaction of a projectile ion and a surface is neutralization of the projectile, as shown by numerous studies [1, 2, 6–9, 21–24]. Estimation of ion survival probability in collisions of ions with surfaces is one of the important characteristics of ion surface interactions. The ion survival probability $S_a$ (percentage of ions surviving the surface collision) is defined as the sum of intensities of all product ions scattered from the target, $\Sigma I_{PT}$, to the intensity of the projectile reactant ions incident on the target, $I_{RT}$, $S_a = 100 \ \Sigma I_{PT}/I_{RT}$ [6]. While $I_{RT}$ was measured in the experiments reported here, $\Sigma I_{PT}$ could not be directly determined and had to be estimated from the sum of intensities of product ions reaching the detector, $\Sigma I_{PD}$, taking into account the discrimination of the apparatus ($D_A$) and the angular discrimination of the scattering differential measurements ($D(\omega)$). A direct measurable quantity was the relative survival probability, $S_{eff} = \Sigma I_{PD}/I_{RT}$, related to $S_a$ (expressed in per cent survival) by $S_a = 100 \ F \ S_{eff}$, where $F$ summarizes the discrimination effects [6–8]. It holds for the intensity of the projectile (reactant) ion (R) registered on the detector ($I_{RD}$) and incident on the target ($I_{RT}$),

$$I_{RD} = D_A \ D(\omega)_R \ I_{RT} \tag{1}$$

and analogously for the scattered product ions (P)

$$I_{PD} = D_A \ D(\omega)_P \ I_{PT} \tag{2}$$

For the estimation of the angular discrimination of the reactant beam, $D(\omega)_R$, and the scattered product ion beam, $D(\omega)_P$, the following simplifications were made:

(a) The area of the detection slit (0.4 × 1.0 mm²) was approximated by an aperture of the same area (diameter 0.72 mm, angular acceptance $\Theta_{ds} = 1.6°$);

(b) The angular distribution of the reactant beam was approximated by its FWHM, in these experiments $\Theta_R(FWHM) = 2.0°$;

(c) The angular distribution of the scattered product beam was approximated by an average of FWHM of several typical product ion distributions as measured in these studies. $\Theta_{P,FWHM} = 14–18°$ for various groups of the experiments.

The factor characterizing the discrimination effect of the apparatus was estimated [6] from the ion intensities in the following way: by putting a potential on the target, one can deflect the incident projectile (reactant) ion beam into the detection slit, measure its angular distribution, and register it on the output of the detector multiplier and determine the ration of the projectile ion beam hitting the detection slit and reaching the detector. The factor $F$ was estimated for each set of experiments [6–8].

The values of $S_a$ (estimated absolute survival in %) are summarized in Table 1 [6, 7] and Table 2 [8] for all hydrocarbon ions measured and for some non-hydrocarbon ions. The $S_a$ estimates may be influenced by the inaccuracy of the simplified evaluation of the discrimination factors, and they are presumably close to the upper limit of the ion survival probability. Though the values in Table 1 are mostly averages of measurements of many spectra, the standard

**Table 1.** Percentage of surviving ions, $S_a$(%), in collisions of $CH_n^+$ and $C_2H_n^+$ ions with room temperature (non-heated) and heated HOPG surfaces [6, 7].

| Projectile | $E_{inc}$ = 11.7 eV $S_a$(%) | $E_{inc}$ = 16.3 eV $S_a$(%) | $E_{inc}$ = 31.3 eV $S_a$(%) | $E_{inc}$ = 46.3 eV $S_a$(%) |
|---|---|---|---|---|
| Non-heated | | | | |
| $CD_3^{+(a)}$ | | $0.12 \pm 0.03$ | $0.22 \pm 0.04$ | $0.26 \pm 0.16$ |
| $CD_4^{+\bullet\,(a)}$ | | $0.37 \pm 0.06$ | $0.34 \pm 0.2$ | $0.27 \pm 0.26$ |
| $CD_5^{+(a)}$ | | $12.5 \pm 5$ | $12.0 \pm 5$ | $18 \pm 7$ |
| $C_2H_2^{+\bullet}$ | $0.1 \pm 0.03$ | | $0.1 \pm 0.03$ | $0.06 \pm 0.01$ |
| $C_2D_2^{+\bullet}$ | | | | $0.08 \pm 0.02$ |
| $C_2H_3^+$ | | $6.4 \pm 0.4$ | $4.1 \pm 0.7$ | $2.4 \pm$ |
| $C_2H_4^{+\bullet}$ | | $2.3 \pm 0.6$ | $1.2$ | $0.7 \pm 0.1$ |
| $C_2D_4^{+\bullet}$ | | | $1.0 \pm 0.4$ | $0.9 \pm 0.2$ |
| $C_2H_5^+$ | $0.3 \pm 0.03$ | $1.1 \pm 0.03$ | $1.0 \pm 0.1$ | $0.3 \pm 0.03$ |
| | | | | |
| Heated | | | | |
| $CD_3^{+(a)}$ | | $0.09$ | | $0.1$ |
| $CD_4^{+\bullet(a)}$ | | $(5)$ | $2.3$ | |
| $CD_5^{+(a)}$ | | | | $23$ |
| $C_2H_2^{+\bullet}$ | $0.1 \pm 0.04$ | | $0.1 \pm 0.04$ | $0.36 \pm$ |
| $C_2D_2^{+\bullet}$ | | | $0.07 \pm 0.2$ | |
| $C_2H_3^+$ | | | $3.6 \pm 0.2$ | $5$ |
| $C_2H_4^{+\bullet}$ | | | $0.2 \pm 0.05$ | $0.8 \pm 0.2$ |
| $C_2D_4^{+\bullet}$ | | | $0.4 \pm 0.05$ | |

[a] Data from Ref. [6]

**Table 2.** Percentage of surviving ions, $S_a$(%), in collisions of $C_3H_m^+$ and non-hydrocarbon simple ions with non-heated HOPG carbon surfaces [8].

| Projectile | $E_{inc}$ = 16.3 eV $S_a$(%) | $E_{inc}$ = 31.3 eV $S_a$(%) | $E_{inc}$ = 46.3 eV $S_a$(%) |
|---|---|---|---|
| Non-heated | | | |
| $C_3H_2^+$(1-propene) | | $0.75 \pm 0.05$ | $1.1$ |
| $C_3H_3^+$(c-propane) | | $1.6 \pm 0.12$ | |
| $C_3H_3^+$(1-propene) | | $3.7 \pm 0.2$ | |
| $C_3H_3^+$(propane) | $6.3$ | $2.6 \pm 0.1$ | $1.7$ |
| $C_3H_4^+$(c-propane) | | $1.0 \pm 0.3$ | $0.9 \pm 0.03$ |
| $C_3H_4^+$(1-propene) | | $0.78 \pm 0.1$ | |
| $C_3H_5^+$(c-propane) | | $1.1 \pm 0.1$ | $0.9 \pm 0.03$ |
| $C_3H_5^+$(1-propene) | | $1.0 \pm 0.4$ | |
| $C_3D_5^+$(D-propane) | | $4.8 \pm 0.6$ | |
| $C_3H_5^+$(propane) | $5.5 \pm 0.3$ | $2.1 \pm 0.1$ | |
| $C_3H_6^+$(c-propane) | | $0.81 \pm 0.2$ | $0.95 \pm 0.05$ |
| $C_3H_6^+$(1-propene) | | $0.32 \pm 0.1$ | $1.7 \pm 0.4$ |
| $C_3D_6^+$(D-propane) | | $2.2 \pm 0.4$ | |
| $C_3H_6^+$(propane) | $3.1 \pm 0.4$ | $3.4 \pm 0.5$ | $3.2 \pm 0.9$ |
| $C_3D_7^+$(D-propane) | | $11.0 \pm 1$ | $8.3$ |
| $C_3H_7^+$(propane) | | $5.9 \pm 1.7$ | $9.0 \pm 2.6$ |
| $C_3D_8^+$(D-propane) | | $0.6 \pm 0.3$ | |
| $C_3H_8^+$(propane) | $0.3 \pm 0.1$ | $1.2 \pm 0.2$ | $1.9 \pm 0.9$ |
| $Ar^+$ | | | $0.002$ |
| $CO_2^+$ | | | $0.0015$ |
| $CO_2^{2+}$ | | | $0.02$ |

deviation is rather large. The ion survival probability on a clean heated carbon surface appears to be similar to that one on the carbon surface covered by hydrocarbons. Also, the data do not show any systematic dependence on the collision energy.

The values of the survival probability show a considerable difference in values for different ions. In general, it appears that ions of recombination energies (usually similar as their ionization potentials) higher than about 10–10.5 eV exhibit $S_a$ values (for this incident angle of 60° with respect to the surface normal) smaller than about 1%, ions of recombination energies lower than this value (e.g. closed shell ions like $CH_5^+$, $C_2H_3^+$, $C_3H_7^+$, $C_3H_3^+$) show $S_a$ values of a few per cent or even higher. Molecular ions of recombination energies close to about 10 eV exhibit $S_s$ values of about 1%. The $S_a$ values depend strongly on the incident angle [8, 21]. The data indicate that by increasing the incident angle (i.e. moving closer to the surface), the $S_a$ values considerably increase, while by decreasing the incident angle (bombarding beam steeper to the surface), they considerably decrease. For instance, decreasing the incident angle from 60° to 45° led to a decrease of the $S_a$ values by a factor of 5–10 [8].

### 3.2. Mass spectra of product ions

#### 3.2.1. Collisions with heated HOPG surface

Collisions of the projectile ions with the HOPG surface heated to about 600°C represent a simpler case. Sample mass spectra of product ions from collisions of $CD_n^+$ (recorded spectra [6]) and $C_2H_n^+$ ($C_2D_n^+$) hydrocarbon ions (stick spectra [7]) are shown in Figs 2 and 3, respectively, at several collision energies. Ion intensities in these and other mass spectra of this contribution are presented as per cent fractions of the total product ion intensity recorded vs. the mass to charge ratio, m/z. The mass spectra are rather simple, showing only product ions of masses lower than the projectile ion, and thus indicate only surface induced fragmentation of the product ions at higher collision energies. As expected, the fragmentation increases with increasing collision energy. No products of chemical reactions with the surface material could be detected.

Fragmentation of the $CD_n^+$ ion occurs by a loss of D atom or $D_2$ molecule [6]. The projectile ion $C_2H_2^{+\bullet}$ ($C_2D_2^{+\bullet}$) remains undissociated at lower collision energies and only at the highest collision energy of 46.3 eV it exhibits a weak dissociation channel (of about 8%) to $C_2H^+$ ($C_2D^+$) by a loss of H(D) [7]. The projectile ion $C_2H_3^+$ dissociates partly by a loss of an H atom to $C_2H_2^{+\bullet}$ (11% and 26% at 31.3 and 46.3 eV, respectively). The main dissociation processes of the cation $C_2H_4^{+\bullet}$ upon surface collision excitation are a loss of H and a loss of $H_2$ to form $C_2H_3^+$ and $C_2H_2^{+\bullet}$ products, respectively, at increasing amounts with increasing incident energy. At 46.3 eV, only about 2% of the projectile ion remain undissociated. No measurable amounts of deeper
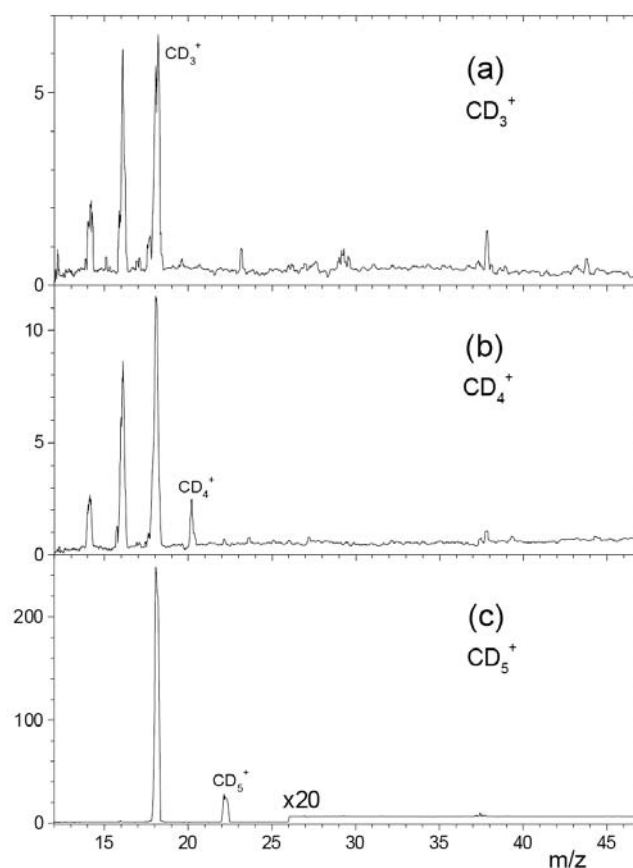
**Figure 2.** Mass spectra of product ions from collisions of $CD_n^+$ with HOPG surfaces heated to 600°C at incident energy of 51.6 eV (incident angle $\Phi_N = 60°$) [6].

fragmentation to $CH_n^+$ ($CH_3^+$, $CH_2^+$) could be detected. The data for $C_3H_n^+$ hydrocarbons show similar dissociation patterns, including loss of hydrocarbon groups [8].

The extent of dissociation as obtained from the mass spectra of product ions upon impact of the projectile $CD_4^{+\bullet}$ can be used to estimate the distribution of energy converted in the surface collision into internal excitation of the projectile, $P(E'_{int})$ (see Fig. 4) [6]. This approach was used earlier [21, 23, 24] and consists of using the breakdown pattern of the projectile polyatomic ion to fit the relative intensities of the product ions by a trial and error distribution function.

The breakdown pattern of the projectile ion $CH_4^{+\bullet}$ is well known and is shown in the lower part of Fig. 4. Because of the simplicity of the breakdown pattern one can expect only approximate information on $P(E'_{int})$. The distribution of internal energy of the projectile ion $CD_4^{+\bullet}$, $P(E'_{int})$, that leads to its dissociation to fragments of the respective intensities after the surface collision is given for several collision energies in Fig. 4. It peaks at increasingly higher incident energies of about 5–6% of the incident energy and exhibits a tailing to higher energies This may be, however, due to the insensitivity of the evaluation method at energies above about 3.5 eV). The average value of $P(E'_{int})$ of about 6% of the incident energy appears to be rather typical for a
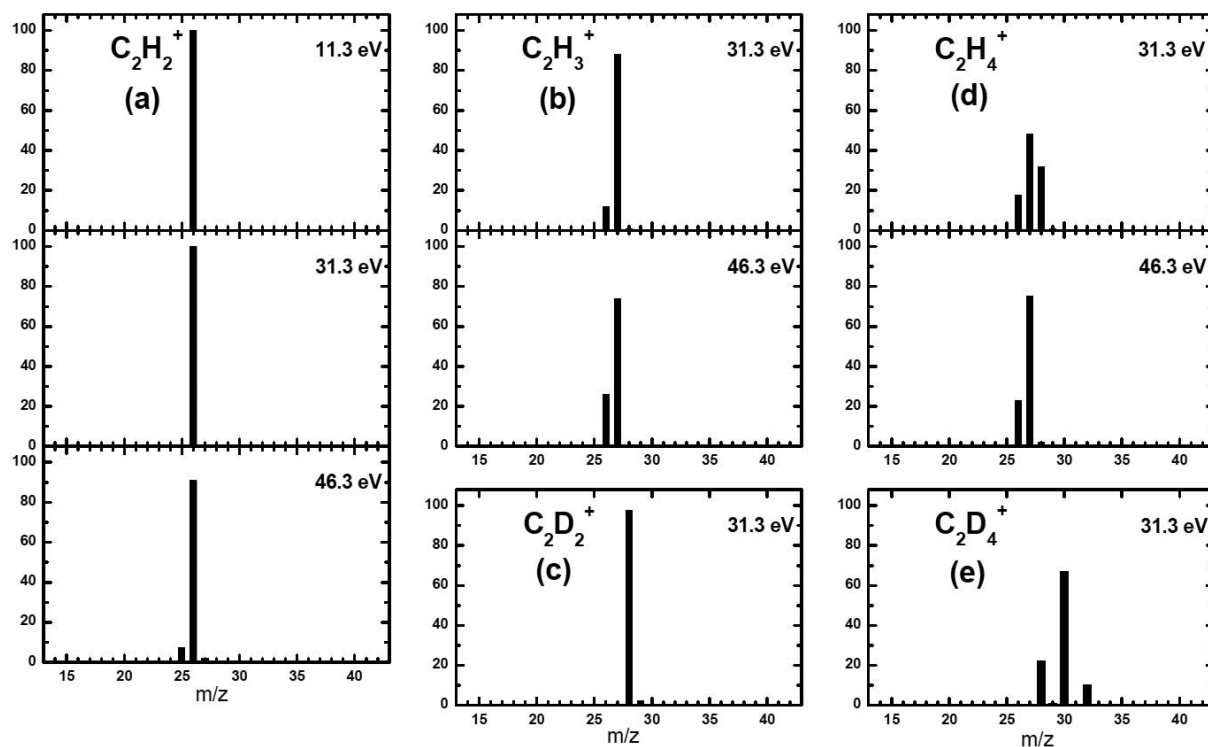
**Figure 3.** Mass spectra of product ions from collisions of $C_2H_2^+$, $C_2H_3^+$, $C_2H_4^+$, $C_2D_2^+$ and $C_2D_4^+$ with HOPG surfaces heated to $600^{\circ}C$ at indicated incident energies (incident angle $\Phi_N = 60^{\circ}$) [7].

variety of polyatomic ions incident on hydrocarbon covered surfaces [21, 23, 24].

The dashed line in Fig. 4, upper part, shows $P(E'_{int})$ for collisions of $CD_4^{+\bullet}$ with a non-heated (hydrocarbon covered) HOPG surface (see further on). Only at this incident energy of 16.6 eV was there a significant difference in $P(E'_{int})$ curves for heated and unheated surfaces; for higher incident energies of 31.6 eV and 51.6 eV these two $P(E'_{int})$ distributions were practically the same [6].

### 3.2.2. Collisions with non-heated (room temperature) HOPG surface. Chemical reactions with surface material

Mass spectra of product ions from collisions of the projectile ions $CD_3^+$, $CD_4^+$ and $CD_5^+$ at the incident energy of 51.3 eV with the HOPG surface at room temperature are shown in Fig. 5 [6], those from collisions of $C_2H_2^{+\bullet}$, $C_2D_2^{+\bullet}$, $C_2H_3^+$, $C_2H_4^{+\bullet}$, $C_2D_4^{+\bullet}$ and $C_2H_5^+$ at indicated incident energies in Fig. 6 [7]. The spectra differ from that obtained on a heated surface in that they also show contributions of ions of masses higher than the mass of the projectile ion. In the spectra projectile ion $CD_4^+$, product ion of $CD_4H^+$ and its dissociation products ($CD_2H^+$, $CD_3^+$) are clearly visible, for all $CD_n^+$ projectiles, product ions of $C_2X_n^+$ and $C_3X_n^+$ (X = H,D) (insets in Fig. 5) can be observed. In case of projectile ions $C_2D_2^+$ ($C_2H_2^+$) and $C_2D_4^+$ ($C_2H_4^+$), formation of protonated projectiles $C_2D_2H^+$ and $C_2D_4H^+$ and their fragmentation products and — to a lesser extent — formation of $C_3X_n^+$ product ions was registered (Fig. 6). In



**Figure 4.** Distribution of energy transformed into internal excitation of the projectile ion $CD_4^+$, $P(E'_{tr})$, at indicated incident energies on heated and non-heated HOPG surfaces. The lower pannel shows the breakdown pattern of the $CD_4^+$ used in the evaluation [6].
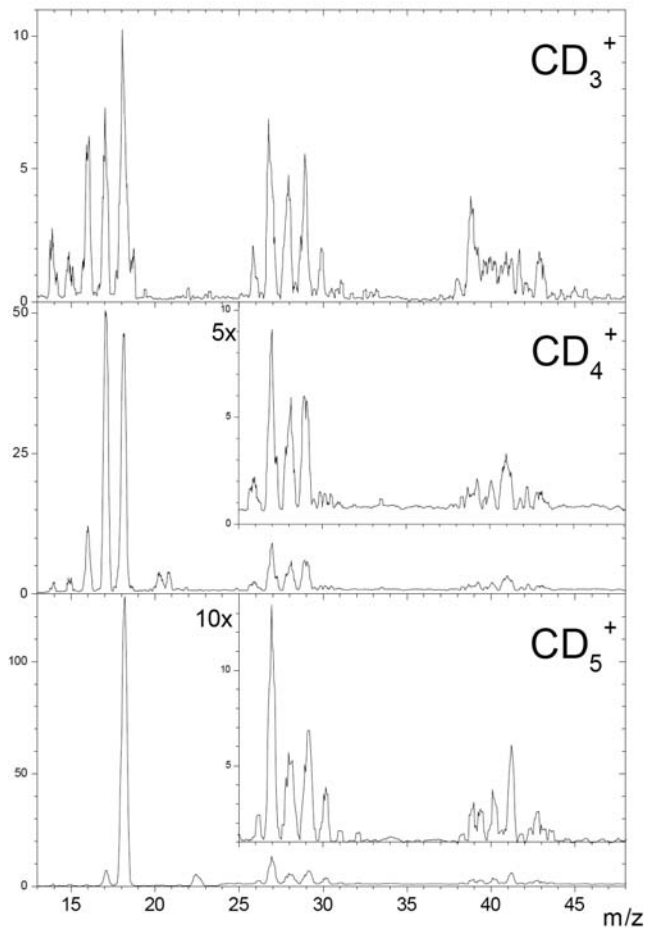
**Figure 5.** Mass spectra of product ions from collisions $CD_n^+$ with room temperature (non-heated) HOPG surfaces at incident energy of 51.6 eV (incident angle $\Phi_N = 60°$). Note increased sensitivity of insets [6].

collisions of $C_3H_n^+$ radical cations ($C_3H_8^+$, $C_3H_6^+$) the H atom transfer reaction was observed, but no formation of ions of the group $C_4$ was detected [8].

Ions containing more carbon atoms than the projectile ion can in principle be formed by sputtering of the surface material or in chemical reactions of carbon chain buildup between the projectile ion and the surface material.

Using D and $^{13}C$ labelled projectiles, the contribution of the sputtering could be subtracted and it could be concluded that a substantial part of these ions was formed in reactions between the projectile ions and the $CH_3$ terminal group of the surface hydrocarbons and subsequent dissociation of the collision intermediate by $H_2$ fragmentation. For instance, the reaction of carbon chain buildup in case of the $CD_4^+$ projectile led to the final product $C_2H_3^+$ via Ref. [6]

$$CD_4^+ + H_3C - S \rightarrow [C_2D_4H_3^+] + \text{-}S \rightarrow$$
$$C_2X_5^+ + X_2 \rightarrow C_2X_3^+ + X_2 \ (X = H,D) \tag{3}$$
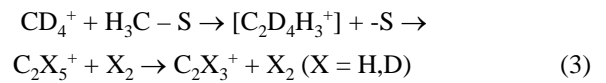
Reactions of $C_2D_2^+$ and $C_2D_4^+$ were shown to lead to the final carbon chain buildup product $C_3X_3^+$ (X = H,D) in an analogous way, e.g. for the $C_2D_2^+$ projectile [7]

$$C_2D_2^+ + H_3C\text{-}S \rightarrow [C_3D_2H_3^+] + \text{-}S \rightarrow$$
$$C_3X_3^+ + X_2 \ (X = H,D) \tag{4}$$
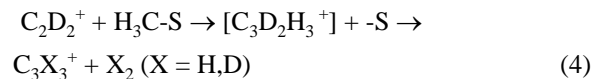
Analysis of the spectrum of the ion products from collisions of the projectile ion $C_2D_2^+$ at 46.3 eV is shown in Fig. 7. Full bars indicate product ion formed in the chemical reaction of:
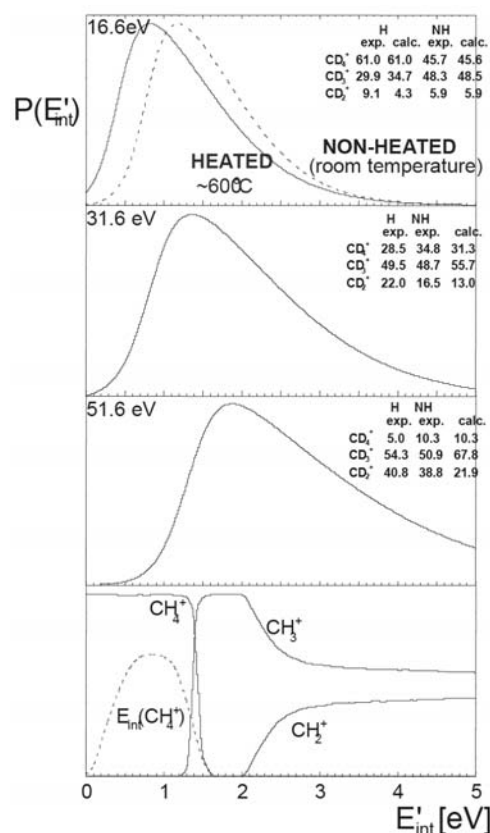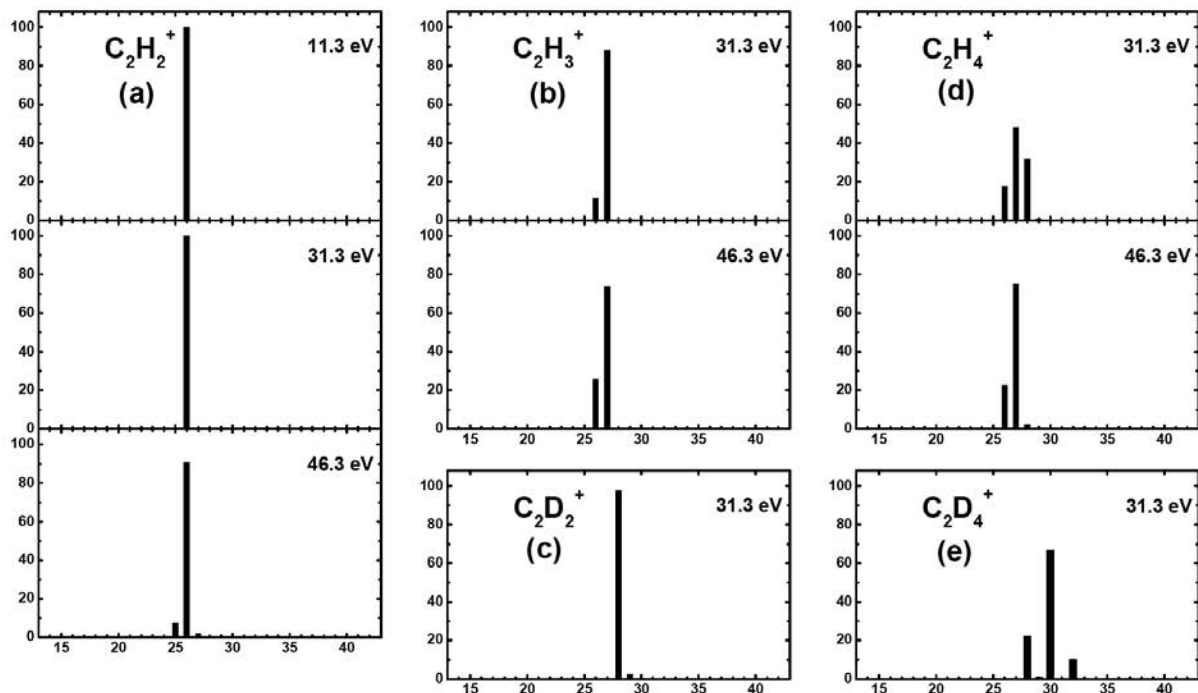


**Figure 6.** Mass spectra of product ions from collisions of $C_2H_2^+$, $C_2H_4^+$, $C_2D_2^+$ and $C_2D_4^+$ with room temperature (non-heated) HOPG surfaces at indicated incident energies (incident angle $\Phi_N = 60°$).
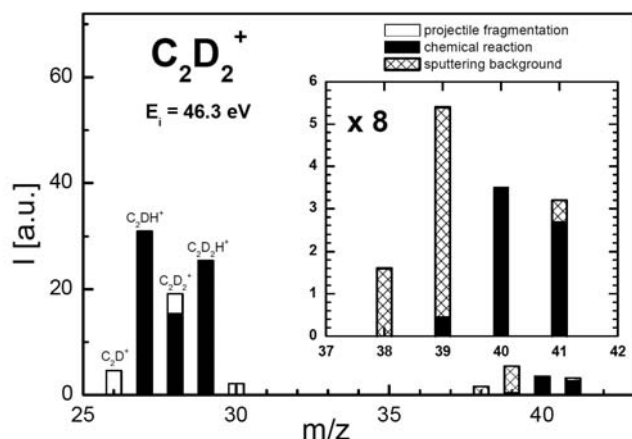
**Figure 7.** Analysis of the contributions to the mass spectrum of product ions from collisions of $C_2D_2^{+\bullet}$ projectiles with the HOPG surface at room temperature at $E_i = 46.3$ eV (see also mass spectrum in Fig. 6). Columns: measured ion intensities, open sections — fragmentation of the projectile ion, black — contributions from chemical reactions, cross-hatched: sputtering background. See text for details.

(a)  H atom transfer and formation of the surface protonated projectile $C_2D_2H^+$ (m/z = 29) and its fragmentation products $C_2D_2^+$ (m/z = 28) and $C_2DH^+$ (m/z = 27);

(b)  Carbon chain buildup products $C_3H_3^+$ (m/z = 39), $C_3DH_2^+$ (m/z = 40), and $C_2D_2H^+$ (m/z = 41) in the ratio 39:40:41 = 0.07:0.53:0.4, which is within the experimental error close to the calculated statistical ratio 39:40:41 = 0.1:0.6:0.3 that assumes interaction of the projectile with the terminal $CH_3$ group of the surface hydrocarbons [7].

The ratio of probabilities of different processes, namely direct dissociation (DD) vs. H atom transfer (HT) vs. $C_{n+1}$ reaction (CR), was about DD:HT:CR = 0.3:1:0.1 for collisions of $CD_4^+$ at 31.2 eV [6], DD:HT:CR = 3.1:1:0.1 for $C_2D_4^{+\bullet}$ collisions at 46.3 and 31.3 eV, and about DD:HT:CR = 0.1:1:0.1 for $C_2D_2^{+\bullet}$ at 46.3 eV [7].

### 3.3. Translational energy distributions of product ions

Translational energy distributions of product ions were measured both for heated and room temperature surfaces. Within the experimental error, the velocity distributions of scattered undissociated projectile ions and main fragment ions peaked at the same velocity and they were very similar. This indicates, in agreement with our earlier finding [21–24], that the surface induced fragmentation of the projectile ions takes place prevailingly after the interaction with the surface in a unimolecular way.

Figure 8 shows, as an example, translational energy distributions, $P(E'_{tr})$, of product ions $CD_5^+$ and $CD_3^+$ from collisions of $CD_5^+$ with heated (left) and room temperature (right) HOPG surfaces at several collision energies [6]. The product ions were formed in strongly inelastic collision with undissociated product energy peaking at about 75% of the incident energy for the heated surface and 44–56% for room temperature surfaces. Thus the collisions with the heated surface were considerably less inelastic. The velocities of both product ions peaked at practically the same velocity, indicating even for these relatively simple projectiles unimolecular decomposition after the interaction with the surface.

Translational energy distributions of typical product ions for the $C_2$ projectile ions are exemplified in Fig. 10 for collisions of $C_2H_3^+$ and $C_2H_4^+$ projectile ions with heated
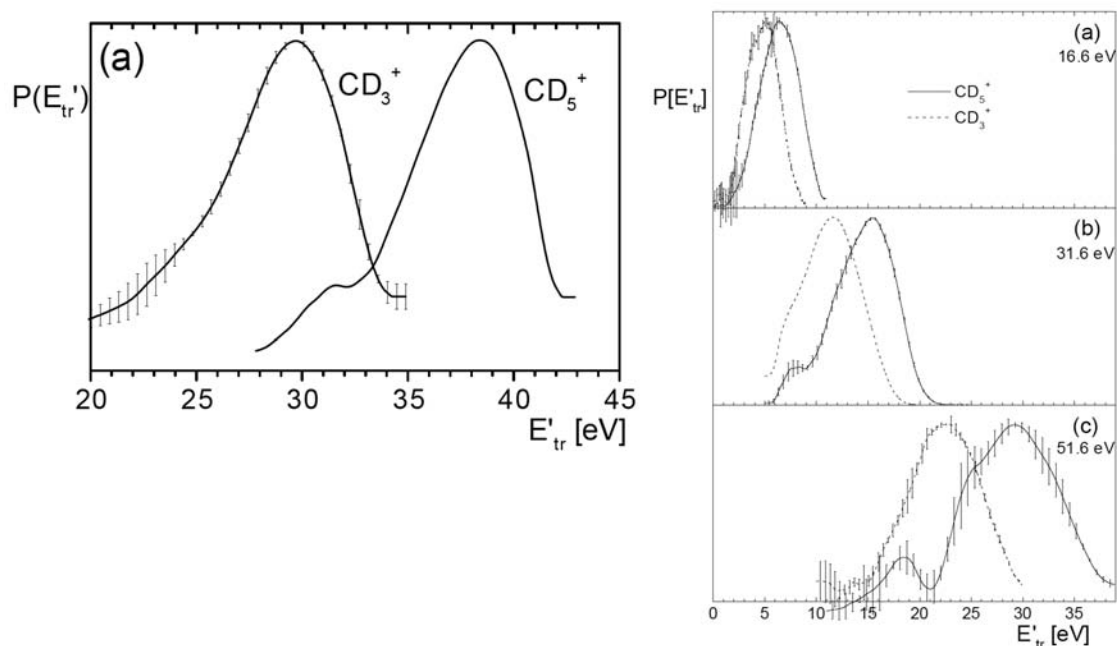


**Figure 8.** Translational energy distributions of product ions $CD_5^+$ and $CD_3^+$ from collisions of $CD_5^+$ with heated (left, 51.3 eV) and non-heated (right, incident energies as indicated) HOPG surfaces [6].
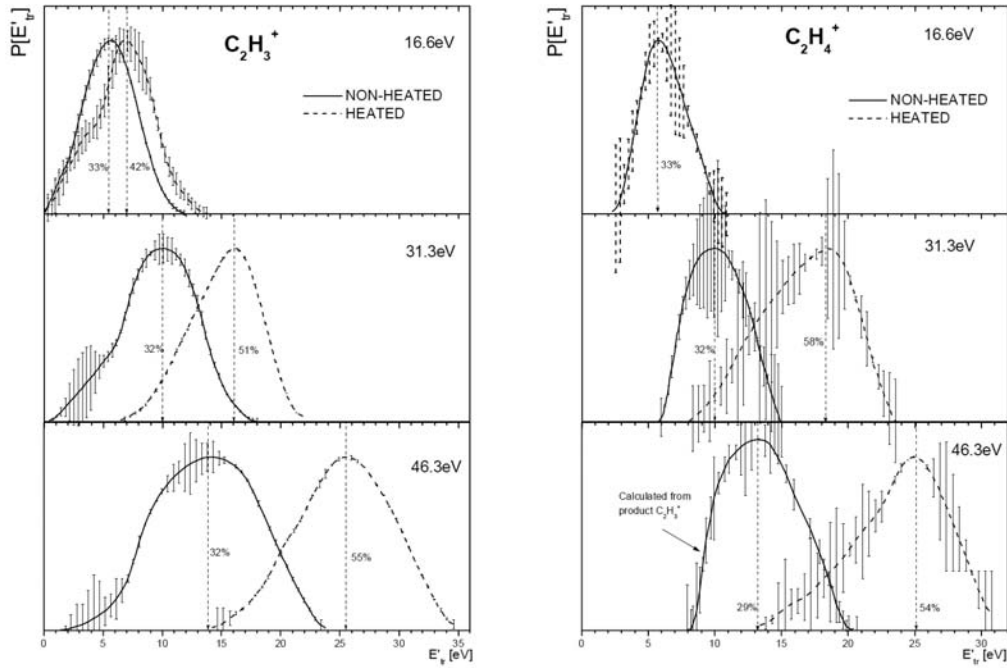
**Figure 9.** Translational energy distributions, P(E'$_{tr}$), of product ions $C_2H_3^+$ and $C_2H_4^+$ from collisions of $C_2H_3^+$ and $C_2H_4^+$ with heated (dashed) and room temperature (solid line) HOPG surfaces at indicated incident energies. Vertical dashed lines and numbers show peak energy of the distributions in % of the incident energy [7].
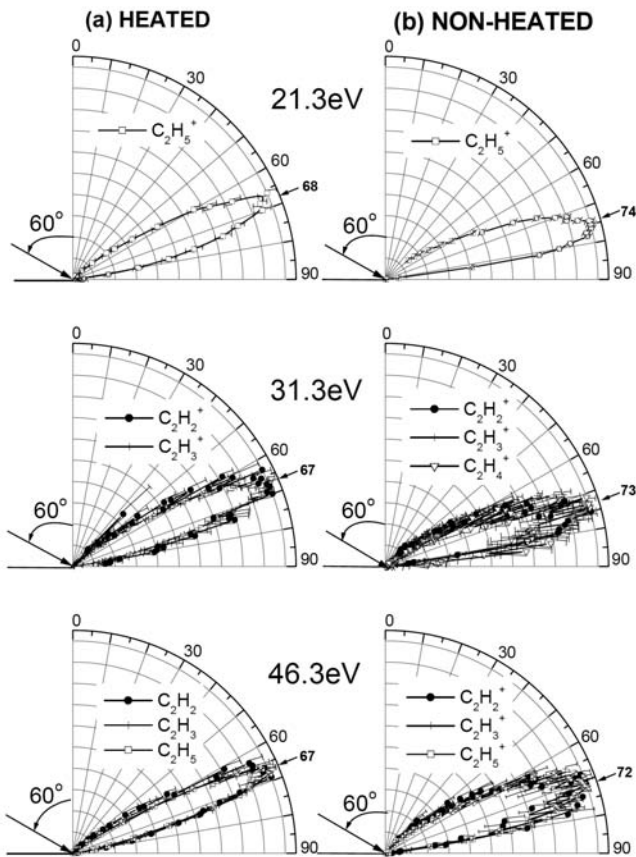


**Figure 10.** Polar plots of angular distributions of product ions (inelastically scattered undissociated projectile ions as indicated in the figure) from collision with heated (left) and non-heated (right) HOPG surfaces at indicated incident energies. Incident angle $\Phi_N = 60°$ (30° with respect to the surface); arrows indicate peaks of angular distributions [7].

(dashed line) and room temperature (non-heated, solid line) HOPG surfaces at three different incident energies [7]. The undissociated product ions exhibit energy distributions peaking mostly at about 50–58% of the incident energy on heated surfaces, and at about 30–33% on non-heated HOPG surfaces. Thus the collisions with heated surfaces are again less inelastic in comparison with collision with non-heated surfaces. However, the inelasticity in both cases was found to be larger for the $C_2H_n^+$ (or $C_2D_n^+$) projectiles than for the $CD_n^+$ projectiles (i.e. 50–58% vs. 75%, respectively, on heated surfaces, and 44–55% vs. 30–33% on non-heated surfaces).

### 3.4. Angular distributions of productions

An example of angular distribution data for different $C_2H_n^+$ projectile ions scattered from heated and non-heated HOPG surfaces at different incident energies is shown in Fig. 10 [7]. In all cases, the incident angle was $\Phi_N = 60°$ (30° with respect to the surface, see Fig. 10). The data are given as polar plots separately for heated and non-heated surfaces, for three incident energies of 21.3, 31.3 and 46.3 eV. Because angular distributions of different product ions on the same surface and at the same incident energy were very similar, data for different ions are given in one picture. There is some difference in peaking of the angular distributions of product ions scattered from the heated ($\Theta_N^{'} \sim 67$–68°, i.e. 22–23° with respect to the surface) and room temperature surface ($\Theta_N^{'} \sim 72$–75°, i.e. 15–18° with respect to the surface). The widths of the angular distributions are about the same for both heated and room temperature surfaces (about 17–20°, full width at half maximum).

For $CH_n^+$ projectile ions the results were analogous. However, the angular distributions peaked on heated HOPG surfaces at a somewhat higher angle than for the $C_2H_n^+$ projectiles ($\Theta_N^{'} \sim 72^o$, i.e. $18^o$ with respect to the surface) and on room temperature surfaces at $\Theta_N^{'} \sim 75\text{–}78^o$, i.e. $12\text{–}15^o$ with respect to the surface. This may be connected with slightly different inelasticities of the processes for $CH_n^+$ and $C_2H_n^+$ ions.

## Acknowledgements

## References

[1]    RABALAIS, J.W., Ed., Low Energy Ion-Surface Interactions, Wiley, New York, 1994.

[2]    COOKS, R.G., AST, T., MABUD, M.D., Int. J. Mass Spectrom. **100** (1990) 209.

[3]    HANLEY, L., Ed., Polyatomic Ion-Surface Interactions, Int. J. Mass Spectrom. **174** (1998).

[4]    GRILL, V., SHEN, J., EVANS, C., COOKS, R.G., Rev. Sci. Instr. **72** (2001) 3149.

[5]    HOFER, W.O., ROTH, J., Eds, Physical Processes of the Interaction of Fusion Plasmas with Solid, Academic Press, San Diego, CA, 1996.

[6]    ROITHOVÁ, J., ŽABKA, J., DOLEJŠEK, Z., HERMAN, Z., J. Phys. Chem. B **106** (2002) 8293.

[7]    JAŠÍK, J., et al., J. Phys. Chem. A **109(45)** (2005) 10208.

[8]    PYSANENKO, A., ŽABKA, J., FEKETEOVÁ, L., MÄRK, T.D., HERMAN, Z. (in press).

[9]    ŽABKA, J., et al., Int. J. Mass Spectrom. **213** (2002) 145.

[10]   SUGAI, H., MITSUOKA, Y., TOYODA, H.J., Vacuum Science Technol. A **16** (1998) 290.

[11]   QUAYYUM, A., et al., Chem. Phys. Lett. **372** (2003) 166.

[12]   QAYYUM, A., et al., Chem. Phys. Lett. **376** (2003) 539.

[13]   QAYYUM, A., et al., J. Phys. Chem. A **108** (2004) 1.

[14]   MORRIS, J.R., KIM, G., BARSTIS, T.L.O., MITRA, R., JACOBS, D.C., J. Chem. Phys. **107** (1997) 6448.

[15]   MAAZOUS, M., BARSTIS, T.L.O., MAAZOUS, P.L., JACOBS, D.C., Phys. Rev. Lett. **84** (2000) 1331.

[16]   KOPPERS, W.R., BEIJERSBERGEN, J.H.M., WEEDING, T.L., KISTEMAKER, P.G., KLEYN, A.W., J. Chem. Phys. **107** (1997) 10736.

[17]   KOPPERS, W.R., et al., J. Chem. Phys. **110** (1999) 2588.

[18]   LOS, J., GLEESON, M.A., KOPPERS, W.R., WEEDING, T.L., KLEYN, A.W., J. Chem. Phys. **111** (1999) 11080.

[19]   BECK, R.D., ROCKENBERGER, J., WEISS, P., KAPPES, M.M., J. Chem. Phys. **104** (1996) 3638.

[20]   WAINHAUS, S.B., LIM, H., SCHULTZ, D.G., HANLEY, L., J. Chem. Phys. **106** (1997) 10329.

[21]   KUBIŠTA, J., DOLEJŠEK, Z., HERMAN, Z., European Mass Spectrom. **4** (1998) 311.

[22]   WÖRGÖTTER, R., KUBIŠTA, J., ŽABKA, J., MÄRK, T.D., HERMAN, Z., Int. J. Mass Spectrom. Ion Proc. **174** (1998) 53.

[23]   ŽABKA, J., DOLEJŠEK, Z., HERMAN, Z., J. Phys. Chem. A **106** (2002) 10861.

[24]   HERMAN, Z., J. Am. Soc. Mass Spectrom. **14** (2003) 1360.

# Elementary processes, transport and kinetics of molecular plasmas

*M. Capitelli[a], R. Celiberto[b], O. De Pascale[c], P. Diomede[a], F. Esposito[c], C. Gorse[a], A. Laricchiuta[c], S. Longo[a], D. Pagano[a]*

[a] Dipartimento di Chimica, Università di Bari, via Orabona 4, 70126 Bari, Italy
[b] DICA, Politecnico di Bari, via Orabona 4, 70126 Bari, Italy
[c] IMIP-CNR, sezione di Bari, via Amendola 122/D, 70126 Bari, Italy

## Abstract

Vibrationally resolved cross-sections have been obtained, in classical and semiclassical approximations, for electron impact induced dissociation, excitation, ionization of molecules and for dissociation and vibrational deactivation in atom–diatom collisions. The influence of atomic excited states on the transport properties of a hydrogen plasma in thermodynamic equilibrium has been investigated systematically. Finally, different approaches for the simulation of negative ion sources through the coupling of vibrational and electron kinetics are presented.

## 1. Introduction

In the last decade, a great effort has been devoted to the theoretical investigation of non-equilibrium plasma systems for many technological applications. In particular, the fundamental role of excited species has been emphasized in the interpretation of some experimental results and, as a consequence, numerical codes, implemented for plasma simulation, have been modified in order to include a detailed state to state kinetics [1]. In this framework the creation of a complete and consistent database of cross-sections for elementary processes involving excited (vibrationally and electronically) molecules and excited atoms is a big challenge. The attempt of including all the effects, linked to the presence of excited species in the plasma, represents the main feature of the work done in our laboratories. From a fundamental point of view, electron induced processes have been studied, calculating the vibrationally resolved cross-sections for dissociation and excitation of $H_2$ molecules. Moreover, calculations on vibration–translation energy exchange (VT processes) and dissociation processes in $H-H_2$ collisions have been completely reviewed, enhancing the accuracy of dynamic results. These data are addressed to the fusion community, being relevant to the modelling of negative ion sources as well as for divertor conditions. Also the ionization of $N_2$ molecule by electron impact has been considered, due to the importance of this process in air gas-discharge plasma and for a plasma of the Earth atmosphere including aurora phenomena and glow processes.

The transport properties of $H_2$ thermal plasmas have been studied a lot in the past [2, 3], however the presence of atomic excited states has been completely ignored, due to the assumption of low concentration of $H(n)$ species. Despite that, excited state collision integrals dramatically depend on the principal quantum number, so that neglecting excited states in the transport equations could be a strong approximation. Transport property calculations have been performed including the effect of atomic excited levels.

Finally, detailed kinetic codes have been developed to describe molecular plasmas, mainly hydrogen plasmas, in different non-equilibrium conditions. The attention has been focused on the modelling of negative ion sources. Recent improvements in these fields will be reported in this paper.

## 2. Electron molecule collision processes

### 2.1. $H_2$ triplet–triplet transitions

Modelling of non-equilibrium $H_2$ plasma systems requires the inclusion not only of vibrational and dissociation kinetics, but also of electronically excited states. However, only a few examples of cross-sections for elementary processes initiated from an excited state are available in the literature [4]. State to state cross-sections for electron impact induced excitation of the $a^3\Sigma_g^+$ and the metastable $c^3\Pi_u$ states of $H_2$ molecules to other excited triplet states have been calculated [5, 6], in the framework of the semiclassical impact parameter method [7, 8]. The following transitions have been considered:

$$H_2(a^3\Sigma_g^+, v_i) + e \rightarrow H_2(d^3\Pi_u) + e$$
$$H_2(c^3\Pi_u, v_i) + e \rightarrow H_2(g^3\Sigma_g^+) + e$$
$$H_2(c^3\Pi_u, v_i) + e \rightarrow H_2(h^3\Sigma_g^+) + e$$
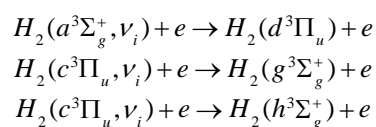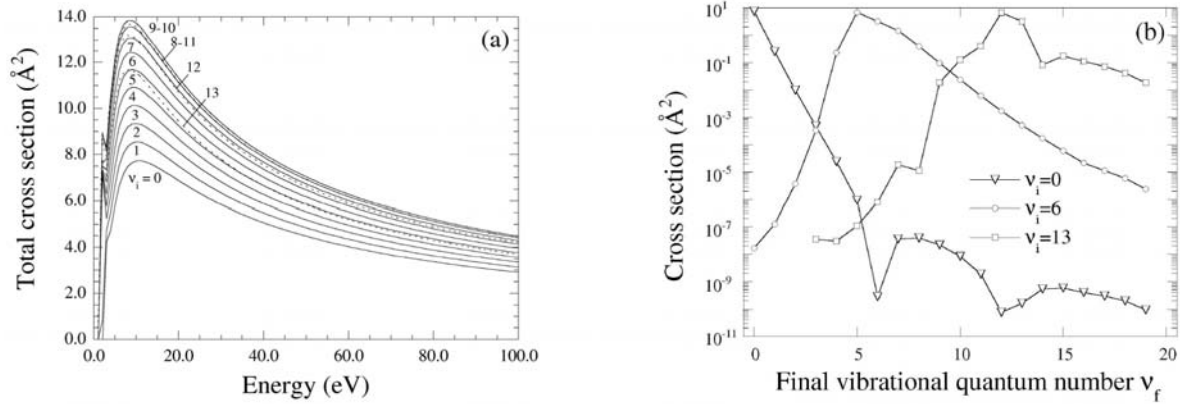
**Figure 1.** (a) Total cross-sections, as a function of collision energy, for the process $H_2(a^3\Sigma_g^+, v_i) + e \rightarrow H_2(d^3\Pi_u) + e$; (b) state to state cross-sections, at a fixed collision energy (E = 10 eV), for the process $H_2(a^3\Sigma_g^+, v_i) + e \rightarrow H_2(d^3\Pi_u, v_f) + e$.
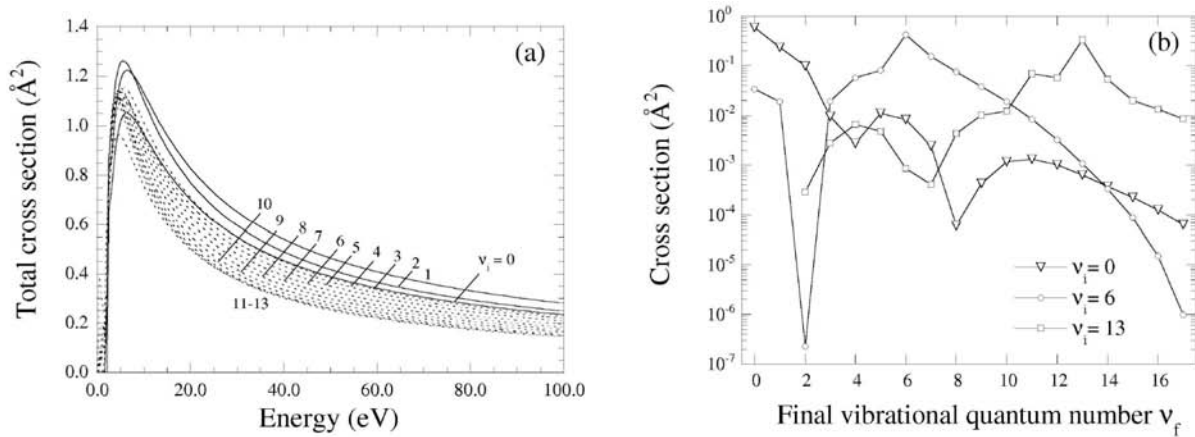


**Figure 2.** (a) Total cross-sections, as a function of collision energy, for the process $H_2(c^3\Pi_u, v_i) + e \rightarrow H_2(g^3\Sigma_g^+) + e$; (b) state to state cross-sections, at a fixed collision energy (E = 10 eV), for the process $H_2(c^3\Pi_u, v_i) + e \rightarrow H_2(g^3\Sigma_g^+, v_f) + e$.

In particular the a → d transition, originating the Fulcher system, is important in spectroscopic diagnostic methods, providing information about vibrational and rotational population of hydrogen plasmas [9]. Total cross-sections (excitation plus dissociation), as a function of collision energy, for different initial vibrational levels, are shown in Fig. 1(a), the dissociative contribution being negligible. State to state excitation cross-sections, at a fixed energy, are displayed in Fig. 1(b) versus the final vibrational quantum number, $v_f$: the vibrational dependence is governed by the irregular behaviour of the 'structural factor', i.e. the transition dipole moment averaged over the vibrational wavefunctions. Same considerations hold for the c → g transition and corresponding results are shown in Fig. 2.

A special treatment is required for the transition to the $h^3\Sigma_g^+$ state, whose adiabatic potential energy curve exhibits a barrier sustaining three quasi-bound vibrational levels ($v' = 4, 5, 6$) above four bound levels ($v = 0$–4). Excitations to these quasi-bound levels can lead to dissociation depending on the ratio between the tunneling and radiative decay lifetimes (obtained by evaluating the semiclassical resonance width, $\Gamma^{WKB}$, and the Einstein coefficients for spontaneous emission, respectively). Quasi-bound state
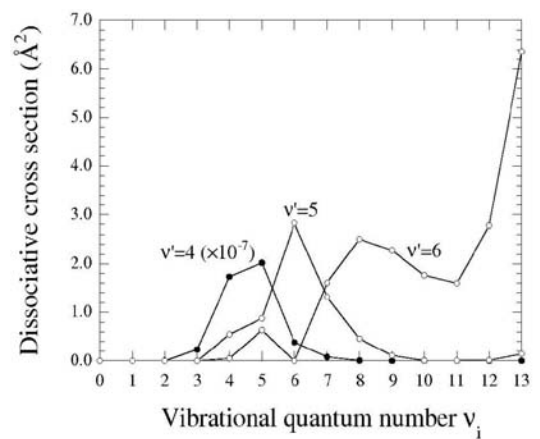


**Figure 3.** Quasi-bound state dissociative cross-section, as a function of initial vibrational quantum number, at the incident energy E = 10 eV, for the process: $H_2(c^3\Pi_u, v_i) + e \rightarrow H_2(h^3\Sigma_g^+, v') + e$.

dissociative cross-sections are shown in Fig. 3. As expected, the last resonance, $v' = 6$, located near the top of the barrier, has a strong dissociative character, while the first state behaves practically as a bound state.

Total and dissociative (not including the dissociation from quasi-bound levels) cross-sections for c → h transition,

45
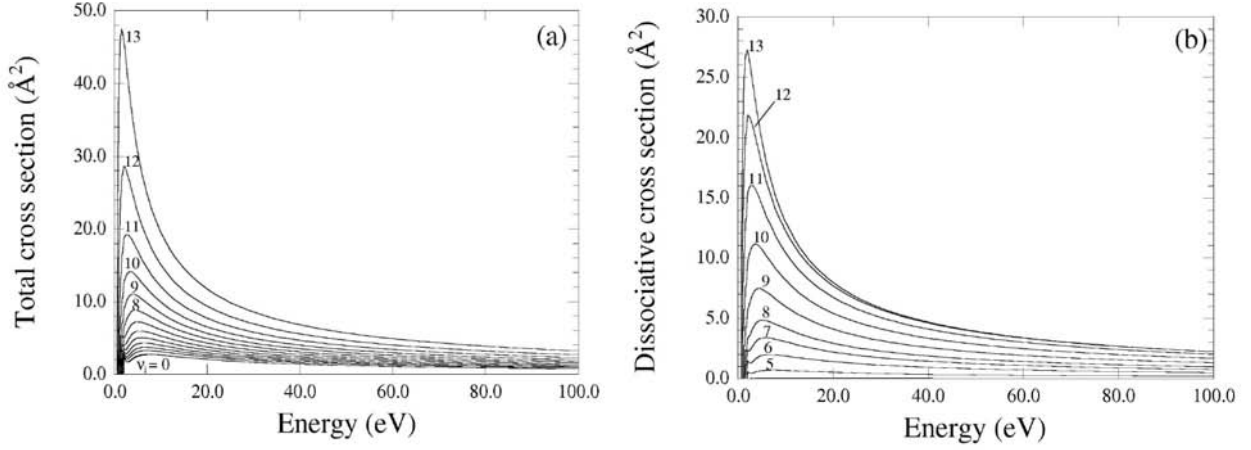
**Figure 4.** Cross-sections as a function of energy for the process (a) $H_2(c^3\Pi_u, \nu_i) + e \rightarrow H_2(h^3\Sigma_g^+) + e$; (b) $H_2(c^3\Pi_u, \nu_i) + e \rightarrow H_2(h^3\Sigma_g^+, \varepsilon) + e \rightarrow H + H + e$.

as a function of the energy and the initial vibrational quantum number, are presented in Fig. 4.

## 2.2. N₂ ionization

The electron impact ionization cross-sections for nitrogen molecules have been calculated, considering both vibrationally and electronically excited targets [10, 11]. The adopted theoretical approach represents an extension of the classical formulation of electron impact induced ionization of atomic particles [12] to diatomic molecules. In this frame the total ionization cross-section with transition from a given electronic and vibrational $v$ state of a molecule to all the electronic and vibrational states can be expressed as:

$$\sigma_{tot} = \sum_i \sum_{v'} n_i \frac{\pi e^4}{J_{v,v'}^2} f\left(\frac{E}{J_{v,v'}}\right) S_{v,v'} \tag{1}$$

where n is the number of identical electrons in the i-th shell of the molecule, E is the energy of the incident electron and J is the electron binding energy, i.e. the ionization potential. $f$ is a universal function, determined on the basis of the experimental data. $S_{v,v'}$ is the Franck–Condon factor, function of the initial and final vibrational quantum numbers of the molecule and of the molecular ion, respectively; the analysis on the basis of the values in Refs [13, 14] for this quantity shows that, for the nitrogen molecule, only three-five vibrational states of the molecular ion mainly contribute to the total ionization cross-section. Hence, one can use vibrational parameters averaged over those vibrational levels of the final state, $v'$ and $v''$, corresponding to coincidence of the classical turning points in the molecule and in the molecular ion. Then the formula (1) for the ionization cross-section can be simplified:

$$\sigma_{ion} = \frac{n\pi e^4}{2}\left[\frac{1}{J_{v,v'}^2} f\left(\frac{E}{J_{v,v'}}\right) + \frac{1}{J_{v,v''}^2} f\left(\frac{E}{J_{v,v''}}\right)\right] \tag{2}$$

For moderate electron energies (up to 50 eV), we consider the following ionization processes:

$$e + N_2(^1\Sigma_g^+) \rightarrow 2e + \begin{matrix} N_2^+(X\,^2\Sigma_g^+) \\ N_2^+(A\,^2\Pi_u) \\ N_2^+(B\,^2\Sigma_u^+) \end{matrix}$$
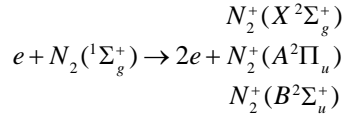
Using the experimental values of $\sigma_{tot}$ [15], defined as $\sigma_{tot} = \sigma(X\,^2\Sigma_g^+) + \sigma(A\,^2\Pi_u) + \sigma(B\,^2\Sigma_u^+)$, we obtain the universal function in the form:

$$f(x) = \frac{6(x-1)}{\pi(x+10)(x+2)} \tag{3}$$

where $x$ is the reduced energy, i.e. $x = E/J$.

Cross-sections for the three principal ionization channels of N₂ molecule, in the ground electronic state, are presented in Tables 1–3, along with the diabatic ionization potentials, $J_{v,v'}$, $J_{v,v''}$. Note that we assume the function $f(x)$ to be identical for different electron transitions of a given molecule.

**Table 1.** Parameters and cross-sections ($10^{-17}$ cm²) of the ionization transitions $e + N_2(X\,^1\Sigma_g^+, v) \rightarrow 2e + N_2^+(X\,^2\Sigma_g^+, v')$.

| $v$ | $J_{v,v'}$ [eV] | $J_{v,v''}$ [eV] | $\sigma(E=20\text{ eV})$ | $\sigma(E=30\text{ eV})$ | $\sigma(E=50\text{ eV})$ |
|---|---|---|---|---|---|
| 0 | 15.8 | 15.4 | 0.82 | 2.1 | 3.4 |
| 4 | 15.8 | 15.1 | 0.87 | 2.2 | 3.5 |
| 8 | 15.9 | 14.9 | 0.92 | 2.2 | 3.6 |
| 12 | 15.9 | 14.7 | 0.92 | 2.2 | 3.6 |
| 16 | 16.0 | 14.6 | 0.92 | 2.3 | 3.6 |
| 20 | 16.1 | 14.4 | 0.97 | 2.3 | 3.7 |
| 24 | 16.1 | 14.2 | 1.0 | 2.4 | 3.8 |
| 28 | 16.2 | 14.1 | 1.0 | 2.4 | 3.8 |
| 32 | 16.2 | 13.9 | 1.1 | 2.5 | 3.9 |
| 36 | 16.2 | 13.8 | 1.1 | 2.5 | 3.9 |
| 40 | 16.3 | 13.7 | 1.1 | 2.5 | 3.9 |

The theoretical branching ratios of different exit channels, i.e. $\sigma(X)/\sigma_{tot}$, $\sigma(B)/\sigma_{tot}$, $\sigma(A)/\sigma_{tot}$, are within the recent experimental values reported by Zyl and Pendleton [16], confirming the reliability of the theoretical approach.

Along with ionization of the nitrogen molecule in the ground electronic state, ionization of electronically excited molecules in the states $A^3\Sigma_u^+$ and $B^3\Pi_g$ have been considered.

**Table 2.** Parameters and cross-sections ($10^{-17}$ cm$^2$) of the ionization transitions $e + N_2(X^1\Sigma_g^+, v) \rightarrow 2e + N_2^+(A^2\Pi_u, v')$.

| v | $J_{v,v'}$ [eV] | $J_{v,v''}$ [eV] | $\sigma(E=20\text{ eV})$ | $\sigma(E=30\text{ eV})$ | $\sigma(E=50\text{ eV})$ |
|---|---|---|---|---|---|
| 0 | 17.8 | 16.8 | 0.79 | 2.9 | 5.2 |
| 4 | 19.0 | 15.7 | 0.90 | 3.1 | 5.3 |
| 8 | 20.0 | 15.2 | 0.95 | 3.2 | 5.4 |
| 12 | 20.6 | 14.8 | 1.0 | 3.3 | 5.5 |
| 16 | 20.4 | 14.5 | 1.2 | 3.5 | 5.8 |
| 20 | 20.0 | 14.2 | 1.4 | 3.7 | 6.1 |
| 24 | 19.6 | 14.1 | 1.5 | 3.9 | 6.4 |
| 28 | 19.2 | 14.0 | 1.6 | 4.1 | 6.6 |
| 32 | 18.8 | 13.9 | 1.8 | 4.3 | 6.8 |
| 36 | 18.4 | 13.8 | 1.8 | 4.4 | 6.9 |
| 40 | 18.0 | 13.7 | 1.9 | 4.5 | 7.3 |

**Table 3.** Parameters and cross-sections ($10^{-17}$ cm$^2$) of the ionization transitions $e + N_2(X^1\Sigma_g^+, v) \rightarrow 2e + N_2^+(B^2\Sigma_u^+, v')$.

| v | $J_{v,v'}$ [eV] | $J_{v,v''}$ [eV] | $\sigma(E=20\text{ eV})$ | $\sigma(E=30\text{ eV})$ | $\sigma(E=50\text{ eV})$ |
|---|---|---|---|---|---|
| 0 | 18.7 | 19.1 | 0.13 | 1.0 | 2.0 |
| 4 | 18.5 | 18.8 | 0.16 | 1.1 | 2.1 |
| 8 | 18.3 | 18.4 | 0.20 | 1.2 | 2.2 |
| 12 | 18.1 | 17.9 | 0.26 | 1.3 | 2.3 |
| 16 | 17.9 | 17.4 | 0.32 | 1.4 | 2.5 |
| 20 | 17.7 | 16.9 | 0.39 | 1.5 | 2.6 |
| 24 | 17.5 | 16.4 | 0.47 | 1.6 | 2.8 |
| 28 | 17.1 | 15.9 | 0.56 | 1.7 | 2.9 |
| 32 | 16.9 | 15.4 | 0.65 | 1.9 | 3.1 |
| 36 | 16.7 | 15.0 | 0.75 | 2.0 | 3.3 |
| 40 | 16.5 | 14.7 | 0.83 | 2.1 | 3.4 |

**Table 4.** Parameters and cross-sections ($10^{-17}$ cm$^2$) of the ionization transitions $e + N_2(A^3\Sigma_u^+, v) \rightarrow 2e + N_2^+(X^2\Sigma_g^+, v')$.
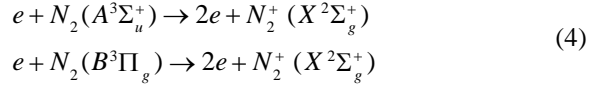
| v | $J_{v,v'}$ [eV] | $J_{v,v''}$ [eV] | $\sigma(E=15\text{ eV})$ | $\sigma(E=25\text{ eV})$ | $\sigma(E=40\text{ eV})$ |
|---|---|---|---|---|---|
| 0 | 9.6 | 11.6 | 1.4 | 3.1 | 4.2 |
| 4 | 8.8 | 12.0 | 1.7 | 3.5 | 4.6 |
| 8 | 8.2 | 12.4 | 2.1 | 4.0 | 5.1 |
| 12 | 7.6 | 12.8 | 2.6 | 4.5 | 5.6 |
| 16 | 7.1 | 13.2 | 3.0 | 5.1 | 6.2 |
| 20 | 6.8 | 13.6 | 3.4 | 5.5 | 6.6 |
| 24 | 6.6 | 14.0 | 3.7 | 5.8 | 6.8 |

**Table 5.** Parameters and cross-sections ($10^{-17}$ cm$^2$) of the ionization transitions $e + N_2(B^3\Pi_g, v) \rightarrow 2e + N_2^+(X^2\Sigma_g^+, v')$.

| v | $J_{v,v'}$ [eV] | $J_{v,v''}$ [eV] | $\sigma(E=15\text{ eV})$ | $\sigma(E=25\text{ eV})$ | $\sigma(E=40\text{ eV})$ |
|---|---|---|---|---|---|
| 0 | 8.2 | 9.0 | 3.0 | 5.3 | 6.6 |
| 4 | 7.9 | 9.8 | 3.5 | 5.8 | 7.1 |
| 8 | 7.6 | 10.1 | 3.9 | 6.3 | 7.5 |
| 12 | 7.3 | 10.3 | 4.4 | 6.9 | 8.1 |
| 16 | 7.0 | 10.5 | 5.0 | 7.5 | 8.7 |
| 20 | 6.7 | 10.7 | 5.3 | 7.8 | 8.9 |
| 24 | 6.4 | 10.8 | 5.3 | 7.9 | 9.0 |

$$e + N_2(A^3\Sigma_u^+) \rightarrow 2e + N_2^+ (X^2\Sigma_g^+)$$
$$e + N_2(B^3\Pi_g) \rightarrow 2e + N_2^+ (X^2\Sigma_g^+) \tag{4}$$

Results of ionization cross-sections, obtained using formula (3) for function $f(x)$, are given in Tables 4 and 5, respectively.

## 3. Atom molecule collision processes

Concerning atom molecule collision processes, after some work about this topic [17–19], we have performed new accurate and detailed quasiclassical calculations, with a more accurate potential energy surface (PES) (BKMP2) [20] than in preceding calculations [21] and with a numerical code [22] rewritten for parallel and distributed computational resources, with the possibility of obtaining translational energy dependent cross-sections for ro-vibrational energy transfer and dissociation. The processes considered are:

– Energy exchange (reactive and non-reactive):
$$M + M_2(v, j) \rightarrow M + M_2(v', j') \tag{5a}$$
– Dissociation:
$$M + M_2(v, j) \rightarrow 3M \tag{4b}$$
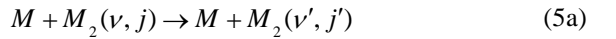
with M = H, D, T. The whole set of ro-vibrational states of each diatom has been obtained by the semiclassical WKB method, including quasibound states (having energy greater than dissociation, classically but not quantally trapped by rotational barrier). Cross-section data having these states as reactants and/or products are fundamental for obtaining recombination rate coefficients [23] and for accurate dissociation treatment. The numerical codes for dynamics as well as all the accessory programmes (determination of ro-vibrational states, trajectory analysis, rate coefficient calculations, recombination rates) have been written entirely in-house [22], and successively parallelized and adapted for intensive distributed calculations on a large scale computational grid.

Particular care has been given to control of numerical error on trajectory integration and optimal time step determination, which are actually of importance for obtaining accurate results with a reasonable amount of computational time. The best strategy for optimal balance between computational load and accuracy of results is, in our experience, to check each step of each trajectory (tj) with a new, more accurate integration, starting from a relatively large initial time step, and progressively reducing it if the test fails. This technique permits accuracy of the order of one erroneously integrated tj in $10^6$, with a mean computational time per tj of the order of twice the time needed for correctly integrating only 90–95% of tjs. This is particularly important for long lasting tjs.

The translational energy varies continuously from $10^{-3}$ to 3 eV, while the density is fixed at 24000 per Å of impact

parameter and eV of translational energy for hydrogen. Stratified sampling is applied. Cross-sections are obtained discretizing the energy axis with 1500 bins in order to have good determinations of thresholds, and smoothing the results with the 'natural smoothing spline' technique, which fits many consecutive spline curves to adjacent pieces of data.

The results for hydrogen are complete, and the database will be published as the fits of cross-sections and rate coefficients have been optimized. For hydrogen isotopes, calculations are at the moment incomplete. Three possibilities could be chosen, due to the favourable circumstance that ratios of masses of the three particles in each combination H-H-H, D-D-D, T-T-T are the same as well as the potential energy surface:

(1) Calculating dynamical data for the whole ladder of ro-vibrational states of the molecule in the two cases of deuterium and tritium (the more expensive and slow solution);

(2) Obtaining approximate results 'scaling' ro-vibrational actions, starting from calculations of H + $H_2$ (computationally rapid, but approximate);

(3) Performing new calculations with unquantized reagent ro-vibrational actions, and then performing pseudo-quantization for both reagents and products, using the appropriate masses and scaled ro-vibrational actions (probably the most efficient solution).

These kinds of calculations have been performed in Ref. [22], with no significant difference from the traditional technique of initially pseudoquantized reagents, but in the best statistical behaviour, due to the use of appropriate weight functions that 'distribute' smoothly reagents and products among quantized states. In this work we have studied the second approximate method, by re-analysing the whole set of trajectories obtained for hydrogen with two new 'filters'. As is well known, classical dynamics are not influenced by the absolute values of masses but only by their ratios (F = $m_D/m_H$ = 2 for deuterium), provided the time is scaled by $\sqrt{F}$ and, obviously, masses are scaled by F. As a consequence, it is easy to show that starting from the definitions of classical diatomic angular momentum and vibrational action:

$$J_r' = \sqrt{F} J_{rH}$$
$$J_v' = \sqrt{F} J_{vH} \tag{5}$$

$$j' = \sqrt{F}(j_H + 1/2)\hbar - 1/2$$
$$v' = \sqrt{F}(v_H + 1/2)h - 1/2 \tag{6}$$

where $j'$, $v'$ are the (deuterium) 'continuous' pseudoquantum numbers corresponding to the dynamics of hydrogen. Of course they are not quantized in general even in the case of pseudoquantized hydrogen numbers, as one can easily see in Fig. 5, where over a lattice of ro-vibrational states of
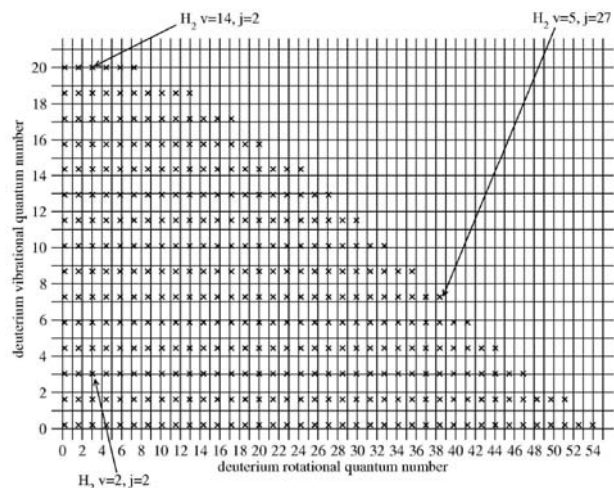


**Figure 5.** Lattice of ro-vibrational states of deuterium (grid) superposed to lattice of hydrogen ro-vibrational states ('x'). Some close correspondences between $H_2$ and $D_2$ states are indicated by arrows, $H_2$ ($v = 2, j = 2$) $\Leftrightarrow$ $D_2$ ($v = 3, j = 3$) and $H_2$ ($v = 14, j = 2$) $\Leftrightarrow$ $D_2$ ($v = 20, j = 3$).

deuterium is shown the modified lattice of hydrogen ro-vibrational actions ('x') after the application of relations (6). Only in some particular cases is there a close coincidence of points representative of different states for deuterium and hydrogen, as for example for ($v = 3, j = 3)_D$ with ($v = 2, j = 2)_H$, or ($v = 20, j = 3)_D$ with ($v = 14, j = 2)_H$.

Concerning products of the dynamics, it is quite easy and essentially not approximate (in the quasiclassical sense) to apply the simple transformations (6), constituting the 'product filter', to final ro-vibrational actions, obtaining the product (continuous) quantum numbers of deuterium, that can easily be pseudoquantized following the standard procedure of the quasiclassical method. The approximation is on the contrary necessary when dealing with reactants, because the calculations on hydrogen have been performed with exactly pseudoquantized $H_2$ states, rarely corresponding to quantum states of $D_2$. In this case we have adopted the procedure of assigning a vibrational weight to each hydrogen trajectory, depending linearly on the 'distance' from the two nearest reactant deuterium vibrational states of the modified H $v$ state, multiplied by a rotational weight obtained in an analogous way. This procedure (the 'reactant filter') is similar to the application of weight functions in quasiclassical calculations, pioneered by Truhlar et al. thirty years ago [24], and also studied in Ref. [22].

In Fig. 6, dissociation cross-sections are shown as a function of translational energy from states ($v = 10, j = 1$), ($v = 15, j = 1$), ($v = 20, j = 0$) of deuterium for the D + $D_2$ collision process. The continuous curves are calculated directly in a quasiclassical manner, while the dashed curves are obtained by filtering the hydrogen calculations as explained before. Essentially, all the results agree within the statistical errors, with good behaviour also in the threshold region. It is worth noting that the three cases shown are quite
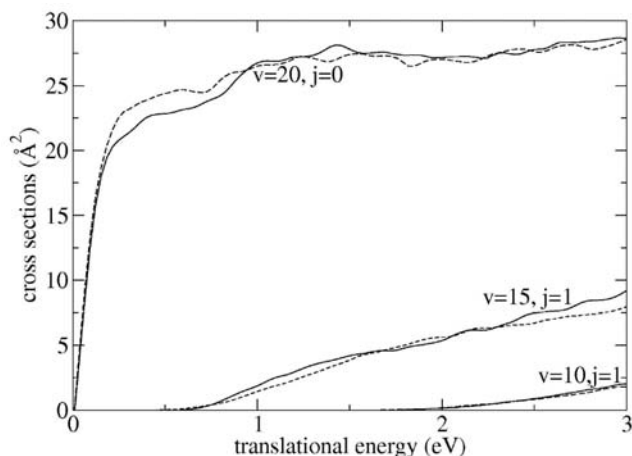
**Figure 6.** Dissociation cross-sections from states indicated for D + $D_2$ ($v$, $j$). Continuous lines: deuterium quasiclassical calculations, dashed lines: results obtained from hydrogen calculations (see text).

different: as visible in Fig. 5, for $v_D = 20$ the vibrational correspondence deuterium–hydrogen is quite good, fairly good for $v_D = 10$ ($\approx v_H = 7$), poor for $v_D = 15$ (between $v_H = 10$ and 11). This is a good confirmation of the reliability of approximate procedure applied to reactants. Other important comparisons concerning both reactants and products can be shown with energy transfer cross-sections, which are also more demanding in terms of computational

resources, because of the high trajectory density (per unit of impact parameter and unit of translational energy) required for accurate and detailed results.

In Fig. 7(a), energy transfer cross-sections for the collision process D + $D_2$ are shown from the initial deuterium state ($v = 20$, $j = 0$) to ($v' = 19$, all $j'$) and ($v' = 12$, all $j'$). As in the preceding figure, continuous lines are calculated results, dashed lines are obtained by filtering hydrogen calculated results: the comparisons appear quite good, even if final deuterium vibrational states are not near any modified hydrogen state (see Fig. 5). Starting from the same initial states shown for dissociation, in Figs 7(b), (c) we show vibrational excitation and de-excitation, respectively, from ($v = 10$, $j = 1$) in Fig. 7(b) to $v' = 12$, $v' = 9$, and from ($v = 15$, $j = 1$) to $v' = 17$ and $v' = 10$ in Fig. 7(c). Also in these cases the agreement is within statistical errors, although none of the final deuterium states is in close correspondence with hydrogen states. Even for low lying deuterium vibrational states the results are comfortable, as can be seen in Figs 7(d) and 8(a) for, respectively ($v = 5$, $j = 1$) to $v' = 2$, 7 and ($v = 1$, $j = 1$) to $v' = 5$, 6, 7.

The problem of this method is clearly visible when one tries to approximate deuterium cross-sections from hydrogen cross-sections that at least partially involve an elastic process for hydrogen, as for the vibrational deactivation: ($v = 1$, $j = 1$) to $v' = 0$, shown in Fig. 8(b). In this case,
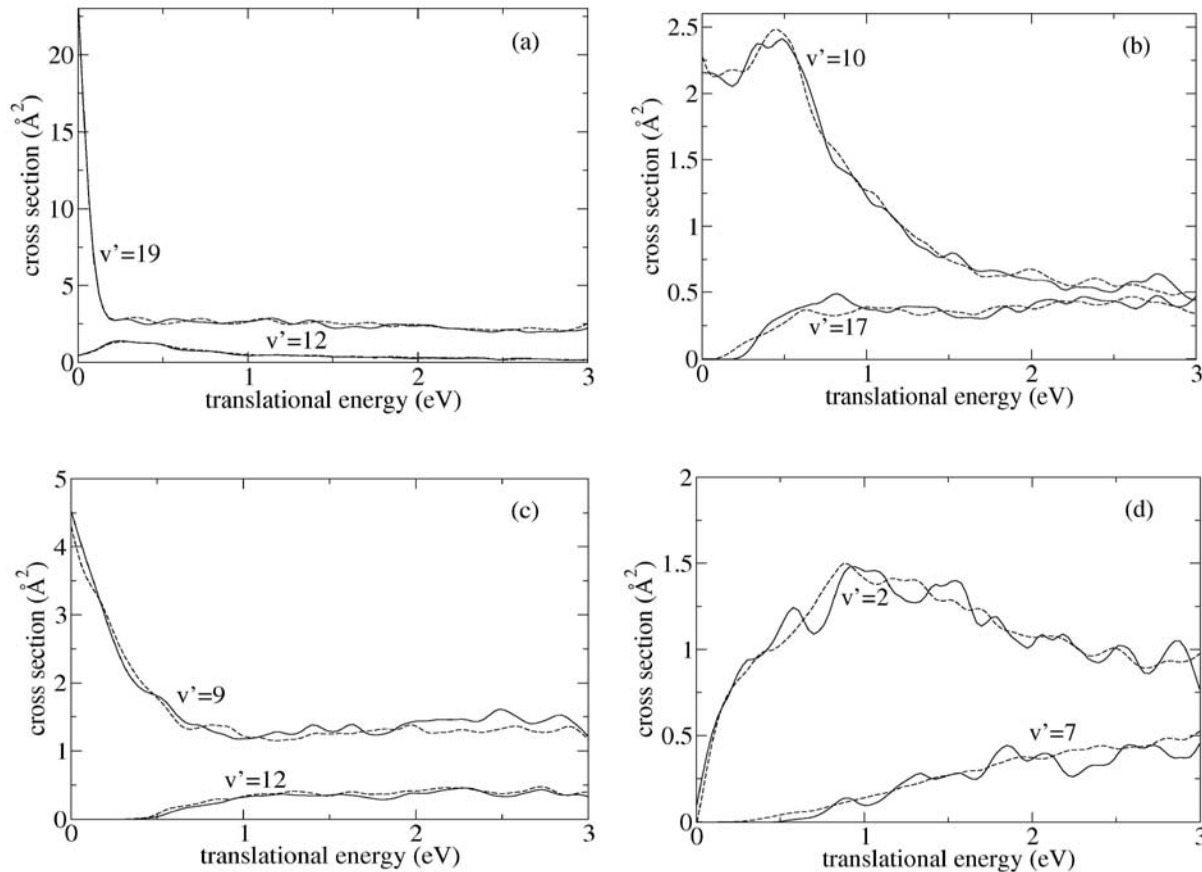


**Figure 7.** Energy transfer cross-sections for the collision process D + $D_2$ ($v$, $j$) → D + $D_2$ ($v'$, $j'$ = all) for $v'$ states indicated. Lines as in Fig. 6. (a) ($v = 20$, $j = 0$); (b) ($v = 15$, $j = 1$); (c) ($v = 10$, $j = 1$); (d) ($v = 5$, $j = 1$).
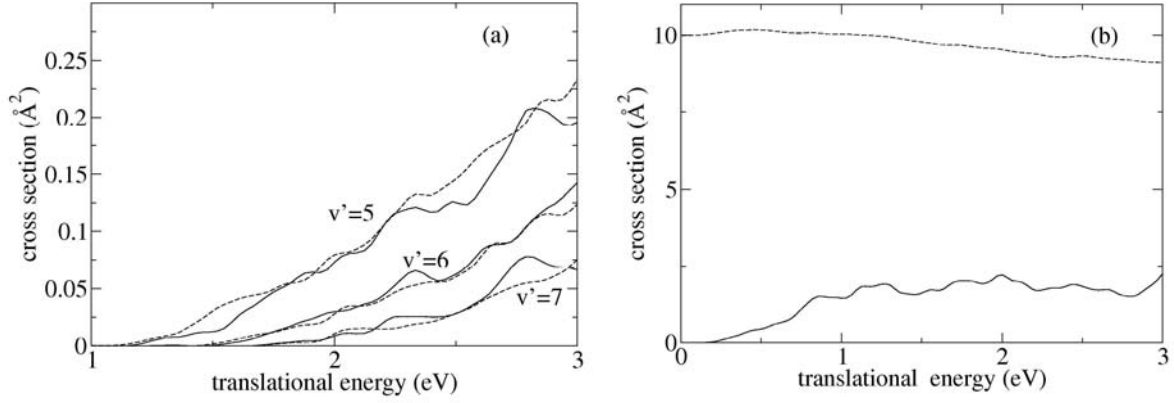
**Figure 8.** Energy transfer cross-sections for the collision process $D + D_2 (v = 1, j = 1) \rightarrow D + D_2 (v', j' = \text{all})$ (a) for $v'$ states indicated and (b) for $(v'= 0, j' = \text{all})$. Lines as in Fig. 6.

as is clear from Fig. 5, hydrogen states involved are $(v = 0, j = 0)_H$, $(v = 0, j = 1)_H$, $(v = 1, j = 0)_H$, $(v = 1, j = 1)_H$, but the final state necessarily involves both $(v = 0, j = 0)_H$, $(v = 0, j = 1)_H$, therefore an elastic unconverged quasiclassical result enters the ro-vibrational approximation, making it totally unuseful, as is shown in Fig. 8(b).

Probably, this problem can be overcome by excluding in some way the elastic part of the calculation, for example considering explicitly also the final rotation $j'$ and filtering out any elastic contribution from non-reactive trajectories.

## 4. Transport properties of H₂ plasma in equilibrium

Transport coefficients (thermal conductivity, viscosity, electrical conductivity) of local thermodynamic equilibrium H₂ plasmas, including atomic excited states, have been calculated for a wide range of pressures, by using the Chapman–Enskog theory (third approximation for the electron component and the first non-vanishing approximation for heavy components) [25].

Saha equations for dissociation and ionization equilibria have been used in order to determine the equilibrium composition of the plasma (H₂, H, H⁺, e); then

the concentration of excited states of atomic hydrogen, H(n), has been calculated through the Boltzmann distribution:

$$n_i = n_T \frac{g_i}{Z(T)} e^{-E_i/k_B T} \tag{7}$$

where $n_i$, $g_i$ and $E_i$ represent the number density, the degeneration and the energy of the i-th H excited state, respectively. $n_T$ is the total number density for atomic hydrogen and $Z(T)$ the corresponding partition function. Excited states up to $n = 12$ have been included in the transport calculation; however, at high pressure (100 atm) the n value has been reduced to 7 on the basis of a very simple cut-off criterion for the partition function, i.e. by considering excited states with a classical Bohr radius not exceeding the interparticle distance [26].

Diffusion, $\Omega^{(1,1)}$, and viscosity type collision integrals, $\Omega^{(2,2)}$, relevant to the interactions involving atomic excited states, have been obtained either through extrapolating procedures (H⁺-H(n), H(n)-H(n) interactions) or by direct integration of transport cross-sections (e-H(n) interaction) [25, 26]. Examples of collision integrals for different interactions are reported in Fig. 9, as a function of $n' = 2 - 1/n^2$, i.e. a modified energy scale.
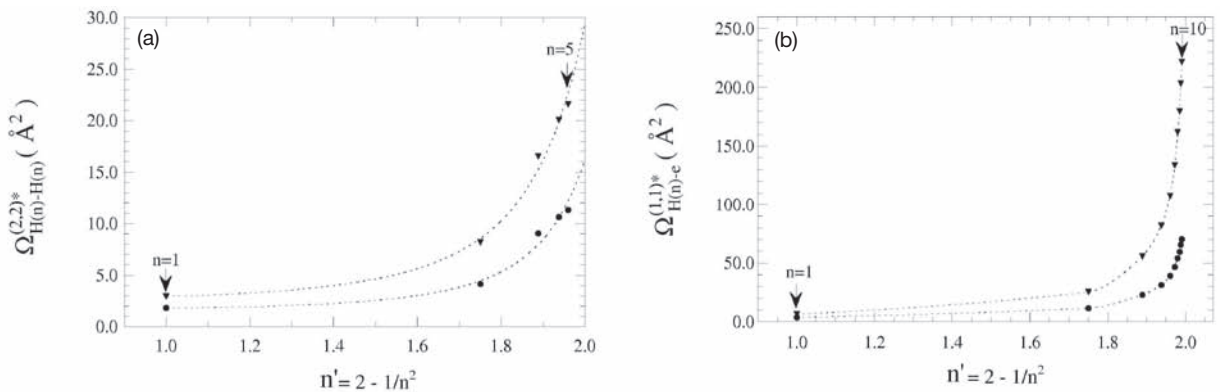


**Figure 9.** (a) Viscosity type collision integrals as a function of n' = (2 − 1/n²), for H(n)-H(n) interactions, at T = 10⁴ (triangles) and 2 × 10⁴ K (circles). Markers represent data of Celiberto et al. [27]. (b) Diffusion type collision integrals as a function of n' = (2 − 1/n²), for e-H(n) interactions, at T = 10⁴ (triangles) and 2 × 10⁴ K (circles), obtained by integration of cross-section data from Ref. [28].
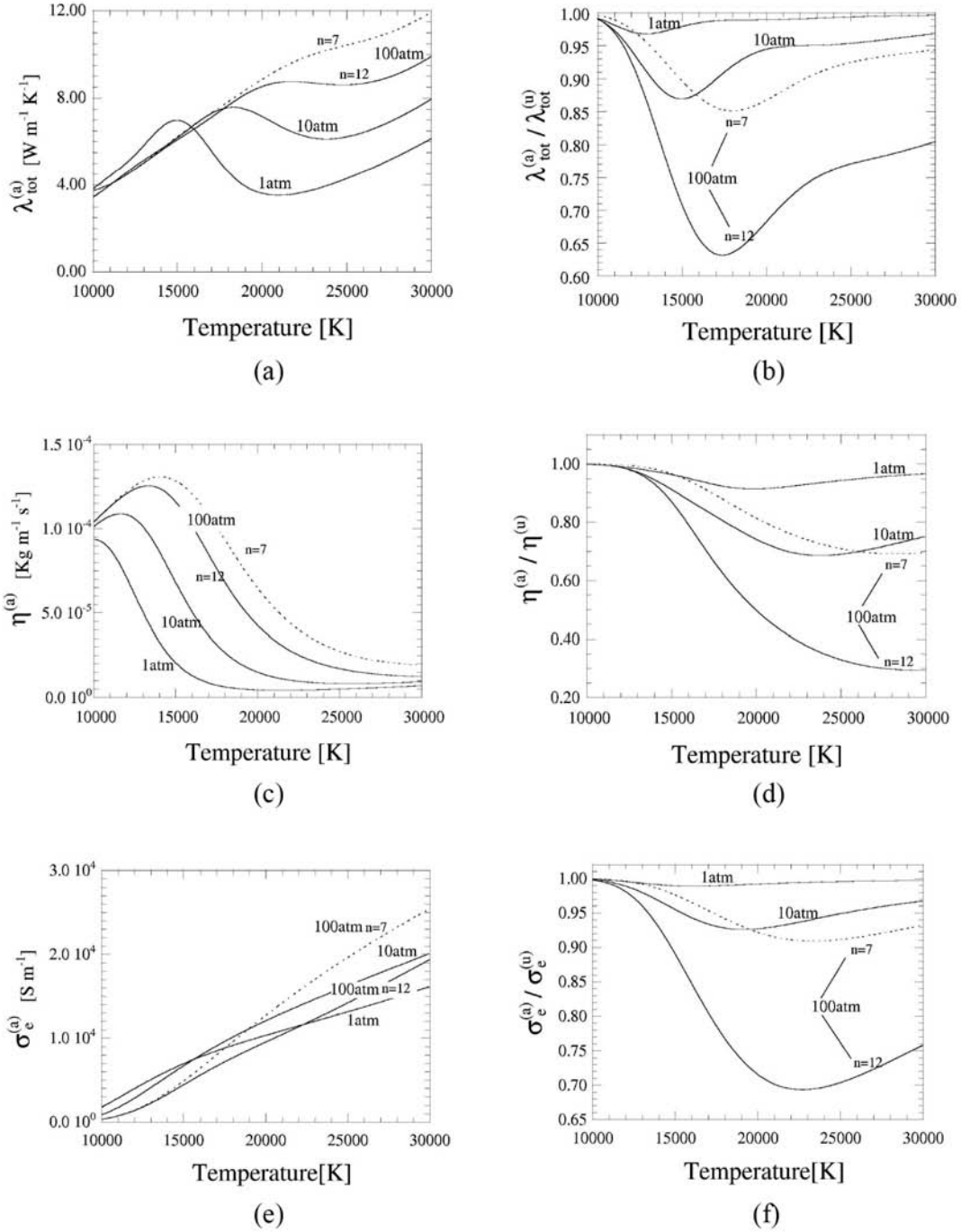
**Figure 10.** Transport coefficient calculated in case (a) (left) and the ratio between case (a) and case (u) (right), as a function of temperature, at different pressures and for different number of atomic levels. (a, b) Total thermal conductivity; (c, d) viscosity; (e, f) electrical conductivity.

Two different approaches have been considered, differing on the set of transport cross-sections used for excited states: in the 'usual' case (indicated by the superscript (u)), collision integrals of excited states are set equal to the ground state ones, while in the 'abnormal' case (superscript (a)) the transport properties calculation includes a complete set of collision integrals for excited states, i.e. collision integrals strongly dependent on the principal quantum number n.

Figures 10(a),(b) report the temperature dependence, for different pressures, of the total thermal conductivity, $\lambda_{tot}^a$,

(resulting from the reactive and translational components) and the corresponding ratio $\lambda_{tot}^a / \lambda_{tot}^u$, respectively. The temperature range considered ($10^4 \leq T \leq 3 \times 10^4$ K) is characterized by a non-negligible concentration of excited states. Inspection of Fig. 10(b) shows that the differences in the ratio strongly increase with the pressure. In fact the pressure increase shifts the ionization equilibrium to higher temperatures, where the electronically excited states start being populated without losing their absolute concentrations. Results obtained at 100 atm, reducing to 7 the maximum value for n, are also presented. As expected, the

51

differences in $\lambda_{tot}^{a}/\lambda_{tot}^{u}$ strongly decrease when reducing the total number of excited states (see the dotted line in Figs 10(a),(b). Similar considerations hold for viscosity (Figs 10(c),(d) and electrical conductivity (Figs 10(e),(f).

These results could open new perspectives in the transport properties under extreme conditions. As an example, the transport cross-sections of electronically excited states can be used to better describe the transport of these species in the divertor plasma, especially in the presence of radiation trapping of Lyman series, when the concentration of excited states can be important [29]. Another application could be in inertial fusion when plasma pressure reaches very high values.

## 5. H₂ plasma kinetics: Negative ion source modelling

Theoretical and experimental investigation on volume plasma sources is oriented to the optimization of device operative conditions in order to increase the negative ion production, driven by the dissociative attachment of low energy electrons to highly vibrationally excited molecules, $H_2(v)$. Modelling of non-equilibrium conditions, established in the plasma, requires a state to state kinetic approach, including excited (vibrationally and electronically) states of the $H_2$ molecule and coupling of the heavy particle and electron kinetics. In fact, the temporal evolution of heavy particle density, described by a set of master equations, depends on the rate coefficients of electron processes, i.e. on the electron energy distribution function (EEDF) variations, and the EEDF, obtained solving the Boltzmann equation, is strongly connected to the heavy particle distribution.

Different models, all applying the same state to state philosophy, have been implemented in order to rationalize experiments for two different kinds of plasma sources: multicusp ion source and RF discharge.

### 5.1. Zero dimensional model of multicusp ion sources

A new approach [30] to couple heavy particle and electron kinetics has been implemented, which shows a higher self-consistent character. In this scheme the electron energy range is discretized and represented by a set of intervals. At each interval, characterized by its mean energy, a different 'kind' of electron is associated, then these 'representative electrons' behave as the vibrationally or electronically excited levels of the hydrogen molecule or atom. It means that also for electrons we can write a state to state set of kinetic equations and the rate coefficients are no more global, i.e. referred to the overall EEDF, but to an electron with a specific energy.

The numerical scheme resulting from this approach has been used to build a zero dimensional model of multicusp ion sources in the driver region. Figure 11(a) shows the stationary vibrational distribution (VDF) of $H_2$, as a function of the vibrational energy, for different pressures: increasing the filling pressure, the number density of the vibrational levels increases, affecting more strongly the low vibrational levels. A pressure variation also influences the behaviour of the electron energy distribution function. Indeed, it acts on the plasma potential that governs the electron wall loss. In the present calulations the plasma potential is calculated self-consistently at each time step, on the basis of the plasma status: in particular it is set, as a first approximation, equal to the electron temperature calculated from the mean energy of the distribution. Table 6 reports the total electron density and electron temperature as a function of the filling pressure: $T_e$ decreases when the pressure increases, thus the plasma potential also decreases, the discharge current and the voltage being kept constant. As a consequence, the number of low energy electrons increases because they are not lost on the walls (see the EEDF reported in Fig. 11(b).
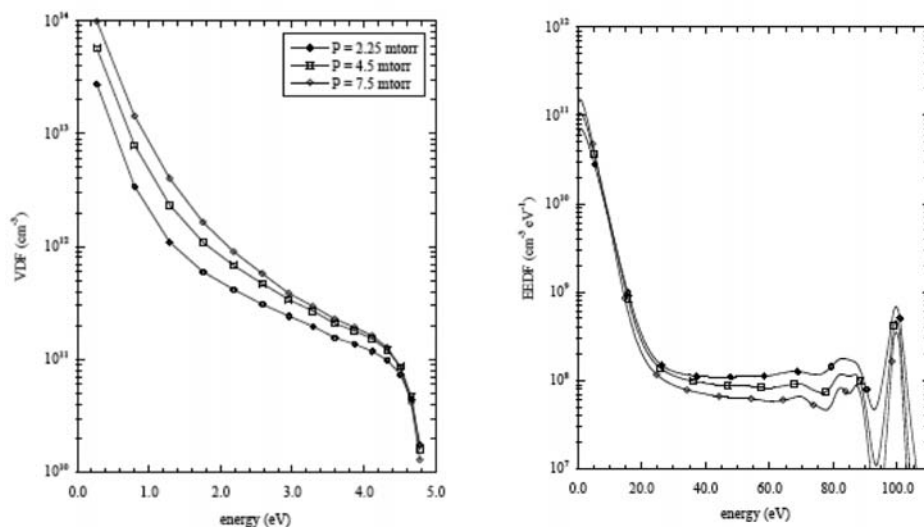


**Figure 11.** $H_2$ VDF (a) and EEDF (b) for different pressures (T = 500 K; discharge current = 10 A; discharge voltage = 100 V) in multicusp ion source simulation.
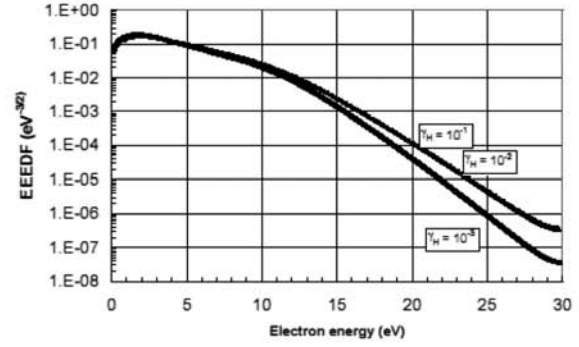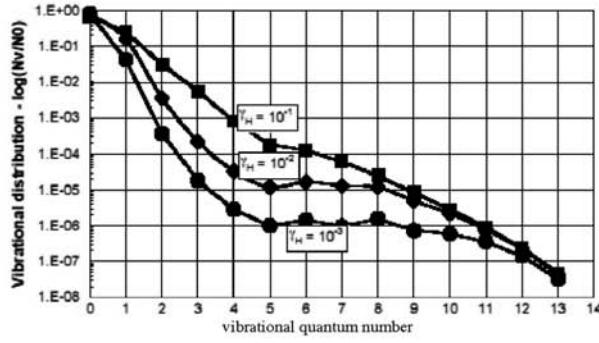
**Figure 12.** $H_2$ VDF (a) and EEDF (b) for different $\gamma_H$ values (pressure = 1 torr; injected power density = 0.5 Wcm$^{-3}$) in microwave discharge simulation.

**Table 6.** Electron temperature as a function of pressure.

| Pressure (mtorr) | Electron density (cm$^{-3}$) | Electron temperature (eV) |
|---|---|---|
| 2.25 | $3.7777 \times 10^{11}$ | 3.84 |
| 4.5 | $5.1126 \times 10^{11}$ | 2.91 |
| 7.5 | $6.2929 \times 10^{11}$ | 2.35 |

### 5.2. Collisional–radiative model of microwave discharge

A detailed kinetic model describing radiofrequency plasmas has been implemented, including submodels for non-equilibrium kinetics of excited states and a quasi-homogeneous plasma transport model for energy and species losses at reactor walls, strongly coupled through radiative and collisional processes [31, 32]. It is assumed that charged and electronically excited species fully recombine/de-excite at the quartz wall, while the heterogeneous vibrational de-activation processes are neglected.

The numerical simulation allows the analysis and interpretation, in terms of elementary processes, of experimental $H_2$ vibrational and rotational temperatures, measured by cars spectroscopy in radiofrequency inductive plasmas [33]. In particular the theoretical vibrational temperature of molecular hydrogen, defined on the basis of the $v = 1$ level to $v = 0$ level population, has been determined as a function of the recombination factor $\gamma_H$, taken as an adjustable parameter, and compared with experimental values (see Table 7).

Increasing the recombination factor reflects on the energy distributions in the discharge, in particular increasing

**Table 7.** Vibrational temperature for different $\gamma$ values for two different RF plasma conditions, compared with experimental values.

| | $T_{vib}$ | | | $T_{exp}$ |
|---|---|---|---|---|
| | $\gamma = 10^{-3}$ | $10^{-2}$ | $10^{-1}$ | |
| Case (a)* | 2000 | 3900 | 6100 | $4000 \pm 500$ |
| Case (b)** | 1250 | 1700 | 2700 | $3200 \pm 250$ |

\* P = 1 torr; injected power density = 0.5 W cm$^{-3}$.

\*\* P = 6 torr; injected power density = 2.0 W cm$^{-3}$.

both the vibrational temperature and the density associated with the plateau of the vibrational distribution (Fig. 12(a)); on the other hand, increasing the $\gamma_H$ strongly affects the EEDF (Fig. 12(b)).

Note that the electron density and the negative ion concentration for the experimental conditions of Table 7 range respectively in the interval $10^{16}$– $6 \times 10^{16}$ m$^{-3}$ and $10^{14}$–$10^{15}$ m$^{-3}$ (see Ref. [31]).

### 5.3. PIC/MCC model of RF parallel plate discharges

A 1-D in space, 2-D in velocity self-consistent particle/continuum model, coupling a particle description of plasma phase with a state to state kinetics of gas phase, has been implemented for the simulation of capacitively coupled RF discharge plasmas in hydrogen [34, 35]. In particular a particle in the cell/MonteCarlo method has been used for the transport equation, while the diffusion/reaction kinetics solved using a grid discretized technique.

The model has been applied to a discharge in pure hydrogen, produced into a parallel plate high frequency reactor (pressure = 1 torr, RF voltage = 300 V, mean electron density in space = $3.7 \times 10^{14}$ m$^{-3}$, electron temperature $T_e = 2.7$ eV, plasma potential in the centre of the discharge = 107 V). In Fig. 13, plasma phase quantities in typical conditions for the probability parameters ($\gamma_v = 0.05$, $\gamma_H = 0.2$) are shown. In particular the number density (Fig. 13(a)) shows a slight electronegative behaviour in the centre of the discharge, as shown by the separation of the positive ion and electron density in the bulk plasma. The EEDF (Fig. 13(b)) significantly deviates from the Maxwell–Boltzmann law, showing the necessity of including a kinetic level description of the electron transport.

Finally, Table 8 reports the results obtained for H$^-$, H and electron density varying the vibrational level on which H atoms recombine at the reactor walls. It can be noticed that the recombination level has a significant effect on H$^-$ density, while the other quantities are not considerably affected. A recent paper [36] confirms the results of Table 8 for multicusp plasma sources. In this case the negative ion concentration increases from $4 \times 10^{15}$ m$^{-3}$, when the recombination of atomic hydrogen pumps only the $v = 0$ level, to
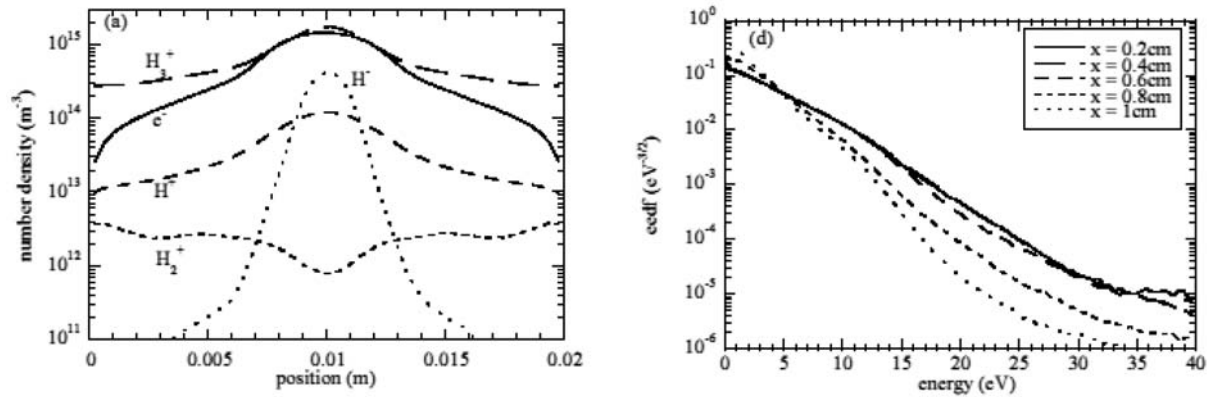
**Figure 13.** Number density as a function of position (a) and EEDF as a function of energy (b) in typical conditions for the probability parameters ($\gamma_v = 0.05$, $\gamma_H = 0.2$) in RF parallel plate discharge simulation.

**Table 8.** H⁻, H and electron density for different choice of the vibrational level for $H_2$ molecules formed in the recombination process (absolute number density of $H_2 = 3.2 \times 10^{22}$ m⁻³).

| Recombination level | Number density [m⁻³] | | |
|---|---|---|---|
| | H⁻ | H | e |
| V = 0 | $3 \times 10^{14}$ | $7.3 \times 10^{18}$ | $1.15 \times 10^{15}$ |
| V = 7 | $5.72 \times 10^{14}$ | $7.4 \times 10^{18}$ | $1.18 \times 10^{15}$ |
| V = 14 | $6 \times 10^{14}$ | $7.4 \times 10^{18}$ | $1.18 \times 10^{15}$ |

$10^{16}$ m⁻³, when the recombination is spread with equal probability over all vibrational levels.

## 6. Conclusions

In the present paper we have reported recent efforts made by our group on the calculation of elementary processes, transport and kinetics of atomic and molecular plasmas for different applications. The atomic data (excitation, dissociation, ionization and transport cross-sections) can be directly used in the modelling of divertor plasmas and negative ion sources, enriching the literature on the subject [37]. Concerning negative ion source modelling we can say that only the multicusp ion sources consider pressure conditions important for fusion research. On the other hand, the considered pressures for microwave discharges and RF parallel plate reactors are too high for the ITER project. However, the obtained results are in any case useful for understanding the kinetics of negative ion production.

## References

[1] CAPITELLI, M., CELIBERTO, R., CACCIATORE, M., in Advances in Atomic, Molecular and Optical Physics, M. Inokuti, Ed., Academic Press, New York (1994) 321.

[2] DEVOTO, R.S., J. Plasma Physics **2** (1968) 617.

[3] MURPHY, T.B., Plasma Chemistry and Plasma Processing **20** (2000) 279.

[4] CELIBERTO, R., et al., At. Data Nucl. Data Tables **77** (2001) 161.

[5] LARICCHIUTA, A., CELIBERTO, R., JANEV, R.K., Phys. Rev. A **69** (2004) 022706.

[6] annarita.laricchiuta@ba.imip.cnr.it.

[7] REDMON, M.J., GARRETT, B.C., REDMON, L.T., MCCURDY, C.W., Phys. Rev. A **32** (1985) 3354.

[8] CELIBERTO, R., RESCIGNO, T. N., Phys. Rev. A **47** (1993) 1939.

[9] FANTZ, U., HEGER, B., WÜNDERLICH, D., Plasma Physics Controlled Fusion **43** (2001) 1.

[10] CAPITELLI, M., LARICCHIUTA, A., CELIBERTO, R., KOSARIM, A.V., SMIRNOV, B.M., 24th International Symposium on Rarefied Gas Dynamics (RGD), Monopoli (Bari), Italy, 10–16 July 2004, Editor M. Capitelli, AIP Conference Proceedings **762** (2005) 910.

[11] KOSARIM, A.V., et al., Chem. Phys. Lett. **414** (2005) 215.

[12] SMIRNOV, B.M., Excited Atoms and Ions in Plasma (Atomizdat, Moscow, 1974; in Russian).

[13] COLLIN, J.E., Can. J. Chem. **40** (1962) 2172.

[14] GILMORE, F.R., LAHER, R.P., ESPY, P.J., J. Phys. Chem. Ref. Data **21** (1992) 1005.

[15] MAERK, T.D., J. Chem. Phys. **63** (1975) 3731.

[16] VAN ZYL, B., PENDLETON Jr., W., J. Geophys. Res. **100** (1995) 23755.

[17] ESPOSITO, F., GORSE, C., CAPITELLI, M., Chem. Phys. Lett. **303** (1999) 636.

[18] ESPOSITO, F., CAPITELLI, M., GORSE, C., Chem. Phys. **257** (2000) 193.

[19] ESPOSITO, F., CAPITELLI, M., GORSE, C., Chem. Phys. Lett. **364** (2002) 180.

[20] BOOTHROYD, A.I., KEOGH, W.J., MARTIN, P.G., PETERSON, M.R., J. Chem. Phys. **104** (1996) 7139.

[21] ESPOSITO, F., CAPITELLI, M., Atomic and Plasma–Material Interaction Data for Fusion **9** (2001) 65.

[22] ESPOSITO, F., PhD Thesis, Department of Chemistry, University of Bari (1999).

[23] ROBERTS, R.E., BERNSTEIN, R.B., CURTISS, C.F., J. Chem. Phys. **50** (1969) 5163.

[24] TRUHLAR, D.G., REID, B.P., ZURAWSKI, D.E., GRAY, J.C., J. Phys. Chem. **85** (1981) 786.

[25] CAPITELLI, M., et al., Phys. Rev. E **69** (2004) 026412.

[26] CAPITELLI, M., et al., Phys. Rev. E **66** (2002) 016403/1.

[27] CELIBERTO, R., LAMANNA, U.T., CAPITELLI, M., Phys. Rev. A **58** (1998) 2106.

[28] IGNJATOVIC, L., MIHAJLOV, A.A., Contributions to Plasma Physics **37** (1997) 309.

[29] KOTOV, V., et al., 10th International Workshop on Plasma Edge Theory in Fusion Devices, 17–19 October 2005, Forschungszentrum Jülich, Germany, Book of Abstracts, paper O10.

[30] PAGANO, D., GORSE, C., CAPITELLI, 24th International Symposium on Rarefied Gas Dynamics (RGD), Monopoli (Bari), Italy, 10–16 July 2004, Editor M. Capitelli, AIP Conference Proceedings **762** (2005) 1151.

[31] HASSOUNI, K., et al., Physics of Plasmas **12** (2005) 00000-1.

[32] HASSOUNI, K., GICQUEL, A., CAPITELLI, M., LOUREIRO, J., Plasma Source Science and Technology **8** (1999) 494.

[33] SHAKHATOV, V.A., et al., Physics of Plasmas **12** (2005) 23504-1.

[34] DIOMEDE, P., LONGO, S., CAPITELLI, M., 24th International Symposium on Rarefied Gas Dynamics (RGD), Monopoli (Bari), Italy, 10–16 July 2004, Editor M. Capitelli, AIP Conference Proceedings **762** (2005) 1157.

[35] DIOMEDE, P., LONGO, S., CAPITELLI, M., European Physics J. AP **26** (2005) 177.

[36] PAGANO, D., GORSE, C., CAPITELLI, Rev. Sci. Instrum. (2006). In press.

[37] JANEV, R.K., REITER, D., SAMM, U., Collision Processes in Low-Temperature Hydrogen Plasmas, Forschungszentrum Jülich, Germany, 2003.

# Effective rate coefficients for molecular processes of hydrogen and hydrocarbons in edge plasmas

*U. Fantz*[*], *D. Wünderlich*[*]

Lehrstuhl für Experimentelle Plasmaphysik, Universität Augsburg, D-86135 Augsburg, Germany

## Abstract

Effective rate coefficients for molecular processes in edge plasmas are calculated in a wide parameter range of electron densities and temperatures on the basis of the latest available cross-sections and rate coefficients for the individual reactions. In case of hydrogen molecules and the isotopomeres a vibrationally resolved molecular database with Franck–Condon factors, transition probabilities and radiative lifetimes are generated. An improved collisional radiative model for molecular and atomic hydrogen is introduced and used to calculate effective rate coefficients with and without taking into account vibrational population in the ground state of the molecule. In case of hydrocarbons, a flexible dissociation model is constructed to obtain effective rate coefficients and particle densities for different dissociation chains.

## 1. Introduction

Hydrogen and hydrocarbon molecules are one of the most dominant molecular species in edge plasmas of fusion devices [1–3]. The recombination of hydrogen particles on surfaces leads to the formation of hydrogen molecules, whereas hydrocarbons are released from carbon (graphite) surfaces due to the chemical erosion process. The molecules penetrate into the plasma and can undergo a variety of reactions: vibrational excitation, dissociation, ionization, recombination, charge exchange — to name some of them. The wide parameter range in electron density and electron temperature in which edge plasmas can operate requires a description of plasma processes by effective rate coefficients [3]. Calculations of effective rate coefficients are either based on collisional radiative (CR) models or on dissociation models or on a combination of both.

For calculation of effective rate coefficients for hydrogen molecules, CR modelling is essential, taking into account the vibrational population of the particles in the ground state. Due to an energy distance of the vibrational levels of approximately 0.4 eV, threshold energies can be reduced drastically for excitation, ionization and dissociation processes. In addition, radiative transitions among the vibrational levels are forbidden, resulting in long lifetimes, which is of particular importance for particle transport calculations [4]. Molecular hydrogen and its ion are directly coupled with atomic hydrogen by dissociation and recombination. Thus, calculations of effective rate coefficients for atomic hydrogen require a coupling to the molecular species.

In the case of hydrocarbons, priority is given to effective dissociation and ionization rate coefficients, and identification of dominant dissociation chains, which in turn require dissociation models. Of course, particle transport is relevant for all radicals. However, underlying principles in dissociation processes can be studied best in clear structured dissociation models which balance formation and destruction rates.

## 2. Transitions of diatomic molecules

The presence of vibrational and rotational degrees of freedom in a molecule leads to a manifold of energy levels with different energy distances. For diatomic molecules vibrational and rotational levels are tightly structured. In a first approach, the vibrational levels of each electronic state should be included in models for calculations of effective rate coefficients. A further starting point is the diagnostic of molecules. In diatomic molecules, vibrational bands coupled with electronic transitions are easily accessible by optical emission spectroscopy. Therefore, vibrationally resolved molecular data are needed, in particular for molecular hydrogen (and its isotopomeres which are of special relevance in fusion plasmas) and diatomic radicals of hydrocarbons. However, up to now the database is scarce.

In order to generate a database for the fundamental data of diatomic molecules the computer code TraDiMo

---
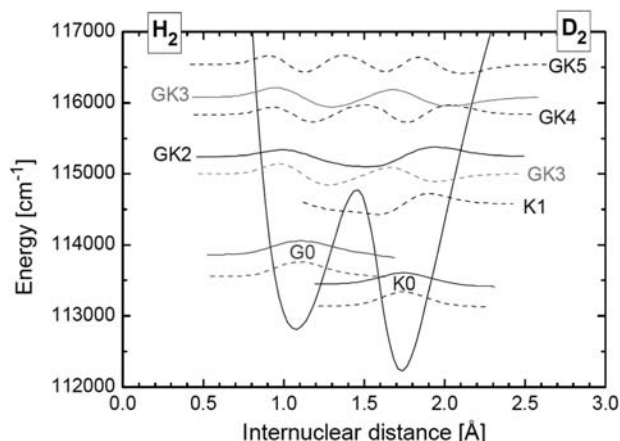
**Figure 1.** Potential curve of the electronic state GK $^1\Sigma_g^+$ of $H_2$ with the vibrational wave functions for $H_2$ (full lines) and for $D_2$ (dashed lines).

(Transitions of Diatomic Molecules) was developed. TraDiMo solves the Schrödinger equation using Born-Oppenheimer potential curves, reduced masses and electronic transition dipole moments, providing vibrational eigenvalues, Franck–Condon factors (FCFs) and vibrationally resolved transition probabilities. One of the huge advantages of TraDiMo is the applicability to bound-bound and bound-free transitions. Double minima potential curves are treated as well. Details of the program and applications to low temperature plasmas, in particular for analysing the continuum radiation of hydrogen molecules (a $^3\Sigma_g^+$ – b $^3\Sigma_u^+$ transition), are given in Ref. [5].

For hydrogen molecules an almost complete input database was compiled from literature for electronic levels up to the quantum number n = 4 (in the united atom approximation) in the singlet and triplet system. Vibrational energy levels, FCSs and vibrationally resolved transition probabilities for $H_2$, $D_2$, $T_2$, HD, HT and DT are calculated. The complete data set is already published in an IAEA report [6] and is available at http://www-amdis.iaea.org.

Figure 1 shows the GK $^1\Sigma_g^+$ state in the singlet system of molecular hydrogen as an example of a double minima potential curve. The vibrational eigenvalues may alter between the two minima. The solution of the Schrödinger equation yields the vibrational wavefunctions and eigenvalues, which are plotted for hydrogen (full lines) and deuterium (dashed lines) in Fig. 1. The notation of the vibrational eigenvalues according the vibrational quantum number is assigned. Due to the higher mass of deuterium the vibrational levels are energetically closer, resulting in this case in two eigenvalues in the right part of the potential curve. As a consequence, corresponding FCFs will be quite different for these vibrational quantum numbers.

With the knowledge of FCSs for electronic transitions, a vibrational population of one electronic state can be projected into another electronic state applying the Franck–Condon principle. Such a projection requires that the inter-



**Figure 2.** Relative vibrational population in the d $^3\Pi_u$ and B $^1\Sigma_u^+$ state, taking into account Franck–Condon factors only or Franck–Condon factors and vibrational transition probabilities. The vibrational population in the ground state ($T_{vib}$) is used as parameter in the calculation.

nuclear distance does not change in the underlying process, which is valid for radiative transitions and can be applied to electron impact processes. Of particular 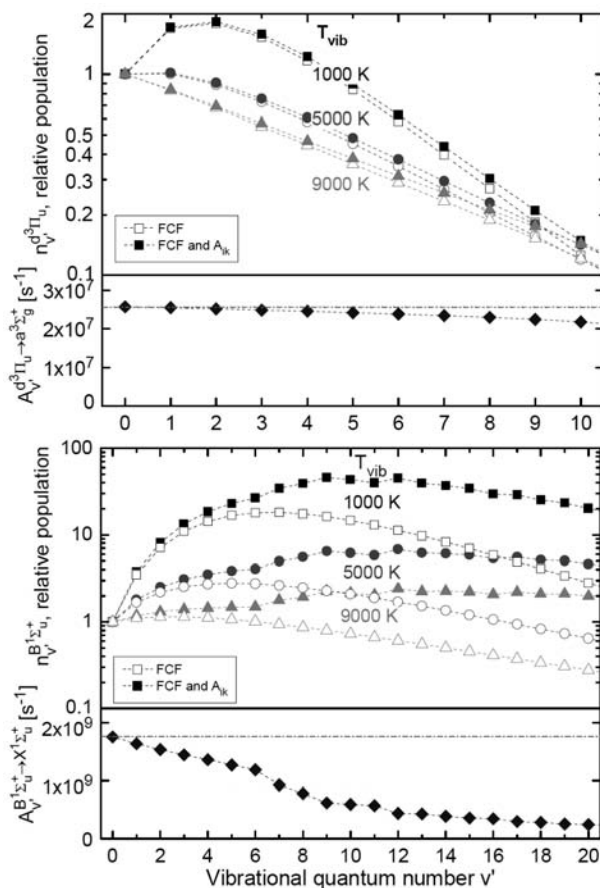interest is the projection of the vibrational population in the ground state into electronically excited states by electron impact excitation representing one of the dominant excitation channels. If the vibrational population in the ground state is unknown, a vibrational population according to a vibrational temperature ($T_{vib}$) can be used as first assumption instead. Figure 2 shows examples of a triplet state (d $^3\Pi_u$) and a singlet state (B $^1\Sigma_u^+$) of hydrogen (full symbols). This method can be improved by considering dominant de-excitation processes for the vibrational levels in the excited state, namely the radiative decay and thus the corresponding vibrationally resolved transition probabilities ($A_{ik}$), as illustrated in Fig. 2. The vibrational population increases for decreasing transition probabilities.

Vibrationally resolved transition probabilities are calculated for optically allowed transitions for which electronic transition dipole moments are available [6]. In a next step, vibrationally resolved radiative lifetimes are calculated, given by the reciprocal value over the sum of all possible transitions into lower electronic states. Finally,

effective radiative lifetimes for electronic states are obtained, assuming that the vibrational population in the excited state is given by the Franck–Condon projection from a ground state population ($T_{vib}$ = 5000 K for $H_2$).

These calculations form the basis for an improvement of the CR model for molecular hydrogen. Calculations are also carried out for transitions of $C_2$ and CH, CD and CT, which are accessible by emission spectroscopy.

## 3. Collisional radiative model for $H_2$ and H

A general introduction in CR models for diatomic molecules like hydrogen is given in Ref. [7]. One of the first CR models for $H_2$ and H was established by Sawada [8] and was soon extended [4]. Details of the model and further improvements are described in Ref. [9], which also gives some applications. The manifold of energy levels in molecular hydrogen and its coupling to atomic hydrogen requires the presence and the collection of a large amount of transition probabilities, cross-sections or rate coefficients for population and de-population processes. Rate coefficients are based on a Maxwell distribution, which is justified by the high ionization degree in edge plasmas (approx. 0.5).

Regarding the molecule, the two multiplet systems (singlet and triplet) are treated separately. The ground state is vibrationally resolved (15 levels for $H_2$). The n = 2 states (in the united atom approximation) are split up in their electronic levels. Due to a lack of atomic and molecular data, approximations and scaling laws have been used. Common problems are discrepancies in the value of cross-sections (rate coefficients) found in literature, which are in the range of an order of magnitude. As a consequence, a crucial selection of data sources has to be done. In addition, data have to be exchanged when the CR model will be applied to isotopes, being of particular importance for vibrationally resolved data.

### 3.1. Vibrational population

The CR model calculates self-consistently the vibrational population in the ground state, taking into account five dominant processes: electron impact excitation and de-excitation, dissociation via the repulsive state b $^3\Sigma_u^+$, ion conversion, dissociative attachment and excitation in electronically excited states followed by spontaneous emission [10]. In order to obtain isotope relations, the corresponding data in the model was exchanged from $H_2$ to $D_2$. As a result, the isotopes show similar populations in their vibrational quantum numbers as shown in Fig. 3. The vibrational population depends on $T_e$ and can be strongly influenced by heavy particle collisions or collisions with surfaces which are both neglected here. The results are in very good agreement with the measurements of vibrational populations [10] for the first four to five vibrational quantum numbers. In addition, it turns out that the population of these first vibra-
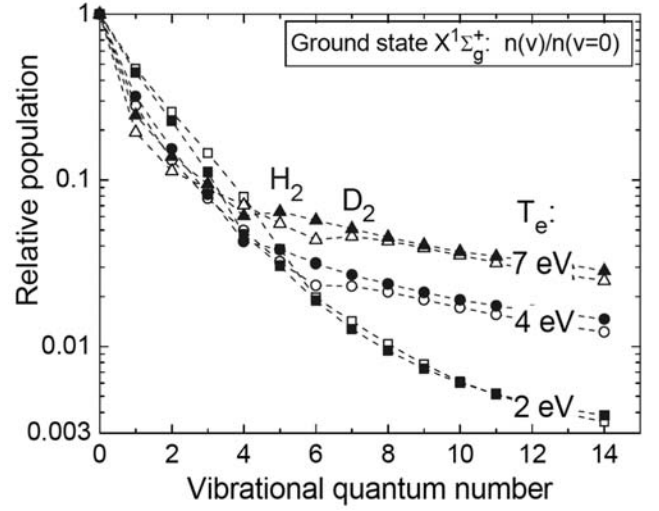


**Figure 3.** Relative vibrational population in the ground state X $^1\Sigma_g^+$ of $H_2$ (full symbols) and $D_2$ (open symbols) calculated with the CR model for three electron temperatures.
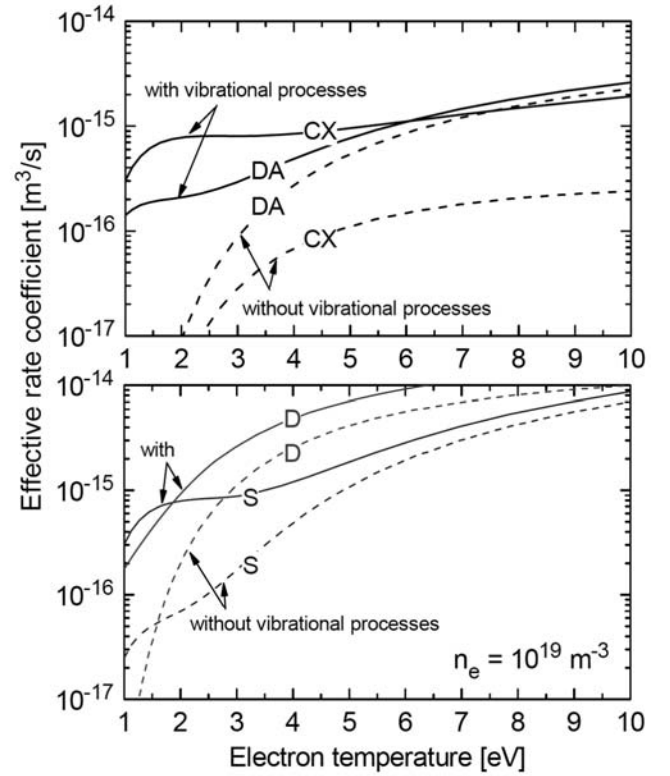


**Figure 4.** Effective rate coefficients for charge exchange (CX), dissociative attachment (DA), dissociation (D) and ionization (S) with and without considering vibrational population in the ground state of $H_2$ [11].

tional levels is well characterized by a vibrational temperature being typically around 5000 K in divertor edge plasmas.

Typical results of such models are effective rate coefficients, which depend not only on $T_e$, but also on $n_e$ and the vibrational population in the ground state [11]. The importance of the vibrational population on some effective rate coefficients can be seen in Fig. 4. Especially for low $T_e$, the enhancement of rate coefficients by vibrational population can exceed one order of magnitude.
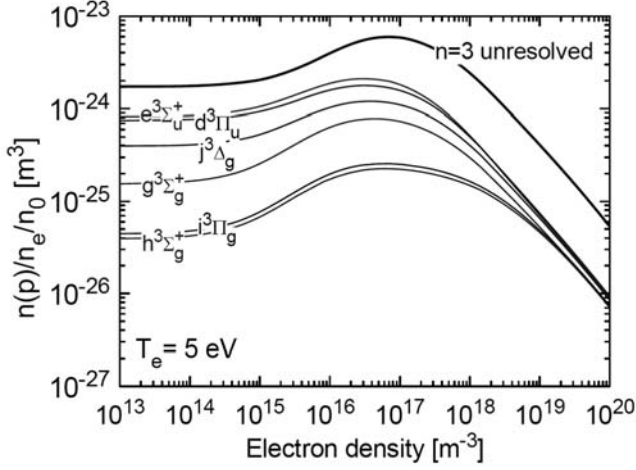
**Figure 5.** Reduced population densities of electronically excited states in the triplet system of $H_2$ with and without resolving the electronic structure in the main quantum number $n = 3$.

## 3.2. Population in electronically excited states

CR modelling should be validated by experimental data. For that purpose, spectroscopic measurements are carried out typically in laboratory plasmas with well defined plasma parameters which are known from other diagnostic techniques. In the visible spectral range several transitions from $n = 3$ to $n = 2$ are accessible. For a comparison of measured population densities with calculated ones the $n = 3$ state must be electronically resolved in the model. Since the largest energy gap among the six levels in each multiplet system is $\approx 0.6$ eV, a population according the statistical weights is assumed often. On the other hand, data required to resolve the states has become available. First results are shown in Fig. 5 for the resolved case and are compared with the $n = 3$ unresolved resolution where the individual statistical weights have to be taken into account for a direct comparison of the levels. Very first experimentally obtained population densities for three of these six levels are in good agreement with $n = 3$ resolved calculations. However, it should be kept in mind that the choice and availability of underlying molecular data play a very crucial role for such calculations.

In a next step the vibrational structure of electronically excited states was resolved. In Fig. 6 relative vibrational populations in electronically excited states are plotted assuming a vibrational temperature in the ground state. The results are compared with the simplified excitation and de-excitation processes as discussed in Section 2 (Fig. 2). Applying the full CR model, populations in electronically excited states change drastically by processes like pre dissociation, auto-ionisation, cascading or quenching which demonstrates the importance of a full treatment of vibrational levels.

## 3.3. Ionization, dissociation and recombination

Effective ionization and dissociation rate coefficients for the hydrogen molecule are already discussed in
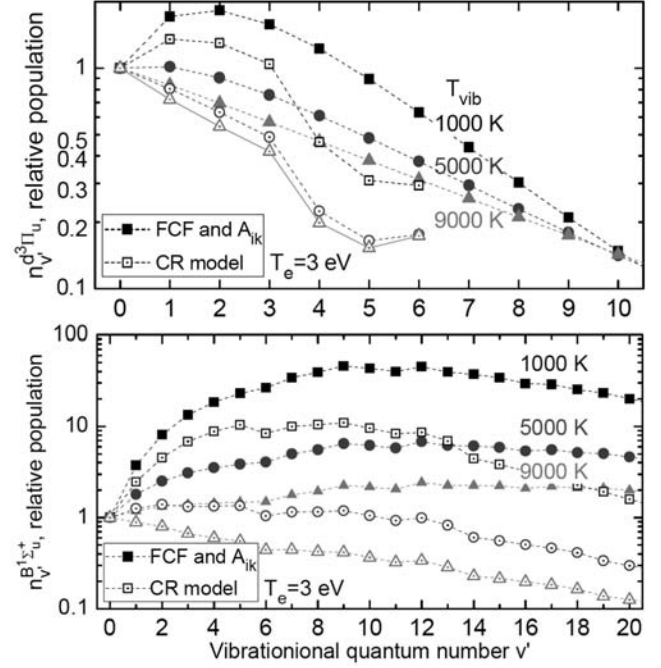


**Figure 6.** Relative vibrational population in the d $^3\Pi_u$ and B $^1\Sigma_u^+$ state, taking into account the Franck–Condon and vibrational transition or using the CR model. The vibrational population in the ground state ($T_{vib}$) is used as parameter in the calculation.
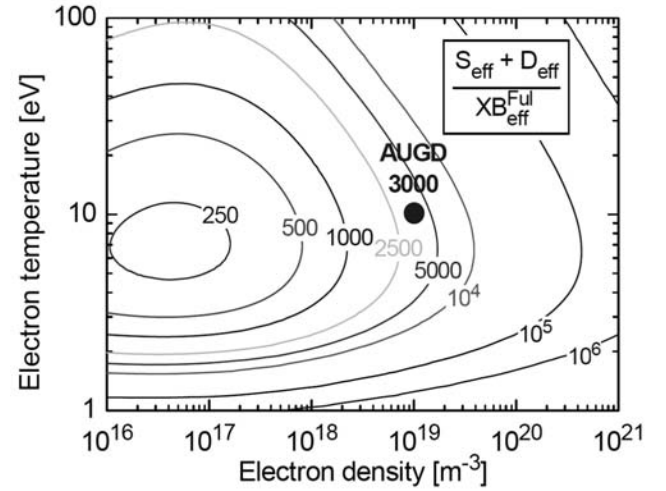


**Figure 7.** Destructions events (ionization and dissociation) per emitted Fulcher photon of $H_2$.

Section 3.1. However, a further and very important parameter for the determination of particle fluxes is the (inverse) photon efficiency. The (inverse) photon efficiency describes the destruction events per emitted photon and is calculated by CR models. In case of molecular hydrogen the measured Fulcher photon flux is correlated with the molecular particle flux by the quantity $(S_{eff} + D_{eff})/XB_{Ful}$ [11]. Again, calculated values have to be validated by experiments which were done for a small parameter range in the divertor region of ASDEX upgrade (AUGD) [12]. Results of calculations and the measured data point are shown in Fig. 7. A good agreement is observed. High
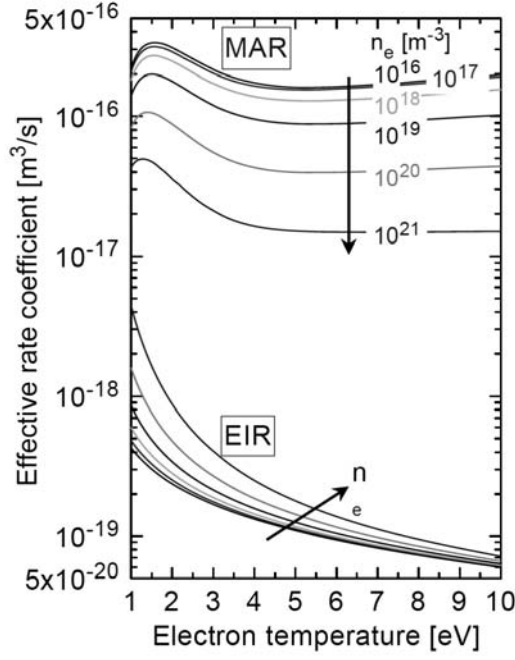
**Figure 8.** Effective rate coefficients for MAR and electron ion recombination (EIR) of hydrogen for different electron densities.

numbers of the (inverse) photon efficiency (for example at high $n_e$ and low $T_e$, i.e. a detached divertor plasma) correspond to low radiation. In other words, weak measured molecular radiation does not automatically mean low molecular fluxes. It is obvious that effective rate coefficients are essential for an interpretation of measured values.

As discussed in Refs [11, 13], hydrogen molecules can contribute to plasma (volume) recombination, in particular in cold detached divertor plasmas. The dominant underlying processes in the so-called molecular assisted recombination (MAR) are the ion conversion of protons with vibrationally excited hydrogen molecules followed by dissociative recombination. Due to the dependence of the ion conversion on the vibrational population and due to the dependence of the reaction chain on $T_e$ and $n_e$, effective rate coefficients from CR modelling are essential for calculating the relevance of (MAR) in high recycling regimes. As shown in Fig. 8 effective rate coefficients for MAR have a maximum around $T_e = 1.5$ eV and decrease with increasing electron density. In contrast, three-body and radiative recombination (electron ion (proton) recombination, EIR) increases strongly with $n_e$ for low $T_e$ (1 eV) as calculated with the CR model. The ratio MAR/EIR is on the order of 100 to 1000. However it should be kept in mind, that molecular densities are lower than atomic densities. Thus, the determination of molecular contribution to plasma recombination depends strongly on the knowledge of particle densities, electron temperature and electron density, and on the vibrational population of the molecules in their ground state.

The link between the model for $H_2$ and the model for H offers a possibility to calculate the influence of molecular processes to the population of excited states in atomic
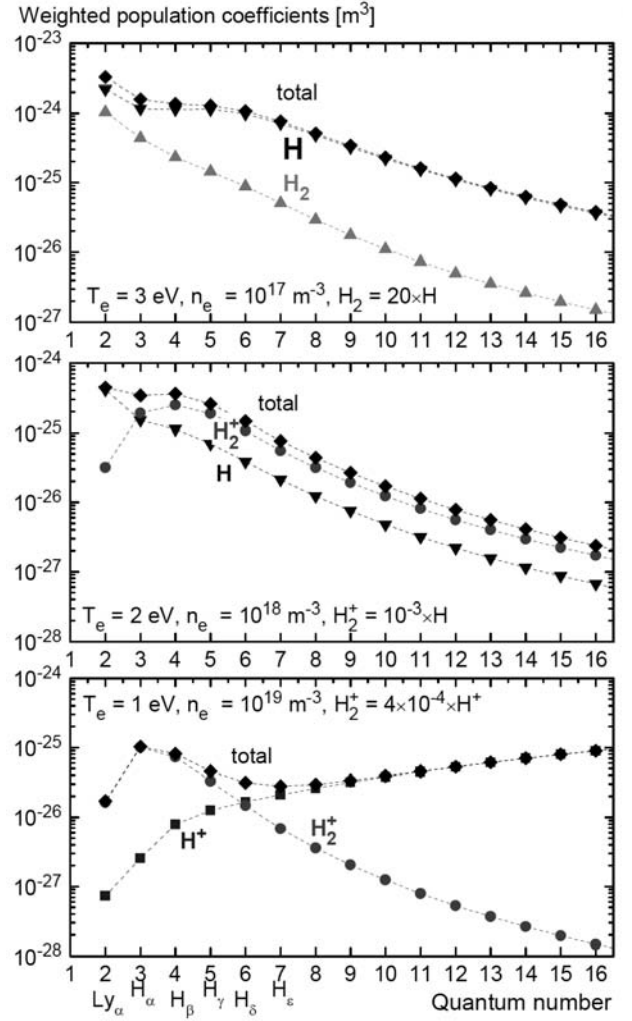


**Figure 9.** Weighted population coefficients of atomic hydrogen for an ionizing plasma with a low degree of dissociation, a partly ionizing and recombining plasma and a recombining plasma (top to bottom).

hydrogen. Besides population processes within the atom and its ion, $H_2$, $H_2^+$ and even $H^-$, can contribute to the population of excited states in H. The correlation with the corresponding particle species is provided by the CR model, which calculates population coefficients R(p) for each electronic level p as a function of $T_e$ and $n_e$. Thus, population density n(p) is given by $n(p) = R_H(p) \, n_H \, n_e + R_{H+}(p) \, n_{H+} \, n_e + R_{H2}(p) \, n_{H2} \, n_e + R_{H2+}(p) \, n_{H2+} \, n_e \, (+ R_{H-}(p) \, n_{H-} \, n_e + \ldots)$. The relevance of the individual particle species to the population depends on $T_e$, $n_e$ and the density ratios of neutrals to ions and molecular ions to protons. For example, in an ionizing plasma recombination can be neglected so that the density ratio of molecules to atoms is the relevant parameter. Using a specific density ratio, a total population coefficient can be defined as the sum of population coefficients for H and $H_2$, whereas the latter is scaled by the density ratio: $R_{total}(p) = R_H(p) + R_{H2}(p) \, n_{H2}/n_H$. These three weighted population coefficients are plotted in the upper part of Fig. 9 for $T_e = 3$ eV and $n_e = 10^{17}$ m$^{-3}$ as a function of the main quantum number. They illustrate the contribution of the two processes
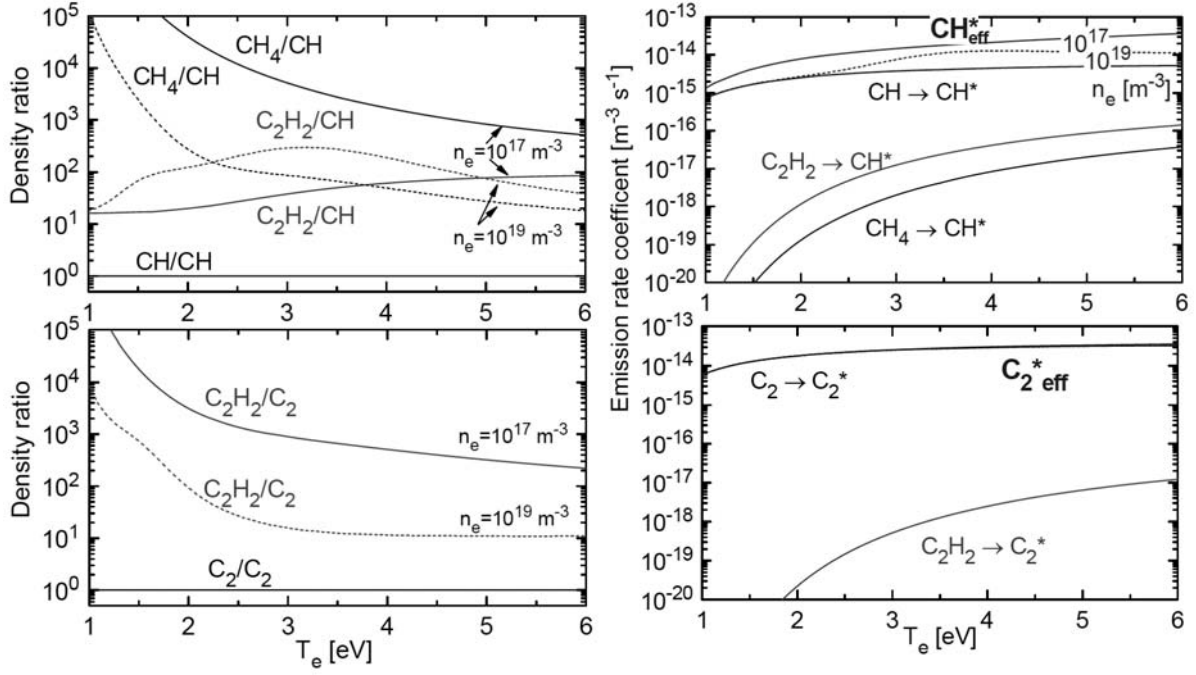
**Figure 10.** Calculated density ratios in methane plasmas for two electron densities (left) and the corresponding rate coefficients for CH and $C_2$ radiation (right).

to the total population. It is obvious that the assumed density ratio of 20 times more molecules than atoms causes only small changes in populations of low main quantum numbers. However, for a quantitative analysis this dissociative excitation (DE) process has to be taken into account. The middle part of Fig. 9 gives an example of a partly ionizing and recombining plasma at $T_e = 2$ eV and $n_e = 10^{18}$ m$^{-3}$. At a density ratio of $10^{-3}$ for molecular ions to atoms, dissociative recombination dominates. Since the dependence on the quantum number is very similar to the one from the atomic population, the overall shape is not affected for $p > 4$. In contrast, the processes compete with each other for low quantum numbers. Both, the change in absolute values and the change in the dependence on the quantum number are of great importance for a correct interpretation of Lyman and Balmer line emission as shown in the figure. The last example, the lower part of Fig. 9, shows a recombining plasma at $T_e = 1$ eV and $n_e = 10^{19}$ m$^{-3}$. Dissociative recombination populates low quantum numbers, whereas electron ion recombination populates high quantum numbers resulting in a complete different shape for the total population, assuming a density ratio of molecular ions to protons $\approx 10^{-4}$. These examples demonstrate clearly that coupled CR models (molecules with atoms) are of particular importance for the wide parameter range in which edge plasmas can operate.

## 4. Dissociation model for hydrocarbons

Hydrocarbons which are released from graphite surfaces by the chemical erosion process are accessible by the radiation of the CH and $C_2$ radicals. A relation with the

parent molecule, i.e. $CH_4$ or $C_2H_y$, and therefore a quantification of the released particles, is given by the corresponding (inverse) photon efficiencies [11, 14], the same correlation as is already applied to molecular hydrogen (Section 3.3). This means that effective dissociation rate coefficients and effective excitation rate coefficients are needed. For this purpose flexible dissociation models are developed for methane dissociation, taking into account in the first case only electron impact collisions. A second model represents a full model including heavy particle collisions and formation and dissociation of the $C_2H_y$ family. A third model calculates dissociation of $C_2H_y$ particles into $C_2$ particles. The models are based on the latest compilation of rate coefficients for hydrocarbons [15, 16]. They balance formation and destruction processes, which is sufficient to identify dominant dissociation paths. One example is the dissociation of the $C_2H_y$ family: $C_2H_6$ and $C_2H_4$ dissociate to $C_2H_2$, which means it is sufficient to analyse $C_2H_2$ dissociation only in detail. Here, the $C_2H$ particle plays a key role in the dissociation path, being also the dominant channel for the $C_2$ formation [11]. In contrast, direct dissociation of methane is not of relevance for $C_2$ formation. The situation is different for CH formation. Here, methane dissociation and dissociation of $C_2H_2$ can contribute in equal shares. From a detailed analysis the relevance of heavy particles can be obtained. The full model is used to calculate particle density ratios, i.e. $CH_4/CH$, $C_2H_y/C_2$ as a function of $T_e$ and $n_e$. Examples are shown in the left part of Fig. 10 for two electron densities.

For an interpretation of the radiation of radicals of hydrocarbons (CH and $C_2$), direct excitation from the ground state is balanced by spontaneous emission, i.e. the

61

corona model can be applied, which means CR modelling is not required. This is based on the fact that the most intense transitions are resonant and originate from the first electronically excited levels with a low excitation energy (around 3 eV). However, coupling to other species has to be considered. Since CH and $C_2$ are radicals formed in the dissociation chain of hydrocarbons, several DE mechanisms can contribute to the radiation of CH (CH*) and $C_2$ ($C_2$*):
$CH^*, C_2^* = n_{CH,C2} \, n_e \, X_{CH,C2} + n_{CH4} \, n_e \, X_{CH4} + n_{C2H2} \, n_e \, X_{C2H2}$.
$X_{particle}$ is the rate coefficient for excitation from the particle species, i.e. direct excitation and dissociative excitation. Commonly, the CH radiation around 431 nm (A–X transition, Gerö band) and the $C_2$ radiation around 516 nm (d–a transition Swan band) are used for an analysis. The corresponding cross-sections can be compiled from literature, the Maxwell integrated rate coefficients are plotted in the right part of Fig. 10, where dissociative excitation of $C_2$ from $CH_4$ is not of relevance. Thus, an effective rate coefficient can be introduced where the individual rate coefficients are weighted by the corresponding density ratios, e.g. $CH^* = n_{CH} \, n_e \, X_{eff,CH}$ with $X_{eff,CH} = X_{CH} + n_{CH4}/n_{CH} \, X_{CH4}/X_{CH} + n_{C2H2}/n_{CH} \, X_{C2H2}/X_{CH}$. Using the density ratio calculated with the dissociation model (left part of Fig. 10), effective rate coefficients are obtained depending on $T_e$ and $n_e$. As can be seen in Fig. 10 (right part) the dissociative excitation channel from $CH_4$ and $C_2H_2$ plays a role for the CH radiation, whereas for $C_2$ radiation the direct excitation channel is always dominant. However, since the CH radical arises mainly from the $CH_4$ dissociation and $C_2$ from dissociation of $C_2H_y$ particles, a method is developed to correlate $CH/C_2$ molecular bands with the particle ratio $CH_4/C_2H_y$ [17].

First results from calculations of the (inverse) photon efficiency with the above mentioned full dissociation model and the effective rate coefficients for CH and $C_2$ radiation are in good agreement with photon efficiencies measured in the divertor plasma of ASDEX Upgrade (taken in a certain parameter range for $n_e$ and $T_e$) [17]. Applying in a next step the correlation of the intensity ratio from $CH/C_2$ molecular bands with the particle ratio $CH_4/C_2H_y$, the formation of higher hydrocarbons can now be taken into account in a quantification of erosion yields of carbon surfaces in hydrogen plasmas.

## 5.    Conclusions

An understanding of molecular processes in edge plasmas requires in a first step cross-sections and rate coefficients for the manifold individual reactions. The complexity of reaction chains for the wide parameter range in which these plasmas operate needs some simplifications. A proper way is the description of reaction chains and processes by effective rate coefficients. Examples are effective ionization, recombination and dissociation coefficients covering a wide range in electron temperature and density. For molecular and atomic hydrogen, CR models are applied. The importance of the vibrational population of the molecular ground state is emphasised. A special feature of the model is its capability to resolve electronically excited states of the molecule, which is of particular importance for diagnostic purposes. In additional, the vibrational levels in excited states could be included due to a generation of a fundamental molecular database for hydrogen. The coupling of the molecule with the atom allows consideration of molecular processes to atomic reactions, for example dissociative excitation and dissociative recombination. For hydrocarbons, a clear structured and flexible dissociation model is developed, providing an insight into dominant dissociation paths. Thus, dominant dissociation chains can be combined to effective processes, providing effective rate coefficients are directly applicable to hydrocarbons in edge plasmas.

## References

[1]    STANGEBY, P.C., The Plasma Boundary of Magnetic Fusion Devices, Institute of Physics Publishing, Bristol, 2000.

[2]    SAMM, U., Plasma Wall Interaction: Status and Data Need, in Nuclear Fusion Research, Springer Series in Chem. Physics. **78**, Eds. R. Clark, D. Reiter, Springer, Berlin Heidelberg, 2005.

[3]    REITER, D., Fusion Reaction Plasma Edge Modelling Code, in Nuclear Fusion Research, Springer Series in Chem. Physics. **78**, Eds. R. Clark, D. Reiter, Springer, Berlin Heidelberg, 2005.

[4]    GREENLAND, P.T., REITER D., The Role of Molecular Hydrogen in Plasma Recombination, Report **JUEL–3258**, 1996.

[5]    FANTZ, U., SCHALK B., BEHRINGER K., New Journal of Physics **2** (2000) 7.1.

[6]    FANTZ, U., WÜNDERLICH, D., Franck–Condon Factors, Transition Probabilities and Radiative Lifetimes for Hydrogen Molecules and Their Isotopomeres, Report **INDC(NDS)–457**, IAEA Vienna, 2004.

[7]    GREENLAND, P.T., Proc. Roy. Soc. Lond. A **457** (2001) 1821.

[8]    SAWADA, K., FUJIMOTO T., J. Appl. Phys. **78** (1995) 2913.

[9]    WÜNDERLICH, D., FANTZ, U., A Collisional-Radiative Model for $H_2$ and H, IPP Report, **IPP 10/18**, 2001.

[10]    FANTZ, U., HEGER, B., Plasma Phys. Control. Fusion **40** (1998) 2032.

[11]    FANTZ, U., Molecular Diagnostics of Cold Edge Plasmas, in Nuclear Fusion Research, Springer Series in Chem. Physics. **78**, Eds. R. Clark, D. Reiter, Springer, Berlin Heidelberg, 2005.

[12]    FANTZ, U., HEGER, B., WÜNDERLICH, D., PUGNO, R., ASDEX Upgrade TEAM, J. Nucl. Mater. **313–316** (2003) 743.

[13]    FANTZ, U., REITER, D., HEGER, B., COSTER, D., J. Nucl. Mater. **290–293** (2001) 367.

[14]    PUGNO, R., KRIEGER, K., KIRSCHNER, A., KALLENBACH, A., ASDEX Upgrade TEAM, J. Nucl. Mater. **337–339** (2005) 985.

[15] JANEV, R.K., REITER, D., Collision Processes of Hydrocarbon Species in Hydrogen Plasmas I and II, Report **JUEL–3966** and **JUEL-4005,** 2002.

[16] TAHARA, H., MINAMI, K., MURAI, A., YASUI, T., YOSHIKAWA, T., Jpn. J. Appl. Phys. **34** (1995) 1972.

[17] FANTZ, U., MEIR, S., ASDEX Upgrade TEAM, J. Nucl. Mater. **337–339** (2005) 1087.

# Reactive collisions between electrons and molecular hydrogen cation isotopomers: Cross-sections and rate coefficients for HD$^+$ and DT$^+$

M.C. Stroe[1, 2], M. Fifirig[2], F.O. Waffeu Tamo[1, 3], O. Motapon[3], O. Crumeyrolle[1], G. Varin-Breant[1], A. Bultel[4], P. Vervisch[4], A. Suzor-Weiner[5], I.F. Schneider[1]

[1] Laboratoire de Mécanique, Physique et Géosciences, Université du Havre, F-76058 Le Havre, France
[2] Department of Physics, Faculty of Chemistry, University of Bucharest, RO-70346 Bucharest, Romania
[3] Center for Atomic, Molecular Physics and Quantum Optics, University of Douala, 00237 Douala, Cameroon
[4] Laboratoire CORIA, Université de Rouen, F-76801 Saint-Etienne du Rouvray, France
[5] Laboratoire de Photophysique Moléculaire, Université Paris-Sud, 91405 Orsay, France

## Abstract

Cross sections for dissociative recombination, dissociative excitation, elastic, inelastic and superelastic collisions of HD$^+$ and DT$^+$ on ground and first three excited vibrational levels, with electrons of energy between 0.01 meV and 13 eV, are computed within a method based on the multichannel quantum defect theory (MQDT). These cross sections, together with the corresponding Maxwell isotropic rate coefficients for electronic temperature between 100 K and 40 000 K, aim at providing input data for the kinetic modelling of edge fusion plasmas and other hydrogen containing plasmas.

## 1. Introduction

The modelling of the edge fusion plasma kinetics [1–5], as well as other hydrogen laboratory plasmas [6–8], is strongly based on the knowledge of cross-sections and rate coefficients of the elementary radiative and collisional processes. Since the balance equation system is most often non-linear, the predicted populations, as well as the related energetic and radiative parameters, are quite sensitive to the input data.

One of the elementary processes which plays a decisive role in the ionization degree and in the energetics of plasmas containing $AB$ molecules is the dissociative recombination (DR) of the molecular cations $AB^+$ with electrons:

$$AB^+ \left( N_i^+, v_i^+ \right) + \; e^-(\varepsilon) \rightarrow A + B \quad (E) \tag{1}$$
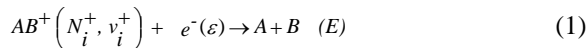
Here, $N_i^+$ and $v_i^+$ are the initial rotational and vibrational quantum numbers of the target molecular ion, $\varepsilon$ is the energy of the incident electron and $E$ is the inter-atomic kinetic energy release following the dissociation.

DR is one of the simplest reactive collisions and one of the most convincing examples of breakdown of the Born–Oppenheimer approximation [9, 10]: the dissociative capture is possible due to the existence of non-adiabatic interactions between the dissociation and the ionization

continua of molecular states, the latter type of continuum being completed by its extrapolation below threshold, the Rydberg bound states. Therefore, a more detailed description of reaction (1) reads:

$$AB^+ \left( N_i^+, v_i^+ \right) + \; e^-(\varepsilon) \rightarrow AB^{**}, \; AB^* \rightarrow A + B \quad (E) \tag{2}$$
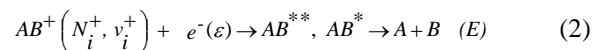
were '**' stands for a dissociative electronic state, i.e. a state whose separated atom energy limit is below the initial rovibrational level of the target ion, and '*' for a bound Rydberg state. These two types of states of the neutral system are related to two mechanisms: the capture into an AB** state is called direct DR, whereas the temporary capture into an AB* state — followed by its quick predissociation by AB** — is the indirect DR. These two mechanisms quantically interfere within the so-called total process, resulting in many series of Fano type — or more complicated — resonances in the shape of the cross-sections [11, 12].

Actually, the DR process is just one of the possible issues of the electron–cation collision. Indeed, autoionization is always a competitive process with respect to the capture, resulting in elastic ($\varepsilon' = \varepsilon$, EC), inelastic ($\varepsilon' < \varepsilon$, IC) or superelastic ($\varepsilon' > \varepsilon$, SEC) collisions:

$$AB^+\left(N_i^+, v_i^+\right)+e^-(\varepsilon) \rightarrow AB^+\left(N_f^+, v_f^+\right)+e^-(\varepsilon') \qquad (3)$$
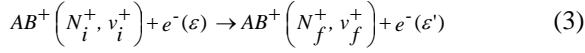
or, above the dissociation threshold of the cation, in dissociative excitation (DE):

$$AB^+\left(N_i^+, v_i^+\right)+ e^-(\varepsilon) \rightarrow A+B^+ (E)+ e^-(\varepsilon) \qquad (4)$$
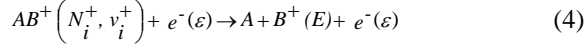
Obviously, all of these reactions will have as intermediate steps the capture into the superexcited states *AB\** and *AB\*\**, being consequently driven by the direct and/or the indirect — actually, the total — mechanism.

In the last two decades, these reactive collisions, involving $H_2^+$ (*A = B = H*) and some of its isotopomers (*HD\+*, $D_2^+$) have been actively studied, both experimentally and theoretically. The most complete experiments on these ions in the last decade have been performed in ion storage rings [13–26], where molecular ions can be stored for several seconds and cooled by electronic collisions, thus allowing high resolution measurements of cross-sections and branching ratios. With some notable exceptions [21, 23], these experiments deal with fully vibrationally relaxed ions, since resolving the vibrational distribution in an ionic beam remains a difficult task. The rotational distribution is still a more difficult subject and, in most cases, Boltzmann distribution is assumed, corresponding to some hundreds of Kelvin [16, 24].

On the theoretical side, most of the studies of the $H_2^+$ (and isotopomers) DR and related electron/molecular cation collisions have been based on the method of Giusti-Suzor [12], emerging from the MQDT [27–32]. One should also mention the time dependent (wave packet) approach of these benchmark systems, a promising way, which still does not handle entirely all the resonant aspects of the collisions [25, 33–35].

This paper presents a systematic MQDT theoretical study of the reactions (1–4) for *HD\+* and *DT\+* in their four lowest vibrational levels — *v = 0, 1, 2, 3* — for energies of the incident electron between .01 meV and 13 eV. These parameters cover a significant range of the standard conditions of the edge fusion plasma localized close to the divertor. The organization of the paper is as follows. In Section 2 we give a brief outline of the theory, underlining the new aspects with respect to previous approaches, the numerical details and the range of validity of our results. The main results (cross-sections and rate coefficients) are given in Section 3. In Section 4 we conclude on the accuracy and applicability of our data, and we outline the plans for future theoretical developments and systematic computations.

## 2. Summary of the theoretical approach

The method we use [12, 36] introduced the dissociative channel into the MQDT approach of the molecular dynamics. This method was refined during the last two decades by increasing the accuracy of the account of the electronic interactions [37, 38], by including a huge number of channels of different natures — major partial waves of the incident electrons [39, 40], all the relevant channels [15, 41, 42] — first order approach of the DE [15, 42], account of the rotational structure [43–46], excited ionic cores [47] and dissociative channels accessible by non-adiabatic interactions [48]. Most of these developments resulted in systematic calculations and numerous comparisons — favourable, with some notable exceptions, which will be briefly described later — with experimental data [21, 23, 45, 49, 50] on isotopomers of $H_2^+$.

The main steps of the MQDT treatment of the electron — molecular cation are briefly summarized here. Since all these reactive processes are treated simultaneously within the same calculation, we shall restrict ourselves to a brief description of the obtaining of the DR cross-section.

In the cases of interest for this study, the DR (together with the EC, IC, SEC and DE) occurs mainly through the electronic interaction — within a quasi-diabatic representation [51] — between the {ground state ion ($1s\sigma_g \ X \ ^2\Sigma^+_g$) + incoming electron} initial configuration and doubly excited states — the '$Q_1$' Rydberg series converging to the first excited electronic state of the ion ($2p\sigma_u \ ^2\Sigma^+_u$) — whose dissociative potential curves cross that of the ion state [52, 53]. Details about the estimations of these interactions, as well as about their account in the interaction '*V*' matrix and, eventually, reaction '*K*' matrix, are given in previous studies [38, 39, 40, 45, 50], together with details about a further type of interaction of a non-adiabatic nature, driven by the quantum defects of the relevant Rydberg series.

A complete analysis, accounting for the direct and the indirect mechanisms, and for the ro-vibrational structure and interactions, can be summarized as follows:

Starting from a given ro-vibrational level ($N_i^+, v_i^+$) of the ion initial electronic state, several values *N* of the total angular momentum of the neutral molecule can be formed by coupling with a specific partial wave *l* of the incoming electron. Each *N* value is a good quantum number conserved during the whole process and is involved in a separate calculation, leading to partial DR cross-sections which are then summed up to yield the total cross-section:

$$\sigma_{d \leftarrow N_i^+ v_i^+} = \sum_N \sigma^{(N)}_{d \leftarrow N_i^+ v_i^+} \qquad (5)$$

where '*d*' is one of the possible capture dissociative states. Within each *N* subspace, rotation is included through a frame transformation [28, 54] between coupling schemes corresponding to the incident electron being decoupled from (external region) or coupled to (internal region) the core electrons. The frame transformation mixes the different *Λ* quantum numbers compatible with a given set of ($N_i^+$, *l, N*) values. The channel mixing coefficients involve angular coupling coefficients combined with electronic and vibrational factors:

$$C_{\ell N^+ v^+, \Lambda\alpha} = \left(\frac{2N^+ + 1}{2N + 1}\right)^{1/2} \left\langle l(\Lambda - \Lambda^+)N^+\Lambda^+ | lN^+N\Lambda \right\rangle \cdot \frac{1 + \tau^+ \cdot \tau(-1)^{N-\ell-N^+}}{\left[2(2 - \delta_{\Lambda^+,0})\left(1 + \delta_{\Lambda^+,0}\,\delta_{\Lambda,0}\right)\right]^{1/2}} \tag{6}$$

$$\cdot \sum_v U_{\ell v,\alpha}^\Lambda \left\langle \chi_{N^+,v^+} \left| \cos\left\{\pi\mu_{\ell\Lambda}(R) + \eta_\alpha^\Lambda\right\} \right| \chi_{N,v}^{\ \Lambda} \right\rangle$$

$$C_{d,\Lambda\alpha} = U_{d,\alpha}^\Lambda \cos\eta_\alpha^\Lambda \tag{7}$$

as well as $S_{N^+\ell v^+,\Lambda\alpha}$ and $S_{d,\Lambda\alpha}$, obtained from Eqs (6) and (7) by replacing 'cos' by 'sin'. The $\chi_{N^+v^+}$ and $\chi_{Nv}^\Lambda$ are the vibrational wave functions of the ground state molecular ion in the $(N^+,\ v^+)$ ro-vibrational level and of a Rydberg monoexcited state in the $(N, v)$ ro-vibrational level respectively, and $\mu_{\ell\Lambda}(R)$ is the electronic quantum defect characterising these $\ell\Lambda$ — Rydberg series. For a given $\Lambda$, the index $\alpha$ denotes the eigenchannels defined through the diagonalization of the electronic reaction sub-matrix $K^\Lambda$, with eigenvalues $-\frac{1}{\pi}\tan(\eta_\alpha^\Lambda)$ and eigenvectors $(U_{\ell v,\alpha}^\Lambda,\ U_{d,\alpha}^\Lambda)$. Each block $K^\Lambda$ of the reaction matrix is evaluated from the electronic coupling functions $V^\Lambda(R)$ between singly and doubly excited configurations with $\Lambda$ symmetry [45, 46, 50]. The quantities $\tau^+$ and $\tau$ (with values ±1) are related to the reflection symmetry of the ion and neutral wave function respectively, and take the values +1 for symmetric states and –1 for antisymmetric ones [46]. The ratio in front of the sum in the right hand side of Eq. (6) contains the selection rules for the rotational quantum numbers.

These channel mixing coefficients allow computation of the scattering matrix $S$ restricted to open channels and containing the resonance structure, once the closed channels have been eliminated following the MQDT procedure of Seaton [29]. Finally, the partial cross-sections in the sum of Eq. (5) are given by:

$$\sigma_{d\leftarrow N_i^+v_i^+}^{(N)} = \frac{\pi\hbar^2}{4m_e\varepsilon}\rho\frac{2N+1}{2N_i^+ + 1}\sum_\ell \left|S_{d\leftarrow\ell N_i^+v_i^+}^{(N)}\right|^2 \tag{8}$$

where $\varepsilon$ is the energy of the incident electron, $m_e$ the electron mass and $\rho$ is the multiplicity ratio between the neutral and the ionic electronic states.

Finally, when computing the cross-sections corresponding to a given vibrational initial number of the target, we have to perform a *300 K* Boltzmann weighted sum of the results of the type (8).

At high energy, the approach briefly summarized above simplifies significantly, as shown in previous studies [45, 46]. First of all, the rotational effects become negligible above *2* eV. On the other hand, capture into Rydberg states is no longer possible above the ion dissociation threshold (*2.6* eV for the ground vibrational state and less for the higher excited states). In this latter case, only the direct process is available.

On the other hand, at high energy the effect of the continuum part of the vibrational spectrum of the molecular ion — not shown explicitly in the preceding formulas — plays a more important role. The most striking effect is the occurence — at the dissociation threshold of the ion — of the DE — Eq. (3), which is the extension into the vibrational continuum of the vibrational excitation. Whereas in the past, a first order approach was used to estimate the magnitude of this process, as well as its influence on the DR [15, 42, 45], a more rigorous method allows us today to consider it via the 'discretization' of the continuum, using the procedure introduced by Takagi [55]:

$$\chi_{E_i}(R) = \frac{1}{\sqrt{\Delta}}\int_{E_i-\Delta/2}^{E_i+\Delta/2}\chi_E(R)\,dE,\ \Delta = E_{i+1} - E_i \tag{9}$$

where the vibrational continuum labelled by the energy $E$ is divided into a number of bands of width $\Delta$ and centred in $E_i$. The importance of this process is illustrated by Fig. 1, where its influence on the DR is proven to be of a factor of two or more in broad energy regions.

## 3. Cross-sections and rate coefficients

The present calculations are mainly devoted to modelling the kinetics of the plasma in the divertor region, where the temperature overpasses 1 eV. Therefore, a complete characterization of the low energy collisions has been postponed [56] and, for energies above 350 meV, we
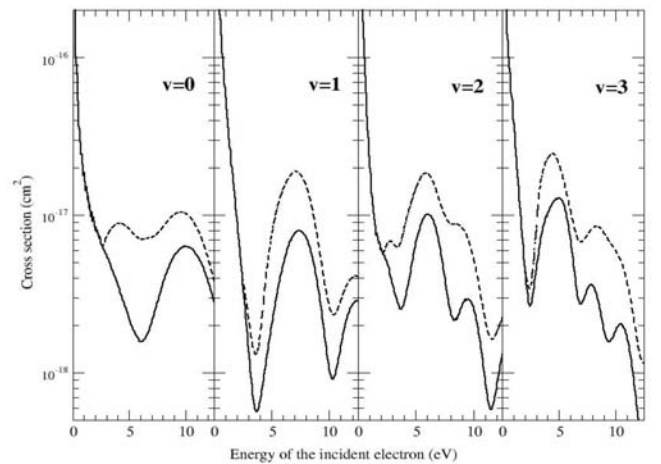


**Figure 1.** Role of the DE on the DR of the HD$^+$ molecular ion in a given vibrational state v: dashed line — DE neglected, full line — DE included. The contribution of the $^1\Sigma_g^+$ symmetry only was considered in this illustrative case.
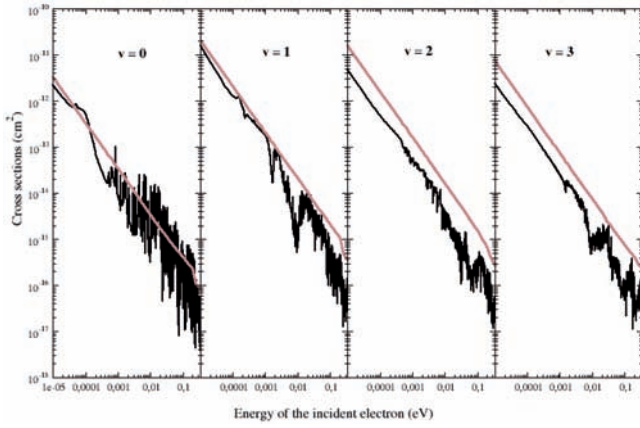
**Figure 2.** DR of HD$^+$ molecular ion in a given vibrational state **v**, at low energy (cross-sections). Black line: indirect process and rotational effects included; grey line: direct process only and rotational effects neglected.
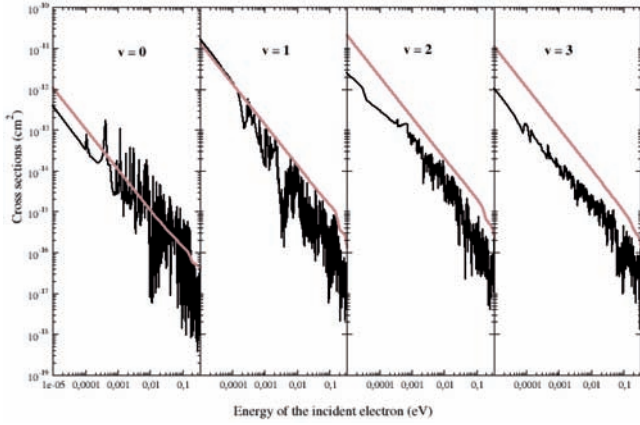


**Figure 3.** DR of DT$^+$ molecular ion in a given vibrational state **v**, at low energy (cross-sections). Black line: indirect process and rotational effects included; grey line: direct process only and rotational effects neglected.
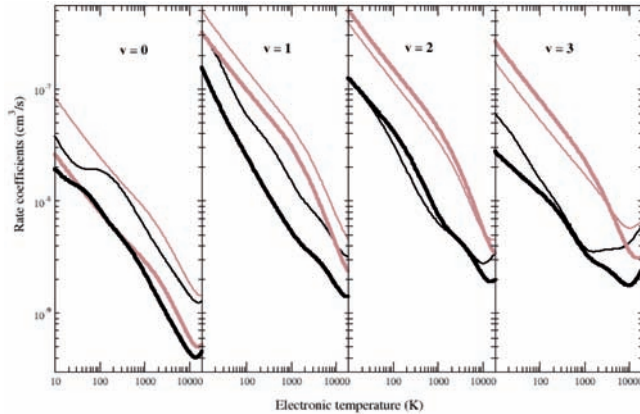


**Figure 4.** DR of HD$^+$ (thin lines) and DT$^+$ (thick lines) molecular ion in a given vibrational state **v**, at low energy (Maxwell rate coefficients). Black line: indirect process and rotational effects included; grey line: direct process only and rotational effects neglected.

have performed calculations accounting for the direct process only. The value of 350 meV is the limit of what we have considered the very low energy region. Below this energy, we did perform accurate — rotational, direct and indirect — calculations, the difference with respect to the direct and non-rotational approach being quite remarkable — as shown in Figs 2–4.

These calculations were performed for DR only, because the other processes are either absent (DE), less important (IC, SEC), or less sensitive (EC) to the resonant structure than DR at very low energy. They involved the lowest doubly excited state of the neutral, $(2p\sigma_u)^2$ $^1\Sigma_g^+$, exclusively.

Above 350 meV, the indirect process and the rotational effects are still present. However, they decrease with energy, becoming impossible and, respectively, negligible around 2 eV, for the vibrational numbers between 0 and 3. Meanwhile, as the energy rises, a complete approach requires taking into account many dissociative states pertaining to all the relevant symmetries: $^1\Sigma_g^+$, $^1\Pi_g$, $^3\Pi_g$, $^1\Pi_u$, $^3\Pi_u$, $^1\Sigma_u^+$, $^3\Sigma_u^+$. We have performed direct calculations between 350 meV and the dissociation limit of the ions, non-rotational but accounting for all the symmetries. Above the dissociation limit, the only approximation remains the neglect of the rotational structure, which is justified, at least in the case of the Boltzmann rotational distribution.

Figures 5 and 6 give the cross-sections for the 5 processes shown in Eqs (1–4), driven by the direct mechanism for $HD^+$ and $DT^+$, respectively. The values appearing between 350 meV and 2 eV are correct within an average factor of two. Below 350 meV, accurate values for DR are available in Figs 2 and 3. Figure 7 illustrates the isotopic effect for a few representative case studies. Finally,
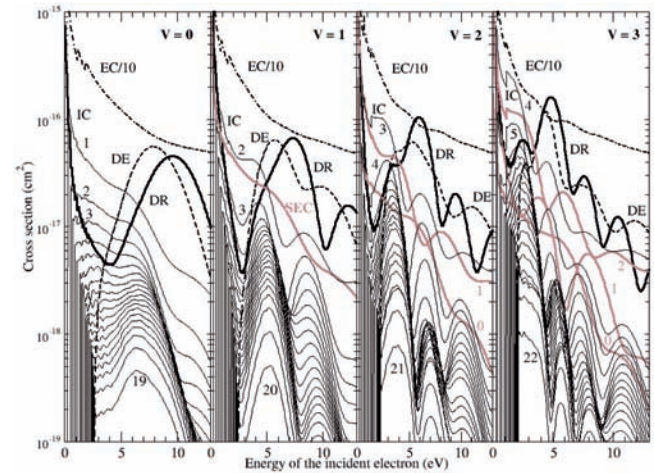


**Figure 5.** Reactive collisions of HD$^+$ molecular ion in a given vibrational state **v** with electrons (cross-sections): bold line — DR, broken line — DE, dashed dotted line — elastic collisions (EC), grey line — superelastic collisions (SEC) and thin line — inelastic collisions (IC). The number attached to the IC and SEC curves stand for the final vibrational states.
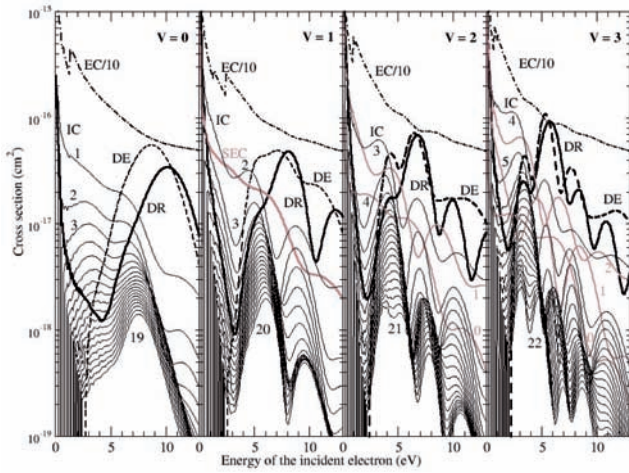
**Figure 6.** Reactive collisions of $DT^+$ molecular ion in a given vibrational state **v** with electrons (cross-sections): bold line — DR, broken line — DE, dashed dotted line — elastic collisions (EC), grey line — superelastic collisions (SEC) and thin line — inelastic collisions (IC). The numbers attached to the IC and SEC curves stand for the final vibrational states.



**Figure 8.** Reactive collisions of $HD^+$ and $DT^+$ molecular ion in a given vibrational state **v** with electrons (Maxwell rate coefficients). Thick lines — $DT^+$, thin lines — $HD^+$. Solid line — DR, broken line — DE, dashed dotted line — elastic collisions (EC), grey line — superelastic collisions (SEC) and fine solid line -inelastic collisions (IC). The numbers attached to the IC and SEC curves stand for the final vibrational states.



**Figure 7.** Isotopic effect ($DT^+$ vs $HD^+$ molecular ions) in reactive collisions of molecular ions with electrons (cross-sections): Thin lines — $DT^+$, thick lines — $HD^+$. The numbers (v) attached to the DR, DE and EC curves stand for the initial vibrational quantum number of ion. The pairs of numbers (v-v') for SEC and IC stand for initial final vibrational quantum numbers.

Fig. 8 provides the Maxwell isotropic rate coefficients corresponding to the cross-sections displayed in Figs 2 and 3.

## 4. Numerical details, conclusions and perspectives

For each vibrational initial level $v$ between 0 and 3, the very low energy (0.01 meV–350 meV) DR calculations have been performed for the first 13 rotational levels — quite sufficient in the assumption of a 300 K Boltzmann distribution. For a given initial rotational level $N_i^+$ of the ion, all the available total rotational levels $N$ of the neutral (typically

3 values) and all the other rotational levels $N^+$ of the ion (typically 3 values for every $N$) accessible via the rules of addition of angular momenta, have been considered in our MQDT calculations [45, 46]. The computations have been performed on an energy grid of 0.01 meV in order to account for the fine resonances due to the ro-vibrational structure and interactions.

At higher energies, where the direct mechanism was considered for all five elementary processes, one calculation per electronic symmetry ($^1\Sigma_g^+$, $^1\Pi_g$, $^3\Pi_g$, $^1\Pi_u$, $^3\Pi_u$, $^1\Sigma_u^+$, $^3\Sigma_u^+$) was performed for each vibrational quantum number ($v = 0$, 1, 2, 3) of the molecular ion target on an energy grid of 50 meV. The vibrational continuum associated with the ion electronic ground state was discretized using bands of width $\Delta = 47.1$ meV, after preliminary convergence tests.

The most complete results presented here correspond to the energy range situated above the dissociation limit of the molecular ion, typically above 2 eV. However, at high energy a second type of DE, related to the vibrational continuum of the first excited electronic state of the ion can play an important role, and this will happen 'sooner' (i.e. at lower energy) for the highly excited vibrational levels ($v = 3$) than for the lower ones ($v = 0$). Therefore, our high energy DR, SEC, IC and EC values are slightly overestimated, whereas our cross-sections are underestimated for the DE process. We believe that these inaccuracies are small for our energy and vibrational quantum number ranges. The inclusion of this type of DE is presently going on [57] in our MQDT treatment, and will allow increasing the accuracy of our calculations, and extending them to higher energy and to states with higher vibrational quantum numbers.

It is more difficult to assess on the accuracy of the low energy calculations. The approach is very accurate in the

very low energy region, since the indirect process and the rotational structure are included but, going to higher energy, the role of further symmetries may increase, becoming quite important in all the 'intermediate/low energy' zone, between 350 meV and about 2 eV. It is in this energy range that our results are probably less accurate. Calculations including all the relevant symmetries are presently going on [56], opening the possibility of increasing the accuracy and computing cross-sections and rates of processes for more excited ions.

When experimental data and other theoretical results were available, we have compared them with ours. In most cases, the agreement is encouraging on DR [16, 21, 23, 45, 49, 50] and DE [45, 55]. The remaining discrepancies on some DR [21] and SEC [50] rates are currently investigated [56, 57].

The production of cross-section and rates will continue for the present isotopes, in parallel with the improvement of our theoretical tools, and will be extended to other isotopomers of interest for the kinetics of the molecular edge fusion plasmas — $H_2^+$, $D_2^+$, $HT^+$ and $T_2^+$.

## Acknowledgements

## References

[1]    JANEV, R. K., Atomic and Molecular Processes in Fusion Edge Plasmas, Plenum, New York, 1995.

[2]    WISCHMEIER, M., et al., Contrib. Plasma Phys. **1–3** (2004) 268.

[3]    TSITRONE, E., et al., Contrib. Plasma Phys. **1–3** (2004) 241.

[4]    FANTZ, U., GREENLAND, P.T., Contrib. Plasma Phys. **6–7** (2002) 694.

[5]    SCHNEIDER, R., et al., Comput. Phys. Commun. **1–3** (2004) 9.

[6]    LOMBARDI, G., DUTEN, X., HASSOUNI, K., CAPITELLI, M., GICQUEL, A., Eur. Phys. J., D At. Mol. Opt. Phys. **2** (2004) 225.

[7]    KALACHE, B., et al., J. Phys., D. Appl. Phys. **13** (2004) 1765.

[8]    SALABAS, A., MARQUES, L., JOLLY, J., GOUSSET, G., ALVES, L.L., J. Appl. Phys. **9** (2004) 4605.

[9]    BATES, D.R., Phys. Rev. A **78** (1950) 492.

[10]    BARDSLEY, J.N., J. Phys. B **1** (1968) 365.

[11]    FANO, U., Phys. Rev. **124** (1961) 1866.

[12]    GIUSTI-SUZOR A., J. Phys. B **13** (1980) 3687.

[13]    FORCK, P., et al., Nucl. Instrum. Methods Phys. Rev. B **79** (1993) 273.

[14]    ZAJFMAN, D., et al., Phys. Rev. Lett. **75** (1995) 814.

[15]    STRÖMHOLM, C., et al., Phys. Rev. A **52** (1995) R4320.

[16]    TANABE, T., et al., Phys. Rev. Lett.**75** (1995) 1066.

[17]    LARSSON, M., et al., Physica Scripta. **3** (1995) 354.

[18]    VAN DER ZANDE, W.J., et al., Phys. Rev. A **54** (1996) 5010.

[19]    ANDERSEN, L.H., et al., Phys. Rev. A **55** (1997) 2799.

[20]    ZAJFMAN, D., et al., Phys. Rev. Lett. **79** (1997) 1829.

[21]    AMITAY, Z., et al., Science **5373** (1998) 75.

[22]     LANGE, M., et al., Phys. Rev. Lett. **83** (1999) 4979.

[23]    AMITAY, Z., et al., Phys. Rev. A **60** (1999) 3769.

[24]    TANABE, T., et al., Phys. Rev. Lett. **83** (1999) 2163.

[25]    LARSON, A., et al., Phys. Rev. A **62** (2000) 042707.

[26]    AL-KHALILI, A., et al., Phys. Rev. A **68** (2003) 042702.

[27]    SEATON, M., Proc. Phys. Soc. **88** (1966a) 801, 815.

[28]    FANO, U., Phys. Rev. A **2** (1970) 353.

[29]    SEATON, M.J., Rep. Prog. Phys. **46** (1983) 167.

[30]    GREENE, C., JUNGEN, Ch., Adv. At. Mol. Phys. **21** (1985) 51.

[31]    JUNGEN, Ch., Molecular Applications of Quantum Defect Theory, IOP Bristol and Philadelphia, 1996.

[32]    TELMINI, M., JUNGEN, Ch., Phys. Rev. A **68** (2003) 062704.

[33]    OREL, A.E., Phys. Rev. A **62** (2000) 020701.

[34]    LARSON, A., OREL, A.E., Phys. Rev. A **64** (2001) 062701.

[35]    OREL, A.E., Journal of Physics: Conference Series **4** (2005) 142.

[36]    GIUSTI-SUZOR, A., BARDSLEY, J.N., DERKITS, C., Phys. Rev. A **28** (1983) 682.

[37]    GUBERMAN, S.L., GIUSTI-SUZOR, A., J. Chem. Phys. **95** (1991) 2602.

[38]    V. NGASSAM, A.I.,  et al., Eur. J. Phys. D **26** (2003) 165.

[39]    SCHNEIDER, I.F., DULIEU, O., GIUSTI-SUZOR, A., J. Phys. B At. Mol. Opt. Phys. **24** (1991) L289.

[40]    SCHNEIDER, I.F., DULIEU, O., GIUSTI-SUZOR, A., Phys. Rev. Lett. **68** (Comment) (1992) 2251.

[41]    SCHNEIDER, I.F., DULIEU, O., GIUSTI-SUZOR, A., ROUEFF, E., Astrophys. J. **424** (1994) 983.

[42]    TAKAGI, H., In Dissociative Recombination: Theory, Experiment and Applications III Word, editors ZAJFMAN, D., MITCHELL, J., ROWE, B., Scientific Word, Singapore-New, Jersey-London-Hong Kong (1995) 174.

[43]    TAKAGI, H., KOSUGI, N., LE DOURNEUF, M., J. Phys. B At. Mol. Opt. Phys. **24** (1991) 711.

[44]    TAKAGI H, J. Phys. B At. Mol. Opt. Phys. **26** (1993) 4815.

[45]    SCHNEIDER, I.F., et al., J Phys B At. Mol. Opt. Phys. **30** (1997) 2687.

[46]    VALCU, B., et al., Eur. Phys. J. D 1 (1998) 71.

[47]    CARATA, L., OREL, A.E., RAOULT, M., SCHNEIDER, I.F., SUZOR-WEINER, A., Phys. Rev. A **62** (2000) 052711.

[48]    FLORESCU, A.I., NGASSAM, V., SCHNEIDER, I.F., SUZOR-WEINER, A., J. Phys. B: At. Mol. Opt. Phys. **36** (2003) 1205.

[49] SCHNEIDER, I.F., SUZOR-WEINER A., Contrib. Plasma Phys. **42** (2002) 578.

[50] NGASSAM, V., et al., Phys.Rev. A **68** (2003) 032704.

[51] SIDIS, V., LEFEBVRE BRION, H., J. Phys. B At. Mol. Phys. **4** (1971) 1040.

[52] GUBERMAN, S.L., J. Chem. Phys. **78** (1983) 1404.

[53] TENNYSON, J., At. Data Nucl. Data Tables **64** (1996) 253.

[54] CHANG, E.S., FANO, U., Phys. Rev. A **6** (1972) 173.

[55] TAKAGI, H., Physica. Scripta. **T96** (2002) 52.

[56] MOTAPON, O., WAFFEU TAMO, F.O., SCHNEIDER, I.F., 2005.

[57] STROE, M.C., WAFFEU TAMO, F.O., FIFIRIG, M., MOTAPON, O., SCHNEIDER, I.F., 2005.

# Cross-section database for collision processes of hydrocarbons with electrons and protons

*R.K. Janev[1], D. Reiter[2]*

[1] Macedonian Academy of Sciences and Arts, Skopje, The Former Yugoslav Republic of Macedonia
[2] Institut für Plasmaphysik, Forschungszentrum Jülich GmbH, EURATOM Association, Trilateral Euregio Cluster, D-52425 Jülich, Germany

## Abstract

The cross-section database for collision processes of electrons and protons with hydrocarbon molecules $C_xH_y$ (x = 1–3; $1 \leq y \leq 2x + 2$) and their ions is reviewed. The considered electron impact processes include dissociative and non-dissociative excitation and ionization of neutral molecules, dissociative excitation and ionization of molecular ions and dissociative electron — ion recombination. The proton impact processes include the charge and particle exchange processes. The available cross-section information on these processes is presented in the form of compact analytic fit functions.

## 1. Introduction

Almost all presently operating large magnetic fusion experimental machines contain carbon as a plasma facing material. Carbon is also anticipated as candidate material in the divertor of the International Thermonuclear Experimental Reactor (ITER). Exposed to the plasma particle bombardment, particularly at low plasma temperatures (1–10 eV) prevailing in the near target divertor region, carbon materials are subject to intense chemical erosion. This produces $C_xH_y$ molecules that enter and contaminate the divertor plasma. Chemical erosion and re-deposition of plasma facing divertor components is a serious reactor operation problem requiring frequent replacement of these components, and thus affecting its economics. The use of carbon as plasma facing divertor material also has other adverse properties (high tritium retention), but its favorable thermo-mechanical properties still keep it as a prime candidate for certain plasma facing components, or part of them. The control of hydrocarbon influxes into the plasma is, thus, becoming an issue of primary interest and the first step in that direction is their quantitative measurement.

The current spectroscopic approaches to measurement of hydrocarbon influxes from carbon containing divertor materials are based on intensity measurements of appropriate carbon (atomic or ionic) lines, or the band emission from CH or $C_2$. The determination of hydrocarbon influxes from these measurements, especially their chemical composition, requires knowledge of the fragmentation paths of $C_xH_y$ molecules originating on carbon surfaces, as well as of their transport in the plasma. Both the molecular catabolism and the transport of the various hydrocarbon species are determined by their collision processes with plasma electrons and protons, at least for plasma and neutral gas parameters typical for divertor plasmas ($T_{e,i}$ ~ 1–100 eV, $T_0$ ~ 0.3 – 5 eV, $n_{e,i}$ ~ $n_0$ ~ $10^{13} – 10^{15}$ cm$^{-3}$).

Numerous dedicated laboratory experiments [1] have shown that after hydrogen particle bombardment of carbon materials the main components of chemical erosion fluxes are $CH_3$, $CH_4$, $C_2H_2$, $C_2H_4$, $C_2H_6$, $C_3H_2$, $C_3H_4$, $C_3H_6$ and $C_3H_8$. The contribution of heavier hydrocarbons to the total erosion yield becomes increasingly more important with decreasing energy of bombarding particles and even dominant in the sub-eV region. During their transport in the plasma the above hydrocarbon molecules are subject to electron impact dissociative excitation (DE) and ionization processes, so that all members of a $C_xH_y$ family (x = 1, 2, 3; $1 \leq y \leq 2x + 2$), as well as their ions $C_xH_y^+$, are present in the plasma. The most important collision processes of these particles with plasma electron and protons in the collision energy region pertinent to fusion divertor plasmas (below ~ 100–150 eV) are the following:

$$e + C_xH_y \rightarrow e + C_xH_y^* \quad (1a)$$
$$\rightarrow e + \Sigma_{k,l} C_{x-k}H_{y-l} + \Sigma_{k,l} C_kH_l \quad (1b)$$
$$e + C_xH_y \rightarrow e + C_xH_y^+ + e \quad (2a)$$
$$\rightarrow e + \Sigma_{k,l} C_{x-k}H_{y-l}^+ + \Sigma_{k,l} C_kH_l + e \quad (2b)$$
$$e + C_xH_y^+ \rightarrow e + \Sigma_{k,l} C_{x-k}H_{y-l}^+ + \Sigma_{k,l} C_kH_l \quad (3)$$
$$e + C_xH_y^+ \rightarrow e + \Sigma_{k,l,m,n}C_{x-k-m}H_{y-l-n}^+ +$$
$$\Sigma_{k,l} C_kH_l^+ + \Sigma_{m,n}C_mH_n + e \quad (4)$$
$$e + C_xH_y^+ \rightarrow \Sigma_{k,l} C_{x-k}H_{y-l} + \Sigma_{k,l} C_kH_l \quad (5)$$
$$H^+ + C_xH_y \rightarrow H + C_xH_y^+ \quad (6a)$$
$$\rightarrow H_2 + \{C_xH_{y-1}^+\} \quad (6b)$$

71
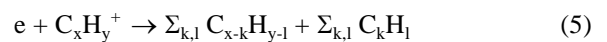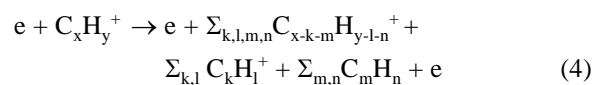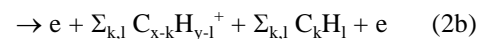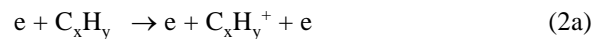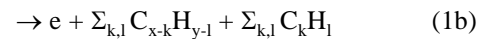
where {....} indicates that the ion $C_xH_{y-1}^+$ may be unstable against dissociation, and the summation runs over all possible reaction channels. It should be noted that the majority of electronically excited states of $C_xH_y$ molecules have dissociative character [2] and process (1a) is most probably not an important one (except for CH) in divertor plasmas.

The available experimental and/or theoretical cross-section information for processes (1)–(6) is rather limited. This is true especially for the cross-sections of the dissociative reaction channels, the separation of which encounters serious difficulties both in the experiments and the theory. On the other hand, the diagnostics of hydrocarbon influxes or the modelling of hydrocarbon transport in the plasma requires cross-section knowledge for all the above listed processes and their dominant reaction channels. In the absence of factual cross-section information for many of these reaction channels, or entire processes for a given hydrocarbon species, certain assumptions have to be adopted regarding their cross-sections. In the attempts to fill in the gaps in the cross-section database for the above listed processes, various authors have followed different approaches, resulting in significant differences in the suggested cross-section data sets. Significant differences in such data collections also exist in terms of the selection of collision processes considered to be the most important ones in a divertor plasma, and especially in the selection of reaction channels for a given collision process of a specific hydrocarbon species. For example, in Ref. [3] only the collision processes of the $CH_y$ ($1 \leq y \leq 4$) family of hydrocarbons were considered, with exclusion of all processes (4) and the particle exchange channels (6b). Reference [4] considers the processes of $C_2H_y$ ($1 \leq y \leq 6$) and $C_3H_y$ ($1 \leq y \leq 6$) hydrocarbon families, but again excludes processes (4) and (6b). The physical basis for adopting the values of the cross-sections not available in the literature is not always justifiable.

More systematic and physically grounded approaches in construction of complete cross-section databases for the ionization processes (2) and charge and particle transfer processes (6) have been followed in Refs [5, 6], respectively. These approaches have also been used to construct the cross-section databases for all processes (1–6) for the $CH_y$ [7] and $C_{2,3}H_y$ [8] families of hydrocarbons. In the remaining part of this paper we shall outline the principles on which the cross-section determination in these references was based and present the cross-section results in a compact analytic form.

## 2. General properties of electron and proton impact processes with hydrocarbons and their cross-sections

### 2.1 Electron impact processes

The basis for deriving the cross-sections for inelastic electron impact processes (1)–(4) on the basis of limited experimental cross-section information lies in the additivity rules for the strengths of chemical bonds in polyatomic molecules, discovered many years ago [9]. These rules do not lose their validity when the molecule is subjected to a long range force, or to delocalization of its free charge, as happens during a collision event [10]. A manifestation of these additivity rules was observed in the total electron impact ionization cross-sections of $C_xH_y$ molecules with x ranging up to x = 5 and y ranging up to y = 12 in the form of a strict linearity of cross-section values with the number of C atoms, x, for a given energy in the region $E \geq 600$ eV [11]. Later on, the x linearity of total electron impact ionization cross-sections of $C_xH_y$ was shown to persist down to energies of ~ 20–30 eV [5]. Moreover, in Ref. [5] it was demonstrated that the total ionization cross-sections also exhibit a strict linearity on the number of H atoms, y, for a given energy above E ~ 20–30 eV. Furthermore, in Ref. [5] it has been shown that not only the total ionization cross-sections exhibit x, y linearity for a given energy but also the partial ones (for the specific reaction channels). The validity of additivity rules for the inelastic processes (1), (3) and (4) was demonstrated in Refs [7, 8].

The electron–molecular ion dissociative recombination process (5) generally proceeds via formation and decay of a doubly excited complex and applicability of additivity rules for this process is less obvious. Nevertheless, the total cross-sections for this process also show a linear dependence on x and y, at least for high x.

Using the limited experimental cross-section information for the considered processes (1)–(5), and the observed validity of additivity rules, one can construct with a good level of confidence the inelastic (total and partial) cross-sections for these processes that are unavailable in the literature (for details, see Refs [7, 8]).

### 2.2. Proton impact processes

The cross-section information for charge and particle exchange processes (6a) and (6b), respectively, is also very limited and certain theoretical arguments and scaling relationships have to be employed in order to derive the missing cross-sections for these processes. The available charge exchange cross-section data indicate that for $C_xH_y$ molecules with $y \geq x + 2$ process (6a) has an energy behaviour typical of the resonant electron capture reactions (a logarithmic increase of the cross-section with decreasing collision energy in the region below ~10–20 keV. Using the known dependence of cross-sections of resonant charge exchange reactions on electron binding energy in the target, one can derive the missing charge exchange cross-sections for $C_xH_y$ molecules with $y \geq x + 2$ on the basis of known ones, at least for collision energies below 10–20 keV. However, for derivation of the cross-sections for non-resonant charge exchange reactions ($y < x + 2$), other theoretical arguments have to be employed (see Ref. [6]). Finally, the total charge and particle exchange cross-section in the thermal energy region can be estimated by using the

Langevin polarization capture model with the known values of polarizabilities of $C_xH_y$ molecules.

## 2.3. Scaling of total cross-sections

The above discussions indicate that the total cross-sections of processes (1)–(6) have distinct scaling properties. Indeed, the observed additivity rules for the electron impact processes (1)–(5) allow representation of their total cross-sections in the general form

$$\sigma_\lambda^{tot} = \sigma_{0\lambda}(E)\, L_\lambda(x,y) \qquad (7)$$

where $\lambda$ indicates the type of the process, $\sigma_{0\lambda}(E)$ is the part of the cross-section that depends on the collision dynamics (E is the collision energy) and $L_\lambda(x,y)$ is a structural factor that, according to above discussions, depends linearly on both x and y. The relation (7) holds also for the resonant charge exchange ($y \geq x + 2$) and particle exchange processes (6a) and (6b), respectively, but in these cases the structural function $L_\lambda(x,y)$ is not linear in x and y. The specific forms of $\sigma_{0\lambda}(E)$ and $L_\lambda(x,y)$ for the considered processes will be given in the next section.

## 2.4. Partial (channel) cross-sections

As shown in Eqs (1)–(6), all considered electron and proton impact processes of hydrocarbon species, except (1a), (2a) and (6a), have many reaction channels related to the dissociation of a temporarily formed intermediate complex (reactions (1b), (2b), (3)–(5)) or particle exchange (reaction (6b)). The total cross-section for a given process $\lambda$ is the sum of the partial cross-sections of all possible reaction channels (dissociative and non-dissociative). The contribution of a given reaction channel *j* to the total cross-section $\sigma_\lambda^{tot}$ of the process $\lambda$ at a given energy E is given by the branching ratio

$$R_\lambda^j = \sigma_\lambda^j(E)/\sigma_\lambda^{tot} \qquad (8)$$

A remarkable feature of branching ratios $R_\lambda^j$, observed experimentally years ago for the electron impact ionization of a number of hydrocarbons [12] and further demonstrated for other electron impact processes of these species [7, 8], is the fact that they are independent of the collision energy for E above 20–30 eV, i.e. well above the thresholds of all reaction channels for a given process $\lambda$. This fact is also a consequence of the additivity of the strengths of chemical bonds in hydrocarbon species and ensures the separability of dynamic and structural factors in the partial cross-sections (i.e. their scalability). The branching ratio $R_\lambda^{j'}$ however, acquires an energy dependence in the low energy region when not all reaction channels are open. Based on the near threshold behaviour of the cross-section for a given process $\lambda$ and the unitarity condition ($\sigma_\lambda^{tot} = \Sigma_j \sigma_\lambda^j$), the energy dependent branching ratios $R_\lambda^j(E)$ can be uniquely determined in the low energy region [8].

## 3. Unified analytic expressions for total cross-sections

By using the limited amount of experimental data for the cross-sections of processes (1)–(6) and by applying the cross-section scaling relationships discussed in the previous section, a complete set of cross-sections for all reaction channels of these processes can be derived. This has been done in Ref. [7] for the $CH_y$ family of hydrocarbons, and in Ref. [8] for the processes of the $C_{2,3}H_y$ families. The total cross-sections for processes (1)–(6) have all been fitted to relatively simple analytic expressions having correct near threshold (when the process has a threshold) and high energy behaviour. An exception is the direct, non-DE process (1a) for which an insufficient amount of reliable data was found in the literature, preventing the successful application of cross-section scaling relationships. Below we present the analytic fit expressions for the total cross-sections of processes (1b)–(6), based on Refs [7, 8].

### 3.1. Electron impact processes

The total cross-sections for processes (1b)–(4), governed by similar physical mechanisms, can all be represented by the same type of analytic fit function

$$\sigma_\lambda^{tot}(E) = A_\lambda\, L_x^\lambda(y)\, (1 - E_{th,\lambda}^{x,y}/E)^{\alpha_\lambda}$$
$$E^{-1}\, \ln(e + c_\lambda E)\, (10^{-16}\, cm^2) \qquad (9)$$

where x and y indicate the number of C and H atoms in the molecular species, respectively, $E_{th,\lambda}^{x,y}$ (expressed in eV units) is the lowest energy threshold for the reactions $\lambda$ of $C_xH_y$ or its ion, $A_\lambda$, $\alpha_\lambda$ and $c_\lambda$ are constants, $L_x^\lambda(y)$ is a scaling function with respect to y for fixed x and $\lambda$, E is the collision energy (expressed in eV units) and $e = 2.71828...$ is the base of natural logarithm. The parameters in Eq. (9), as well as the linear functions $L_x^\lambda(y)$ are known for all processes $\lambda = $ 1b, 2, 3, 4, and are given in Refs [7, 8]. Without significant loss of the accuracy, the cross-sections $\sigma_\lambda^{tot}(E)$ can be written in scaled form [13]. This can be achieved by introducing the scaled energy $\varepsilon = E/E_{th,\lambda}^{x,y}$ and combining the functions $L_x^\lambda(y)$ into one function $F_\lambda(x,y)$ for a given process $\lambda$. The cross-section (9) then becomes

$$\sigma_\lambda^{tot}(\varepsilon) = (A_\lambda/E_{th,\lambda}^{x,y})\, F_\lambda(x,y)\, (1-1/\varepsilon)^{\alpha_\lambda}$$
$$\varepsilon^{-1}\, \ln(e + a_\lambda \varepsilon)\, (10^{-16}\, cm^2) \qquad (10)$$

where $a_\lambda = c_\lambda\, av\{E_{th,\lambda}^{x,y}\}$, and $av\{E_{th,\lambda}^{x,y}\}$ is an average (e.g. mean) value of $E_{th,\lambda}^{x,y}$. Since the dispersion of $E_{th,\lambda}^{x,y}$ around their mean value is generally small (within a factor of two at the most), the replacement of $c_\lambda E_{th,\lambda}^{x,y}$ by $a_\lambda = $ const in the argument of the logarithm introduces only an insignificant error (smaller than $\ln2/\varepsilon$) in the reduced energy region where the logarithmic factor in Eq. (10) considerably affects the cross-section value (i.e. at $\varepsilon \gg 1$). Defining now a reduced (scaled) total cross-section by the relation

$$\sigma_{0\lambda}^{tot}(\varepsilon) = \sigma_\lambda^{tot}(\varepsilon)\, E_{th,\lambda}^{x,y}/F_\lambda(x,y) \qquad (11)$$

one obtains from Eq. (10)

$$\sigma_{0\lambda}^{\text{tot}}(\varepsilon) = A_\lambda \, (1-1/\varepsilon)^{\alpha_\lambda} \, \varepsilon^{-1} \, ln(e + a_\lambda \varepsilon) \, (10^{-16} \, \text{cm}^2) \quad (12)$$

The scaled cross-section for the process $\lambda$ is a universal function that depends only on the scaled (reduced) energy $\varepsilon$.

The constants $A_\lambda$, $\alpha_\lambda$ and $a_\lambda$ for the processes $\lambda = 1b, 2, 3, 4$ have the following values:

$$A_{1b} = 34.6, \; \alpha_{1b} = 3.0, \; a_{1b} = 1.27$$

$$A_2 = 84.0, \; \alpha_2 = 3.0, \; a_2 = 0.96$$

$$A_3 = 29.4, \; \alpha_3 = 2.5, \; a_3 = 7.02$$

$$A_4 = 30.1, \; \alpha_4 = 1.55, \; a_4 = 14.5$$

The scaling functions $F_\lambda(x,y)$ for these processes have the forms:

$$F_{1b}(x,y) = (1 + 0.29y) + 1.25(x-1)$$
$$[0.28(x-1) - 0.36y/x^2] \quad (13a)$$

$$F_2(x,y) = (1 + 0.373y) + 0.47(x-1)$$
$$\{[1 + (x+5.65)/x] - 0.655y \, (1 - \delta_{x,1})/$$
$$(x-1)]\} \quad (13b)$$

$$F_3(x,y) = 1 + 0.71(y-1) + (x-1)\{0.45 +$$
$$[0.19y(1 - \delta_{x,1})/(x-1)]\} \quad (13c)$$

$$F_4(x,y) = 1 + 0.086(y-1) + (x-1)$$
$$[0.40 + 0.488y/x] \quad (13d)$$

where $\delta_{i,j}$ is the Kronecker symbol.

The y and x linearity of $F_\lambda(x,y)$ for $\lambda = 2, 3, 4$ is obvious from the above expressions. For $F_{1b}(x,y)$, the y linearity is also obvious, while its x linearity is violated for high values of x. This is a consequence of the small x values ($x = 1, 2, 3$) used in the fitting procedure and not of the invalidity of additivity rules. However, for $x = 1, 2, 3$ $F_{1b}(x,y)$ remains linear in x.

For the process of dissociative recombination of electrons on hydrocarbon ions (5), there are not sufficient experimental cross-section data for derivation of a general form of the cross-section for all $C_xH_y^+$ ions ($x = 1, 2, 3$). However, sufficient experimental data exist for the rate coefficients of these reactions that allow determination of the scaling functions $L_x^{(5)}(y)$, $x = 1, 2, 3$ for this process [7, 8]. Furthermore, the $L_x^{(5)}(y)$ functions can be combined into one scaling function $F_5(x,y)$ that allows representation of the total rate coefficients for the dissociative recombination process in a unified form:

$$K_5^{\text{tot}}(T) = 4.15 \, F_5(x,y) \, T^{-1/2}$$
$$(1 + 0.27T^{0.55})^{-1} \, (10^{-9} \, \text{cm}^3/\text{s}) \quad (14)$$

where the (electron) temperature T is expressed in eV units, and $F_5(x,y)$ has the form:

$$F_5(x,y) = 1 + 6.48(x-1) \, [1 + 1.75(x-2)/x^2]$$
$$+ 2y[1 + 0.776(x-1)/(x-0.95)^{2.62}] \quad (15)$$

The scaling properties of $K_5^{\text{tot}}(T)$ are obvious from Eq. (14), and the reduced rate coefficient:

$$K_{0,5}^{\text{tot}}(T) = K_5^{\text{tot}}(T)/F_5(x,y) \quad (16)$$

is a universal function of T.

### 3.2. Charge and particle exchange processes

The rate coefficients for the total charge and particle exchange processes in proton collisions with $C_xH_y$ molecules, $K_{CX}^{\text{tot}}$, in the thermal energy region are known from astrophysical literature [14]. Using these rate coefficients, the cross-sections for the electron capture and particle exchange processes (6a) and (6b), respectively, can be written as [6]:

$$\sigma_{CX}^{(a)} = 7.26 \, R_{CX}^{(a)} K_{CX}^{\text{tot}} \, E^{-1/2} \, (10^{-16} \, \text{cm}^2) \quad (17a)$$

$$\sigma_{CX}^{(b)} = 7.26 \, R_{CX}^{(b)} K_{CX}^{\text{tot}} \, E^{-1/2} (1 + aE^\beta)^{-1}$$
$$(10^{-16} \, \text{cm}^2) \quad (17b)$$

where $K_{CX}^{\text{tot}}$ is expressed in units of $10^{-9}$ cm$^3$/s, E is the relative collision energy, expressed in eV units, $R_{CX}^{(a)}$ and $R_{CX}^{(b)}$ are the branching ratios for the reaction channels (6a) and (6b), respectively, and $a$ and $\beta$ are known constants [7, 8]. The validity of the above cross-sections can be extended up to the region of about 1 eV. For higher collision energies the particle exchange cross-section $\sigma_{CX}^{(b)}$ decreases very rapidly ($\beta = 2.5$–3) and becomes negligible with respect to the electron capture cross-section. At these higher energies (above ~5 eV), the cross-sections of resonant ($y \geq x + 2$) charge exchange (electron capture) reactions continue to be large and in a wide energy region (up to 10–20 keV) can all be represented in a unified form [8]:

$$\sigma_{CX,\text{res}}^{(a)} = 2.76 \, (Ry/I_p^{x,y}) \, y^{1/2} \, E^{-0.14} \, (10^{-15} \, \text{cm}^2) \quad (18)$$

where $I_p^{x,y}$ is the ionization potential of the $C_xH_y$ molecule (expressed in eV units), Ry = 13.595 eV, and E is the collision energy (expressed in eV units). The scaling property of $\sigma_{CX,\text{res}}^{(a)}$ is obvious from Eq.(18). The reduced cross-section:

$$\sigma_{CX,\text{res},0}^{(a)} = (I_p^{x,y}/Ry) \, y^{-1/2} \, \sigma_{CX,\text{res}}^{(a)} =$$
$$2.76 \, E^{-0.14} \, (10^{-15} \, \text{cm}^2) \quad (19)$$

depends on the collision energy E only.

The cross-sections of non-resonant charge exchange reactions are characterized by a broad maximum in the energy region 10–30 keV with a rapid decrease on both sides of the maximum. For collision energies below 1–10 eV, however, the cross-sections of these reactions start to increase with decreasing energy, reaching their limiting values in the thermal energy region given by Eq. (17a). Analytic expressions for these cross-sections are given in Refs [7, 8].

## 3.3. Accuracy of unified total cross-sections

The accuracy of the unified analytic expressions for the total cross-sections of processes (1b)–(6) is different for different processes and families of hydrocarbons. It also varies with the energy region; at the higher energies it is usually better than in the threshold region. The estimated uncertainties of total cross-sections represented by the formulae given in the above sub-sections are as follows (for all E, if otherwise not specified):

$\lambda = 1b$: smaller than 70% for all x;

$\lambda = 2$: smaller than 20% for x = 1, below 50% for x = 2, and below 70% for x = 3;

$\lambda = 3, 4$: smaller than 50% for all x;

$\lambda = 5$; smaller than 30–40% for all x and E below ~ 20–30 eV;

$\lambda = 6a$ (res.): smaller than 20% for E in the range $0.1–10^4$ eV.

It should be noted that the analytic representations of total cross-sections in the form of Eq. (9) (i.e. for each x separately), provided in Refs [7, 8], have much higher accuracies than those of the unified formulae presented here. Moreover, the available experimental cross-sections for certain processes and specific targets have been fitted directly to the expressions of the form (9), or even to more involved analytic expressions, ensuring an accuracy close to that of the fitted original data (that in many cases is better than 15–20%).

## 4. Determination of dissociative reaction channels

The experimental studies of processes (1)–(6) usually provide information only for the total cross-sections. Only in the case of electron impact ionization of a limited number of $C_xH_y$ molecules, the partial cross-sections for production of specific ion fragments have been measured. These ion production cross-sections, however, are in many cases also composite cross-sections, since a given ion production process may include several neutral fragmentation sub-channels. The main problem in experimental determination of individual reaction channel cross-sections is related to the difficulty of detection of neutral reaction products in coincidence (and per se as well, when they are not excited, as it is usually the case). Therefore, when constructing a complete cross-section database for electron impact collision processes of hydrocarbon species, one of the main problems is the determination of the most important reaction channels contributing to the total reaction cross-section. For the dissociative processes (1b)–(4) one can use, as a guiding principle, the fact that all these processes involve an electronic (excitation) transition to a dissociative molecular state and that the maximum value of the excitation cross-

section is inversely proportional to the square of transition (threshold) energy. Therefore, the expectation that reaction channels with smaller thresholds will give the main contribution to the total reaction cross-section seems to be reasonably founded. The existing experimental partial cross-sections for dissociative ionization also abundantly confirm this expectation that follows from simple theoretical models (such as the Born-Bethe approximation and some classical models). The threshold energies for various reaction channels can be estimated on the basis of existing tables for thermochemical properties (such as enthalpy, ionization energy, etc) of atomic and molecular species (see, e.g. Ref. [2]) and, when necessary, by using reasonable assumptions about the range of excitation energies of dissociative states. Such an approach has been followed in Refs [7, 8] and tested on the existing experimental material.

In the case of a dissociative recombination process that proceeds with no threshold, the fragmentation patterns are less clear, but the existing experimental information still can provide useful guidance. The determination of the important dissociative channels accompanying the particle exchange process (6b) can be based on the reaction exothermicity, with possible inclusion of internal degrees of freedom of the fragments.

Another important issue related to the partial (channel) cross-sections is the determination of their contribution to the total cross-section (their branching ratio, see Eq. (8)). In the case of processes (1b)–(4) this can be done by an analysis of near threshold behaviour of the corresponding total cross-section, the details of this analysis being given in Ref. [7]. For the dissociative recombination process (5) measurements of the branching ratios have been performed recently for a number of hydrocarbon ions that give sufficient guidance for the assignment of branching ratios in cases where their direct measurement has not yet been performed.

## 5. Concluding remarks

In the present paper, we have briefly presented the status of cross-section database for the most important collision processes (1)–(6) of hydrocarbon molecules $C_xH_y$ ($x \leq 1, 2, 3; 1 \leq y \leq 2x + 2$) and their ions with electrons and protons taking place in a fusion divertor plasma. The cross-section database for these processes is contained in the publications [7, 8], where additional information about the reaction energetics (energy loss of projectile/energy gain of products) is also given. The total number of important reaction channels in the database exceeds 300 and it is obvious that it is impossible to present the details here. We have, therefore, limited ourselves to the presentation of a unified total cross-section for processes (1b–4, 6a) and the total reaction rate coefficient for process (5). In order to calculate the total cross-section for processes (1b–4) on the basis of Eq. (10) for any hydrocarbon species, one needs only the smallest threshold energy of that species for the

considered process (available, e.g., in Refs [7, 8]). The rate coefficient for the total dissociative electron recombination on any hydrocarbon ion can be calculated by using Eq. (14) alone. Finally, the cross-section calculation for resonant charge exchange of protons on hydrocarbon molecules with $y \geq x + 2$ in the energy range below ~10 keV can be done by using Eq. (18), in which only the ionization potential of that molecule is required (available in Ref. [2] or [8]). Such cross-section estimates have an accuracy specified in sub-section 3.3.

It should be noted that the database for collision processes of hydrocarbon species with electrons and protons contained in Refs [7, 8], although the much more elaborate and of superior accuracy with respect to other similar databases (e.g. Ref. [3, 4]), it still contains significant uncertainties, especially in its parts related to the partial (channel) cross-sections and reaction energetics. The source of these uncertainties is the lack of quantum chemistry information on the excited dissociative states of hydrocarbon molecules and their ions, through which the majority of these processes proceed. Such information is the prerequisite for making the next serious step in constructing a more reliable database for these species.

## References

[1]    HAASZ, A.A., STEPHENS, J.A., VIETZKE, E., et al., Atom. Plasma-Mater. Interact. Data Fusion **7** part A (1998) 5.

[2]    www.NIST Chemistry WebBook (2001).

[3]    EHRHARDT, A.B., LANGER, W.D., "Collision processes of hydrocarbons in hydrogen plasmas", Report PPPL-2477, Princeton Plasma Physics Laboratory, Princeton, NJ, Sept. 1987.

[4]    ALMAN, D.A., RUZIC, D.N., BROOKS, J.N., Phys. Plasmas **7** (2000) 1421.

[5]    JANEV, R.K., WANG, J.G., MURAKAMI, I., KATO, T., "Cross-sections and rate coefficients for electron-impact ionization of hydrocarbon molecules", Report NIFS-DATA-68, National Institute for Fusion Science, Tokai, Japan, Oct. 2001.

[6]    JANEV, R. K., WANG, J. G., KATO, T., "Cross-sections and rate coefficients for charge exchange reactions of protons with hydrocarbon molecules", Report NIFS-DATA-64, National Institute for Fusion Science, Tokai, Japan, May 2001.

[7]    JANEV, R.K., REITER, D., Phys. Plasmas **9** (2002) 4071.

[8]    JANEV, R.K., REITER, D., Phys. Plasmas **11** (2004) 780.

[9]    BENSON, S.W., BUSS, J.H., J. Chem. Phys. **29** (1958) 546.

[10]   BATES, D.R., Int. J. Mass-Spectrom. Ion Processes **8** (1987) 1.

[11]   SCHRAM, B.L., van der WIEL, M.J., de HEER, F.J., MOUSTAFA, H.R., J. Chem. Phys. **44** (1966) 49.

[12]   MELTON, C.E., J. Chem. Phys. **37** (1962) 562.

[13]   JANEV, R.K., REITER, D., J. Nucl. Materials **313–316** (2003) 1202.

[14]   MILLAR, T.J., FACQUHAR, R.R.A., WILLACY, K., Astron. Astrophys. Suppl. Ser. **121** (1997) 139.

# Photoabsorption, photoionization, and neutral dissociation cross-sections of hydrocarbon moloecules: Physicochemical aspects of molecular processes in fusion edge plasmas

*Y. Hatano*

Department of Molecular and Material Sciences, Kyushu University, Kasuga-shi, Fukuoka 816-8580, and Department of Chemistry, Tokyo Institute of Technology, Meguro-ku, Tokyo152-8551, Japan
Present address: Advanced Research Centre, Japan Atomic Energy Agency, 2-4 Shirakata Shirane, Tokai-mura, Naka-gun, Ibaraki 319-1195, Japan

**Abstract**

A survey is given of recent progress in the measurements of absolute cross-sections for photoabsorption, photoionization, and neutral dissociation of simple and complex molecules in the vacuum ultraviolet region, where a major part of their oscillator strength distributions due to the interactions of photons with molecules exists. Emphasis is placed on the discussion of the neutral dissociation (i.e. the dissociative excitation) of these molecules which has been considered as one of the most difficult processes to be studied experimentally. From the viewpoints of the studies on molecular processes in fusion edge plasmas, simple hydrocarbon molecules are chosen for the discussion of the measured cross-section values and the spectroscopy and dynamics of the corresponding processes. It has been shown that these optical cross-section data are of great importance to understand the fundamental processes, not only in photon collision induced reactions but also in electron collision induced reactions.

## 1. Introduction

A decisive step in the physical and physicochemical stages of the fundamental processes in the phenomena in ionized gases such as molecular processes in fusion edge plasmas is collisions of electrons in a wide energy range with molecules [1–4].

Ionization and excitation of molecules in collisions with electrons with energy higher than about $10^2$ eV are well elucidated quantitatively by the Born–Bethe theory [5]. This result has been utilized to obtain optical cross-section values from the electron energy loss experiments with high energy incident electrons as virtual photons [6] because the optical cross-sections, particularly in the vacuum ultraviolet (VUV) region, have not been obtained easily using real photons. Platzman [7] showed in the theoretical analysis of the inter-actions of ionizing radiation with molecules in which collisions of electrons in a wide energy range with molecules are important that the number of product species $j$ formed per unit energy absorbed by a molecule is approxi-mately proportional to the dipole matrix element squared to form $j$, $M_j^2$, which is written as follows:

$$M_j^2 = (R/E_j) f_j (E_j), \qquad (1)$$

Where $f$, is the optical oscillator strength to form $j$ and $E$, is its excitation energy. $R$ is the Rydberg energy. The dipole matrix element for ionization is given by:

$$M_i^2 = \int_I^\infty \eta (E) \frac{R}{E} \frac{df}{dE} dE \qquad (2)$$

where $\eta(E)$ is the quantum yield for ionization at the excitation energy $E$ and $df/dE$ is the oscillator strength distri-bution. $I$ represents the first ionization potential. The quantum yield for ionization is given by:

$$\eta(E) = \sigma_i(E) / \sigma_t(E) \qquad (3)$$

where $\sigma_i(E)$ and $\sigma_t(E)$ are, respectively, the photoionization cross-section and the photoabsorption cross-section.

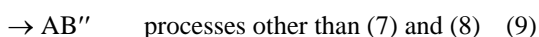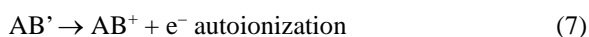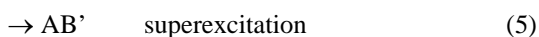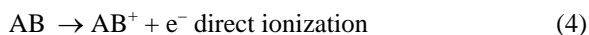This theory, which is called the optical approximation, is reasonable when it is not applied to a narrow specific excitation energy range near its threshold, where optically forbidden transitions are relatively important in comparison with optically allowed ones but applied to a wide excitation energy range [1–4, 8–10]. Optical cross-section data are thus of fundamental importance to understand fundamental

processes not only in the photon collision induced reactions but also in the electron collision induced reactions [1–4, 8–10].

Optical oscillator strength values had long been measured for various molecules in the wavelength regions at least longer than the near ultraviolet (UV) region, whereas until recently measurements in the wavelength region shorter than the LiF cutoff at 105nm (at which the photon energy is 11.8 eV) were relatively few because of experimental difficulties in obtaining appropriate photon sources and because no suitable window materials were available. The cutoff energy of 11.8 eV corresponds, roughly speaking, to the ionization potentials of commonly occurring molecules. The sum of the oscillator strengths below 11.8 eV amounts to only a few per cent of the total, which is equal to the total number of electrons in a molecule, $Z$ according to the Thomas-Kuhn-Reiche (TKR) sum rule [1, 2, 11–16]. The absorption in the VUV and soft X ray (VUV-SX) region is much stronger than in all other wavelength regions. Since there have been remarkable advances in synchrotron radiation (SR) research and related experimental techniques in the VUV-SX region, many measurements in this region are now available [1, 2, 11–16].

Platzman [7, 17] considered theoretically the interactions of ionizing radiation with atoms and molecules and pointed out that atoms and molecules receive a large fraction of energy from ionizing radiation with a spectrum determined by their optical oscillator strength distributions according to the optical approximation. He presented the idea of an important role of highly excited electronic states, particularly superexcited states, in the primary action of ionizing radiation. This idea has recently been substantiated experimentally [1, 12–16, 18–21]. In the following, the spectroscopy and dynamics studies of molecular superexcited states are briefly summarized.

The absorption of energy by a molecule in the electronically ground state changes its electronic state from the ground state to a final excited or ionized state as follows [13, 14, 16]:

$$AB \rightarrow AB^+ + e^- \quad \text{direct ionization} \quad (4)$$

$$\rightarrow AB' \qquad \text{superexcitation} \quad (5)$$

$$\rightarrow AB^* \qquad \text{excitation} \quad (6)$$

$$AB' \rightarrow AB^+ + e^- \quad \text{autoionization} \quad (7)$$

$$\rightarrow A + B \qquad \text{dissociation} \quad (8)$$

$$\rightarrow AB'' \qquad \text{processes other than (7) and (8)} \quad (9)$$

When a molecule AB receives energy which is larger than its $I$, AB is directly ionized and is excited to form AB', which was named by Platzman a 'superexcited' molecule. The superexcited AB' can ionize or dissociate into neutral fragments. Since $\eta$ is defined by Eq. (3), the value of $1-\eta$ shows the importance of the dissociation process in the total decay channels of AB' because process (9) is not so

important in the decay of such extremely highly excited states. As one of process (9), ion pair formation, $AB' \rightarrow A^+ + B^-$, has been extensively studied to clarify the dynamics of superexcited molecules although its cross-section is much smaller than those of processes (7) and (8). The value of $\eta$ is, therefore, smaller than unity in the energy range even above $I$, which means that the molecules excited into this energy range are not always ionized, but use their energy for processes other than ionization. It is concluded, therefore, that $\sigma_t$ is the sum of the cross-sections for processes (4), (5), and (6), and that $\sigma_i$ is that of the cross-sections for processes (4) and (7). The cross-section for process (8), the neutral dissociation or the DE, is thus given by $\sigma_t - \sigma_i \, (\equiv \sigma_d)$.

The Platzman's concept of the superexcited state had made a profound influence on the science of excited states and motivated people in a wide field to find new objectives of research. In order to study experimentally the superexcited states or to substantiate, Platzman's ideas, it was necessary to find the way to produce superexcited states which is classified as follows [13, 14, 16, 20, 21]:

(a)　Electron impact spectroscopy;

(b)　Discharge lamp photon impact spectroscopy;

(c)　Laser photon impact spectroscopy;

(d)　SR photon impact spectroscopy;

(e)　Coincident electron energy loss spectroscopy.

Electron beams and discharge lamp photons were mainly used in the 1960s and 1970s, and still are now, for this purpose, whereas after the 1980s laser multiphotons and SR have also been used. Details of the electronic states of superexcited molecules at least in the optically allowed states and the mechanism of their autoionization and dissociation have been quickly clarified, mainly by means of SR as an excitation source [1, 12–16, 18–21]. The coincident electron energy loss spectroscopy has been recently developed as a new experimental method for molecular optically forbidden superexcited states [20, 22].

The spectroscopy and dynamics of the formation and decay processes of molecular superexcited states, in particular the neutral dissociation process, have been recently surveyed comprehensively by the present author and his coworkers [11–16, 18–22]. It is concluded in these review and feature papers that superexcited states are molecular high Rydberg states converging to each ion state which are vibrationally/rotationally, doubly or inner core excited. Non–Rydberg superexcited states are also observed. The dissociation dynamics as well as the products of dissociation of these states are highly different from those of the states excited below about ionization thresholds. Neutral dissociation is unexpectedly important in comparison with ionization when molecules absorb energy in the region above their ionization thresholds.

The present paper introduces important features of these conclusions with some examples of molecules. From

the viewpoints of the studies of molecular processes in fusion edge plasmas simple hydrocarbon molecules are also chosen for the discussion of the measured cross-section values and the spectroscopy and dynamics of the corresponding processes.

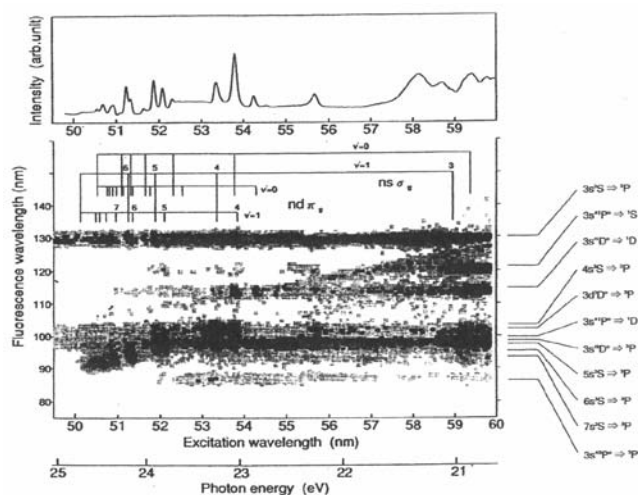## 2.    Dissociative excitation of simple molecules

Primary and secondary processes following the photoabsorption of molecules in the VUV region are strongly influenced by superexcited states. Among various decay processes of molecular superexcited states the dissociation, especially neutral dissociation, in competition with the autoionization has been shown to play an important role, as briefly introduced in the preceding section, in the VUV photophysics and photochemistry above ionization thresholds. The difficulties of detecting neutral products, however, hampered the experimental investigation of neutral dissociation. Thus, in the region far beyond the ionization threshold, most of the experimental studies have been restricted to those of photoionization and the measurements of photoabsorption spectra. Since, however, they are not so sensitive to superexcitation owing to a huge contribution from direct ionization, most superexcited states, especially those having repulsive potential curves or surfaces, had not yet been revealed even in diatomic molecules.

The observation of neutral dissociation of simple molecules by detecting undispersed fluorescence from excited fragments using optical filters has been shown to be a useful tool for studying the decay of superexcited states. This fluorescence technique has made it possible to get the information on repulsive potential structures of molecular superexcited states, as well as on well defined vibrational levels of bound superexcited states. However, it has not provided detailed information on particular dissociation products and precise dissociation limits, which is indispensable for understanding the dissociation and autoionization dynamics of superexcited states.

Since the spectroscopy and dynamics of the superexcited states of molecular hydrogen and other simple molecules have been comprehensively surveyed elsewhere [11–16, 18–22], these are only briefly introduced below.

From a careful and comprehensive survey of the potential energy curves or surfaces of these simple molecules and of the related data on the interaction of photons and electrons with these molecules, it has been concluded that there has been very little information on the superexcited states, i.e. on the neutral excited states in the energy range above the ionization thresholds, in particular on their dissociation dynamics.

A powerful new experimental method, the two-dimensional fluorescence spectroscopy, has therefore been developed to reveal a birds eye view of the neutral dissociation dynamics of molecular superexcited states in a wide excitation energy range [23]. In the two-dimensional fluorescence spectroscopy, the yield spectra of dispersed



**Figure 1.** Two-dimensional fluorescence spectrum of excited atomic oxygen produced from the neutral dissociation of superexcited molecular oxygen as a function of both the excitation photon wavelength and fluorescence wavelength in the photoexciation of molecular oxygen [23].

fluorescence radiation or the dispersed fluorescence excitation spectra emitted from neutral fragments produced by the dissociation of molecular superexcited states have been simultaneously measured as a function of the excitation wavelength of SR in a wide range. This method has been applied to $O_2$, $N_2$, CO, and $N_2O$ [13, 23–27]. The potential energy curves or surfaces as well as their dissociation dynamics, which are vibrationally energy resolved, have been thus substantiated experimentally for the first time.

In the two-dimensional spectroscopy of the dissociation dynamics of state resolved molecular superexcited states, monochromatized SR is focused into a gas cell that contains target molecules. VUV fluorescence emitted from dissociation fragments produced from superexcited states is dispersed, as shown in Fig. 1 [23], by a secondary monochromator equipped with a holographic grating. A fluorescence spectrum is recorded using a resistive anode type position sensitive detector (PSD) behind a microchannel plate (MCP) [27].

Figure 1 shows an example of the two-dimensional fluorescence excitation spectra emitted from dissociatively excited neutral oxygen atoms, $O^*$, which are formed in the photoexcitation of $O_2$ as a function of the excitation wavelength $\lambda_{ex}$ for $50 \leq \lambda_{ex} \leq 60$ nm (24.8–20 eV) [23]. Each of the horizontal line structures in Fig. 1 presents the partial fluorescence yield from individual $O^*$ atoms produced in the neutral dissociation of superexcited molecular oxygen $O_2^{**}$. Figure 1 shows clearly the following two striking behaviour of the dissociation dynamics of vibrationally resolved superexcited molecular oxygen. One is the state to selective neutral dissociation, in which the n quantum number is conserved,

$$O_2^{**} (c^4\Sigma_u^- ns\sigma_g \text{ or } nd\pi_g) \rightarrow O^* (ns^3S) + O(^3P) \quad (10)$$

79

The other is a vibrationally selective neutral dissociation. In process (10), the dissociation of the v' = 1 state of $O_2^{**}$ is much more enhanced than that of the v' = 0 state of $O_2^{**}$. This is clear evidence of a vibrationally resolved tunneling predissociation.

## 3. Oscillator strength distributions and photoionization quantum yields of hydrocarbons and other polyatomic molecules

To understand the dynamics of superexcited states of molecules, in general, as pointed out in the introduction, it is necessary to measure absolute cross-sections of photoabsorption, photoionization, and neutral dissociation processes as well as absolute photoionization quantum yields [11–16]. These cross-section values had been measured for a variety of molecules only in the wavelength region longer than the LiF cutoff at 105 nm, while those in the wavelength region shorter than 105 nm had been very few. Recently, however, those cross-section values for both simple and polyatomic molecules have been measured and critically compiled [21]. When the TKR sum rule is compared with the sum of the obtained $\sigma_t$ or $f_j$ values for a molecule in the wavelength region longer than 105 nm which corresponds, roughly speaking, to about the first ionization potential of most molecules, it is found that the sum of the $f_j$ values corresponds to only less than a few per cent of the value of Z. It is, therefore, concluded that the interaction of a photon with a molecule in the VUV-SX region, where SR is the most promising photon source, is predominant over all the other wavelength regions.

Optical oscillator strength distribution is, therefore, of fundamental importance in understanding the interaction of photons with molecules, providing important information about energy spectra for the formation of superexcited states. Instead of measuring these cross-sections for a variety of complex molecules at random, these cross-sections for molecules in several stereo-isomer series have been systematically measured and compared with one another or with the sum rule [28–31]. Since isomer molecules consist of the same kind and the same number of atoms, the $df/dE$ of isomers is expected to have the following properties:

(a) The sum of $df/dE$ of an isomer over all the energy region is expected to be equal to that of another isomer, and also to the number of electrons in the molecule, according to the TKR sum rule.

(b) The gross features of the $df/dE$ of isomers are expected to be almost identical with each other in the wavelength region where inner core electrons are excited, because the molecular structure of isomers would have relatively little influence on the excitation of inner core electrons. Moreover, the value of $df/dE$ in such a wavelength region would be almost equal to the sum of the $df/dE$ values of the constituent atoms.
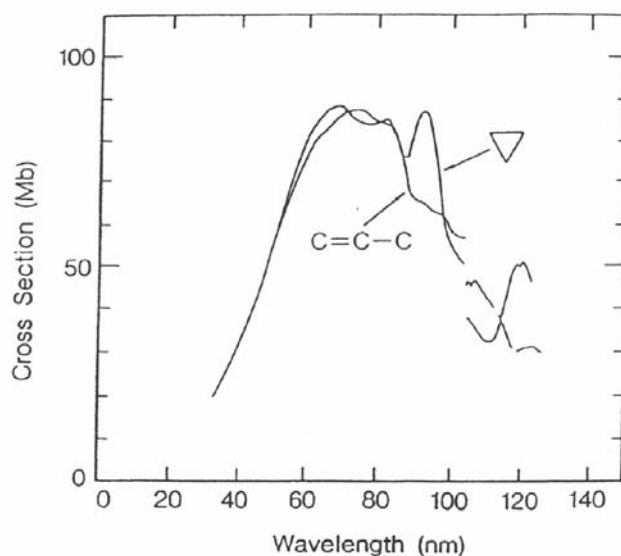


**Figure 2.** Absolute photoabsorption cross-sections of cyclopropane and propylene [28].

With the above-mentioned expectation, the photoabsorption cross-sections have been measured for isomers; $C_3H_6$ (cyclopropane and propylene), $C_4H_8$ (1-butene, isobutene, *cis*-2-butene, and *trans*-2-butene), $C_6H_{12}$ (cyclohexane, 1-hexene, and tetramethylethylene), $C_2H_6O$ (ethyl alcohol and dimethyl ether), and $C_3H_8O$ (*n*-propyl alcohol, *i*-propyl alcohol, and ethyl methyl ether) in the wavelength region from about 30 to 140 nm, and compared with one another and with the sum rule from the above viewpoints. Figure 2 shows, as an example, the absorption cross-sections, i.e. the oscillator strength distributions of $C_3H_6$ isomer molecules, cyclopropane and propylene [28]. Similar cross-section data have also been obtained for the other isomer series listed above, giving the common new features of absorption cross-sections or oscillator strength distributions summarized as follows:

(1) The $\sigma_t$ values show a maximum at about 70–80 nm (about 16–18 eV) for each molecule.

(2) In the wavelength region shorter than that at the maximum the $\sigma_t$ values are almost the same among the isomer molecules, e.g. cyclopropane and propylene as shown in Fig. 3, and equal to the sum of the cross-sections for the constituent atoms.

(3) In the longer wavelength region, the cross-sections have different peaks and shoulders depending on the isomer, i.e. on its molecular structure, as shown again in Fig. 2. The sum of the cross-sections in this wavelength region is, however, almost equal among the isomer molecules which means, therefore, that the total oscillator strength distribution normalized to Z according to the TKR sum rule can be divided to the two regions, i.e. the longer and shorter wavelength regions, and that the sum of the oscillator strength in each region do not depend on the molecular structure of an
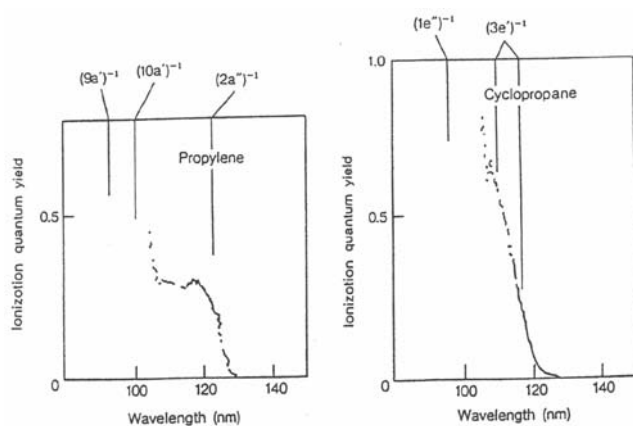
**Figure 3.** Photoionization quantum yields of cyclopropane and propylene [30].

**Table 1.** Sum of the oscillator strength distributions of cyclopropane and propylene [28].

| Wavelength (nm) | Cyclopropane | Propylene |
|---|---|---|
| Below Ip | 0.746 | 0.507 |
| Ip–105 | 0.715 | 0.666 |
| 105–35 | 11.744 | 12.176 |
| 35 > | | 10.251 |
| Total | 23.46 | 23.60 |
| Z | 24 | 24 |

isomer and is constant among the isomer molecules; in other words, that the partial sum rule satisfies the oscillator strength distribution in each region.

These results have made an important contribution to chemical physics and physical chemistry, particularly to motivate the development of new quantum chemistry [32], and have also made a helpful contribution to radiation research in estimating the energy deposition spectra of molecules in the interaction of ionizing radiation with molecules [1–4, 8–10]. The results, e.g. those in Fig. 2, well satisfy the TKR sum rule as summarized in Table 1 [28]. The agreement is extremely good between the sum of the obtained oscillator strength values partly including semi-empirical ones in the higher energy region and the number of electrons, Z. Table 1 also clearly shows that the sum of the oscillator strength distributions in the energy region below the first ionization potential occupies only a few per cent of the total and the distributions in the VUV-SX region are of great importance in understanding the ionization and excitation of molecules.

A photoionization quantum yield $\eta$, which is the absolute photoionization probability of an atom or a molecule on a single photoabsorption event or the number of electrons produced following the absorption of a single photon by a molecule, is the quantity of considerable importance to evaluate photoabsorption processes above the first ionization potential, i.e. the competition between direct ionization and excitation into the superexcited states opening to autoionization and dissociation. The measurement of $\eta$ is, therefore, of great importance for further characterizing superexcited states. However, it has been extremely difficult to measure absolute $\eta$ values.

Figure 3 shows, for example, the $\eta$ curves for cyclopropane and propylene [30]. These are very different from each other; the curve for cyclopropane increases almost monotonically and much more steeply than that for propylene, which increases and shows a step or a shoulder with decreasing wavelength. The obtained $\eta$ curves for these

molecules show common new features as functions of wavelength or photon energy; the energy difference between the first and the second ionization potentials correlates well with the shape of the $\eta$ curves. The larger in the energy difference corresponds to the longer in the step length. This result means that the $\eta$ value increases steeply in the wavelength or energy region just close to the ionization potential, and is explained by the conclusion that the most important part of the superexcited states is high Rydberg states converging to each ion state.

Figure 4 shows the ionization quantum yields for some molecules measured in the wavelength region of 54–92 nm, together with those in the wavelength region longer than 105 nm [13]. No data are shown in the wavelength region between the two because there is practically no thin metal window which is convenient for the measurement of ionization quantum yields and because there exists a relatively large effect of higher order light in this wavelength region. The results may be summarized as follows:

(i)   $\eta$ values in the region above, but close to, the first ionization potential are much less than unity, which means that most molecules are not easily ionized even when they have a sufficient amount of their internal energies. In this region, therefore, the neutral fragmentation of superexcited molecules is of great importance in the total decay channels.
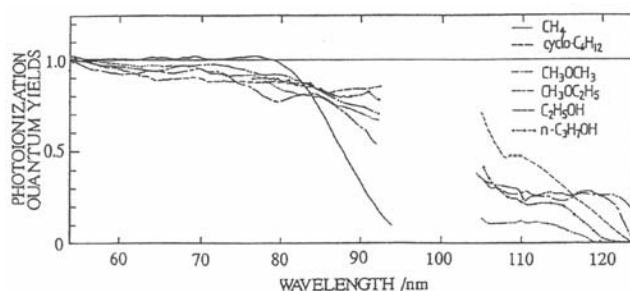


**Figure 4.** Photoionization quantum yields of several complex polyatomic molecules [13].
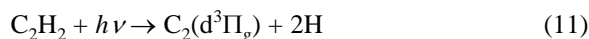
(ii) $\eta$ values do not reach unity, even in the energy range more than about 10 eV above the first ionization potential.

(iii) $\eta$ values increase with increasing photon energy and reach unity in the absolute scale at the energy range above about 23 eV (or 54 nm).

(iv) $\eta$ curves show interesting structures.

It is concluded from the results (1)–(4) that non-ionizing processes, such as the neutral fragmentation of superexcited molecules, have an important role in their decay channels. Since there exists an important part of the magnitude of the oscillator strength distributions of most molecules in the wavelength range of 60–100 nm, in which the $\eta$ values are clearly and largely deviated from unity, it is concluded in general that molecules are not easily ionized but dissociated into neutral fragments even when they have energies much larger than their ionization thresholds.

## 4. Dissociative excitation of hydrocarbons and other polyatomic molecules

Neutral fragments formed from the dissociation of superexcited molecules often have excess energies electronically, vibrationally, rotationally, and/or translationally excited, because the photon energies corresponding to the wavelengths in Fig. 4 are much higher than the bond dissociation energies to form fragments in their ground states. It is, therefore, of great interest to observe optical emissions from excited fragments as a function of wavelength, i.e. to obtain excitation spectra of optical emission and to compare with the structures in $\eta$ curves. In the following, acetylene is chosen as an example from recent experiments of a variety of kinds of polyatomic molecules for such a comparison to clarify in detail the spectroscopy and dynamics of superexcited polyatomic molecules.

The photoionization quantum yields of acetylene are compared in Fig. 5 with the excitation spectra of fluorescence from excited fragments produced in the dissociation of a superexcited acetylene molecule, providing a conclusion of the observed dissociation processes as follows [33]:

$$C_2H_2 + h\nu \rightarrow C_2(d^3\Pi_g) + 2H \tag{11}$$

$$C_2(C^1\Pi_g) + 2H \tag{12}$$

$$CH(A^2\Delta) + CH \text{ (or } CH(A^2\Delta)) \tag{13}$$

$$H(2p) + C_2H \text{ (or } C_2 + H) \tag{14}$$

The precursor superexcited states for these dissociation processes (11)–(14) have been assigned in detail to high Rydberg states and/or innervalence excited states which have been investigated theoretically.

The excitation spectrum in Fig. 5(d), as well as the corresponding dissociation (13), is of particular interest from chemical viewpoints because of a predominant
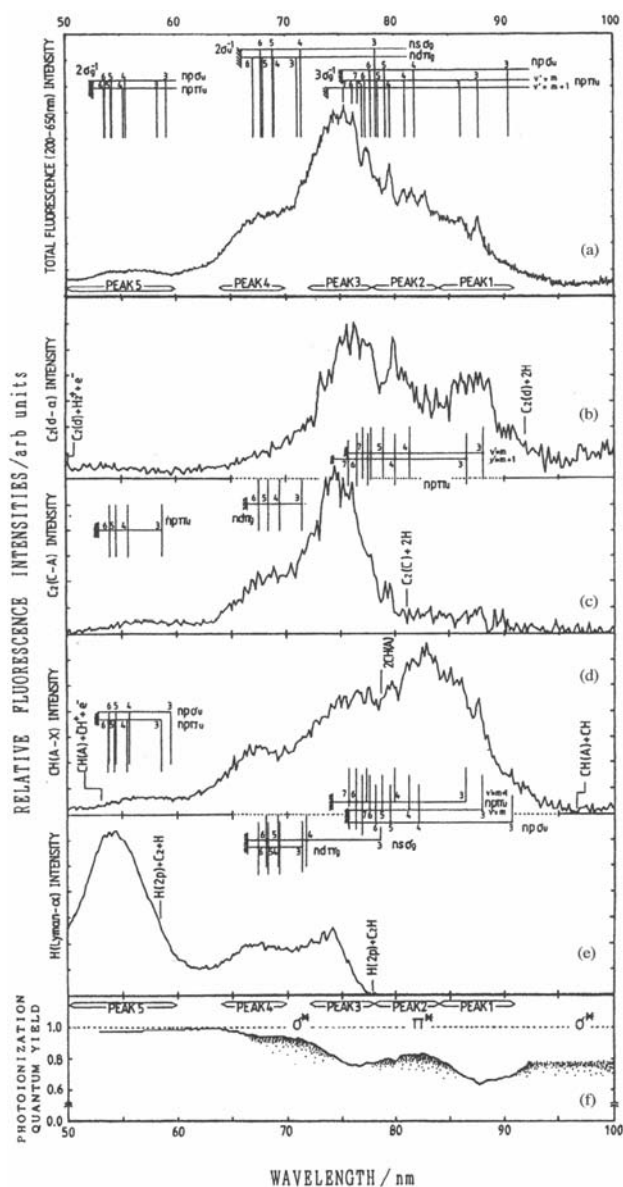


**Figure 5.** Fluorescence excitation spectra for (a) the total optical emission in 200–650 nm detection range. (b), (c), (d), and (e) are the optical emissions of the corresponding electronic transitions. (f) is the photoionization quantum yield [33].

breaking of the triple bond of acetylene in a specific energy range. Other simple hydrocarbons have also been studied to substantiate the electronic states and dissociation dynamics of the superexcited states of these molecules [34]. Figure 6 shows, for example, the absolute $\sigma_t$, $\sigma_i$, $\sigma_d$ values of methane as a function of the photon energy. The $\sigma_d$ curve clearly shows that there exist superexcited states in the energy range of 13–16 eV and in the range of 19–24 eV.

The former is assigned to the Rydberg states converging to the $(1t_2)^{-1}$ ion state, while the latter is assigned to the Rydberg states converging to the $(2a_1)^{-1}$ ion state. Excitation spectra of fluorescence emitted from dissociation fragments produced from these state assigned superexcited states are observed using the two-dimensional spectroscopy.
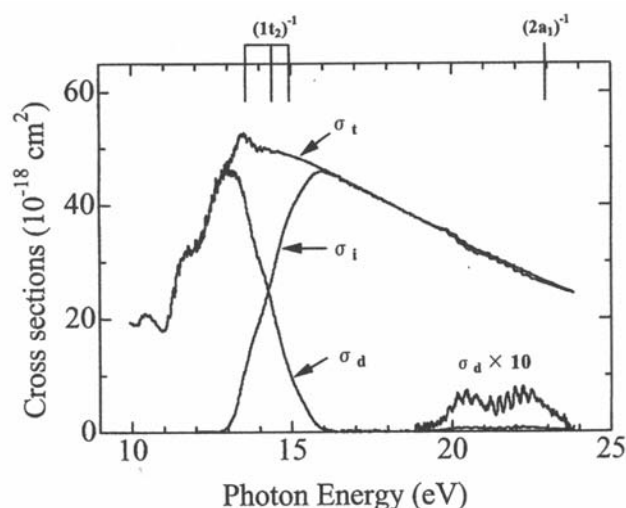
**Figure 6.** Photoabsorption, photoionization, and photodissociation cross-sections of methane as a function of photon energy [34]

## 5. Other related remarks

The information on the spectroscopy and dynamics of the formation and decay processes of molecular superexcited states or of the DE of molecules is of fundamental importance to understand the essential features of the dynamics of electron-ion and ion-ion recombination, Penning ionization, and electron attachment processes because important roles of superexcited states have been pointed out both theoretically and experimentally as collision complex species or reaction intermediate in these collision processes [13].

An important role of superexcited states of molecules and dissociation fragments formed in chemical reactions in the radiolysis of molecular compounds was first pointed out theoretically by Platzman [7, 17] and experimentally by the present author and coworkers [16, 35–38]. These investigations and similar ones [39, 40] in radiation chemistry and photochemistry had motivated electron- and photon impact experiments as described in the introduction. Based on the current status of the understanding of superexcited states, as described in the preceding sections, a similarly important role of superexcited states is also considered reasonably in other types of reaction systems such as various phenomena in ionized gases; electric discharge plasmas, particularly reactive plasmas [3], and collisions in the upper atmosphere and planetary space, and further also in fusion edge plasmas. It has been also accepted that superexcited states of molecules have an important role not only in the reaction mechanism of radiolysis but also in the energy deposition and track structure in the interaction of ionizing radiation with matter [41]. An important role of superexcited states has been also pointed out in the interpretation of the magnitude of *W* values [42].

The investigation of superexcited states in the condensed phase is closely related with that of ionization itself in the condensed phase [13]. It is a still unresolved important problem, as described below, to understand the ionization potential of condensed matter or to discriminate ionized states from highly excited states in the condensed phase. It is of great importance also to investigate in detail geminate electron-ion pairs and high Rydberg states in the condensed phase. It should be noted that a key experiment to clarify these problems, on which there have been very few reports, is the absolute measurement of ionization quantum yields in the condensed phase using SR [13].

## Acknowledgements

## References

[1] MOZUMDER, A., HATANO, Y. (Eds.), Charged Particle and Photon Interactions with Matter, Marcel Dekker, New York, 2004.
[2] HATANO, Y., INOKUTI, M., Chapter 5 in Atomic and Molecular Data for Radiotherapy and Radiation Research, IAEA-TECDOC-799, (INOKUTI, M., Ed.), IAEA, Vienna, 1995.
[3] HATANO, Y., Adv. At. Mol. Opt. Phys. **43** (2000) 231.
[4] HATANO, Y., Radiat. Phys. Chem. **67** (2003) 187.
[5] INOKUTI, M., Rev. Mod. Phys. **43** (1971) 297.
[6] CHAN, W. F., COOPER, G., BRION, C. E., Chem. Phys. **178** (1993) 387, and references therein.
[7] PLATZMAN, R.L., Radiat. Res. **17** (1962) 419.
[8] HATANO, Y., p.35 in Radiation Research, (FIELDEN, E.M., FOWLER, J.F., HENDRY, J.H., SCOTT, D., Eds), Taylor & Francis, London, 1987.
[9] HATANO, Y., p.86 in Radiation Research, 2, (HAGEN, U., HARDER, D., JUNG, H., STREFFER, C., Eds), Univ. Wurzburg Press, Wurzburg, 1995.
[10] HATANO, Y., Radiat. Environ. Biophys. **38** (1999) 239.
[11] HATANO, Y., Chapter 6 in Dynamics of Excited Molecules, (KUCHITSU, K., Ed), Elsevier, Amsterdam, 1994.
[12] HATANO, Y., p.67 in The Physics of Atomic Collisions, (DUBE, L.J., MITCHELL, J.B.A., MCCONKEY, J. W., BRION, C. E. (Eds.), AIP Press, New York, 1995.

[13] HATANO, Y., Phys. Rep. **313** (1999) 109.

[14] HATANO, Y., J. Electron Spectrosc. Relat. Phenom. **119** (2001) 107.

[15] HATANO, Y., Chapter 2 in Chemical Applications of Synchrotron Radiation, (SHAM, T.K., Ed.), World Scientific, Singapore, 2002.

[16] HATANO, Y., Bull. Chem. Soc. Japan **76** (2003) 853.

[17] PLATZMAN, R.L., Vortex **23** (1962) 372.

[18] UKAI, M., J. Electron Spectrosc. Relat. Phenom. **79** (1996) 423.

[19] KOUCHI, N., UKAI, M., HATANO, Y., J. Phys. B: At. Mol. Opt. Phys. **30** (1997) 2319.

[20] KOUCHI, N., p.301 in Photonic, Electronic, and Atomic Collisions, (AUMAYR, F., WINTER, H., Eds), World Scientific, Singapore, 1998.

[21] KAMETA, K., KOUCHI, N., HATANO, Y., p.4-1 in Interactions of Photons and Electrons with Molecules, Landolt-Boernstein, New Series, Vol. I/17C, (ITIKAWA, Y., Ed.), Springer-Verlag, Berlin, 2003.

[22] ODAGIRI, T., KOUCHI, N., Phys. Scripta **T110** (2004) 183.

[23] UKAI, M., et al., Phys. Rev. Lett. **74** (1995) 239.

[24] EHRESMANN, A., et al., J. Phys. B: At. Mol. Opt. Phys. **28** (1995) 5283.

[25] EHRESMANN, A., et al., J. Phys. B: At. Mol. Opt. Phys. **29** (1996) 3629.

[26] EHRESMANN, A., et al., J. Phys. B: At. Mol. Opt. Phys. **30** (1997) 1907.

[27] MACHIDA, S., et al., J. Phys. Chem. A **101** (1997) 656.

[28] KOIZUMI, H., et al., J. Chem. Phys. **82** (1985) 4856.

[29] KOIZUMI, H., et al., J. Chem. Phys. **85** (1986) 4276.

[30] KOIZUMI, H., et al., Radiat. Phys. Chem. **32** (1988) 111.

[31] KOIZUMI, H., SHINSAKA, K., HATANO, Y., Radiat. Phys. Chem. **34** (1989) 87.

[32] NAKATSUKASA, T., YABANA, K., J. Chem. Phys. **114** (2001) 2550.

[33] UKAI, M., et al., J. Chem. Phys. **95** (1991) 4142.

[34] KAMETA, K., KOUCHI, N., UKAI, M., HATANO, Y., J. Electron Spectrosc. Relat. Phenom. **123** (2002) 225.

[35] HATANO, Y., SHIDA, S., SATO, S., Bull. Chem. Soc. Japan **41** (1968) 1120.

[36] HATANO, Y., Bull. Chem. Soc. Japan **41** (1968) 1126.

[37] HATANO, Y., SHIDA, S., INOKUTI, M., J. Chem. Phys. **48** (1968) 940.

[38] SHIDA, S., HATANO, Y., Int. J. Radiat. Phys. Chem. **8** (1976) 171.

[39] MAKAROV, V.I., POLAK, L.S., High Energy Chem. **4** (1970) 1.

[40] AUSLOOS, P.J., LIAS, S.G., Annu. Rev. Phys. Chem. **22** (1971) 85.

[41] PARETZKE, H.G., p.89 in Kinetics of Nonhomogeneous Processes (FREEMAN, G.R., Ed.), Wiley, New York, 1987.

[42] KIMURA, M., KOWARI, K., INOKUTI, M., BRONIC, I.K., SRDOC, D., OBELIC, B., Radiat. Res. **125** (1991) 237.